

**Phenomenological Aspects of Neutrino
Masses, Mixings and Oscillations**

A thesis submitted in partial fulfillment of
the requirements for the degree of

Doctor of Philosophy

by

Newton Nath

(Roll No. : 11330024)

Under the supervision of

Dr. Srubabati Goswami

Professor

Theoretical Physics Division

Physical Research Laboratory, Ahmedabad, India.



DISCIPLINE OF PHYSICS

INDIAN INSTITUTE OF TECHNOLOGY GANDHINAGAR

Year of submission: 2017

*to
my dida
&
maa-bappi*

Declaration

I declare that this written submission represents my ideas in my own words and where others' ideas or words have been included, I have adequately cited and referenced the original sources. I also declare that I have adhered to all principles of academic honesty and integrity and have not misrepresented or fabricated or falsified any idea/data/fact/source in my submission. I understand that any violation of the above will be cause for disciplinary action by the Institute and can also evoke penal action from the sources which have thus not been properly cited or from whom proper permission has not been taken when needed.

Signature

Name: Newton Nath

(Roll No: 11330024)

Date:

CERTIFICATE

It is certified that the work contained in the thesis titled “**Phenomenological Aspects of Neutrino Masses, Mixings and Oscillations**” by **Mr. Newton Nath** (Roll No. 11330024), has been carried out under my supervision and that this work has not been submitted elsewhere for a degree.

Prof. Srubabati Goswami
(Thesis Supervisor)
Professor,
Theoretical Physics Division
Physical Research Laboratory,
Ahmedabad, India.

Date:

Acknowledgments

A ‘sweet’ and ‘sour’ journey of long five years of PhD ends with the submission of the thesis. A journey which could not have been possible without the involvement of some wonderful people. It gives me immense pleasure to take this opportunity to express my sincere gratitude to all of them.

Firstly, I would like to express my deepest respect and sincere thanks to my advisor Prof. Srubabati Goswami for her continuous support during my Ph.D. tenure. I have extremely benefited from her expertise on the subject, her insight and her ability to explain the physics issues in a lucid manner. I am thankful to her for introducing me to the fascinating and challenging world of neutrinos. Her support and encouragement has allowed me to move ahead and inspired me to work harder. Moreover, she gave me the moral support and the freedom that I needed to move forward. It was a great experience working with her and I consider myself fortunate to have her as my thesis supervisor.

I also feel fortunate enough to get an opportunity to work with Prof. Anjan Joshipura. I find no words to express his kind behavior. The work done with him has taught me how to be passionate about the subject on which you work and also to achieve goals which seems impossible to begin with. I am thankful to my DSC members, Prof. R. Rangarajan and Dr. P. Konar, for reviewing my thesis and motivating me constantly during this period. Their valuable comments and constructive criticisms at different stages were very much useful for my research work. I am also thankful to Prof. S. Mohanty for teaching many useful courses which had helped me to learn different aspects of high energy physics. I also thank all the members of the Theoretical Physics division for their support.

My heartfelt gratitude to Dr. Sushant K. Raut for his encouragement and guidance during my doctoral period. His friendly nature has always made me feel at ease with him. For any support during my Ph.D, I have always looked back on him. I take this opportunity to thank Dr. Monojit Ghosh, my senior, who is always with me from the day one of my Ph.D. and with whom I have enjoyed working on various research projects. I am very much indebted to him and I wholeheartedly acknowledge his help and support. I am also thankful to Dr. Pomita Ghoshal, Dr. Shivani Gupta and Dr. Deepthi K N for being wonderful collaborators, from whom I have learnt various aspects of neutrino physics.

I would like to extend my sincere thanks to Dr. Subrata Khan, Dr. Gulab Bambhaniya and Dr. Ujjal Kumar Dey from whom I learnt many aspects of particle physics. I am very pleased to acknowledge Dr. Deepthi K N, Dr. Lakshmi S Mohan and Mr. Kaustav Chakraborty for their valuable suggestions for improving

the thesis. I also extend my thanks to Mr. Chandan Gupta and Mr. Vishnudath K N for various discussions.

It gives me an immense pleasure to thank Prof. André de Gouvêa for giving me an opportunity to visit Northwestern University, Chicago, USA and to have many useful discussions regarding neutrino physics during my visit. I am also grateful to Prof. Stephen Parke for giving me a chance to visit Fermilab, USA and I acknowledge the insightful discussions.

I thank the Director, Dean, Registrar, all the members of academic committee of PRL and IIT Gandhinagar for their constant support I would like to thank all the staff members of the administration, the computer center, the library, the account section, the non-academic staff and the dispensary staff for their support. It is my duty to acknowledge HEP-INSPIRE-HEP, arXiv and ResearchGate for keeping me updated.

I am grateful to Prof. N. M. Ashok, Prof. J. Banerji, Dr. B. Bapat, Dr. R. Bhattacharyya, Dr. D. Chakrabarty, Dr. R. D. Deshpande, Dr. N. Mahajan, Dr. J. Pabari, Dr. V. K. Rai, Prof. R. Rangarajan, Dr. N. Rastogi, Prof. S. D. Rindani, Dr. L. K. Sahu, Dr. A. B. Sarbadhikari, Prof. A. D. K. Singh, Prof. K. P. Subramanian and Prof. P. Venkatakrishnan for teaching various courses during my course work at PRL. I am also thankful to Dr. N. Mahajan and Dr. D. Chakrabarty for their valuable guidance during project work done with them as a part of the course work.

I thank all the faculty members of the School of Physics, University of Hyderabad, Hyderabad who taught me during my M.Sc. I also take this opportunity to thank all the faculty members of Department of Physics, Gurucharan College, Silchar, Assam who taught me during my B.Sc. My heartiest thanks to Prof. Surajit Sen, head of the department, from whom I first heard the word ‘neutrino’ during our introductory particle physics course and also for inspiring me towards higher studies in physics.

I thank my Ph.D. batch-mates, Rahul, Jinia, Bivin, Chandana, Deepak, Dipti, Lalit, Pankaj, Venkatesh for their incredible support. I am thankful to my seniors—Fazlul, Gaveshna, Gaurav, Mansi, Ananta, Ranjita, Ila, Avdhesh, Girish C, Yashpal, Arko, Girish G, Arun, Manu, Guru, Abhaya, Tanmoy, Alok, Sanjay, Anirban, Shradhha, Ikshu, Kuldeep, Chithrabhanu, Nazim and juniors—Navpreet, Chandan, Rupa, Satish, Prahlad, Kuldeep, Jabir, Bharti, Niharika, Pradeep, Aman, Nijl, Bhavesh, Akanksha, Balbeer, Ashish, Richa, Arvind for making my stay comfortable and enjoyable at PRL.

I am grateful to the wonderful members of our PRL lunch group—Rukmani, Nabyendu, Sudip, Pankaj, Shweta, Diganta, Manpreet, Sampurn, Soumya and

Nidhi for both academic and non-academic discussions. I would also like to give a special thanks to Pankaj Bhalla for being wonderful officemate and for various ‘useful’ & ‘useless’ discussions.

I take this opportunity to thank all my room-mates (Pinak, Dhruvo and Anirban) with whom I have shared my student-days at different stages of my life for their friendly nature and caring attitude. I would also like to thank my friends—Sumit, Narayan, Anvesha, Dhruvo, Sona, Karthika, Jubair, Jhansi, Pompee, Pooja, Chinmoy, Alam whom I met at different periods of life and who are always with me with their support and encouragement. A special thanks to Sumit Chakraborty for being a wonderful friend. His confident attitude has always been an inspiration of my life.

A special thanks to ‘Ellen DeGeneres’ for hosting such a beautiful show for mankind which generates food for stressful human mind and give hope to move forward.

Finally, I feel deep gratitude for my grandmother and mom-dad who taught me fundamental values of life. Their priceless care, love and support have always been my strength. Their patience will remain my inspiration throughout my life. I will always remain grateful to them for encouraging and supporting me. I thank my siblings—Sudeb, Dipton and Tonik for their love, affection and support. A special thanks to all my cousins and relatives for their love and affection.

Newton Nath

Abstract

Neutrino, meaning “*the little neutral one*” (in Italian) is a sub-atomic fundamental particle. It is the most abundant particle in the universe after the photon. In 1930, Wolfgang Pauli first postulated the existence of the neutrino to explain the conservation of energy and the angular momentum in nuclear beta-decay. In the Standard Model (SM) of particle physics, there are three types of neutrinos (namely electron, muon and tau neutrino) which are electrically neutral, spin-half and massless fermions. Neutrinos cover a wide range of energies from 10^{-6} eV to 10^{18} eV which have been detected by different experiments – starting from detection of MeV neutrinos e.g, in nuclear beta-decay, solar and reactor experiments to very high energy PeV neutrinos in the IceCube experiment. In this doctoral work, we study some of the very interesting aspects of neutrino physics from both phenomenological as well as theoretical point of view.

Last few decades have witnessed remarkable developments in the field of neutrino physics coming from the observation of neutrino oscillation in terrestrial experiments. Neutrino oscillation requires that at least two of the neutrinos possesses small but non-zero mass and there is mixing between different flavors of neutrinos. Since in the SM neutrinos are massless, the phenomenon of neutrino oscillation implies physics beyond the SM. The three-flavor neutrino oscillation framework containing six oscillation parameters ($\theta_{12}, \theta_{13}, \theta_{23}, \Delta m_{21}^2, |\Delta m_{31}^2|$ and δ_{CP}) is now well established. Global analysis of neutrino oscillation data have determined some of these parameters with considerable precision. At the current juncture, the three unknown neutrino oscillation parameters are the neutrino mass hierarchy ($\Delta m_{31}^2 > 0$, known as the normal hierarchy or $\Delta m_{31}^2 < 0$, known as the inverted hierarchy), octant of the mixing angle θ_{23} ($\theta_{23} < 45^\circ$, known as the lower octant or $\theta_{23} > 45^\circ$, known as the higher octant) and the CP phase δ_{CP} . A major part of this doctoral work is devoted to the determination of these unresolved parameters using different oscillation experiments.

The main obstacle for an unambiguous determination of these unknowns are the presence of parameter degeneracies which means different sets of oscillation parameters giving the same probability. In our study, we advocate a comprehensive way to study the remaining parameter degeneracies in the form of a generalized “*hierarchy*– θ_{23} – δ_{CP} ” degeneracy. To analyze this, we consider long baseline neutrino oscillation exper-

iments $\text{NO}\nu\text{A}$ and T2K and atmospheric neutrino oscillation experiment ICAL@INO. We discuss their physics reach and illustrate their synergistic effects to resolve the different degenerate solutions. We also explore the potential of the next generation super-beam experiment, DUNE to determine the different unknowns in neutrino oscillation parameters. Our study mainly focuses on the determination of the octant of θ_{23} and the CP phase δ_{CP} . In particular, we emphasize on the role played by the antineutrinos, the broadband nature of the beam and the matter effect.

Theoretically, the challenge is to construct models of neutrino masses and mixing which can explain the observed values of the mass squared differences and the mixing angles. We discuss consequences of the assumption that the (Majorana) neutrino mass matrix M_ν and the charged lepton mass matrix M_l satisfy, $S_\nu^T M_\nu S_\nu = -M_\nu$, $T_l^\dagger M_l M_l^\dagger T_l = M_l M_l^\dagger$ with respect to some discrete groups S_ν, T_l contained in A_5 group. These assumptions lead to a neutrino mass spectrum with a massless neutrino and a degenerate pair of neutrinos and also constrain the mixing among them. We derive possible mixing patterns considering the various subgroups of A_5 .

Another interesting question in neutrino physics is the existence of light sterile neutrinos. There are many experimental evidences which seem to support such a hypothesis. In this direction, we consider the “minimal extended type-I seesaw” (MES) model which naturally gives rise to a light sterile neutrino. We focus on the texture zero study of the various fermion mass matrices involving the charged leptons and neutrinos in this model. In this study, we obtain only two allowed one-zero textures in the neutrino mass matrix, m_ν , namely $m_{e\tau} = 0$ and $m_{\tau\tau} = 0$, having inverted hierarchical mass ordering. In the context of the MES model, we obtain extra correlations among neutrino oscillation parameters which can be tested in future oscillation experiments.

Keywords: Neutrino Physics, Neutrino Oscillation, PMNS matrix, Long-Baseline Neutrino Experiments, Atmospheric Neutrino Experiments, CP Phases, Sterile Neutrino, Texture Zero, Neutrino Mass Matrix, Flavor Antisymmetry, Type-I seesaw, MES model.

Acronyms and Abbreviations

SM	Standard Model
BSM	Beyond Standard Model
CC	Charge Current Interaction
NC	Neutral Current Interaction
LEP	Large Electron-Positron collider
VEV	Vacuum Expectation Value
PMNS	Pontecorvo Maki Nakagawa Sakata Matrix
$0\nu\beta\beta$	Neutrinoless Double Beta Decay
SSM	Standard Solar Model
DAR	Decay at Rest
DIF	Decay in Flight
UHE	Ultra High Energy
AGN	Active Galactic Nuclei
GRB	Gamma Ray Burst
GUT	Grand Unified Theories
MSW	Mikheyev Smirnov Wolfenstein Effect
PREM	Preliminary Reference Earth Model
GLOBES	General Long Baseline Experiment Simulator
NH	Normal Hierarchy
IH	Inverted Hierarchy
LO	Lower Octant
HO	Higher Octant
CPV	Charge conjugation-Parity Violation
LHP	Lower Half-Plane of δ_{CP}
UHP	Upper Half-Plane of δ_{CP}
POT	Protons on Target
LBL	Long Baseline Experiments

T2K	Tokai to Kamioka
SURF	Sanford Underground Research Facility
DUNE	Deep Underground Neutrino Experiment
NuMI	Neutrinos at the Main Injector
NO ν A	NuMI Off-axis ν_e Appearance
MINOS	Main Injector Neutrino Oscillation Search
INO	India-based Neutrino Observatory
ICAL	Iron Calorimeter Detector
SK	Super-Kamiokande
SNO	Sudbury Neutrino Observatory
KATRIN	Karlsruhe Tritium Neutrino experiment
LSND	Liquid Scintillator Neutrino Detector
LArTPC	Liquid Argon Time Projection Chamber
TASD	Totally Active Scintillator Detector
ND	Near Detector
FD	Far Detector
G_F	Fermi coupling constant
SBL	Short Baseline Experiments
MES	Minimal Extended type-I Seesaw
NLO	Next-to-leading Order
Λ CDM	Λ cold dark matter

Contents

Acknowledgments	i
Abstract	v
Acronyms and Abbreviations	ix
Contents	ix
List of Figures	xiii
List of Tables	xvii
1 Introduction	1
1.1 The Discovery of Neutrinos	2
1.2 Standard Model and Neutrinos	3
1.3 Neutrino Oscillation	7
1.4 Generation of Neutrino Mass	8
1.5 Neutrinos Beyond Three Flavors	10
1.6 Unresolved Issues	12
1.7 Layout of the thesis	13
2 Production and Detection of Neutrinos	15
2.1 Sources of Neutrinos : Natural and Artificial	15
2.2 Detector Technologies	21
2.3 Overview of a Few Detectors	23
2.4 Summary	26

3	Neutrino Oscillation in Vacuum and Matter	27
3.1	Introduction	27
3.2	Two Flavor Neutrino Oscillation	29
3.3	Three flavor neutrino oscillation	33
3.4	Neutrino Propagation Through Matter	35
3.4.1	Effective matter potential	36
3.4.2	Two flavor formalism	38
3.4.3	Three flavor formalism	39
3.5	Evidences for Neutrino Oscillations	44
3.6	Present Status of Neutrino Oscillation Parameters	46
3.7	Summary	48
4	Parameter Degeneracies and Their Resolution	49
4.1	Introduction	49
4.2	Details of Experimental Configuration	52
4.3	Details of Statistical Analysis	53
4.4	Identifying Degeneracies	54
4.4.1	Degeneracies in Neutrino Oscillation Parameters	54
4.4.2	Identifying degeneracies using oscillation experiments	56
4.4.3	Chi-squared (χ^2) level study	61
4.5	Resolution of Degeneracies	64
4.5.1	Resolution of degeneracies using $\text{NO}\nu\text{A}[3+3]$	64
4.5.2	Combined effects of $\text{NO}\nu\text{A}$, T2K and ICAL@INO	66
4.6	Distinguishability between 0° and 180°	68
4.7	Summary	70
5	The Role of Antineutrinos at DUNE	73
5.1	Introduction	73
5.2	Specification of the Experiment	75
5.3	Identifying Degeneracies at DUNE	75
5.4	Resolution of degeneracies	77
5.4.1	Octant discovery χ^2	77

5.4.2	Antineutrinos, Octant Degeneracy and CPV discovery potential of DUNE	87
5.4.3	Percentage of antineutrino run	90
5.5	Summary	91
6	Flavor Antisymmetry in Neutrinos	93
6.1	Introduction	93
6.2	Relating Mixing Angles with Symmetry Groups	95
6.3	A_5 and Its Abelian Subgroups	96
6.4	Flavor Antisymmetry and Neutrino Mass Textures	100
6.4.1	The allowed residual symmetries in A_5	102
6.5	Mixing Patterns in A_5	104
6.5.1	$S_\nu = Z_2$ and $T_l = Z_3$ or Z_5	106
6.5.2	$S_\nu = Z_2 \times Z_2$ and $T_l = Z_3$ or Z_5	107
6.5.3	$S_\nu = Z_2 \times Z_2$ and $T_l = Z_2$	107
6.5.4	$S_\nu = Z_2$ and $T_l = Z_2 \times Z_2$	109
6.5.5	$S_\nu = Z_2 \times Z_2$ and $T_l = Z_2 \times Z_2$	110
6.6	Explicit Realization with $A_5 \times Z_3$ Symmetry	110
6.7	Summary	114
7	Texture Zero Studies in the Minimal Extended type-I Seesaw Model	117
7.1	Introduction	117
7.2	Minimal Extended type-I Seesaw Mechanism	120
7.3	Formalism	122
7.3.1	5 zeros in M_D and diagonal M_R	123
7.3.2	5 zeros in M_D and non-diagonal M_R corresponding to $L_e - L_\mu$ flavor symmetry	124
7.3.3	5 zeros in M_D and non-diagonal M_R corresponding to $L_e - L_\tau$ flavor symmetry	125
7.3.4	5 zeros in M_D and non-diagonal M_R corresponding to $L_\mu - L_\tau$ flavor symmetry	126
7.4	Active Neutrino Mass Matrix with 1-Zero Texture	127

7.4.1	Case I: $m_{e\tau} = 0$	130
7.4.2	Case II: $m_{\tau\tau} = 0$	131
7.5	Comparison of low and high energy neutrino mass matrix elements	132
7.5.1	NLO correction for MES model	137
7.6	Symmetry realization	138
7.7	Summary	141
8	Summary	143
	Appendices	147
A	Numerical Details	147
A.1	Event calculation	147
A.2	χ^2 Analysis	149
B	Synergy between the oscillation probabilities and the role of antineutrinos	151
	Bibliography	155
	List of Publications	177
	Publications attached with thesis	179

List of Figures

2.1	Fluxes of neutrinos from different neutrino sources with varying energy ranges [64].	16
3.1	Graphical representation of two-flavor neutrino oscillations.	33
3.2	Tree level Feynman diagrams for the CC potential V_{CC} generate through W exchange and the NC potential V_{NC} generate through Z exchange.	36
3.3	Possible mass patterns of neutrinos. Here, left (right) panel is for NH (IH). Color compositions of the various bands represent the proportion of flavor eigenstates of neutrinos in the mass eigenstates.	47
4.1	The oscillation probability $P_{\mu e}$ as a function of δ_{CP} . Here, upper (lower) row represents oscillation probability for $\text{NO}\nu\text{A}$ (T2K). The left (right) panel is for neutrinos (antineutrinos).	57
4.2	The oscillation probability $P_{\mu e}$ as a function of energy for $L = 7500$ km. The left (right) panel is for neutrinos (antineutrinos).	60
4.3	Here details are same as figure 4.1 except that we used fixed energy $E = 6$ GeV. . .	60
4.4	Contour plots in test $(\theta_{23} \times \delta_{CP})$ plane for $\text{NO}\nu\text{A}[6+0]$ with true values of $\theta_{23} = 39^\circ, 42^\circ, 48^\circ, 51^\circ$ in successive rows. The 3-columns correspond to $\delta_{CP} = -90^\circ, 0^\circ, +90^\circ$ respectively.	62
4.5	Here, columns correspond to the true $\delta_{CP} = -90^\circ, 0^\circ, 90^\circ$ respectively whereas each row correspond to the true $\theta_{23} = 39^\circ, 42^\circ, 48^\circ$ and 51° respectively for $\text{NO}\nu\text{A}[3+3]$	65
4.6	Here, columns correspond to the true $\delta_{CP} = -90^\circ, 0^\circ, 90^\circ$ respectively whereas each row correspond to the true $\theta_{23} = 39^\circ, 42^\circ, 48^\circ$ and 51° respectively for $\text{NO}\nu\text{A}[3+3]+\text{T2K}[8+0]$	67

4.7	Here, columns correspond to the true $\delta_{CP} = -90^\circ, 0^\circ, 90^\circ$ respectively whereas each row correspond to the true $\theta_{23} = 39^\circ, 42^\circ, 48^\circ$ and 51° respectively for $\text{NO}\nu\text{A}[3+3]+\text{T2K}[8+0]+\text{ICAL}$	69
5.1	Left panel (right panel) represents $P_{\mu e}(P_{\bar{\mu} e})$ for DUNE. Here the bands are over current 3σ range of θ_{23} [225]. For LO, NH (LO, IH) we consider the range of θ_{23} over $38.8^\circ - 45^\circ$ ($39.4^\circ - 55^\circ$) and for HO, NH (HO, NH) we consider the range of θ_{23} over $45^\circ - 53.3^\circ$ ($45^\circ - 53.1^\circ$).	76
5.2	Octant discovery χ^2 for DUNE. Left (right) panel is for LO (HO), where true(θ_{23}) is considered as $39^\circ(51^\circ)$ and test(θ_{23}) is marginalized over (45° to 55°) for LO and (35° to 45°) for HO. The labels NH, IH inside the plots signifies test hierarchy.	78
5.3	Here, left panel (right panel) represents $P_{\mu e}(P_{\bar{\mu} e})$ as a function of energy for DUNE and hierarchy corresponds to orange (light blue) curve is NH (IH).	79
5.4	Octant χ^2 vs test(δ_{CP}) for DUNE.	80
5.5	Octant sensitivity χ^2 for DUNE. Left (right) panel is for $\delta_{CP} = -90^\circ(+90^\circ)$, where true hierarchy is considered as NH(IH) for upper(lower) row. Here black, magenta and yellow lines represent χ^2 value at $2\sigma, 3\sigma$ and 4σ respectively.	84
5.6	Contour plots in true $\theta_{23} \times \delta_{CP}$ -plane, here true hierarchy is NH (IH) for upper (lower) row and left(right) panel is for LO (HO). Marginalization over hierarchy is done. The allowed regions are to the right (left) side of the contours in the left (right) panel.	85
5.7	θ_{23} precision plots of DUNE in True (θ_{23}) - Test (θ_{23}) plane at 3σ (99.73%) C. L. Here top (bottom) row is for NH (IH).	86
5.8	CPV χ^2 for DUNE when hierarchy and octant are unknown.	88
5.9	CPV χ^2 for DUNE when hierarchy and octant are known.	89
5.10	CPV discovery χ^2 at 3σ C.L. in (% of $\delta_{CP}(\text{True})$, % of $\bar{\nu}$ -run) plane. Here, y-axis represents the % of $\bar{\nu}$ -run out of total 10 years of $[\nu + \bar{\nu}]$ run in DUNE.	90
5.11	CPV discovery χ^2 at 3σ C.L. for DUNE[6+4] for all true θ_{23} when hierarchy and octant are unknown.	91
7.1	Left (right) panel corresponds to allowed mass spectrum in 3+1 scheme for SNH (SIH).	122

7.2	Correlation plots of $m_{e\tau} = 0$ for IH with vanishing m_3 in 3 neutrino paradigm. . .	130
7.3	Correlation plots of $m_{\tau\tau} = 0$ for IH with vanishing m_3 in 3 neutrino paradigm. . .	131
7.4	Correlation plots for case II.	135
7.5	Sterile neutrino mass from Eqs.(7.5.16) for $m_{\tau\tau} = 0$. The yellow line is the current upper bound on m_s as given by global analysis of 3+1 neutrino oscillation data. . .	137
7.6	This plot shows the allowed parameter spaces of M_D (GeV), M_R (in units of 10^{15} GeV) and M_S (GeV) which lead to NLO correction term $\sim 10^{-5}$ eV or less.	138
B.1	The plots in the upper row are for $\text{NO}\nu\text{A}$ running only in the neutrino mode i.e. $\text{NO}\nu\text{A}[6+0]$. Those in the lower row are for $\text{NO}\nu\text{A}$ running in equal neutrino and antineutrino mode i.e $\text{NO}\nu\text{A}[3+3]$. To generate these plots, we have assumed true $\theta_{23} = 39^\circ$, true $\delta_{CP} = -90^\circ$ and true hierarchy = NH, whereas test parameters are marginalized over the range given in table 3.2. The plots in the middle panel are generated for a fixed value of the test $\delta_{CP} (= -90^\circ)$	153

List of Tables

1.1	Fermionic representation of the SM fermions under $SU(3)_C \otimes SU(2)_L \otimes U(1)_Y$ group. We calculate the charges of the individual particles using the formula $Q = T_3 + Y/2$	4
3.1	Various energies and baselines and the value of mass squared difference that give maximum oscillation affect. Here, SBL=short baseline, LBL=long baseline and VLB=very long baseline oscillation experiments.	32
3.2	Current best fit and 3σ ranges of neutrino oscillation parameters [163].	47
4.1	Various possibilities of degeneracy in the probability $P_{\mu e}$. Here, R=right, W=wrong, H=hierarchy and O=octant.	51
4.2	χ^2 sensitivity for test $\delta_{CP} = 90^\circ, 180^\circ$ with true values of $\delta_{CP} = 0^\circ$ for NH-39°.	70
5.1	The octant degenerate parameter space for neutrinos and antineutrinos. Here, LO = Lower octant, HO = Higher octant, UHP = Upper half plane ($0^\circ < \delta_{CP} < 180^\circ$) and LHP = Lower half plane ($-180^\circ < \delta_{CP} < 0^\circ$).	77
5.2	Here, [10+0], [7+3] and [5+5] refers to $(\nu + \bar{\nu})$ runs of DUNE , where as (8+0), (5+3) and (4+4) refers to $(\nu + \bar{\nu})$ runs of T2K. The numbers in the parenthesis correspond to T2K. Also “Test parameters” refer to the test values where χ^2 minimum appears and remaining oscillation parameters are same as true parameters.	82
6.1	Elements of the five $Z_2 \times Z_2$ subgroups of A_5 along with their combined diagonalizing matrices U_c defined in the text. S_1, S_2, S_3 together with identity form a $Z_2 \times Z_2$ subgroup of A_5	98

7.1	Neutrino mass spectrum for normal and inverted hierarchies. $\Delta m_{12}^2, \Delta m_{31}^2$ (Δm_{32}^2) are the solar and atmospheric mass squared differences and Δm_{41}^2 (Δm_{43}^2) is the active sterile mass squared difference. The allowed ranges of these three mass squared differences are given in table (7.2).	121
7.2	The latest best-fit and 3σ ranges of active ν oscillation parameters from [297]. The current constraints on sterile neutrino parameters are from the global analysis [298–300]. Here R_ν is the solar to atmospheric mass squared difference ratio.	123
7.3	Here, \bar{D}_{Ll} denote $SU(2)_L$ doublets and l_R, ν_{lR} ($l = e, \mu, \tau$) are the right-handed (RH) $SU(2)_L$ singlet for charged lepton and neutrino fields respectively. Also, ϕ, ϕ' and ϕ'' are the Higgs doublets.	139
7.4	Here, scalar singlet χ_1 and χ_2 give M_R whereas λ_1 and λ_2 give M_S	140
7.5	The fields descriptions are same as given in table (7.3).	141

Chapter 1

Introduction

*“Do not say, It is morning, and dismiss it with a name of yesterday.
See it for the first time as a newborn child that has no name.”*

Rabindranath Tagore

Neutrinos ! the miraculous subatomic fundamental particles are the lightest among all the Standard Model (SM) particles (except photons and gluons which are massless) and interact only via the weak interactions among all the fundamental interactions. As a result, it is an utmost difficult task to detect the neutrinos. They are omnipresent in nature, being produced both naturally and artificially. Naturally produced neutrinos come to the Earth from the Sun, supernovae, collisions of cosmic rays with nuclei in the atmosphere, natural radio activity of the Earth, etc. whereas those produced in accelerators and nuclear reactors are examples of artificial or the man-made neutrinos. The naturally produced neutrinos carry information from deep inside stars and hence can help to understand the stellar evolution processes. In the SM neutrinos are massless. Thus generation of neutrino mass signifies physics beyond the SM (BSM). This can also be related to some of the unresolved fundamental queries, like, the unification of forces, the matter-antimatter asymmetry, etc. Thus neutrinos are believed to hold the key to a deeper understanding of nature.

The plan of this chapter goes as follows : in the next section (1.1), we discuss the discovery of the neutrino whereas in section (1.2) we present a discussion of the neutrinos in the SM. A brief overview of neutrino oscillation is presented in section

(1.3). In section (1.4), we discuss the neutrinos beyond the SM and the generation of neutrino mass. Section (1.5) is devoted to the discussion of sterile neutrinos. We mention some of the unresolved issues of neutrino physics in section (1.6). At the end of this chapter, in section (1.7), we give the layout of the doctoral work presented in this thesis.

1.1 The Discovery of Neutrinos

The history behind the discovery of the neutrino goes back to 1914, when J. Chadwick first demonstrated the observed beta-decay spectrum from radioactive sources. An unstable radioactive nucleus undergoes beta-decay where a neutron decays to a proton and an electron. However, experimental observation demonstrated a continuous behavior of the electron energy spectrum, unlike alpha or gamma-decay spectrum which showed a discrete nature [1]. This continuous nature of the spectrum questioned the hypothesis of energy conservation in nuclear beta-decay. As a solution, in 1930, W. Pauli postulated the existence of a new particle *neutrino* to account for the mismatch between the observed and expected energy spectra of the electron *, thus saving the principle of conservation of energy in nuclear beta-decay. In this hypothesis, neutrinos are electrically neutral and spin half fermions to save the conservation of electric charge and angular momentum. Pauli also postulated the neutrinos to be massless. These neutrinos take part only in the weak interactions and hence can escape detection †. Therefore, it is not astonishing that the first neutrino was discovered 26 years after it was first proposed. The very first observation of the neutrino was made at the Savannah River Nuclear Reactor in 1956, by Reines and Cowan [2]. Only neutrino that was known at that time was the electron neutrino (ν_e). After that two more types of neutrinos were discovered corresponding to the two other charged leptons– muon and tau. The second type of neutrino, named as the muon neutrino (ν_μ), was discovered in 1962 by L. Lederman, M. Schwartz and J. Steinberger [3]. In July 2000, the DONUT collaboration [4] announced the discovery of the third type of neutrino called the tau neutrino (ν_τ).

In the mid-1960s R. Davis proposed the Homestake experiment to test the hypoth-

*Note that Pauli called this particle as “neutron” and later Fermi coined the name “neutrino”.

†In 1933, Fermi formulated the theory of beta decay via weak interactions.

esis of solar energy generation by observing the neutrinos coming from the sun [5]. This detection was based on the reaction of the neutrinos with chlorine giving rise to an isotope of argon. It was observed that the detected neutrino flux was lower than the expected theoretical predictions of the Standard Solar Model (SSM) developed by J. Bahcall [6]. There could be three reasons to explain this mismatch : (i) the experimental results were wrong, (ii) the calculation of neutrino fluxes from the SSM were not correct and (iii) the electron neutrinos coming from the Sun were getting transformed into some other flavors of neutrino and they simply crossed the detector undetected since the detector was sensitive only to the electron neutrino. Neutrino oscillation proposed by B. Pontecorvo in 1957 was counted as a possible solution of number (iii) above [7, 8]. Neutrino oscillation requires non-zero neutrino mass which is a signal of *new physics* beyond the SM. Subsequent solar neutrino experiments confirmed the shortfall and finally the SNO [9, 10] experiment established the disappearance of the solar neutrinos on a firm footing. Around 1998, the SK experiment declared their atmospheric neutrino measurement and the zenith angle dependence of the data conclusively established neutrino oscillations [11]. These discoveries led to the prestigious Nobel Prize in the field of Neutrino Physics in the year 2015 for T. Kajita of the SK and A. B. McDonald of the SNO collaboration. KamLAND [12] experiment confirmed solar neutrino oscillations using reactor neutrinos whereas accelerator based long baseline experiments, K2K [13, 14] and MINOS [15] and later, T2K [16] and NO ν A [17, 18] corroborated the atmospheric neutrino oscillation using man-made sources.

1.2 Standard Model and Neutrinos

The Standard Model (SM) of particle physics is a gauge quantum field theory based on the internal symmetries of the unitary product group $SU(3)_C \otimes SU(2)_L \otimes U(1)_Y$, where subscript C denotes color, L implies left handed chirality and Y is the hypercharge. In nature, there are four low energy fundamental interactions. The SM includes three of them namely, electromagnetic, weak and strong interactions whereas it does not explain the gravitational interaction. The representation of the SM fermions and their quantum numbers under the unitary gauge groups are given in table (1.1). The ele-

Lepton doublet	Quark doublet	Lepton singlet	Up Quark	Down Quark
$L_L(1,2,-1)$	$Q_L(3,2,\frac{1}{3})$	$l_R(1,1,-2)$	$U_R(3,1,\frac{4}{3})$	$D_R(3,1,-\frac{2}{3})$
$\begin{pmatrix} \nu_e \\ e \end{pmatrix}_L$	$\begin{pmatrix} u \\ d \end{pmatrix}_L$	e_R	u_R	d_R
$\begin{pmatrix} \nu_\mu \\ \mu \end{pmatrix}_L$	$\begin{pmatrix} c \\ s \end{pmatrix}_L$	μ_R	c_R	s_R
$\begin{pmatrix} \nu_\tau \\ \tau \end{pmatrix}_L$	$\begin{pmatrix} t \\ b \end{pmatrix}_L$	τ_R	t_R	b_R

Table 1.1: Fermionic representation of the SM fermions under $SU(3)_C \otimes SU(2)_L \otimes U(1)_Y$ group. We calculate the charges of the individual particles using the formula $Q = T_3 + Y/2$.

mentary fermions are divided in two categories namely, Leptons and Quarks. In this model the left-handed leptons and quarks are $SU(2)_L$ doublets whereas their corresponding right-handed partners are singlets under $SU(2)_L$. Also each quark comes in three colors i.e. they carry color quantum number whereas leptons are color singlets. The first row of the table (1.1) shows the quantum numbers corresponding to the SM gauge group. As an example, the three entries of $L_L(1, 2, -1)$ imply that the lepton doublet (L_L) is a color singlet under $SU(3)_C$, doublet under $SU(2)_L$ and carries hyper-charge (-1). The number of rows of the table (1.1) correspond to the number of generations of the fermion family. The mediators of the low energy SM interactions are the gauge bosons and these are the W^\pm , Z bosons which mediate the weak interaction, gluons which are the mediators of the strong interaction and the photon which is the carrier of the electromagnetic interaction. In the SM, neutrinos interact via both the W^\pm and Z bosons exchange processes and these are called the charge current (CC) and neutral current (NC) interactions respectively. The existence of the three types of neutrinos in the SM were further confirmed by the Large Electron-Positron Collider (LEP) experiment at CERN. This experiment measured the invisible decay width of the Z-boson into neutrinos, which indicated the number of light neutrinos in the SM to be three [19].

We also notice from the table (1.1) that there are no right-handed partners for the neutrinos. The reason behind the absence of right-handed neutrinos in the SM is mo-

tivated by the observation of parity violation in weak interactions. In 1956, T. D. Lee and C. N. Yang conjectured that parity is violated in weak interactions [20] to solve the famous Tau-Theta Puzzle. In the same year, Madam Wu experimentally confirmed parity violation in weak interactions, where she observed that for the ^{60}Co nuclei nuclear spin of the electron is always opposite to its momentum [21]. This mismatch can only be explained by the presence of left handed electrons (e_L) and right handed antineutrinos ($\bar{\nu}_R$) and the corresponding absence of mirror image state, left handed antineutrino ($\bar{\nu}_L$)[‡]. Further, the experimentally measured helicity of neutrinos by M. Goldhaber et.al. [22] confirmed that the neutrinos are indeed left handed.

In the SM, mass terms of the fermions appear in the Lagrangian as a result of the breaking of the underlying symmetries and the mechanism responsible for this is known as the Higgs Mechanism or Englert-Brout-Higgs-Guralnik-Hagen-Kibble mechanism [23], [24], [25], [26], [27], [28]. The Higgs-lepton Yukawa Lagrangian for the charged leptons in flavor basis can be written as

$$\mathcal{L}_Y = - \sum_{\beta, \alpha=e, \mu, \tau} Y_{\beta\alpha} \bar{L}_{\beta L} \Phi l_{\alpha R} + H.c., \quad (1.2.1)$$

where Y is the Yukawa coupling and Φ is the Higgs doublet. In the unitary gauge, Φ can be written as

$$\Phi = \frac{1}{\sqrt{2}} \begin{bmatrix} 0 \\ v + H(x) \end{bmatrix}, \quad (1.2.2)$$

where, v is the vacuum expectation value or vev that arises from the spontaneous breaking of the SM symmetry,

$$SU(2)_L \times U(1)_Y \rightarrow U(1)_Q, \quad (1.2.3)$$

where $U(1)_Q$ is the gauge symmetry group corresponding to the electromagnetic interactions. Also, $H(x)$ is the field corresponding to the physical Higgs boson.

Using equation (1.2.2) in equation (1.2.1), the Higgs-lepton Yukawa Lagrangian can be written as

$$-\mathcal{L}_Y = \left(\frac{v + H}{\sqrt{2}} \right) \sum_{\beta, \alpha=e, \mu, \tau} Y_{\beta\alpha} \bar{l}_{\beta L} l_{\alpha R} + H.c. \quad (1.2.4)$$

[‡]Note that in the massless limit, *helicity* of a particle is right-handed if the spin and the motion of the particle is in same direction whereas if they are in opposite direction then the particle is left-handed.

And the mass terms for the charged leptons can be written as,

$$-\mathcal{L}_m = \sum_{\alpha=e,\mu,\tau} m_{\beta\alpha} \bar{l}_{\beta L} l_{\alpha R} + H.c., \quad (1.2.5)$$

where $m_{\beta\alpha} = Y_{\beta\alpha} v / \sqrt{2}$ is the charged lepton mass matrix which is proportional to the Higgs v . In the SM, there are no right-handed neutrinos and hence one can not write a mass term for the neutrinos unlike the charged leptons and quarks.

SM is sometimes regarded as a “theory of almost everything” and an extremely successful model from both theoretical and experimental point of view. Successes of the SM include : (i) the prediction of the W and Z bosons, the gluons, the top and the charm quark, long before they were observed experimentally, (ii) precise agreement with measurements of the fine structure constant $\alpha = 1/137.035999070$, (iii) the prediction of the Higgs boson. The recent discovery of the last missing piece of the SM namely, Higgs boson firmly established this model[§]. But there are a number of issues which can not be addressed within the SM and one needs to go beyond the SM to explain these. One of the fundamental phenomenon that the SM does not incorporate is the gravity. There are some ad hoc features in the SM namely, (i) the unification of gauge couplings does not happen in SM , (ii) it has 19 free parameters which are known experimentally but the origin of the values are still unknown, (iii) there is no explanation of the hierarchy between fermion masses, (iv) the Higgs mass receives large quantum corrections, dominantly from the top loop and a severe fine tuning is required in order to keep Higgs mass light (the naturalness problem), etc. Other phenomena such as – explanation regarding the dark matter and dark energy, matter-antimatter asymmetry, the disagreement of the massless nature of neutrinos with the observed neutrino oscillations, etc also remain unexplained within the SM. Therefore, there are several attempts towards the formulation of a more fundamental theory at a higher scale whose low energy realization could be the SM. The experimental observations of neutrino oscillation puts an emphasis on the *beyond the SM* scenarios which could successfully explain the neutrino mass generation. In the next section, we present a brief overview on the mechanism of neutrino oscillation.

[§]The Nobel Prize in Physics 2013 was awarded jointly to F. Englert and P. W. Higgs for predicting the existence of Higgs boson which subsequently detected at the Large Hadron Collider (LHC) [29,30].

1.3 Neutrino Oscillation

The concept of oscillation of neutrinos was first put forward by B. Pontecorvo in 1957 and later in 1962 a quantitative theory of neutrino oscillation was first developed by Maki, Nakagawa and Sakata. Neutrino oscillation is a quantum mechanical phenomenon where three mass eigenstates ($|\nu_k\rangle$, $k = 1, 2, 3$) of neutrinos are related to three flavor eigenstates ($|\nu_\alpha\rangle$, $\alpha = e, \mu, \tau$) via an unitary mixing matrix. Mathematically,

$$|\nu_\alpha\rangle = \sum_k U_{\alpha k}^* |\nu_k\rangle, \quad (1.3.1)$$

where the mixing matrix U is referred to as the Maki-Nakagawa-Sakata (MNS) matrix or as the Pontecorvo-Maki-Nakagawa-Sakata (PMNS) matrix. In the three flavor framework U is parameterized by three mixing angles ($\theta_{12}, \theta_{13}, \theta_{23}$) and a CP phase δ_{CP} . The probability that a neutrino in its initial flavor α , will later be detected as flavor β in vacuum is,

$$P_{\nu_\alpha \rightarrow \nu_\beta} = \delta_{\alpha\beta} - 4 \sum_{k>j} \text{Re}(U_{\alpha k}^* U_{\beta k} U_{\alpha j} U_{\beta j}^*) \sin^2(\Delta_{kj}) + 2 \sum_{k>j} \text{Im}(U_{\alpha k}^* U_{\beta k} U_{\alpha j} U_{\beta j}^*) \sin(2\Delta_{kj}) \quad (1.3.2)$$

where $\Delta_{kj} = \Delta m_{kj}^2 L/4E = (m_k^2 - m_j^2)L/4E$ gives the two mass squared differences, Δm_{21}^2 , Δm_{31}^2 . We note here that the three flavor neutrino oscillation framework depends on six oscillation parameters, namely three mixing angles $\theta_{12}, \theta_{13}, \theta_{23}$ and a CP phase δ_{CP} which are contained in U and two mass squared differences, Δm_{21}^2 , Δm_{31}^2 . A detailed description of the mechanism of neutrino oscillation considering neutrino propagation in vacuum as well as matter will be discussed in chapter (3). Neutrino oscillation have been observed in many experiments. This has established the fact that at least two of them have tiny but non-zero mass and there is flavor mixing necessitating the extensions of the SM. In the next section, we discuss the generation of neutrino mass via *minimal extension of the SM*.

1.4 Generation of Neutrino Mass

In the *minimal extension of the SM*, the neutrino mass term can be written by adding a right-handed singlet fermion ν_R . With the inclusion of ν_R , a Dirac neutrino mass term can be written as,

$$-\mathcal{L}_m^D = m_D(\overline{\nu}_L\nu_R + \overline{\nu}_R\nu_L), \quad (1.4.1)$$

where, $\nu_{L,R} = P_{L,R} \nu$ with $P_{L,R} = (1 \mp \gamma^5)/2$ and $m_D = y_\nu v/\sqrt{2}$ as given by the equation (1.2.5). This implies that the Dirac neutrino mass term is proportional to the Higgs $v\bar{e}e$ like other charged leptons and quarks. But the neutrino masses are very small which requires minuscule Yukawa couplings. However there is no natural explanation for this in the SM.

As neutrinos are electrically neutral, in principle neutrinos can be their own anti-particle unlike other SM fermions. Such a fermion is known as a Majorana fermion after the Italian theoretician Z. Ettore Majorana who first proposed this [¶]. In this case, the charge conjugated field $(\nu_L)^C = (\nu^C)_R$ serves as the right-handed partner. Then the Majorana neutrino mass term can be written as,

$$-\mathcal{L}_m^M = \frac{1}{2}m_L(\overline{\nu}_L^C\nu_L + \overline{\nu}_L\nu_L^C) + \frac{1}{2}M_R(\overline{\nu}_R^C\nu_R + \overline{\nu}_R\nu_R^C), \quad (1.4.2)$$

where C is the charge conjugation operator. The terms in the equation (1.4.2) violates lepton number by 2 units. However although neutrinos carry no charge they carry leptonic quantum number which is +1 for the neutrinos and -1 for the charge conjugate states. Thus Majorana mass term breaks this quantum number. At the current juncture, there is no experimental evidence which can tell whether the neutrino is a Dirac or a Majorana like fermion. To resolve this issue will be one of the most fascinating tasks for future neutrino experiments. The most promising experiments which can establish lepton number violation and can probe the Majorana nature of the neutrinos are the neutrinoless double beta-decay ($0\nu\beta\beta$) experiments [31]. The half life for the $0\nu\beta\beta$ can be expressed as,

$$\frac{1}{T_{1/2}^{0\nu}} = G^{0\nu}|M^{0\nu}|^2|m_{ee}|^2, \quad (1.4.3)$$

[¶] Note that the Dirac fermion is not its own anti-particle.

where, $G^{0\nu}$ is the phase space factor and $M^{0\nu}$ is the nuclear matrix element coming from nuclear physics. m_{ee} is the effective Majorana neutrino mass which can be written by considering only the contribution from the three active neutrinos as,

$$m_{ee} \equiv m_{eff} = \sum_i U_{ei}^2 m_i, \quad (1.4.4)$$

where U_{ei} are the elements of the leptonic mixing matrix. These experiments also give bounds on m_{eff} by measuring the life time of the $0\nu\beta\beta$ processes. Current bounds on $m_{eff} \leq (0.12 - 0.25)$ eV came from the combined study of KamLAND-ZEN and EXO-200 [32]. A large number of experiments such as CUORE [33], GERDA [34], SuperNEMO [35], KamLAND-ZEN [32] and EXO [36] aim to discover the evidences for neutrinoless double beta decay. Bounds on the sum of the neutrino masses also come from cosmology which implies $\sum_i m_i \leq 0.17$ eV [37]. The upcoming beta-decay experiment, KATRIN, will measure $m_\beta = \sqrt{|U_{ei}^2| m_i^2}$ with an expected sensitivity of 0.2 eV at 90% C.L [38]. This can also give information on the absolute neutrino mass scale.

Considering both Dirac and Majorana mass terms, the most general Lagrangian for neutrino mass can be written as,

$$\begin{aligned} -\mathcal{L}_{mass} &= \mathcal{L}_m^D + \mathcal{L}_m^M, \\ &= \bar{\nu}_R m_D \nu_L + \frac{1}{2} \bar{\nu}_L^C m_L \nu_L + \frac{1}{2} \bar{\nu}_R M_R \nu_R^C + H.c., \\ &= \frac{1}{2} \bar{\nu}_R m_D \nu_L + \frac{1}{2} \bar{\nu}_L^C m_D^T \nu_R^C + \frac{1}{2} \bar{\nu}_L^C m_L \nu_L + \frac{1}{2} \bar{\nu}_R M_R \nu_R^C + H.c., \end{aligned} \quad (1.4.5)$$

$$= \frac{1}{2} \bar{n}_L^C \mathcal{M} n_L + H.c., \quad (1.4.6)$$

where, $n_L = (\nu_L \ \nu_R^C)^T$, we have used $\bar{\nu}_R m_D \nu_L = \bar{\nu}_L^C m_D^T \nu_R^C$ in the third line and

$$\mathcal{M} = \begin{bmatrix} m_L & m_D^T \\ m_D & M_R \end{bmatrix}. \quad (1.4.7)$$

This mass matrix can be diagonalized using an unitary mixing matrix [39]. In the approximation $m_L \ll m_D \ll M_R$ we get

$$M_{light} = m_L - m_D^T M_R^{-1} m_D. \quad (1.4.8)$$

Considering $m_L = 0$ the light neutrino mass matrix can be written as $m_\nu = -m_D^T M_R^{-1} m_D$ and diagonalization of this leads to masses and mixing for the three active neutrinos.

This is the famous type-I *seesaw mechanism* which provides an elegant way to generate light neutrino masses considering M_R ($\sim 10^{14}$ eV) close to the Grand Unified Theory (GUT) scale.

The origin of the seesaw mechanism can be explained by the effective dimension-5 Weinberg operator [40, 41] which is compatible with the SM gauge group. This is given by

$$\mathcal{L}_5 \sim \kappa_5 L_L L_L \Phi \Phi, \quad (1.4.9)$$

where L_L and Φ are the SM lepton and Higgs doublets respectively and $\kappa_5 = a_5/\Lambda$ is the effective coupling, suppressed by some high energy scale Λ which can be taken as the scale of some new physics beyond the SM. There are 4 possible ways to construct a gauge singlet term from the two lepton and Higgs doublets where $L \sim (1, 2, -1)$ and $\Phi \sim (1, 2, 1)$ under the $SU(3)_C \times SU(2)_L \times U(1)_Y$ gauge group.

- Case 1: each $L - \Phi$ forms a fermion singlet which generates neutrino mass by exchanging a right handed singlet fermion. This corresponds to the Type-I seesaw mechanism [42–45].
- Case 2: each $L - L$ and $\Phi - \Phi$ forms a scalar triplet and generates a singlet term by the tree level exchange of a heavy Higgs triplet giving rise to the Type-II seesaw mechanism [46–49].
- Case 3: each $L - \Phi$ forms a fermion triplet and this process generates neutrino mass through the Type-III seesaw mechanism by the tree level exchange of a right-handed fermion triplet [50–52].
- Case 4: each $L - L$ and $\Phi - \Phi$ pair forms a scalar singlet but this will lead to terms like $\overline{\nu}_L^C e_L$ which does not generate neutrino mass.

Note that \mathcal{L}_5 violates lepton number by 2 units and hence seesaw mechanism implies neutrinos are Majorana particles.

1.5 Neutrinos Beyond Three Flavors

Sterile neutrinos are singlets under the SM unitary product group and do not take part in weak interactions. But they can couple with the active neutrinos (ν_e , ν_μ and ν_τ)

through the mass term in the Lagrangian. Thus they can mix with the active neutrinos via active-sterile mixing and hence can be probed in oscillation experiments. Presently, there are no bounds on the number of light sterile neutrinos and their mass scales.

The standard three flavor neutrino oscillation scenario is now very well established and the results from the solar, reactor, atmospheric and long baseline oscillation experiments have reported neutrino oscillations with the mass squared difference of $\sim 10^{-5} \text{ eV}^2$ and $\sim 10^{-3} \text{ eV}^2$ respectively. The short baseline neutrino oscillation experiment LSND reported the evidence of neutrino oscillations with the mass squared difference of $\sim \text{eV}^2$ [53–55]. This requires the introduction of a fourth neutrino to accommodate three independent mass squared differences. But $Z \rightarrow \nu \bar{\nu}$ implies only three active neutrinos with masses $< 45 \text{ GeV}$ are possible in the SM. So the fourth neutrino has to be SM singlet or sterile. LSND results could be explained by the existence of at least one sterile neutrino. MiniBooNE experiment [56] was built to verify LSND results. The results of MiniBooNE experiment showed some overlap with the LSND results and hence supported the existence of the sterile neutrino. Recently, two solar neutrino detectors, GALLEX and SAGE reported the deficit of measured electron neutrinos from the intense artificial radioactive sources ^{51}Cr and ^{37}Ar . They reported that the number of measured events are $\sim 2.8\sigma$ smaller than the prediction which is termed as the ‘‘Gallium anomaly’’ [57]. The reactor electron antineutrino flux studies have also provided evidence for sterile neutrinos [58]. Their analysis with recalculated reactor fluxes [58] showed a deficit in the observed rate as compared to the predicted rate and the ratio is 0.943 ± 0.023 at 98.6% C.L. It has been illustrated that Gallium anomaly can be explained by considering $\Delta m^2 \gtrsim 0.35 \text{ eV}^2$ [57] whereas explanation of reactor anomaly needs $\Delta m^2 \gtrsim 0.5 \text{ eV}^2$ [59]. Recent results of the Planck experiment also shows the possibility of light sterile neutrino if one deviates slightly from the base ΛCDM model [37]. Note that the seesaw mechanism [40, 41] discussed above, considers sterile or singlet neutrinos with masses of the order of TeV or as heavy as GUT scale. However theoretically it is challenging to have light sterile neutrinos and many works have addressed this issue [60–62]. Thus, at the present juncture, the scenario with a light sterile neutrino is quite fascinating both theoretically and experimentally and many future experiments are proposed to confirm/falsify this [63].

1.6 Unresolved Issues

The past decades have seen tremendous progress in our knowledge about neutrinos due to a host of remarkable experimental results. These results have enriched the field of high energy physics. However, there are still many unresolved questions both on the experimental and theoretical side. These include ;

- Determination of the remaining unknown neutrino oscillation parameters namely, the mass hierarchy, octant of 2-3 mixing angle and the CP phase δ_{CP} .
- To understand the nature of leptonic mixing matrix which is very much different than the mixing matrix in the quark sector.
- The smallness of neutrino mass compared to that of other fermions, like charged leptons and quarks.
- Whether neutrinos are Dirac or Majorana particles. This answers if the neutrinos and antineutrinos are different particles or they are the same.
- Existence of new species of neutrinos other than the three active neutrinos.
- New physics effect on neutrino oscillations, like non-standard interactions which can affect neutrino production, propagation and detection significantly.
- Existence of other new physics effects on neutrino oscillations like non-unitarity, extra-dimensions, long range forces, etc.
- The issue of generation of baryon asymmetry via leptogenesis, which is possible in seesaw models, and its connection with low energy CP violation.
- Does the neutrino possess a non-zero neutrino magnetic moment?
- Does the neutrino sector violate Lorentz or CPT symmetry ?

In this thesis we address some of the above issues.

1.7 Layout of the thesis

In the next chapter (2), we briefly discuss the various sources of neutrinos – both natural and artificial. We also give a brief overview of the different detector technologies that are being used in the current neutrino oscillation experiments. Apart from that we discuss the experimental set-ups and physics goals of four specific experiments namely, T2K, NO ν A, DUNE and ICAL@INO which have been considered in this thesis to study neutrino oscillation phenomenology.

In chapter (3), we discuss the formalism of neutrino oscillation. First we consider the simple two flavor neutrino oscillation mechanism. We next describe how the vacuum oscillation phenomenon can change in presence of matter. We also present approximate expressions of oscillation probabilities in constant density matter. At the end of chapter (3), we discuss the current status of various neutrino oscillation parameters and mention the unknowns. How these unknown oscillation parameters can be determined via oscillation experiments constitute a major part of the doctoral work.

Chapter (4) is dedicated to the study of degeneracies in neutrino oscillation parameters and their resolutions. We explore the potential of the neutrino oscillation experiments T2K, NO ν A and INO to resolve the degeneracies in neutrino oscillation parameters. We describe the parameter degeneracies both at the probability level as well as at the χ^2 level. We point out a comprehensive way to discuss the parameter degeneracies in the form of a generalized “hierarchy– θ_{23} – δ_{CP} ” degeneracy. We illustrate the different degenerate solutions by considering 6 years neutrino runs for NO ν A. Next, we study the resolution of these degeneracies considering (3+3) years of ($\nu + \bar{\nu}$) run for NO ν A. We then describe successively, (i) the role of T2K and NO ν A and (ii) the combined effect of NO ν A, T2K and INO to resolve the degeneracies. In chapter (5), we explore the potential of the next generation superbeam experiment, DUNE to determine the different unknown neutrino oscillation parameters. We mainly focus on the study of the octant of θ_{23} and the determination of the CP phase δ_{CP} . It is well known that the precise determination of octant and δ_{CP} is interlinked through the octant– δ_{CP} degeneracy. Thus, we concentrate on the resolution of these two unknowns. We illustrate the role played by the antineutrinos, the broadband nature of the

beam and the matter effect. We also discuss the synergistic effects between neutrino and antineutrino runs by considering their different run times.

Chapter (6) is devoted to understand the neutrino masses and mixing angles from a theoretical point of view. A systematic approach based on flavor symmetries has evolved in last several years which provide concrete framework to understand this. In this respect, we emphasize on the implications of an ansatz of flavor antisymmetry in the context of the flavor group A_5 . We discuss the consequences of an assumption that the (Majorana) neutrino mass matrix M_ν and the charged lepton mass matrix M_l satisfy, $S_\nu^T M_\nu S_\nu = -M_\nu$, $T_l^\dagger M_l M_l^\dagger T_l = M_l M_l^\dagger$ with respect to some discrete groups S_ν, T_l contained in A_5 . These assumptions lead to a neutrino mass spectrum with two degenerate and one massless neutrino and also constrain mixing among them. We study all the subgroups of A_5 which predicts neutrino mixing patterns.

In chapter (7), we discuss the “minimal extended type-I seesaw” (MES) model which can give rise to \sim eV scale sterile neutrinos. In this model, we extend the SM with three right handed neutrinos and one extra singlet S to generate a light sterile neutrino. The active neutrino mass matrix, depends on the Dirac neutrino mass matrix, Majorana neutrino mass matrix and the mass matrix which formed by the coupling of the right handed neutrinos and the singlet. We study the texture zeros in this fermion mass matrices. In our study, we obtain only two allowed forms of m_ν ($m_{e\tau} = 0$ and $m_{\tau\tau} = 0$), having inverted hierarchical mass spectrum. In the context of the MES model, we find some extra correlations among neutrino oscillation parameters which can be tested in future neutrino oscillation experiments. We conclude our thesis in chapter (8) where we summarize our findings.

Chapter 2

Production and Detection of Neutrinos

*“A theory is something nobody believes, except the person who made it.
An experiment is something everybody believes, except the person who made it.”*

– Albert Einstein

Neutrinos are *elusive* in nature but they are also very *abundant* in the universe. It is very difficult to detect neutrinos because they interact very weakly. Hence, one needs a huge detector to detect sufficient number of neutrinos. In this chapter, we outline different sources of neutrinos and discuss about some of the detectors for detecting neutrinos. In section (2.1) of this chapter, we start with a brief overview of the various sources of neutrinos. Later, in section (2.2), we present a discussion on some of the different detector technologies which are used in the neutrino oscillation experiments. This includes Čerenkov detectors, scintillator detectors, liquid argon detectors, iron detectors etc. We also present, in section (2.3), a short description of all the experimental configurations that we have considered in our study presented in the subsequent chapters.

2.1 Sources of Neutrinos : Natural and Artificial

In this section, we discuss about both natural and artificial sources of neutrinos. Neutrinos are the most abundant particles in the universe after the photon. The energy of

the neutrinos ranges from 10^{-6} eV to 10^{18} eV as can be seen from the figure (2.1). The neutrinos coming from the natural sources include relic neutrinos, solar neutrinos, atmospheric neutrinos, supernovae neutrinos, geoneutrinos, ultra high energy neutrinos, etc. whereas man made or artificially produced neutrinos are those neutrinos which come from accelerator beams and nuclear reactors.

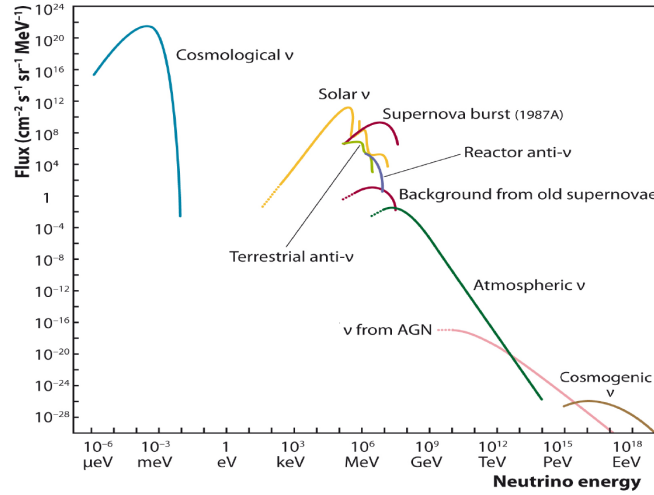


Figure 2.1: Fluxes of neutrinos from different neutrino sources with varying energy ranges [64].

Relic neutrinos : Relic neutrinos or cosmological neutrinos having the smallest energy but maximum flux as described in figure (2.1) constitute the Cosmic Neutrino Background ($C\nu B$). Standard Big-Bang theory also predicts the existence of $C\nu B$ along with the cosmic microwave background (CMB) radiation. In the early universe, neutrinos were in the thermal equilibrium in the form of hot plasma interacting with other particles via the weak interactions. During that era, the weak interaction processes before the decoupling of the neutrinos were,

$$n e^+ \rightleftharpoons p \bar{\nu}_e, \quad p e^- \rightleftharpoons n \nu_e, \quad n \rightleftharpoons p e^- \bar{\nu}_e. \quad (2.1.1)$$

As the rate of the weak interaction processes decreased with the expansion of the universe, the neutrinos started decoupling. These happened when the weak interaction rate became smaller than the expansion rate. These relativistic decoupled neutrinos are the hot relics. The universe was about 1 s old and the temperature was of the order 10^{10} K at that epoch. Today, temperature of $C\nu B$ is around 1.95 K and they continue

information of the early universe after Big-Bang [65]. However, unlike CMB, this has not been detected directly. But there are compelling indirect evidences for the existence of $C\nu B$. One of the most promising method to observe $C\nu B$ are in the tritium decay experiments, which are dicussed in Refs. [65,66] whereas looking for evidences for $C\nu B$ considering circular polarization of CMB are discussed in Ref. [67].

Solar neutrinos : Neutrinos coming from the Sun are produced in the solar core via thermonuclear fusion reaction processes. Energy (E_ν) of these neutrinos are in the range $0.2 \leq E_\nu \leq 15$ MeV. The thermonuclear energy production process can be expressed in terms of the following reaction :



This is the net result of two cycles (namely, pp and CNO cycle). Energy is released in this process mostly through photons and a small fraction of the total energy released are carried away by the neutrinos ($\langle 2E_{\nu_e} \rangle = 0.59\text{MeV}$). These neutrinos can be directly detected at the detectors on Earth which provide a unique tool to study the interior of the Sun. In 1968, R. Davis first observed the solar neutrinos in the pioneering Homestake gold mine experiment in Lead, South Dakota [5]. Later, various other neutrino experiments have detected the solar neutrinos; these are, Homestake [68], Kamiokande [69], GALLEX [70], SAGE [71], GNO [72], SNO [73] and Borexino [74].

Geoneutrinos : Geoneutrinos are mainly electron antineutrinos ($\bar{\nu}_e$) produced inside the Earth by the natural decay of the radioactive nuclei. The radioactive nuclei that undergo beta-decay and emit electron antineutrinos are mainly, ${}^{238}\text{U}$ and ${}^{232}\text{Th}$. The principal reactions to observe electron antineutrinos ($\bar{\nu}_e$) are the capture of free protons followed by the detection of neutron. The capture and detection reactions are as follows,



These neutrinos are produced in the sub-MeV to a few MeV range. Recently, two experiments have reported the detection of geoneutrinos namely KamLAND [75] and Borexino [76].

Supernova neutrinos : When a massive star, at the end of its life collapses to a neutron star or a black hole via a supernova explosion, almost 99% of the gravitational binding energy is carried away by the neutrinos. The energy range of these neutrinos are \sim MeV [77], [78]. These neutrinos come in all the three flavors. The confirmation on the detection of the supernova neutrinos came on 23rd February 1987, when neutrinos from the supernova SN1987A were detected by the Kamiokande experiment (detected 11 events) in Japan [79] and the IMB experiment (detected 7 events) in USA [80].

Reactor neutrinos : Nuclear reactors are one of the major sources of electron antineutrinos which are produced in the β -decays of neutron rich nuclei (like, ^{235}U , ^{238}U , ^{239}Pu , ^{241}Pu) via controlled nuclear fission processes. The energy range for the reactor antineutrinos is of the order few MeV. These neutrinos have been used all along from the first detection of neutrinos in 1956 by Reines and Cowan [2] using inverse beta decay process ($\bar{\nu}_e p \rightarrow e^+ n$) up to the most recent oscillation studies. There were a number of short baseline (source to detector distance < 1 km) reactor neutrino experiments which reported null result for oscillation *. The KamLAND experiment having source to detector distance 180 km, was the first to observe oscillations of the reactors antineutrinos [12]. Later, Daya Bay [81], RENO [82], Double Chooz [83] experiments also reported the detection and oscillation of reactor antineutrinos.

Accelerator neutrinos : Neutrinos produced at the particle accelerators are one of the major sources of artificially created neutrinos. These are generated as the final products of pion or kaon decay when protons are bombarded on a target. There are two methods to produce neutrinos from pion decays namely, (i) the decay of pions in flight (DIF) and (ii) the decay of pions at rest (DAR). In the DIF mechanism, while pions and kaons are travelling through decay pipe, they decay to muon-neutrinos (ν_μ) and muon-antineutrinos ($\bar{\nu}_\mu$). In this process ν_μ beams are produced by the decay of π^+ , $K^+ \rightarrow \mu^+ \nu_\mu$ which contain about 1% of $\bar{\nu}_\mu$ and 1% of ν_e because of the further decays of $\mu^+ \rightarrow e^+ \nu_e \bar{\nu}_\mu$. Depending on the polarity of the focusing horn one gets pure

*Note that, later the results of this short baseline experiments were discussed incorporating an \sim eV sterile neutrino [59].

ν_μ or $\bar{\nu}_\mu$ beams. The typical energy range for the neutrinos produced in this mechanism are of a few tens of MeV to a few GeV. In the case of DAR mechanism, the beam is composed of $\bar{\nu}_\mu$ coming from the decay of the π^+ [†] in the following manner,

$$\begin{aligned}\pi^+ &\rightarrow \mu^+ \nu_\mu, \\ \mu^+ &\rightarrow e^+ \nu_e \bar{\nu}_\mu\end{aligned}\tag{2.1.5}$$

The produced $\bar{\nu}_\mu$ beam has energy in the range of the order of a few times 10 MeV and this are used to study $\bar{\nu}_\mu \rightarrow \bar{\nu}_e$ oscillations. In addition, the flux of electron neutrinos (ν_e) coming from the second decay chain being small, it is possible to search for $\nu_\mu \rightarrow \nu_e$ oscillations as well.

Three largely used accelerators based beams are :

1. The neutrinos at the main injector (NuMI) [84] beam from Fermilab [15]. The neutrino detectors that used the NuMI beam were MINOS, MINER ν A whereas NO ν A is currently taking data based on the NuMI beam.
2. The CNGS beam from CERN to Gran Sasso [85]. Neutrino detectors like, OPERA [86] and ICARUS [87], [88] used neutrinos from the CNGS beam to detect neutrinos.
3. The muon neutrino beam from Japan proton accelerator research complex or J-PARC. The on-going neutrino oscillation experiment, T2K [89] is using the J-PARC neutrino beam. Two next generation experiments T2HK and T2HKK will also use the J-PARC neutrino beam [90,91].

The neutrino oscillation experiments like, LSND [55] and MiniBooNE [92] studied the oscillations of the neutrinos in the MeV energy range whereas long baseline accelerator experiments like K2K [14,93], MINOS [15] studied neutrino oscillations in the GeV energy range. Also, on going experiments like, T2K [89] and NO ν A [94] study neutrino oscillations in the GeV energy range.

Atmospheric neutrinos : Atmospheric neutrinos are created when cosmic rays collide with the nuclei in the Earth's atmosphere and produce charged particles

[†]Note that in this process π^- are being absorbed by the nuclei.

like pions and kaons. They decay to produce muons and muon neutrinos :

$$\pi^+ \rightarrow \mu^+ \nu_\mu, \quad \pi^- \rightarrow \mu^- \bar{\nu}_\mu \quad (2.1.6)$$

These muons further decay to give rise to electrons, electron neutrinos and muon neutrinos,

$$\mu^+ \rightarrow e^+ \nu_e \bar{\nu}_\mu, \quad \mu^- \rightarrow e^- \bar{\nu}_e \nu_\mu \quad (2.1.7)$$

Kaons produced in the atmosphere also contribute to the production of muons and muon neutrinos. Energy of the atmospheric neutrinos lies in sub-GeV to multi-TeV order [95]. The first report on the detection of atmospheric neutrinos came, in 1965, from the Kolar Gold Field Mine in India [96, 97] and the East Rand Proprietary Gold Mine in South Africa [98]. Later, Kamiokande [99], IMB [100], Soudan-2 [101] experiments have also reported the detection of atmospheric neutrinos. Most recently, the high statistics Super-Kamiokande [102] established the detection of atmospheric neutrinos on firm footing.

Ultra High Energy Neutrinos : Neutrinos having energies greater than 10^{15} eV are known as the Ultra High Energy Neutrinos (UHE). Currently proposed astrophysical sources of high energy cosmic neutrinos include those from active galactic nuclei (AGN) [103] and gamma ray bursts (GRB) [104]. Production of these UHE neutrinos depend on the interaction of protons with the soft photons or matter. The protons in these sources are accelerated via Fermi acceleration mechanism to very high energies before they collide with matter [105]. UHE neutrino telescopes were planned to study the neutrinos coming from the distant astrophysical sources [106]. These neutrinos cover a very long path from their sources to reach the Earth. Due to such a long distance, the oscillation of this high energy neutrinos get averaged out. Hence, their final flavor composition depends on the initial sources of the neutrinos as different sources can have different initial flavor and the neutrino mixing angles. The ANITA or ANtarctic Impulsive Transient Antenna is a balloon-borne radio pulse detector system, designed to search for UHE neutrinos with energies greater than 10^{18} eV [107]. It has completed its three launch successfully and recently its 4th phase, ANITA-IV, launched in December 2016. The IceCube Neutrino Observatory at the South Pole is currently the most sensitive detector for the detection of astrophysical neutrinos. Recently, IceCube collaboration has reported the results of an all sky search of the UHE

neutrino events in the energy range between 30 to 2000 TeV [108]. They have detected a total of 37 neutrino events.

2.2 Detector Technologies

In this section, we discuss about the various detection techniques of neutrinos. Neutrinos are electrically neutral and interact only via weak interactions. Hence, neutrino detectors must be very large to detect a significant number of neutrinos. Neutrinos interact in two ways namely, charged current (CC) and neutral current (NC) interactions via W^\pm and Z boson exchange processes respectively :

$$\nu_l + N \rightarrow l^- + X \quad : \text{CC}, \quad (2.2.1)$$

$$\nu_l + N \rightarrow \nu_l + X \quad : \text{NC}, \quad (2.2.2)$$

where $l = e, \mu, \tau$, N is the nucleon and X is the final state hadron. Various categories of detectors used for the neutrino experiments are, Čerenkov detectors, scintillator detectors, iron detectors, radiochemical detectors, emulsion detectors, etc. We discuss some of these below.

Čerenkov detectors : The radiation of Čerenkov light occurs, if the speed of a charged particle is greater than the speed of light in a medium. In these kind of detectors, the detection medium is mainly purified water or heavy water (D_2O) contained in a large tank surrounded by photomultiplier tubes (PMT's) which detect the Čerenkov radiation emitted by the final state particles. Inside the medium, Čerenkov photons are emitted in a cone which allows one to identify the particle and reconstruct its energy and direction. Some of the neutrino detectors which have used the Čerenkov detection principle are : (i) The IMB detector [109] located at the Morton Salt mine, Ohio (USA) used water Čerenkov detectors to detect atmospheric neutrinos. (ii) The Kamiokande detector and its upgraded version Super-Kamiokande (SK) [110] in Japan are also examples of water Čerenkov detector which have studied neutrinos from different sources including the Sun, supernovae, the atmosphere, and accelerators. (iii) The SNO detector [111], which was designed to study solar neutrinos located in the Creighton mine, used heavy water as the detection medium. (iv) Currently running IceCube experiment also use Čerenkov detection technique to detect high energy neutrinos.

Scintillator detectors : A scintillator is any material (like mineral oil) that can release a photon in the UV or visible light range, when an excited electron returns to its minimum energy state or ground state in the scintillator. Later, these scintillation photons are detected by PMTs and converted into an electronic signal. In 1903, W. Crookes first built the scintillator counter and used zinc sulfide screen for the visual observation of the light flashes. The long baseline neutrino oscillation experiments, like NO ν A [94] and reactor experiments, like KamLAND [12], Double-CHOOZ [112], Daya-Bay [113], RENO [114] have used scintillator detectors.

Liquid argon detectors : These represent an innovative technology for a new class of very large detectors for the detection of particle events. The Liquid argon time projection chambers (LArTPC) measure the ionization energy loss of the charged particles, in order to trace the particle trajectory and momentum [115]. Under the influence of an uniformly applied electric field within the detector volume, ionized charged particles' tracks are drifted towards the other side of the detector on the collection plane. For all the charged particles, precise charge amplitude and the arrival times are recorded and used to reconstruct the event topology. The scintillation light emitted during the event is also detected by the PMTs. Liquid argon has several advantages due to which the neutrino community has shown a lot of interest to use LArTPC as a detectors for neutrino experiments [116]. Liquid argon is dense and relatively inexpensive, making large-scale experiments economically viable. Also argon is a noble element with a vanishing electronegativity. So the ionized electrons will not be absorbed as they drift towards the detector. This makes liquid argon an ideal detector medium to detect the neutrino interactions. ICARUS is the very first experiment where this technology has been tested [88]. Ongoing neutrino experiment MicroBooNE is using LArTPC as a detector and the proposed experiment DUNE is also planning to use LArTPC as a detector.

Iron detectors : Iron is a dense material, so using an iron detector, one can detect more neutrino events compared to a lighter target like water. Also, iron can be magnetized and hence such detectors can identify the charge of the final state particles. Thus these detector can be used to record neutrino or antineutrino events separately. Some of the neutrino detectors which used iron as a detection medium are : (i) Soudan

2, a 960 ton iron tracking calorimeter detector located in the Soudan Mine in Northern Minnesota (USA) whose primary goal was to search for proton decay [117]. Later, it also reported the measured to expected atmospheric neutrino neutrino flavor ratio [118]. (ii) The long baseline experiment, MINOS is an example of steel-scintillator tracking calorimeter detector [119], [15]. It has two detectors, the mass of the near detector which is 1 km away from the source is 0.98 kton whereas mass for the far detectors which is 735 km away from the source is 5.4 kton. (iii) Proposed atmospheric neutrino experiment, India-based neutrino observatory (INO) has also plans to use 50 kton magnetised Iron CALorimeter (ICAL) detector [120, 121]. A detailed description of the ICAL detector are discussed in the next section.

2.3 Overview of a Few Detectors

In this section, we describe the experimental set-ups and physics goals of the experiments that we have considered in the analysis performed in this thesis. These are T2K, NO ν A, DUNE and ICAL@INO. Out of these four experiments, first three are long baseline beam based experiments and the last one is an atmospheric neutrino experiment. Among these, first two are currently taking data and the remaining two are proposed next generation experiments. T2K and NO ν A are off-axis experiments whereas DUNE will be an on-axis experiment[‡]. In the off-axis case as the detector is kept at a certain angle, the neutrino flux decreases but peaks sharply. In that case, if the oscillation maxima can be made to coincide with the flux peak, then the signal can be enhanced and the background events can be reduced sufficiently.

T2K : The Tokai to Kamioka (T2K) is a currently running long-baseline neutrino oscillation experiment in Japan. In this experiment, neutrinos travel a long path of 295 km from J-PARC high intensity proton accelerator facility in Tokai with 30 GeV proton beam energy and 750 kW proton beam power [123]. This proton beam strikes a graphite target to produce charged mesons (e.g. pions and kaons), which are focused by three magnetic horns before they further decay. By using polarity of the horn current these mesons are separated either in positively or negatively charged beams largely

[‡]Off-axis [122] means that the detector is kept at a certain angle from the neutrino source whereas on-axis means the source and detector are at the same beamline.

composed of ν_μ or $\bar{\nu}_\mu$. These neutrino beams are measured by two near detectors (ND) namely , INGRID and ND280 which are located at 280 m from the target and a far detector (FD) which is 2.5° off-axis angle from the beam direction. The FD is the Super-Kamiokande water Čerenkov detector with 50 kton mass placed in Kamioka mine. The off-axis muon neutrino energy spectrum peaks at 0.6 GeV. This reduces the backgrounds compared to on-axis spectrum. T2K started taking data in neutrino mode from January 2010 till May 2016 with total exposure of 7.482×10^{20} protons on target (POT). From May 2014, it has started taking data in antineutrino mode with an exposure of 7.471×10^{20} POT [124]. The first combined analysis of neutrino and antineutrino for T2K are given in [124]. Future plans with increase in exposure to 20×10^{21} POT are discussed in [125]. The main objectives of this experiment are as follows [123] :

- Precision measurements of oscillation parameters (namely, $\sin^2 2\theta_{23}$, Δm_{31}^2) in the disappearance channel ($\nu_\mu \rightarrow \nu_\mu$) mode.
- To look for CP violation in the leptonic sector using the appearance channel ($\nu_\mu \rightarrow \nu_e$) mode.

NO ν A : The NuMI Off-axis ν_e Appearance (NO ν A) experiment at Fermi National Accelerator Laboratory (Fermilab), USA is a long baseline neutrino oscillation experiment which is presently taking data. A muon neutrino (ν_μ) beam having a beam power of 0.7 MW with 120 GeV proton energy corresponding to 6.0×10^{20} POT from NuMI beamline travels a distance of 810 km before it gets detected by the Totally Active Scintillator Detector (TASD) in Ash River, Minnesota. In this case, a FD with 14 kton mass is located at the surface at an angle of 14 mrad (0.8°) off-axis from the neutrino beamline in such a way that the ν_μ -beam peaks around 2 GeV. It also has a ND with the 290 ton detector mass which is located 100 m underground at the Fermilab site. Experimental details of NO ν A experiment has been discussed in [94, 126, 127]. The primary goals of NO ν A include [126],

- Precision measurements of the appearance channel which will provide : (i) the precise value of $\sin^2 2\theta_{13}$. Its goal is to increase the sensitivity by an order of magnitude as compared to the MINOS experiment. (ii) To observe the mass

hierarchy. (iii) The determination of the CP violating phase δ_{CP} in the leptonic sector and (iv) to find the octant of θ_{23} .

- The study of ν_μ or $\bar{\nu}_\mu$ disappearance will improve precision of θ_{23} and the atmospheric mass squared difference ($|\Delta m_{32}^2|$).

Recently, the first measurements of electron neutrino appearance [17] and disappearance [18] channel results for NO ν A have been published.

DUNE : The Deep Underground Neutrino Experiment (DUNE) is a future generation high statistics superbeam accelerator experiment at Fermilab. It is an on-axis (broad band beam) experiment where a ν_μ -beam will travel a distance of 1300 km from Fermilab to a far detector at Sanford Underground Research Facility (SURF) in Lead, South Dakota which is ~ 1478 m underground. The beam of neutrinos will be from Fermilab's Main Injector accelerator as a proton source. The beam for DUNE is expected to be the highest intensity neutrino beam in the world. For the initial run, which is planned to start in 2026, a proton beam power of 1.2 MW with a proton energy of 120 GeV having an exposure of 1.0×10^{21} POT/year is planned. Also the FD will be a 10 kton LArTPC detector which will be upgraded to 40 (or 34) kton later. It will also have a ND which will be at the Fermilab site [128–130]. The primary science programs for DUNE are [128],

- To find the CP violating phase δ_{CP} in the leptonic sector.
- Determination of the correct mass ordering.
- Measurement of the mixing angle θ_{23} and its octant.
- To search for proton decay.
- To look for supernova neutrinos by detecting ν_e flux from the core-collapse supernova.

Other than the primary physics goals, DUNE can also look for a number of new physics scenarios. These include sterile neutrino searches, non-standard interaction effects, measurement of tau neutrino appearance probability, dark matter searches, etc [128].

INO : The India-based Neutrino Observatory (INO) is one of the major neutrino oscillation projects which will study atmospheric neutrinos in an underground laboratory [120]. It is proposed to be built in Bodi West Hills, in Theni district of Tamil Nadu in South India. The detector of this project is planned to be a 50 kton magnetized iron calorimeter (ICAL) detector which is sensitive to mainly ν_μ or $\bar{\nu}_\mu$ events generally in the energy range 0.5-25 GeV [131]. There will be 151 layers of Resistive Plate Chambers (RPCs) in this detector interleaved with 5.6 cm thick iron plates. These plates act as the target while the RPCs are the active detector elements which will detect the final state particles. Moreover, due to the applied magnetic field of strength 1.5 T, ICAL detector can distinguish between μ^+ and μ^- . This is a unique feature of this detector. It is optimized to detect muons when they propagate through the detector by identifying their charges and the accurate determination of their energies and directions [132, 133]. Detailed specifications are mentioned in [121]. ICAL detector can also be used to reconstruct energy of hadrons produced in a neutrino interaction. The sensitivity study which include hadronic information are discussed in [134]. The primary physics goals of this project include,

- Precise measurement of the 2-3 neutrino oscillation parameters using atmospheric neutrino data and to determine the octant of θ_{23} .
- Determination of the neutrino mass hierarchy by studying the Earth matter effect on atmospheric neutrinos.

Apart from these, various possible new physics scenarios that INO can look for include, the study of the non-standard interactions, CPT violation, dark matter searches, sterile neutrinos, magnetic monopoles, etc [121].

2.4 Summary

In this chapter, we first present a discussion of the various sources of neutrinos including both natural and artificial sources. In section (2.2), we give an overview of the various detector technologies which are used to detect neutrinos. In section (2.3), we describe the various experimental set ups that we have considered in our study and mention their main physics goals.

Chapter 3

Neutrino Oscillation in Vacuum and Matter

*“You can’t change how people treat you or what they say about you.
All you can do is change how you react to it.”*

– Mahatma Gandhi

3.1 Introduction

Neutrino oscillation or flavor conversion is a quantum mechanical phenomenon in which a neutrino produced with a definite flavor (say, ν_α , $\alpha = e, \mu$ or τ) is later converted to some other flavor. This was first proposed by B. Pontecorvo in late 1950s in analogy with the neutral K-mesons oscillations [7]. Pontecorvo proposed the concept of neutrino oscillation between left-handed neutrinos and antineutrinos. Since left-handed antineutrinos do not take part in weak interactions, Pontecorvo named them as sterile neutrinos. Note that at that time, the only known active neutrino was the electron neutrino (ν_e). Although the sterile neutrino (a neutral fermion), does not take part in weak interaction, it can mix with the active neutrinos and hence can take part in oscillation. After the discovery of the muon-neutrino, concepts behind the neutrinos flavor conversion among active neutrinos became clear. This required neutrinos to have definite masses and mixing among flavors. In 1962, Maki-Nakagawa-Sakata first considered the mixing of three different flavors of neutrinos [135].

Neutrinos of three definite flavors ν_e, ν_μ, ν_τ are produced in charged current (CC)

weak interaction processes in association with charged leptons e, μ, τ respectively. The charged current weak interaction Lagrangian can be written as,

$$\begin{aligned} -\mathcal{L}_I^{CC} &= \frac{g}{\sqrt{2}} \sum_{\alpha=e,\mu,\tau} \bar{\nu}_{\alpha L} \gamma^\rho l_{\alpha L} W^\rho + H.c. \\ &= \frac{g}{\sqrt{2}} \sum_{\alpha=e,\mu,\tau} \sum_{k=1,2,3} U_{\alpha k}^* \bar{\nu}_{kL} \gamma^\rho l_{kL} W^\rho + H.c. \end{aligned} \quad (3.1.1)$$

where, g is the coupling constant associated with $SU(2)_L$ and ν_k are fields with definite mass. Note that the second line of the above equation is obtained when leptonic fields are transformed from the flavor basis to the mass basis. Here, we consider only three massive neutrinos ν_{kL} (i.e. $k=1,2,3$) corresponding to the three active neutrinos. In principle, there can be more than three neutrinos and additional neutrinos can be treated as sterile. The equation (3.1.1) shows that the mass and flavor states are related as,

$$|\nu_\alpha\rangle = \sum_k U_{\alpha k}^* |\nu_k\rangle \quad (3.1.2)$$

where U is the PMNS mixing matrix.

In general, a $N \times N$ unitary mixing matrix contains N^2 independent parameters of which $N(N-1)/2$ are mixing angles and $N(N+1)/2$ are phases. But among all the phases, $(2N-1)$ phases are unphysical and can be absorbed by the proper re-phasing of the Dirac fields leaving $(N-1)(N-2)/2$ physical phases. If neutrinos are Majorana fermions then one can only re-phase the N phases of the charged lepton fields, leaving $N(N-1)/2$ physical phases. Out of these $(N-1)(N-2)/2$ are the usual Dirac phases, while $(N-1)$ are specific to the Majorana case and are named as Majorana phases. Thus, in the two flavor framework (i.e. for $N=2$) the unitary mixing matrix has no phase and the only independent parameter is the mixing angle. Considering $N=3$ i.e. in the three flavor formalism, we have three mixing angles and one CP phase. Thus, to have CP violation in the leptonic sector, one needs minimum three generation of neutrinos.

The plan of this chapter is as follows: in the next section (3.2), we discuss the standard quantum mechanical formalism of neutrino oscillation considering a simple two flavor formalism in vacuum. In the section (3.3) of this chapter we extend the discussion to the three flavor case. If neutrinos propagate through matter rather than

vacuum as discussed in the section (3.4.1) then interaction with matter modifies the propagation and this brings significant changes in the neutrino oscillation probabilities. We calculate the neutrino oscillation probabilities considering two flavor framework in presence of matter in section (3.4.2). In the three flavor formalism it is difficult to exactly solve the propagation equation in presence of matter. Therefore, in the section (3.4.3), we discuss the various approximation methods to calculate neutrino oscillation probability for the three flavor framework and present the probability expressions. In the section (3.5), we present a brief discussion on the various experimental evidences of neutrino oscillation. We end this chapter with section (3.6), where we discuss the current status of all the oscillation parameters in the three flavor formalism and tabulate the various unknowns in neutrino oscillation physics.

3.2 Two Flavor Neutrino Oscillation

We derive the neutrino oscillation probability by considering a simple plane wave approximation. In 1975-76, the standard theory of neutrino oscillation using the plane wave approximation was developed by Eliezer and Swift [136], Fritzsche and Minkowski [137], Bilenky and Pontecorvo [138, 139] *. For the two flavor case the flavor states (say ν_e and ν_μ) are the linear superpositions of the two mass eigenstates (say ν_1 and ν_2). The unitary mixing matrix which relates mass eigenstates to flavor eigenstates in 2-flavor paradigm contains one independent parameter namely, one mixing angle. The basis transformation from the mass eigenstates to the flavor eigenstates can be written as

$$\begin{pmatrix} |\nu_e\rangle \\ |\nu_\mu\rangle \end{pmatrix} = \begin{pmatrix} \cos \theta & \sin \theta \\ -\sin \theta & \cos \theta \end{pmatrix} \begin{pmatrix} |\nu_1\rangle \\ |\nu_2\rangle \end{pmatrix}, \quad (3.2.1)$$

where θ is the mixing angle corresponding to rotations in the two dimensional plane. Let, at initial time $t = 0$, neutrino is in the flavor state $|\nu_e\rangle$ i.e.

$$|\nu_e(t = 0)\rangle = \cos \theta |\nu_1\rangle + \sin \theta |\nu_2\rangle. \quad (3.2.2)$$

*A more realistic approach is to consider the wave packet treatment [140]. However for the neutrino oscillation phenomenology that we have considered in this doctoral work, the wave packet effects are not important [141].

The mass eigenstates are the eigenstates of the Hamiltonian, i.e.

$$\begin{aligned}\mathcal{H}_0|\nu_k\rangle &= E_k|\nu_k\rangle, \\ &= \sqrt{p^2 + m_k^2}|\nu_k\rangle, \\ &\simeq \left(p + \frac{m_k^2}{2p}\right)|\nu_k\rangle, \quad \left(\frac{m}{p} \ll 1\right)\end{aligned}\quad (3.2.3)$$

where E_k ($k = 1, 2$) are the energy eigenvalues. We also use, $c = 1 = \hbar$ in the above equation (the natural unit), as is the usual practice in particle physics. Assuming mass eigenstates propagate with same momentum we get,

$$E_2 - E_1 = \frac{m_2^2 - m_1^2}{2p} \approx \frac{\Delta m^2}{2E}. \quad (3.2.4)$$

Notice that $\Delta m^2 = m_2^2 - m_1^2$ is the mass squared difference of the two mass eigenstates and we use $E \simeq p$ in the denominator for the ultra-relativistic neutrinos.

The time evolution of Schrödinger equation for the mass eigenstates $|\nu_k\rangle$ is,

$$i\frac{d}{dt}|\nu_k(t)\rangle = \mathcal{H}_0|\nu_k(t)\rangle. \quad (3.2.5)$$

This implies that the neutrino mass eigenstates evolve in time as

$$|\nu_k(t)\rangle = e^{-iE_k t}|\nu_k\rangle. \quad (3.2.6)$$

Hence, after a finite time t , the flavor eigenstates, $|\nu_e(t = t)\rangle$ can be written as,

$$|\nu_e(t = t)\rangle = \cos\theta|\nu_1\rangle e^{-iE_1 t} + \sin\theta|\nu_2\rangle e^{-iE_2 t}. \quad (3.2.7)$$

Using equation (3.2.1), $|\nu_1\rangle, |\nu_2\rangle$ can be expressed in terms of flavor states to give :

$$|\nu_e(t = t)\rangle = a(t)|\nu_e\rangle + b(t)|\nu_\mu\rangle, \quad (3.2.8)$$

where,

$$a(t) = \cos^2\theta e^{-iE_1 t} + \sin^2\theta e^{-iE_2 t}, \quad (3.2.9)$$

$$b(t) = \cos\theta \sin\theta (e^{-iE_2 t} - e^{-iE_1 t}). \quad (3.2.10)$$

Any non-zero value of $b(t)$ indicates neutrino flavor transition from electron neutrino at time ($t=0$) to muon neutrino at time ($t=t$). Here, $|a(t)|^2$ gives the survival probability of electron neutrino or the disappearance channel probability (P_{ee}) and $|b(t)|^2$ gives the

appearance probability of electron neutrino to muon neutrino or appearance channel probability ($P_{e\mu}$). These are given by,

$$\begin{aligned} P_{\nu_e \rightarrow \nu_e} = P_{ee} &= 1 - \sin^2 2\theta \sin^2 \left(\frac{E_2 - E_1}{2} t \right), \\ &= 1 - \sin^2 2\theta \sin^2 \left(\frac{\Delta m^2 L}{4E} \right), \quad \left\{ E_2 - E_1 = \frac{\Delta m^2 L}{2E} \right\} \end{aligned} \quad (3.2.11)$$

$$P_{\nu_e \rightarrow \nu_\mu} = P_{e\mu} = \sin^2 2\theta \sin^2 \left(\frac{\Delta m^2 L}{4E} \right), \quad (3.2.12)$$

where we use $t \simeq L$, the length travelled by the neutrino before its detection and one can assume it safely because of the ultra-relativistic nature of the neutrinos. We notice from equation (3.2.12) that a non-zero oscillation probability requires neutrinos masses to be non-degenerate i.e. $m_1 \neq m_2$ and the mixing angle to be non-zero. We also notice from the mixing matrix as given by equation (3.2.1) that two-flavor neutrino oscillation probability does not depend on any phase and hence there are no CP or T violation. Therefore, it is clear that, in the two-flavor paradigm, the direct and the time reversed transition probabilities of neutrinos and antineutrinos are equal :

$$P_{\nu_\alpha \rightarrow \nu_\beta} = P_{\nu_\beta \rightarrow \nu_\alpha} = P_{\bar{\nu}_\alpha \rightarrow \bar{\nu}_\beta} = P_{\bar{\nu}_\beta \rightarrow \bar{\nu}_\alpha}. \quad (3.2.13)$$

After inserting appropriate conversion factors, the probability expression given by the equation (3.2.12) can be written as

$$P_{\nu_e \rightarrow \nu_\mu} = \sin^2 2\theta \sin^2 \left(1.27 \frac{\Delta m^2 L}{E} \right), \quad (3.2.14)$$

where L is in km (m), E is in GeV (MeV) and Δm^2 is in eV^2 .

This expression can also be written in terms of the *neutrino oscillation length*, \mathcal{L}_{osc} , as

$$P_{\nu_e \rightarrow \nu_\mu} = \sin^2 2\theta \sin^2 \left(\pi \frac{L}{\mathcal{L}_{osc}} \right), \quad (3.2.15)$$

where,

$$\mathcal{L}_{osc} = 2.47 \frac{E(\text{GeV})}{\Delta m^2(\text{eV}^2)} \text{ km}. \quad (3.2.16)$$

We notice from the equation (3.2.15) that $\sin^2 2\theta$ represents the amplitude of the flavor conversion which is maximum for $\theta = 45^\circ$. Also, if the source to detector distance is less than the oscillation length i.e. $L \ll \mathcal{L}_{osc}$, then a definite flavor has no time to convert to another flavor whereas if $L \gg \mathcal{L}_{osc}$, then very rapid oscillations occur

and only average effect of the probability will be detectable. To have maximum flavor conversion, one needs $\mathcal{L}_{osc} = 2L$ i.e. source to detector distance has to be double of the oscillation length. This maximum flavor conversion also implies,

$$\begin{aligned} 1.27 \frac{\Delta m^2 L}{E} &\sim \frac{\pi}{2}, \\ \frac{\Delta m^2 L}{E} &\sim 1. \end{aligned} \quad (3.2.17)$$

$$\Delta m^2 \sim \frac{E(\text{MeV})}{L(\text{m})} = \frac{E(\text{GeV})}{L(\text{km})}. \quad (3.2.18)$$

Traditionally, various types of neutrino oscillation experiments are classified depending on the average values of L/E and this determines the sensitivity to the mass squared differences (Δm^2). In the table (3.1), we present the various source-detector distances and energies of different type of experiments and to what value of Δm^2 they are sensitive.

Experiments	L	E	Δm^2 (eV ²)
Reactor SBL	~ 10 m	~ 1 MeV	~ 0.1
Accelerator SBL	~ 10 m – 1 km	~ 10 MeV – 10^2 GeV	$\sim (1-10^2)$
Reactor LBL	~ 1 km	~ 1 MeV	$\sim 10^{-3}$
Accelerator LBL	$\sim 10^3$ km	$\gtrsim 1$ GeV	$\gtrsim 10^{-3}$
Atmospheric	$\sim 20 - 10^4$ km	$0.5 - 10^2$ GeV	$\sim 10^{-4}$
Reactor VLB	$\sim 10^2$ km	$\gtrsim 1$ MeV	$\sim 10^{-5}$
Solar	$\sim 10^{11}$ km	$0.2 - 15$ MeV	$\sim 10^{-12}$

Table 3.1: Various energies and baselines and the value of mass squared difference that give maximum oscillation affect. Here, SBL=short baseline, LBL=long baseline and VLB=very long baseline oscillation experiments.

In figure (3.1), we present the appearance and disappearance probabilities against the neutrino energy as given by equations (3.2.11, 3.2.12). For illustrative purpose, we consider $L = 1000$ km, the mixing angle between the two flavors as maximal (i.e. $\theta = 45^\circ$) and the mass squared difference : $\Delta m^2 = 2.5 \times 10^{-3} \text{ eV}^2$. We observe from

the figure that for this baseline at energy $E = 2$ GeV (where first oscillation maximum occurs), an electron type neutrino is fully converted to a muon type giving rise to maximum flavor conversion probability (i.e. $P_{e\mu} = 1$) whereas survival probability becomes zero (i.e. $P_{ee} = 0$).

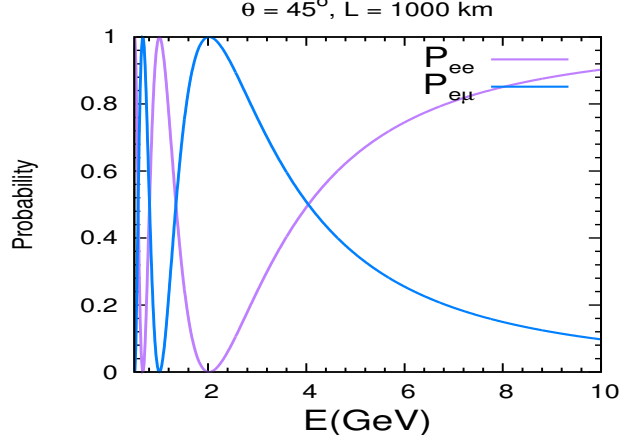


Figure 3.1: Graphical representation of two-flavor neutrino oscillations.

3.3 Three flavor neutrino oscillation

In this section, we obtain the neutrino oscillation probabilities in vacuum for a three neutrino framework. This formalism is a simple extension of the two flavor picture with an increase in the number of oscillation parameters. The transformation that relates mass eigenstates to the flavor eigenstates can be written as

$$\begin{pmatrix} |\nu_e\rangle \\ |\nu_\mu\rangle \\ |\nu_\tau\rangle \end{pmatrix} = U^* \begin{pmatrix} |\nu_1\rangle \\ |\nu_2\rangle \\ |\nu_3\rangle \end{pmatrix}. \quad (3.3.1)$$

where, U is the 3×3 PMNS mixing matrix. This mixing matrix can be parameterized in terms of three mixing angles (θ_{ij} , $j > i = 1, 2, 3$) and a CP phase as discussed above. In the three-flavor formalism, one can have various parameterizations for the unitary mixing matrix, as discussed in Ref. [142]. We adopt the standard parameterization of

the leptonic mixing matrix U from the Particle Data Book [143], which is given by,

$$U = U(\theta_{23})U(\theta_{13}, \delta)U(\theta_{12}),$$

$$= \begin{bmatrix} c_{12}c_{13} & s_{12}c_{13} & s_{13}e^{-i\delta} \\ -s_{12}c_{23} - c_{12}s_{23}s_{13}e^{i\delta} & c_{12}c_{23} - s_{12}s_{23}s_{13}e^{i\delta} & s_{23}c_{13} \\ s_{12}s_{23} - c_{12}c_{23}s_{13}e^{i\delta} & -c_{12}s_{23} - s_{12}c_{23}s_{13}e^{i\delta} & c_{23}c_{13} \end{bmatrix}, \quad (3.3.2)$$

where, U_{ij} are the rotation matrices in $(i \times j)$ -plane and $s_{ij} = \sin \theta_{ij}$ and $c_{ij} = \cos \theta_{ij}$. The mixing matrix for the antineutrinos are obtained by changing the sign of Dirac CP phase ($\delta \rightarrow -\delta$).

Equation (3.3.1) gives the relation between the flavor and the mass eigenstates at time ($t=0$). The time evolution equation, at a later time (t), can be expressed as

$$|\nu_\alpha(t)\rangle = U_{\alpha k}^* |\nu_k\rangle e^{-iE_k t}. \quad (3.3.3)$$

Using the inverse transformation from equation (3.1.2) for $|\nu_k\rangle$, we can write the above equation as,

$$|\nu_\alpha(t)\rangle = U_{\alpha k}^* U_{\beta k} |\nu_\beta\rangle e^{-iE_k t}, \quad (3.3.4)$$

where $\alpha, \beta = e, \mu, \tau$.

The transition probability that a neutrino, originally of flavor α , will later be detected as flavor β in vacuum is,

$$P_{\nu_\alpha \rightarrow \nu_\beta} = |\langle \nu_\beta | \nu_\alpha(t) \rangle|^2, \quad (3.3.5)$$

$$= \left| \sum_k U_{\alpha k}^* U_{\beta k} e^{-iE_k t} \right|^2, \quad (3.3.6)$$

$$= \sum_{k=j} |U_{\alpha k}|^2 |U_{\beta j}|^2 + \sum_{k \neq j} U_{\alpha k} U_{\beta j} U_{\alpha j}^* U_{\beta k}^* e^{-i(E_k - E_j)t}. \quad (3.3.7)$$

Using the relation

$$\left| \sum_k U_{\alpha k} U_{\beta k}^* \right|^2 = \sum_i |U_{\alpha i}|^2 |U_{\beta i}|^2 + \sum_{k \neq j} U_{\alpha k} U_{\beta j} U_{\alpha j}^* U_{\beta k}^*, \quad (3.3.8)$$

and the unitarity condition,

$$\sum_k U_{\alpha k} U_{\beta k}^* = \delta_{\alpha\beta}. \quad (3.3.9)$$

One can express the probability as

$$\begin{aligned}
P_{\nu_\alpha \rightarrow \nu_\beta} &= \delta_{\alpha\beta} - 4 \sum_{k>j} \text{Re}(U_{\alpha k}^* U_{\beta k} U_{\alpha j} U_{\beta j}^*) \sin^2\left(\frac{\Delta m_{kj}^2 L}{4E}\right) \\
&\quad + 2 \sum_{k>j} \text{Im}(U_{\alpha k}^* U_{\beta k} U_{\alpha j} U_{\beta j}^*) \sin\left(\frac{\Delta m_{kj}^2 L}{2E}\right) \\
&= \delta_{\alpha\beta} - 4 \sum_{k>j} \text{Re}(U_{\alpha k}^* U_{\beta k} U_{\alpha j} U_{\beta j}^*) \sin^2(\Delta_{kj}) + 2 \sum_{k>j} \text{Im}(U_{\alpha k}^* U_{\beta k} U_{\alpha j} U_{\beta j}^*) \sin(2\Delta_{kj})
\end{aligned} \tag{3.3.10}$$

where,

$$\Delta_{kj} = \frac{\Delta m_{kj}^2 L}{4E} = \frac{(m_k^2 - m_j^2)L}{4E}. \tag{3.3.11}$$

We can see from the probability expression as given by equation (3.3.10) that it depends on six oscillation parameters. These are the three mixing angles (θ_{ij} , $i < j = 1, 2, 3$) and the Dirac CP phase δ contained in the unitary mixing matrix U and the two independent mass squared differences (Δm_{21}^2 , Δm_{31}^2)[†].

Similarly, one can calculate probability expression for the antineutrinos by following the steps as discussed above and by considering the basis transformation as,

$$|\bar{\nu}_\alpha\rangle = \sum_k U_{\alpha k} |\bar{\nu}_k\rangle, \tag{3.3.12}$$

giving the antineutrino probability ($P_{\bar{\nu}_\alpha \rightarrow \bar{\nu}_\beta}$) as,

$$\begin{aligned}
P_{\bar{\nu}_\alpha \rightarrow \bar{\nu}_\beta} &= \delta_{\alpha\beta} - 4 \sum_{k>j} \text{Re}(U_{\alpha k}^* U_{\beta k} U_{\alpha j} U_{\beta j}^*) \sin^2(\Delta_{kj}) - 2 \sum_{k>j} \text{Im}(U_{\alpha k}^* U_{\beta k} U_{\alpha j} U_{\beta j}^*) \sin(2\Delta_{kj}).
\end{aligned} \tag{3.3.13}$$

3.4 Neutrino Propagation Through Matter

In this section, we start the discussion with the interaction potential experienced by the neutrinos while propagating through matter. Later, using this potential we derive the neutrino oscillation probabilities considering both two flavor and three flavor formalism.

[†]Note that $\Delta m_{21}^2 - \Delta m_{31}^2 + \Delta m_{32}^2 = 0$, hence oscillation experiments are only sensitive to two independent mass squared differences.

3.4.1 Effective matter potential

In 1978, L. Wolfenstein first pointed out that neutrino propagation in matter is significantly different than that in the vacuum because of coherent forward elastic scattering of neutrinos with matter [144]. Later, in 1985 S.P. Mikheev and A.Yu. Smirnov elaborated these concepts [145, 146]. A very important point to be noted here is that the coherent forward elastic scattering amplitudes are not the same for all the active neutrinos. The reason behind this is that the normal matter is made up of electrons (also protons and neutrons) but not muons or taus and hence, electron neutrino is significantly affected while propagating through matter. Thus, ν_e encounters both charge current (CC) and neutral current (NC) interactions with the electrons whereas ν_μ or ν_τ interacts with matter only via NC interaction. CC (NC) neutrino interaction with matter is shown in left (right) column of fig. (3.2) using Feynman diagrams. The effective

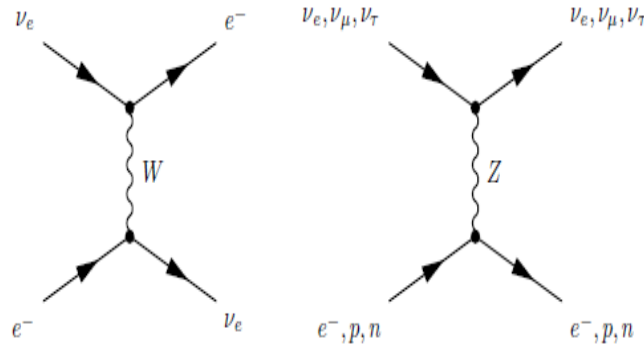


Figure 3.2: Tree level Feynman diagrams for the CC potential V_{CC} generate through W exchange and the NC potential V_{NC} generate through Z exchange.

Hamiltonian for the CC interaction can be written as [‡]

$$H_{\text{eff}}^{CC} = \frac{G_F}{\sqrt{2}} [\bar{\nu}_e \gamma^\mu (1 - \gamma_5) e] [\bar{e} \gamma_\mu (1 - \gamma_5) \nu_e], \quad (3.4.1)$$

where G_F is the Fermi constant. Using the Fierz transformation we obtain,

$$H_{\text{eff}}^{CC} = \frac{G_F}{\sqrt{2}} [\bar{\nu}_e \gamma^\mu (1 - \gamma_5) \nu_e] [\bar{e} \gamma_\mu (1 - \gamma_5) e]. \quad (3.4.2)$$

[‡]Notice that, one can also calculate the contribution to the matter potential due to NC interactions. Since it is the same for all the flavors and appears as a phase with all the flavors, it does not have any overall effect in the flavor transition probabilities. Therefore, we do not consider this in our study [147].

The interaction potential is given by the average of the effective Hamiltonian over the electron background i.e.,

$$\langle H_{\text{eff}}^{CC} \rangle = \frac{G_F}{\sqrt{2}} [\bar{\nu}_e \gamma^\mu (1 - \gamma_5) \nu_e] \langle \bar{e} \gamma_\mu (1 - \gamma_5) e \rangle. \quad (3.4.3)$$

In the non-relativistic limit using the explicit forms of Dirac spinors one can show that [148, 149]

$$\langle \bar{e} \gamma_0 e \rangle = N_e, \quad (3.4.4)$$

$$\langle \bar{e} \gamma_\mu \gamma_5 e \rangle \sim \text{spin}, \quad (3.4.5)$$

$$\langle \bar{e} \gamma_i e \rangle \sim \text{velocity}, \quad (3.4.6)$$

where, N_e is the electron number density of the medium. In the rest frame of unpolarized electrons only the first term (equation(3.4.4)) is non-zero and thus we obtain,

$$\langle H_{\text{eff}}^{CC} \rangle = \sqrt{2} G_F N_e \bar{\nu}_{eL} \gamma^0 \nu_{eL}, \quad (3.4.7)$$

$$= V_{CC} \bar{\nu}_{eL} \gamma^0 \nu_{eL}, \quad (3.4.8)$$

$$= V_{CC} J_\nu, \quad (3.4.9)$$

where $\nu_{eL} = P_L \nu_e = \frac{1 - \gamma_5}{2} \nu_e$, $J_\nu = \bar{\nu}_{eL} \gamma^0 \nu_{eL}$ and V_{CC} is the interaction potential given by

$$V_{CC} = \sqrt{2} G_F N_e. \quad (3.4.10)$$

For antineutrinos, we have to consider the charge conjugate field ν_{eL}^C and in that case,[§] we obtain,

$$J_\nu^C = \nu_{eL}^T (\gamma^0)^T \bar{\nu}_{eL}^T \quad (3.4.11)$$

$$= -\bar{\nu}_{eL} \gamma^0 \nu_{eL}, \quad (3.4.12)$$

and thus for the antineutrinos the effective Hamiltonian becomes

$$\langle H_{\text{eff}}^{CC} \rangle = -\sqrt{2} G_F N_e \bar{\nu}_{eL} \gamma^0 \nu_{eL}, \quad (3.4.13)$$

which gives the interaction potential for the antineutrinos as

$$\overline{V_{CC}} = -\sqrt{2} G_F N_e. \quad (3.4.14)$$

[§]We have, $\nu_{eL}^C = C \bar{\nu}_{eL}^T$, $\bar{\nu}_{eL}^C = -\nu_{eL}^T C^{-1}$ and $C^{-1} \gamma^0 C = (-\gamma^0)^T$, using this transformation one can calculate the current term J_ν^C for antineutrinos.

3.4.2 Two flavor formalism

As discussed earlier, the Hamiltonian in the flavor basis in case of vacuum can be written as

$$H_f^0 = \frac{\Delta m^2}{4E} \begin{pmatrix} -\cos 2\theta & \sin 2\theta \\ \sin 2\theta & \cos 2\theta \end{pmatrix}. \quad (3.4.15)$$

With the inclusion of the matter potential V_{CC} , the Hamiltonian in the flavor basis becomes,

$$H_f^m = \frac{1}{4E} \begin{pmatrix} -\Delta m^2 \cos 2\theta + 4EV_{CC} & \Delta m^2 \sin 2\theta \\ \Delta m^2 \sin 2\theta & \Delta m^2 \cos 2\theta \end{pmatrix}, \quad (3.4.16)$$

$$= \frac{1}{4E} \begin{pmatrix} -\Delta m^2 \cos 2\theta + 2A & \Delta m^2 \sin 2\theta \\ \Delta m^2 \sin 2\theta & \Delta m^2 \cos 2\theta \end{pmatrix}, \quad (\text{using } A = 2EV_{CC}) \quad (3.4.17)$$

$$= \frac{1}{4E} \begin{pmatrix} A - \Delta m^2 \cos 2\theta & \Delta m^2 \sin 2\theta \\ \Delta m^2 \sin 2\theta & -A + \Delta m^2 \cos 2\theta \end{pmatrix}, \quad (3.4.18)$$

where we have used,

$$\begin{pmatrix} 2A & 0 \\ 0 & 0 \end{pmatrix} = \begin{pmatrix} A & 0 \\ 0 & A \end{pmatrix} + \begin{pmatrix} A & 0 \\ 0 & -A \end{pmatrix}. \quad (3.4.19)$$

The first term of this equation is just the constant multiple of an identity matrix and this changes the eigenvalues by an additive factor and eigenvectors by a phase. Hence, this does not affect the oscillation probabilities.

The energy eigenvalues of H_f^m are obtained by diagonalising the equation (3.4.18) as,

$$E_{1,2} = \frac{1}{4E} \left[A \pm \sqrt{(\Delta m^2 \cos 2\theta - A)^2 + (\Delta m^2 \sin 2\theta)^2} \right]. \quad (3.4.20)$$

Now using the fact that $E_2 - E_1 = (m_2^2 - m_1^2)/2E$, we obtain the modified mass squared difference in the presence of matter as,

$$(\Delta m^2)_M = \sqrt{(\Delta m^2 \cos 2\theta - A)^2 + (\Delta m^2 \sin 2\theta)^2}. \quad (3.4.21)$$

Let us denote the mixing angle in the presence of matter as “ θ_M ” and mixing matrix as “ U_M ”. The basis transformation which relates the flavor basis with the mass basis is given by,

$$H_M^m = U_M^\dagger H_f^m U_M. \quad (3.4.22)$$

After solving this, we obtain,

$$\tan 2\theta_M = \frac{\Delta m^2 \sin 2\theta}{\Delta m^2 \cos 2\theta - A}, \quad (3.4.23)$$

and using this modified mixing angle and mass squared difference in presence of matter, the probability expression for $P_{e\mu}$ in constant matter density becomes,

$$P_{e\mu} = \sin^2 2\theta_M \sin^2 \left(\frac{1.27(\Delta m^2)_M L}{E} \right). \quad (3.4.24)$$

Another interesting phenomenon in this case is the Mikheyev-Smirnov-Wolfenstein or MSW resonance [145, 146]. This happens when

$$\Delta m^2 \cos 2\theta = A \quad (3.4.25)$$

$$= 0.000076 \rho(g/cc) E(GeV) eV^2. \quad (3.4.26)$$

where ρ is the matter density.

If this condition is satisfied then we see from equation (3.4.23) that the mixing angle becomes maximal i.e. 45° . This leads to the possibility of total flavor transition between the two generation of neutrinos. Since A is positive for neutrinos, resonance can only occur for $\Delta m^2 > 0$ and $\theta < 45^\circ$ or $\Delta m^2 < 0$ and $\theta > 45^\circ$. Similarly, for the antineutrinos where A is negative, the resonance condition is given by $\Delta m^2 > 0$ and $\theta > 45^\circ$ or $\Delta m^2 < 0$ and $\theta < 45^\circ$. This shows that the fact that the neutrino and antineutrino probabilities depend on the sign of Δm^2 and octant of θ in matter. Thus the experiments which can observe this resonance effect can lead to the determination of the same.

3.4.3 Three flavor formalism

The time evolution of the Schrödinger equation, in presence of matter, can be written in the flavor basis as

$$i \frac{d}{dt} |\nu_\alpha(t)\rangle = \mathcal{H} |\nu_\alpha(t)\rangle, \quad \text{with } |\nu_\alpha(t=0)\rangle = |\nu_\alpha\rangle, \quad (3.4.27)$$

where,

$$\mathcal{H} = U^T \mathcal{H}_0 U^* + \mathcal{H}_I. \quad (3.4.28)$$

Here, U is the PMNS mixing matrix as defined by equation (3.3.2), \mathcal{H}_0 is the vacuum Hamiltonian and \mathcal{H}_I is the interaction Hamiltonian in presence of matter with,

$$\mathcal{H}_0 |\nu_k\rangle = E_k |\nu_k\rangle, \quad (3.4.29)$$

$$\mathcal{H}_I |\nu_\alpha\rangle = V_\alpha |\nu_\alpha\rangle, \quad (3.4.30)$$

where, $V_\alpha = V_{CC}$ is the matter potential and

$$\begin{aligned} E_k &= \sqrt{p^2 + m_k^2}, \\ &= E + \frac{m_k^2}{2E}, \end{aligned} \quad (3.4.31)$$

using the fact that for ultra-relativistic neutrinos $p \simeq E$. After solving the time evolution equation as given by equation (3.4.27) in the flavor basis, the probability that a neutrino created at time, $t = 0$ with flavor α and detected at later time, $t = t$ can be calculated as

$$P_{\nu_\alpha \rightarrow \nu_\beta} = |\langle \nu_\beta | \nu_\alpha(t) \rangle|^2 = |\Psi_{\alpha\beta}(t)|^2, \quad (3.4.32)$$

where, $\Psi_{\alpha\beta}(t) = \langle \nu_\beta | \nu_\alpha(t) \rangle$ is the transition amplitude from $\nu_\alpha \rightarrow \nu_\beta$.

Now, the time evolution of the Schrödinger equation using the total Hamiltonian as given by equation (3.4.28) can be expressed in terms of the transition amplitudes in the flavor basis as

$$\begin{aligned} i \frac{d}{dt} \Psi_{\alpha\beta}(t) &= \sum_\gamma \left[\sum_k U_{\beta k} E_k U_{\gamma k}^* + \delta_{\beta\gamma} V_{CC} \right] \Psi_{\alpha\gamma}(t), \\ &= \sum_\gamma \left[\sum_k U_{\beta k} \frac{\Delta_{k1}^2}{2E} U_{\gamma k}^* + \delta_{\beta\gamma} \delta_{\gamma e} V_{CC} \right] \Psi_{\alpha\gamma}(t). \end{aligned} \quad (3.4.33)$$

To get the final form of equation (3.4.33), we have subtracted $m_1^2 \mathbb{I}/2E$ from the Hamiltonian using the fact that the subtraction of a constant times identity matrix does not affect the probability calculation. Note that we have also used equation (3.4.31) to get the final form. We notice that the first term of the r.h.s correspond to vacuum oscillation and second term is an additional term due to matter interactions. The above equation can be expressed as

$$i \frac{d}{dx} \psi_\alpha = \mathcal{H}_{\mathcal{F}} \psi_\alpha \quad (3.4.34)$$

where for ultra-relativistic neutrinos, one can assume $t \simeq x$.

Here, $\psi_\alpha = (\psi_{\alpha e}, \psi_{\alpha\mu}, \psi_{\alpha\tau})^T$ and $\mathcal{H}_{\mathcal{F}}$ is the Hamiltonian in the flavor basis which can be defined as

$$\mathcal{H}_{\mathcal{F}} = \frac{1}{2E} (U \mathbb{M}^2 U^\dagger + \mathbb{A}), \quad (3.4.35)$$

with

$$\mathbb{M}^2 = \text{diag}(0, \Delta_{21}, \Delta_{31}), \quad \mathbb{A} = \text{diag}(A, 0, 0). \quad (3.4.36)$$

where A is defined in equation (3.4.25). Now, we use equation (3.4.36) and \mathbb{A} in equation (3.4.35) and introduce one more parameters, $\alpha = \Delta_{21}/\Delta_{31}$ with this, equation (3.4.35) can be written as

$$\mathcal{H}_{\mathcal{F}} = \frac{\Delta_{31}}{2E} U \text{diag}(0, \alpha, 1) U^\dagger + \frac{1}{2E} \text{diag}(A, 0, 0). \quad (3.4.37)$$

The unitary matrix which will diagonalize this Hamiltonian ($\mathcal{H}_{\mathcal{F}}$), given by equation (3.4.37), will give the mixing angles in presence of matter and the eigenvalues will give the mass squared differences. However, it is difficult to solve equation (3.4.37) to find the exact eigenvalues and the eigen functions and hence calculate the oscillation probability. But, it is possible to use various approximations to solve this equation analytically as discussed in [150–152] namely, (i) one mass scale dominance (OMSD), (ii) double expansion upto second order in $(\alpha - s_{13})$, (iii) first order in α and exact dependence on s_{13} . Below we present a brief overview of these approximations.

(i) **One Mass Scale Dominance (OMSD)** : In this approximation, the measured small mass squared difference Δ_{21} can be neglected as compared to Δ_{31} (see table 3.2 for the values). Under this approximation, the oscillation probabilities do not depend on the solar parameters θ_{12} , Δ_{21} and the CP violating phase δ . The probability expressions $P_{\mu\mu}$ and $P_{e\mu}$ derived under this approximation are given by [¶],

$$\begin{aligned} P_{\mu\mu} &= 1 - \cos^2 \theta_{13}^M \sin^2 2\theta_{23} \sin^2 \left(\frac{\Delta_{31} + A + \Delta_{31}^M}{4E} \right) L \\ &\quad - \sin^2 \theta_{13}^M \sin^2 \theta_{23} \sin^2 \left(\frac{\Delta_{31} + A - \Delta_{31}^M}{4E} \right) L \\ &\quad - \sin^4 \theta_{23} \sin^2 2\theta_{13}^M \sin^2 \left(\frac{\Delta_{31}^M L}{4E} \right), \\ P_{e\mu} &= \sin^2 \theta_{23} \sin^2 2\theta_{13}^M \sin^2 (\Delta_{31}^M L / 4E) \end{aligned} \quad (3.4.38)$$

with

$$\Delta_{31}^M = \sqrt{(\Delta_{31} \cos 2\theta_{13} - A)^2 + (\Delta_{31} \sin 2\theta_{13})^2}. \quad (3.4.40)$$

and,

$$\tan 2\theta_{13}^M = \frac{\Delta_{31} \sin 2\theta_{13}}{\Delta_{31} \cos 2\theta_{13} - A}. \quad (3.4.41)$$

[¶]Note that, Δ_{31}^M and θ_{13}^M are the matter modified mass squared difference and mixing angle respectively.

Note that, above equation (3.4.41) gives resonance in the 1-3 sector. Further, in this approximation reactor mixing angle (θ_{13}) is exact. Hence, the physics near the resonance region can be explained better using this approximation. For this reason one can use the OMSD approximation to understand the oscillation results of the atmospheric neutrino experiments [153] and to study MSW resonance effect [145, 146]. The validity of OMSD approximation implies, $\Delta_{21}L/E \ll 1$ this leads to $L/E \ll 10^4(km/GeV)$. For instance the OMSD condition can be violated by considering neutrinos having energy, $E \simeq 1$ GeV and baseline, $L \geq 10^4$ km.

(ii) **Double expansion upto second Order in $(\alpha - s_{13})$:** After inspecting the current best fit value and 3σ ranges of six oscillation parameters as given in table (3.2), one can consider two small fundamental expansion parameters to find oscillation probabilities [152]. These are $\alpha = \Delta_{21}/\Delta_{31} \simeq 0.0299$, $\sin \theta_{13} = 0.15$. Numerical values are obtained by using the best fit values of the parameters as in table (3.2). Considering these two small parameters in the perturbative expansions, the oscillation probability that are relevant in our study are given by,

$$\begin{aligned}
P_{\mu\mu} = & 1 - \sin^2 2\theta_{23} \sin^2 \Delta + \alpha^2 c_{12}^2 \sin^2 2\theta_{23} \Delta \sin 2\Delta \\
& - \alpha^2 \sin^2 2\theta_{12} c_{23}^2 \frac{\sin^2 \hat{A}\Delta}{\hat{A}^2} - \alpha^2 c_{12}^4 \sin^2 2\theta_{23} \Delta^2 \cos 2\Delta \\
& + \frac{1}{2\hat{A}} \alpha^2 \sin^2 2\theta_{12} \sin^2 2\theta_{23} \left[\sin \Delta \frac{\sin \hat{A}\Delta}{\hat{A}} \cos(\hat{A} - 1)\Delta - \frac{\Delta}{2} \sin 2\Delta \right] \\
& - 4 s_{13}^2 s_{23}^2 \frac{\sin^2(\hat{A} - 1)\Delta}{(\hat{A} - 1)^2} - \frac{2}{\hat{A} - 1} s_{13}^2 \sin^2 2\theta_{23} \left[\sin \Delta \cos \hat{A}\Delta \frac{\sin(\hat{A} - 1)\Delta}{\hat{A} - 1} - \frac{\hat{A}}{2} \Delta \sin 2\Delta \right] \\
& - 2 \alpha s_{13} \sin 2\theta_{12} \sin 2\theta_{23} \cos \delta_{CP} \cos \Delta \frac{\sin \hat{A}\Delta}{\hat{A}} \frac{\sin(\hat{A} - 1)\Delta}{\hat{A} - 1} \\
& + \frac{2}{\hat{A} - 1} \alpha s_{13} \sin 2\theta_{12} \sin 2\theta_{23} \cos 2\theta_{23} \cos \delta_{CP} \sin \Delta \\
& \times \left[\hat{A} \sin \Delta - \frac{\sin \hat{A}\Delta}{\hat{A}} \cos(\hat{A} - 1)\Delta \right] \tag{3.4.42}
\end{aligned}$$

$$\begin{aligned}
P_{\mu e} = & \alpha^2 \sin^2 2\theta_{12} c_{23}^2 \frac{\sin^2 \hat{A}\Delta}{\hat{A}^2} + 4 s_{13}^2 s_{23}^2 \frac{\sin^2(\hat{A} - 1)\Delta}{(\hat{A} - 1)^2} \tag{3.4.43} \\
& + 2\alpha s_{13} \sin 2\theta_{12} \sin 2\theta_{23} \cos(\Delta + \delta_{CP}) \frac{\sin \hat{A}\Delta}{\hat{A}} \frac{\sin(\hat{A} - 1)\Delta}{\hat{A} - 1}
\end{aligned}$$

where, $\hat{A} = A/\Delta_{31}$, $s_{ij} = \sin \theta_{ij}$, $c_{ij} = \cos \theta_{ij}$, $\Delta = \Delta_{31}L/4E$. To derive these expressions it is considered that $\alpha, s_{13} \ll 1$. Validity of the above expressions implies $\alpha\Delta = \Delta_{21}L/4E \ll 1$ (or $L/E \ll 10^4$ km) i.e. when solar mass squared difference has no significant impact on the oscillations. One also notices from these expressions that in absence of matter i.e. when $A = 0$ and when $A = 1$, the probability expressions diverge and one would expect that the approximations are no longer valid. However, it turns out that the oscillation probability remains finite once the limiting cases $A \rightarrow 0$ and $A \rightarrow 1$ are taken in consideration.

(iii) **First Order in α and Exact Dependence on s_{13}** : In this approximation, we calculate the oscillation probabilities considering upto first order in α whereas we have used exact dependency of the mixing angle θ_{13} in terms of s_{13} . The muon-neutrino to electron-neutrino conversion probability can be written as [152],

$$\begin{aligned}
P_{\mu e} = & s_{23}^2 \sin^2 2\theta_{13} \frac{\sin^2 C_{13}}{C_{13}^2} \Delta - 2s_{12}^2 s_{23}^2 \sin^2 2\theta_{13} \frac{\sin C_{13}}{C_{13}^2} \Delta \\
& \times \left(\Delta \frac{\cos C_{13} \Delta}{C_{13}} (1 - A \cos 2\theta_{13}) - A \frac{\sin C_{13} \Delta}{C_{13}} \frac{\cos 2\theta_{13} - A}{C_{13}} \right) \\
& + s_{13} \sin 2\theta_{12} \sin 2\theta_{23} \frac{\sin C_{13} \Delta}{AC_{13}^2} \left\{ \sin \delta_{CP} [\cos(1+A)\Delta - \cos C_{13}\Delta] C_{13} \right. \\
& \left. + \cos \delta_{CP} [C_{13} \sin(1+A)\Delta - (1 - A \cos 2\theta_{13}) \sin C_{13}\Delta] \right\} + \mathcal{O}(\alpha^2) \quad (3.4.44)
\end{aligned}$$

where, $\Delta = \Delta_{31}L/4E$ and

$$C_{13} \equiv \sqrt{\sin^2 2\theta_{13} + (A - \cos 2\theta_{13})^2} \quad (3.4.45)$$

Like the previous case, this approximation is also valid in the limit $\alpha\Delta = \Delta_{21}L/4E \ll 1$ or in the region where solar mass squared difference is not important. This is an improvement over OMSD.

Probability expressions derived above using various approximations are calculated assuming constant matter density approximation. Similar approximate expressions for antineutrinos can be obtained by replacing $A \rightarrow -A$ and $\delta_{CP} \rightarrow -\delta_{CP}$. In our study, we consider the ‘‘double expansion upto second order in $(\alpha - s_{13})$ ’’ approximation for analytic explanations. However in numerical calculations, we consider the full three flavor neutrino propagation equation [154] assuming the Preliminary Reference Earth Model (PREM) density profile [155].

In general, we can see that the three flavor neutrino oscillation probability depends on total eight parameters and the matter potential,

$$P_{\alpha\beta} = P_{\alpha\beta}(\Delta m_{21}^2, \Delta m_{31}^2, \theta_{12}, \theta_{13}, \theta_{23}, \delta_{CP}, E, L, V(x)) \quad (3.4.46)$$

First six-parameters are the fundamental oscillation parameters whereas E and L depend on the experimental configuration and $V(x)$ ($x \in (0, L)$) depends on the path travelled by the neutrino.

3.5 Evidences for Neutrino Oscillations

In this section we discuss the various evidences of neutrino oscillations.

Solar neutrino problem : In 1968, R. Davis first detected the solar neutrinos at the Homestake gold mine experiment in South Dakota [5] using the following reaction,



The experimentally measured flux by the Homestake experiment was reported to be one-third of the theoretically predicted flux of SSM developed by J. Bahcall [6]. This was known as the *Solar neutrino problem*. Neutrino oscillation or flavor conversion phenomenon developed by B. Pontecorvo in 1957 [7, 8] was considered as one of the possible solutions to this problem. In 1991, Kamiokande experiment [156] in Japan first time cross checked the shortfall observed in the Homestake experiment. Kamiokande, being a real time experiment, using the neutrino-electron scattering, also verified for the first time that the neutrinos are indeed coming from the sun. Later, other solar neutrino experiments like GALLEX [70], SAGE [71] and GNO [72] also confirmed this deficit. These experiments used Gallium (Ga) instead of Chlorine (Cl) because Ga is sensitive to the low energy pp neutrinos coming from the Sun. These are the neutrinos which are mainly responsible for solar luminosity. In 1998, high statistics SuperKamiokande (SK) experiment [69] also endorsed the shortfall of the solar neutrinos. Combining SK with Chlorine and Gallium data, a solution in terms of modification of SSM became highly unlikely and flavor oscillation became a front runner in explaining the deficit. Finally, the Sudbury Neutrino Observatory (SNO) experiment in Canada experimentally verified the neutrino flavor conversion by measuring

the ratio between CC to NC events [9, 10]. This also confirmed the presence of muon and tau neutrino flavor in the solar electron neutrino flux. Total measured 8B flux by this experiment via NC reaction was also in good agreement with the predictions of the SSM. Thus the neutrino oscillation observed by SNO resolved the solar neutrino problem. The data from solar neutrino experiments imply $\Delta m_{21}^2 \sim 8.0 \times 10^{-5} \text{eV}^2$ and $\theta \sim 33.9^\circ$ and confirm the MSW effect [157].

The reactor experiment KamLAND (Kamioka Liquid scintillator AntiNeutrino Detector) (L = 180 km) [12] in Japan was designed to observe the oscillation of the electron antineutrinos coming from nuclear reactors. The L/E of KamLAND is 180 km/1 MeV corresponding to a sensitivity of $\sim 10^{-4} \text{eV}^2$ for the mass squared difference. This is the region of sensitivity of the solar neutrinos as well. Thus KamLAND verified the solar neutrino oscillation using reactor neutrinos. Addition of KamLAND data improved the global fit of solar neutrino data and significantly restricted the allowed range of solar mass squared difference [158].

Atmospheric neutrino problem : Atmospheric neutrino experiments have also observed the flavor conversion of neutrinos. When cosmic rays collide with the nuclei in the Earth's atmosphere, they produce charged particles like pions and kaons. These later decay to muons and muon neutrinos and the muons further decay giving neutrinos as follows,

$$\begin{aligned}\pi^\pm(K^\pm) &\rightarrow \mu^\pm + \nu_\mu(\bar{\nu}_\mu) \\ \mu^\pm &\rightarrow e^\pm + \nu_e(\bar{\nu}_e) + \bar{\nu}_\mu(\nu_\mu)\end{aligned}\tag{3.5.2}$$

By inspecting the above decay chain, one expects that the ratio between the muon and the electron neutrinos to be 2 : 1. However, various atmospheric neutrino experiments, like Kamiokande [99], IMB [100], Soudan 2 [101] reported that the observed fluxes have mismatch with the expected fluxes. This was known as the *Atmospheric Neutrino Anomaly*. Later, high statistics SK experiment has also confirmed this anomaly. This experiment had enough statistics to study the zenith angle dependence of the up-going and down-going neutrinos. The down-going neutrinos travel a distance ~ 10 km before they reach the detector, whereas up-going neutrinos coming from the other side of the Earth cover larger baselines upto $\simeq 10000$ km and can oscillate to other flavors. This can lead to an up-down asymmetry in the neutrino data and SK observed this

asymmetry in the zenith angle distribution of their data [11]. This can be explained by two flavor $\nu_\mu - \nu_\tau$ oscillation [159, 160]. The three flavor fit of SK data has also been performed [161].

The LBL experiment KEK to Kamioka or K2K ($L = 250$ km) [13, 14] at Japan was built to confirm the oscillation of atmospheric neutrinos using man-made sources. Its reported results were in good agreement with that of SK atmospheric neutrino experiment. Later, the Main Injector Neutrino Oscillation Search or MINOS ($L = 735$ km) experiment [15] at Fermilab also reported neutrino oscillations with Δm^2 in the same ballpark as required to explain the atmospheric neutrino oscillations. Ongoing experiments T2K [16], NO ν A [17, 18] which are also sensitive to atmospheric oscillation parameters have confirmed the neutrino oscillation phenomenon and their measured mass squared differences also fall in the region expected to describe atmospheric neutrino oscillations.

3.6 Present Status of Neutrino Oscillation Parameters

As discussed above, the three-flavor neutrino oscillation probability is sensitive to six fundamental oscillation parameters, these are the three mixing angles ($\theta_{12}, \theta_{13}, \theta_{23}$), two mass squared differences ($\Delta m_{21}^2, \Delta m_{31}^2$) and a CP phase δ_{CP} . The last mixing angle that was measured is θ_{13} . This parameter is also named as the reactor mixing angle as it has been measured by the reactor experiments, like Double CHOOZ [83], Daya Bay [81], RENO [82]. These experiments have determined θ_{13} to be non-zero upto 5σ C.L. In the approximation, where θ_{13} is small, the sub-leading effects of the probability expressions can be neglected. In that scenario, the solar neutrino oscillations are governed by solar parameters ($\theta_{12}, \Delta m_{21}^2$) which have been measured by solar neutrino experiments, Homestake, GALLEX, SAGE, GNO, SNO [9] and KamLAND [12] while the atmospheric neutrino experiments are governed by atmospheric parameters ($\sin^2 2\theta_{23}, |\Delta m_{31}^2|$) which have been determined by atmospheric neutrino experiment SK and long baseline neutrino experiments like (MINOS [15], T2K [16] and NO ν A [17, 18]). Accelerator experiments MINOS [162] and T2K [16] have also measured θ_{13} to be non-zero. In a full three generation framework, this mixing angle affects both solar and atmospheric oscillation analysis and hence it plays a crucial role

in the global analysis of neutrino oscillation data. In table (3.2), we present the current best fit values and 3σ ranges of neutrino oscillation parameters from the global analysis data from all the neutrino oscillation experiments [163].

Parameter	Best Fit $\pm 1\sigma$	3σ range
$\Delta_{21}[10^{-5} \text{ eV}^2]$	$7.50^{+0.19}_{-0.17}$	7.03 – 8.09
$ \Delta_{31}[10^{-3} \text{ eV}^2] $ (NH)	$2.524^{+0.039}_{-0.040}$	2.407 – 2.643
$ \Delta_{31}[10^{-3} \text{ eV}^2] $ (IH)	$2.514^{+0.038}_{-0.041}$	2.399 – 2.635
$\sin^2 \theta_{12}$	0.306 ± 0.012	0.271 – 0.345
$\sin^2 \theta_{13}$ (NH)	0.02166 ± 0.00075	0.01934 – 0.02392
$\sin^2 \theta_{13}$ (IH)	0.02179 ± 0.00075	0.01953 – 0.02408
$\sin^2 \theta_{23}$ (NH)	$0.441^{+0.027}_{-0.021}$	0.385 – 0.635
$\sin^2 \theta_{23}$ (IH)	$0.587^{+0.020}_{-0.024}$	0.393 – 0.640

Table 3.2: Current best fit and 3σ ranges of neutrino oscillation parameters [163].

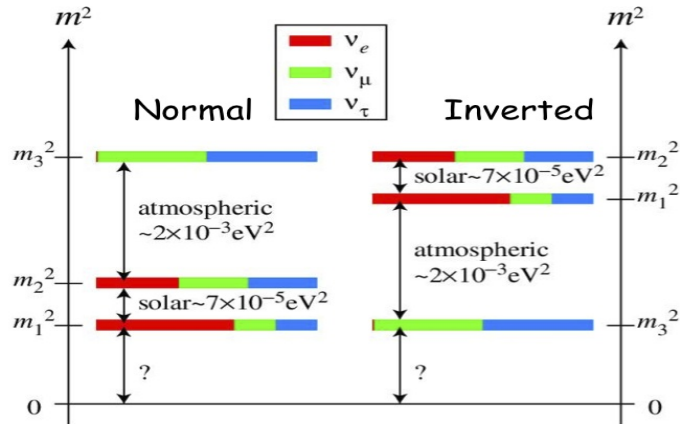


Figure 3.3: Possible mass patterns of neutrinos. Here, left (right) panel is for NH (IH). Color compositions of the various bands represent the proportion of flavor eigenstates of neutrinos in the mass eigenstates.

In table (3.2), δ_{CP} has not been included, as it's value is still unknown. However, recently the on going accelerator experiment, T2K has hinted that the Dirac CP phase is close to its maximal value (i.e. $\delta_{CP} \sim 257^\circ$) for normal hierarchy using both neutrino and antineutrino runs and including appearance and disappearance channel data [124]. Any value of this parameter other than 0° and $\pm 180^\circ$ would signal

CP violation in the leptonic sector. In this case it is often useful to talk in terms of lower half-plane (LHP) with $-180^\circ < \delta_{CP} < 0^\circ$ and upper half-plane (UHP) with $0^\circ < \delta_{CP} < 180^\circ$. Other major unknowns to be determined by the future neutrino oscillation experiments are: (i) the neutrino mass hierarchy i.e. whether $m_3 > m_2 > m_1$ (normal hierarchy (NH)) or $m_3 < m_1 \approx m_2$ (inverted hierarchy (IH)). In figure (3.3), we show the schematic diagram of neutrino mass hierarchy considering both NH and IH. (ii) the octant of θ_{23} ($\theta_{23} > 45^\circ$ is known as Higher Octant (HO) and $\theta_{23} < 45^\circ$ is known as Lower Octant (LO)). The latest NO ν A analysis considering both appearance and disappearance channel data in neutrino mode, shows that there are two best fit points occurring for normal mass ordering, namely, $\sin^2 \theta_{23} = 0.404$, $\delta_{CP} = 1.48\pi$ and $\sin^2 \theta_{23} = 0.623$, $\delta_{CP} = 0.74\pi$ [164]. This result is in tension with the measurements of T2K which gives best fit ~ 0.53 for $\sin^2 \theta_{23}$ [124].

3.7 Summary

In this chapter, we start the discussion with the phenomenon of neutrino oscillation in vacuum considering simple two-flavor formalism. Later, we extend our discussion to the full three-flavor formalism and derive the probability expressions in vacuum. However, propagation of neutrinos can be significantly affected in presence of matter which can modify the neutrino oscillation probabilities. Hence, we calculate the effective interaction potential in presence of matter and present the expressions of the neutrino oscillation probabilities in matter considering a simple two flavor framework. In the three flavor formalism in presence of matter, exact analytical calculation of neutrino oscillation probability is difficult. Therefore, we present various approximate methods to calculate neutrino flavor transitions in the three flavor formalism. In section (3.5), we give a brief illustration of the various evidences of neutrino oscillation. At the end of this chapter, we discuss the current status of all the neutrino oscillation parameters and tabulate their allowed 3σ ranges with the best fit values from the global analysis of data from neutrino oscillation experiments. We also mention yet undetermined parameters in the neutrino oscillation physics. Determination of these unknowns in future neutrino oscillation experiments is the main theme of the next two chapters.

Chapter 4

Parameter Degeneracies and Their Resolution

*“Success can only come to you by courageous
Devotion to the task lying in front of you.”*

– C. V. Raman

4.1 Introduction

At the present juncture, the three major unknown neutrino oscillation parameters are the mass hierarchy, the octant of the mixing angle θ_{23} and the CP phase δ_{CP} . The appearance channel ($P_{\mu e}$), often known as the “golden channel”, can measure all the three unknown parameters described above*. However, the measurement is complicated by the fact that different sets of values of parameters can give the same oscillation probability. This gives rise to degeneracies that render an unambiguous determination of the true parameters difficult. It was discussed in Ref. [165] that there can be eight-fold degeneracies in neutrino oscillation probabilities which are (a) the intrinsic or $\theta_{13} - \delta_{CP}$ degeneracy [166], (b) the hierarchy- δ_{CP} degeneracy [167] and (c) the intrinsic octant degeneracy [168]. The intrinsic degeneracy refers to clone solutions occurring due to a different θ_{13} and δ_{CP} value. This degeneracy can be removed to a large extent by using spectral information [169]. Moreover, the current precision determination of θ_{13}

*Originally, $P_{\mu e}$ was termed as the golden channel because of its sensitivity to θ_{13} , hierarchy and δ_{CP} .

[170–173] has removed this degeneracy to a great extent. The hierarchy- δ_{CP} degeneracy leads to wrong-hierarchy solutions occurring for a different value of δ_{CP} other than the true value. The intrinsic octant degeneracy refers to duplicate solutions occurring for θ_{23} and $\pi/2 - \theta_{23}$.

Many papers have discussed the possibilities of the resolution of these degeneracies by using different detectors in the same experiment [174–176]. The synergistic combination of data from different experiments was also discussed as an effective means of removing such degeneracies by virtue of the fact that the oscillation probabilities offer different combinations of parameters at varying baselines and energies [169, 177–184]. In particular, the synergy between long-baseline (LBL) experiments $\text{NO}\nu\text{A}$ and T2K in resolving the hierarchy- δ_{CP} degeneracy has been discussed recently in Refs. [185–188].

It has been shown in Refs. [182, 189, 190] that a precise measurement of the mixing angle θ_{13} is helpful for the removal of octant degeneracy. Octant sensitivity in the T2K and $\text{NO}\nu\text{A}$ experiments has been studied recently in Refs. [191, 192] in view of the measurement of a non zero θ_{13} . The octant degeneracy is different for neutrinos and antineutrinos and hence a combination of these two data sets can be conducive for the removal of this degeneracy for most values of δ_{CP} [193–195].

Since atmospheric neutrino baselines experience strong Earth matter effects, these effectively remove the overlap between the right and wrong-hierarchy solutions [196–199]. In particular, atmospheric neutrino experiments, capable of distinguishing neutrinos and antineutrinos, can be very useful in resolving degeneracies related to the mass hierarchy [199–209]. The octant sensitivity of the atmospheric neutrinos comes from both the appearance [210] and disappearance channels [211], and also benefits from significant matter effects, especially facilitated by the large value of θ_{13} measured by the reactor experiments. Atmospheric neutrinos also provide a synergy with LBL experiments in terms of probability behavior with respect to the parameters, so that the combination of atmospheric neutrino data with LBL data exhibits reduced effect of the hierarchy and octant degeneracies [192, 206, 212–214].

In this chapter, we show that with the high precision measurement of θ_{13} by reactor experiments, the degeneracies can be discussed in an integrated manner in terms of a

generalized “hierarchy- θ_{23} - δ_{CP} ” degeneracy. A good way to visualize the different degenerate solutions is in terms of contours in the test ($\theta_{23} - \delta_{CP}$) plane for different choices of true values of parameters[†]. These plots also give an indication regarding the precision of the parameters δ_{CP} and θ_{23} . Although hierarchy degeneracy is discrete, the $\theta_{23} - \delta_{CP}$ degeneracy is continuous for the appearance channel probability $P_{\mu e}$. Inclusion of the information from the disappearance channel $P_{\mu\mu}$ restricts θ_{23} and discrete degenerate solutions are generated. We classify, for the first time the wrong-hierarchy and wrong-octant solutions with respect to right or wrong δ_{CP} values. This also allows us to understand how the hierarchy and octant degeneracies can affect the precision in δ_{CP} . We observe that since the wrong-hierarchy and wrong-octant solutions can occur for wrong values of δ_{CP} as well, there can exist, in principle, a total of eight degenerate solutions corresponding to different combinations of hierarchy, octant and δ_{CP} . This is summarized in table 4.1[‡]. Note that these solutions are different from the eight-fold degenerate solutions that have been discussed in the literature.

Solutions with right δ_{CP}	Solutions with wrong δ_{CP}
I. RH-RO-R δ_{CP}	V. WH-WO-W δ_{CP}
II. RH-WO-R δ_{CP}	VI. RH-RO-W δ_{CP}
III. WH-RO-R δ_{CP}	VII. RH-WO-W δ_{CP}
IV. WH-WO-R δ_{CP}	VIII. WH-RO-W δ_{CP}

Table 4.1: Various possibilities of degeneracy in the probability $P_{\mu e}$. Here, R=right, W=wrong, H=hierarchy and O=octant.

The plan of this chapter is as follows : in section (4.2), we provide the details of the various experiments that we have considered to study parameter degeneracies and their resolution in neutrino oscillation physics. In section (4.3), we give the details of the statistical analysis performed to study the phenomenology of the various experiments. We then show the presence of degeneracies in the neutrino oscillation parameters and

[†]Note that prior to the discovery of a nonzero value of θ_{13} , the degeneracies were studied mainly in $\theta_{13} - \delta_{CP}$ plane.

[‡] It is to be noted in this connection that if the δ_{CP} precision is not good then there can be continuous regions connecting right and wrong δ_{CP} solutions and hence it may not always be possible to identify discrete wrong δ_{CP} solutions.

discuss the degeneracies in $\text{NO}\nu\text{A}$, T2K and INO at the probability level in section (4.4). Next, we explore the degeneracies at the χ^2 -level considering 6 years of neutrino run of $\text{NO}\nu\text{A}$ in subsection (4.4.3). In section (4.5), we illustrate the resolution of the degeneracies. We first discuss the role of antineutrinos considering $\text{NO}\nu\text{A}[3+3]$ years of $(\nu + \bar{\nu})$ run. Next, we discuss the combined effect of $\text{NO}\nu\text{A}$ and T2K. Subsequently, we also describe the role of INO in conjunction with $\text{NO}\nu\text{A}$ and T2K to resolve the various degenerate regions. We also discuss the capability to distinguish $\delta_{CP} = 0^\circ$ from 180° in section (4.6). We summarize our findings in section (4.7).

4.2 Details of Experimental Configuration

For the numerical studies, we use the GLOBES package [215, 216] (along with the required auxiliary files [217, 218]) for the LBL experiments. For the simulation of T2K data, we consider 22.5 kton Super-Kamiokande Water Čerenkov detector and 0.75 MW neutrino beam power with 30 GeV proton beam energy. This beam power corresponds to the exposure of 1.0×10^{21} POT/year. T2K has been proposed to run for a total luminosity of 7.8×10^{21} protons on target (POT). In case of $\text{NO}\nu\text{A}$, we consider a 14 kton totally active scintillator detector (TASD) as the far detector with a beam power of 700 kW with 120 GeV proton energy which correspond to an exposure of 6.0×10^{20} POT/year. For the simulation of $\text{NO}\nu\text{A}$ data, we consider the re-optimized $\text{NO}\nu\text{A}$ set up from Refs. [187, 219].

The atmospheric neutrino detector considered by us is the magnetized iron calorimeter detector (ICAL) planned by the INO collaboration. In our analysis, we take a 50 kton detector for ICAL@INO with a runtime of 10 years. We also use constant angular and energy resolutions of 10° and 10% respectively and 85% overall efficiency. ICAL has an advantage over other detectors because it can be magnetized which allows charge identification, thus providing the facility to distinguish between μ^+ and μ^- . The muon resolutions from INO simulation codes can be found in Ref. [220]. We have verified that the constant resolutions used in our works give similar results to those obtained using resolutions from INO simulation [205, 206].

4.3 Details of Statistical Analysis

In this section, we give a brief overview of the statistical analysis that we have done in our study [§]. In our numerical analysis, we do the χ^2 test to find the sensitivity and precision of the various oscillation parameters. We define the total χ^2 as

$$\chi^2 = \chi_{\text{stat}}^2 + \chi_{\text{pull}}^2 + \chi_{\text{prior}}^2. \quad (4.3.1)$$

We discuss the details about χ_{pull}^2 and χ_{prior}^2 analysis in the appendix A.

Depending on the number of events in each bin one can consider the Poissonian or Gaussian distribution of the statistical χ_{stat}^2 . In principle, if the number of events in each bin are more than five then one can consider the Gaussian distribution. In the Gaussian formalism the χ_{stat}^2 is given by,

$$\chi_{\text{stat}}^2 = \text{Min} \frac{(N_{\text{ex}}^{\text{true}} - N_{\text{th}}^{\text{test}})^2}{\sigma(N_{\text{ex}}^{\text{true}})^2}, \quad (4.3.2)$$

where,

$N_{\text{ex}}^{\text{true}}$ is the total number of simulated experimental or true events,

$N_{\text{th}}^{\text{test}}$ is the total number of simulated theoretical or test events events,

and σ is the error in measuring the experimental or true events.

However, if the number of events in each bin are less than five then one uses Poissonian distribution. In this formalism the χ_{stat}^2 is given by,

$$\chi_{\text{stat}}^2 = \text{Min} \left[2 \left\{ N_{\text{th}}^{\text{test}} - N_{\text{ex}}^{\text{true}} - N_{\text{ex}}^{\text{true}} \log \left(\frac{N_{\text{th}}^{\text{test}}}{N_{\text{ex}}^{\text{true}}} \right) \right\} \right], \quad (4.3.3)$$

In our analysis, we incorporate marginalisation over the systematic errors by the method of pulls [221, 222]. We also include 5% prior of the oscillation parameter θ_{13} to take into account the constraints on this parameter from the reactor experiments [¶]. We add the resultant χ^2 of the various experiments and finally marginalize over the oscillation parameters in their allowed 3σ range.

Following are the χ^2 tests that we do for the various quantities :

[§]The detailed analysis and the steps to calculate the number of events are discussed in the appendix A.

[¶]The method of inclusion of pulls for the systematic errors and the prior in our numerical simulation are discussed in appendix A.

- The mass hierarchy sensitivity,

$$\chi_{\text{stat}}^2 = \text{Min} \frac{[N_{\text{ex}}^{\text{true}}(NH) - N_{\text{th}}^{\text{test}}(IH)]^2}{\sigma(N_{\text{ex}}^{\text{true}}(NH))^2} \quad (4.3.4)$$

Similar tests can also be performed by replacing NH by IH and vice-versa.

- The octant sensitivity,

$$\chi_{\text{stat}}^2 = \text{Min} \frac{[N_{\text{ex}}^{\text{true}}(LO) - N_{\text{th}}^{\text{test}}(HO)]^2}{\sigma(N_{\text{ex}}^{\text{true}}(LO))^2} \quad (4.3.5)$$

Similar tests can also be performed by replacing LO by HO and vice-versa.

- Precision on θ_{23} ,

$$\chi_{\text{stat}}^2 = \text{Min} \frac{[N_{\text{ex}}(\theta_{23}^{\text{true}}) - N_{\text{th}}(\theta_{23}^{\text{test}})]^2}{\sigma(N_{\text{ex}}(\theta_{23}^{\text{true}}))^2} \quad (4.3.6)$$

- The CP violation discovery χ^2 ,

$$\chi_{\text{stat}}^2 = \text{Min} \frac{[N_{\text{ex}}(\delta_{CP}^{\text{true}}) - N_{\text{th}}(\delta_{CP}^{\text{test}} = 0, \pm 180^\circ)]^2}{\sigma(N_{\text{ex}}(\delta_{CP}^{\text{true}}))^2} \quad (4.3.7)$$

In our analysis, the representative neutrino oscillation parameters that we have considered are consistent with the results obtained from global-fit of world neutrino data [163, 223–225].

4.4 Identifying Degeneracies

4.4.1 Degeneracies in Neutrino Oscillation Parameters

To understand the various degeneracies at the probability level, we mention the relevant oscillation probabilities considering the Earth matter density to be constant ^{||}. The probability expressions are as follows [226–228]:

$$P_{\mu e} = \alpha^2 \sin^2 2\theta_{12} c_{23}^2 \frac{\sin^2 \hat{A} \Delta}{\hat{A}^2} + 4s_{13}^2 s_{23}^2 \frac{\sin^2(\hat{A} - 1)\Delta}{(\hat{A} - 1)^2} \quad (4.4.1)$$

$$+ 2\alpha s_{13} \sin 2\theta_{12} \sin 2\theta_{23} \cos(\Delta + \delta_{CP}) \frac{\sin \hat{A} \Delta \sin(\hat{A} - 1)\Delta}{\hat{A} \hat{A} - 1}$$

$$P_{\mu\mu} = 1 - \sin^2 2\theta_{23} \sin^2 \Delta + \mathcal{O}(\alpha, s_{13}) \quad (4.4.2)$$

^{||}We have discussed in detail regarding the derivation of the probability expressions in chapter (3).

where $s_{ij}(c_{ij}) = \sin \theta_{ij}(\cos \theta_{ij})$ for $j > i$ ($i, j = 1, 2, 3$). We use the following notation: $\Delta = \Delta m_{31}^2 L/4E$, $\hat{A} = A/\Delta m_{31}^2$, where $A = 2EV = 0.000076 \times \rho(\frac{g}{cc}) \times E(\text{GeV})$ is the Wolfenstein matter term. The antineutrino oscillation probability can be obtained by replacing $\delta_{CP} \rightarrow -\delta_{CP}$ and $V \rightarrow -V$. As we have discussed earlier, $\Delta m_{31}^2 > 0$ for NH and $\Delta m_{31}^2 < 0$ for IH. The matter term A is positive for neutrinos and negative for antineutrinos. Therefore, in the case of neutrino, $\hat{A} > 0$ for NH and $\hat{A} < 0$ for IH while the opposite is true for the antineutrinos. The presence of the matter term \hat{A} brings the hierarchy sensitivity in the oscillation probability. This implies that greater is the baseline, larger will be the value of \hat{A} and hence hierarchy sensitivity will be more.

We observe the following salient features from the probability expressions:

- The leading order term in $P_{\mu\mu}$ is proportional to $\sin^2 2\theta_{23} \sin^2 \Delta$. This gives rise to the intrinsic hierarchy and octant degeneracies:

$$P_{\mu\mu}(\Delta) = P_{\mu\mu}(-\Delta) \quad (4.4.3)$$

$$P_{\mu\mu}(\theta_{23}) = P_{\mu\mu}(\pi/2 - \theta_{23}). \quad (4.4.4)$$

This leads to a loss of sensitivity to the hierarchy and octant, when the measurement is performed using this channel.

- The appearance channel $P_{\mu e}$ does not have intrinsic degeneracies but suffers from the combined effect of different parameters, which leads to the following sets of degeneracies:

$$P_{\mu e}(\theta_{13}, \delta_{CP}) = P_{\mu e}(\theta'_{13}, \delta'_{CP}) \quad (4.4.5)$$

$$P_{\mu e}(\Delta, \delta_{CP}) = P_{\mu e}(-\Delta, \delta'_{CP}). \quad (4.4.6)$$

Equations (4.4.4, 4.4.5, 4.4.6) constitute the eight-fold degeneracy discussed in Ref. [165].

Recently, it has been discussed that in the context of probabilities which are dependent on $\sin^2 \theta_{23}$, the octant degeneracy can be generalized to include all values of θ_{23} in the second octant [192] and can also be correlated with δ_{CP} [192, 229]. The pattern of parameter degeneracies in the three-dimensional $\theta_{23} - \theta_{13} - \delta_{CP}$ space arising from

the appearance probability $P_{\mu e}$ has been discussed in Ref. [230]. This is a continuous degeneracy and can be expressed as

$$P_{\mu e}(\theta_{23}, \theta_{13}, \delta_{CP}) = P_{\mu e}(\theta'_{23}, \theta'_{13}, \delta'_{CP}) \Rightarrow \text{generalized octant degeneracy.} \quad (4.4.7)$$

However the reactor experiments have measured $\sin^2 \theta_{13}$ with a high degree of accuracy and future measurements are expected to improve it further. This has reduced the impact of θ_{13} uncertainty on octant degeneracy to a large extent [192]. Therefore, we consider another generalized degeneracy which is the hierarchy- θ_{23} - δ_{CP} degeneracy:

$$P_{\mu e}(\theta_{23}, \Delta, \delta_{CP}) = P_{\mu e}(\theta'_{23}, -\Delta', \delta'_{CP}) \Rightarrow \\ \text{generalized hierarchy} - \theta_{23} - \delta_{CP} \text{ degeneracy.} \quad (4.4.8)$$

This degeneracy can be observed best in the test $(\theta_{23} - \delta_{CP})$ plane. Studying it in this fashion allows us to view the degeneracies arising out of the remaining unknown parameters in a comprehensive manner. We note that while the hierarchy degeneracy is always discrete, the $\theta_{23} - \delta_{CP}$ degeneracy arising out of the appearance channel is continuous. On the other hand, the intrinsic octant degeneracy arising from the $P_{\mu\mu}$ channel is independent of δ_{CP} and discrete in θ_{23} except for θ_{23} values close to maximal. Thus combining the survival and conversion probabilities give rise to disconnected degenerate regions in the $\theta_{23} - \delta_{CP}$ plane. We have elaborated this point in the Appendix B. We study the occurrence of the above degeneracies in next subsection in terms of probabilities for $\text{NO}\nu\text{A}$, T2K and INO to identify the different possible degenerate solutions at the probability level.

4.4.2 Identifying degeneracies using oscillation experiments

For the understanding of the presence of degeneracies at the probability level, we consider the baseline 295 km (T2K), 810 km ($\text{NO}\nu\text{A}$) and a baseline 7500 km which is a typical baseline traversed by the upward going atmospheric neutrinos. Figure 4.1 shows the probability $P_{\mu e}$ for neutrinos (left panel) and antineutrinos (right panel) as a function of δ_{CP} for both NH and IH. The plots in the upper panel correspond to $\text{NO}\nu\text{A}$ with energy, $E = 2$ GeV while those in the lower panel are for T2K with energy, $E = 0.6$ GeV. These probabilities are plotted for the energy where the neutrino

flux peaks. The hatched area denotes variation over θ_{23} . For the lower (higher) octant, we vary θ_{23} between $39^\circ - 42^\circ$ ($48^\circ - 51^\circ$). This is a good assumption for θ_{23} not too close to its maximal value, for the purpose of illustrating the physics, since for a given $\theta_{23}(\text{true})$, the disappearance channel anyway excludes values away from $\theta_{23}(\text{true})$ and $\pi/2 - \theta_{23}(\text{true})$. Thus, these plots implicitly assume information from the disappearance channel.

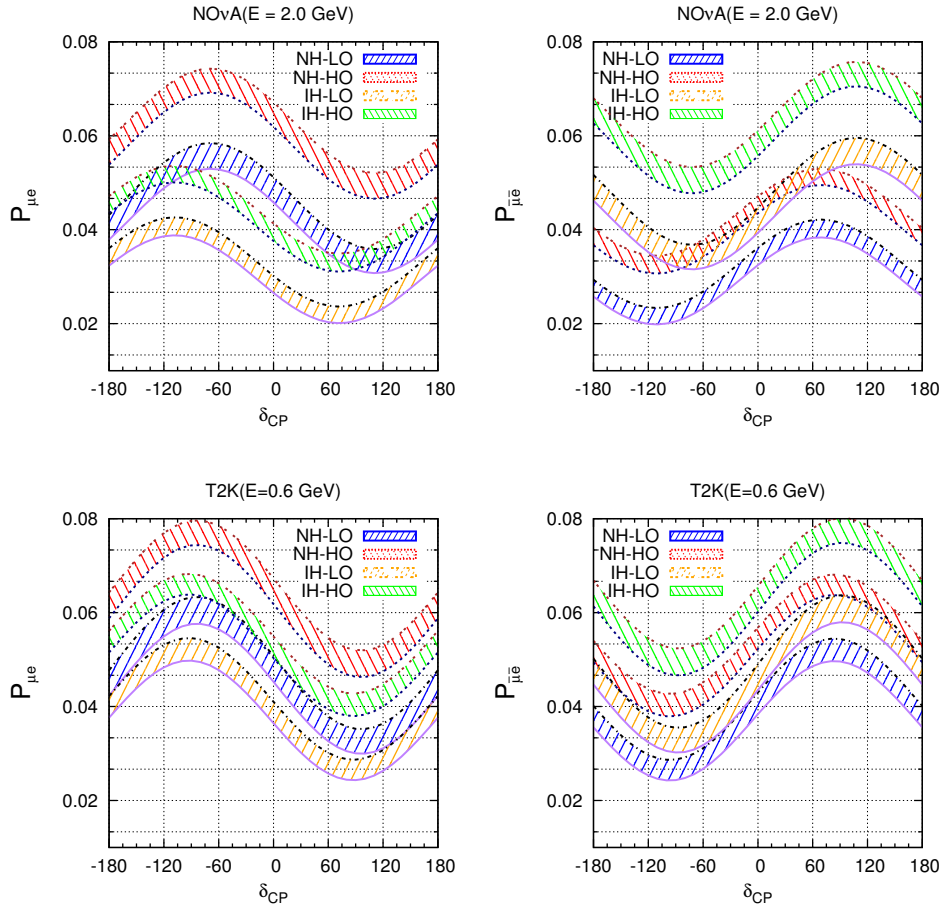


Figure 4.1: The oscillation probability $P_{\mu e}$ as a function of δ_{CP} . Here, upper (lower) row represents oscillation probability for $\text{NO}\nu\text{A}$ (T2K). The left (right) panel is for neutrinos (antineutrinos).

From Fig. 4.1, the following points can be noted.

For neutrinos – :

- The NH probabilities are higher than the IH probabilities. This is because of enhanced matter effect for neutrinos for NH in the Earth's matter.
- For both NH and IH the probabilities are higher in the LHP **.

**Note that $-180^\circ < \delta_{CP} < 0^\circ$ and $0^\circ < \delta_{CP} < 180^\circ$ correspond to LHP and UHP respectively.

- The probabilities for higher octant are higher for both NH and IH.

while, for antineutrinos – :

- The matter term A changes its sign, and IH probabilities become higher than NH.
- The flip in sign of δ_{CP} makes both the NH and IH probabilities higher in the UHP.
- Like neutrinos, the probabilities for a higher octant remains higher for both NH and IH.

For both neutrinos and antineutrinos the lowest line in the LO (HO) band corresponds to 39° (48°), while the highest point corresponds to 42° (51°), due to the $\sin^2 \theta_{23}$ dependence of the leading order term.

The overlapping regions between the various curves at a specific value of the δ_{CP} indicate the degeneracy occurring *for the right value of δ_{CP}* , while the same value of probability for different δ_{CP} values denotes the degeneracy occurring *at wrong values of δ_{CP}* . Below, we explain the occurrence of the different degenerate combinations of (hierarchy, θ_{23} , δ_{CP}) taking the $\text{NO}\nu\text{A}$ neutrino probabilities in figure (4.1) as an example :

1. The overlapping regions between the NH-LO (blue) and IH-HO (green) bands around $\delta_{CP} = -120^\circ$ and 90° give rise to WH-WO- $\text{R}\delta_{CP}$ degenerate solutions in the probability. However, for the antineutrinos these bands are well separated. Thus, combining $\text{NO}\nu\text{A}$ neutrino and antineutrino data can help in removing these solutions.
2. The probability corresponding to UHP of the NH-LO (blue) band can be the same as those for the LHP of the IH-LO (yellow) band for $\theta_{23} = 39^\circ$. This can give rise to WH-RO- $\text{W}\delta_{CP}$ solutions. Note that this degeneracy is present in the antineutrinos for the same values of δ_{CP} . Thus, for true NH, UHP (i.e. $0^\circ < \delta_{CP} < 180^\circ$) is the unfavorable half-plane of δ_{CP} , and this degeneracy cannot be resolved by using $\text{NO}\nu\text{A}$ data alone. For T2K, the probability exhibits a sharper variation with δ_{CP} , and hence this degeneracy is less pronounced between the

UHP and LHP. Hence, the addition of T2K data to NO ν A can be helpful in removing this degeneracy. For LHP (i.e. $-180^\circ < \delta_{CP} < 0^\circ$), which is the favorable half-plane of δ_{CP} in NH, there is no WH-RO-W δ_{CP} solution for both NO ν A and T2K.

3. For $\delta_{CP} \in$ UHP, the NH-HO (red) band can share same value of probability with NH-LO (blue) band for $\delta_{CP} \in$ LHP. This is the reason for the RH-WO-W δ_{CP} solution. For the antineutrinos, the degeneracy is seen to be between NH-HO-LHP and NH-LO-UHP. Thus, a combination of neutrinos and antineutrinos helps to remove this degeneracy.
4. The WH-WO-W δ_{CP} solution can be observed along the isoprobability line that intersects the NH-LO (blue) and IH-HO (green) bands at different values of δ_{CP} . This degeneracy can be seen for instance between {NH, 39° , -180° } and {IH, 51° , 0° }. Again, the antineutrino probability does not suffer from this degeneracy, and thus combining neutrino and antineutrino data can be helpful in removing these solutions.
5. One can also have RH-RO-W δ_{CP} solutions as a result of a so called *intrinsic CP degeneracy* that occurs for the same hierarchy and same value of θ_{23} but at a different value of δ_{CP} . This is due to the harmonic dependence of the probability on δ_{CP} . For instance, within the NH-HO (blue) band, $\delta_{CP} = 0^\circ$ and $\delta_{CP} \approx -135^\circ$ have the same value of probability for $\theta_{23} = 39^\circ$. However, for antineutrinos, this occurs for $\delta_{CP} = 0^\circ$ and $\delta_{CP} = +135^\circ$. Thus, a combination of neutrino and antineutrino data can help to get rid of this degeneracy. This can also be seen to occur for T2K, for {NH, 48° , -180° } and {NH, 48° , 0° }. For T2K, since the flux peak coincides with the probability peak, the CP-dependent term is proportional to $\sin \delta_{CP}$ and thus this degeneracy occurs for δ_{CP} and $\pi - \delta_{CP}$ [229]. For NO ν A, since the flux and the probability peaks are not at the same energy, the degeneracy does not correspond exactly to δ_{CP} and $\pi - \delta_{CP}$. It is interesting to note that this degeneracy does not occur for $\delta_{CP} = \pm 90^\circ$.

Thus, among the 8-solutions listed in table (4.1), only the WH-RO-R δ_{CP} and RH-WO-R δ_{CP} solutions do not exist even at the probability level for NO ν A. At the χ^2 -

level, many of these may not appear as discrete degeneracies. In particular, for a C.L. beyond the reach of a particular experiment's precision, the different discrete degenerate solutions merge, and the degeneracy becomes continuous.

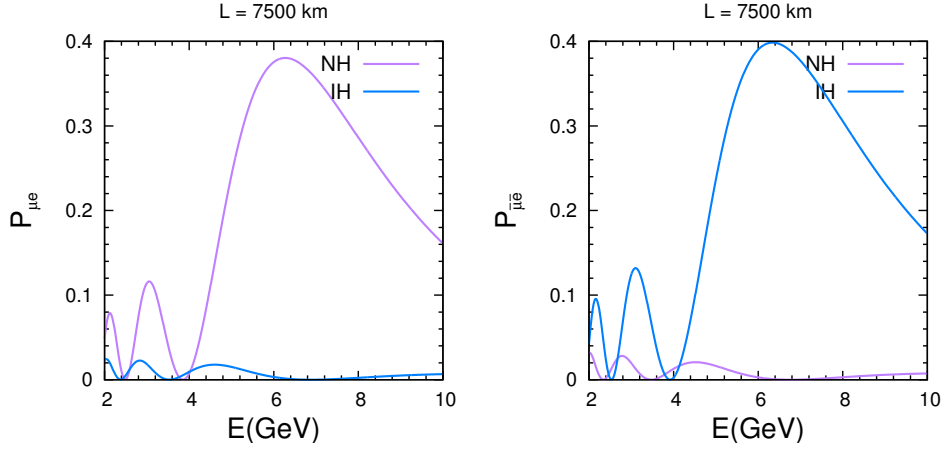


Figure 4.2: The oscillation probability $P_{\mu e}$ as a function of energy for $L = 7500 \text{ km}$. The left (right) panel is for neutrinos (antineutrinos).

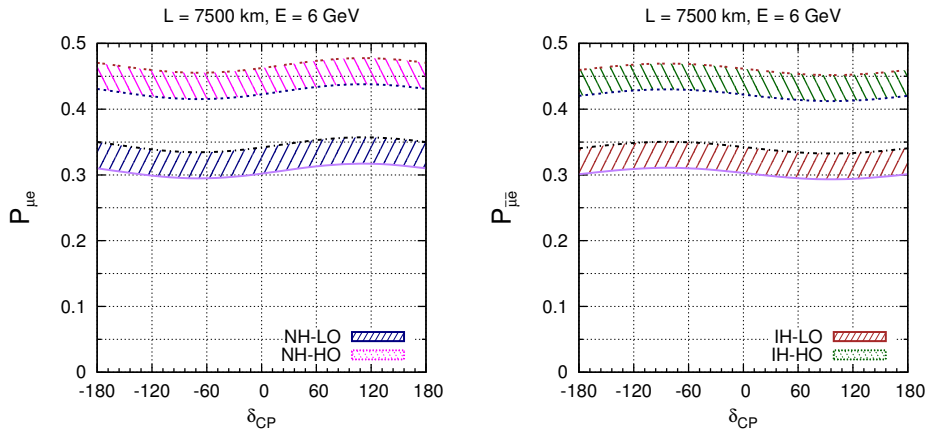


Figure 4.3: Here details are same as figure 4.1 except that we used fixed energy $E = 6 \text{ GeV}$.

In figure 4.2, we plot the appearance channel probability considering a baseline of 7500 km. We notice that because of the longer baseline and very high matter effect, mass hierarchy degeneracy can be resolved. From the left panel of the figure, we see that at energy of 6 GeV neutrinos have a very high probability for NH whereas probability for the IH is almost zero. This descriptions get reversed for the antineutrinos. Thus to understand the probability behaviour at 6 GeV, we plot the probability against δ_{CP} for this fixed energy in figure 4.3. The bands are for θ_{23} as described in figure 4.1.

But we consider the case NH (IH) for neutrinos (antineutrinos) as the IH (NH) probability is almost zero for neutrinos (antineutrinos). We observe that for the 7500 km there is no hierarchy as well as octant degeneracy at the probability level. We notice here an important point that $P_{\mu e}$ is not sensitive to CP. Thus atmospheric neutrinos can be used to resolve degeneracies of neutrino oscillation parameters.

In the next subsection we present a detailed descriptions of the degeneracies at the χ^2 level considering 6 years neutrino runs of NO ν A .

4.4.3 Chi-squared (χ^2) level study

In this section, we discuss the presence of different degenerate solutions at the χ^2 level. In figure (4.4), we present a set of contour plots in the $(\theta_{23} - \delta_{CP})$ test-parameter plane assuming only neutrino run (6 years) of NO ν A [6+0] to show the different degeneracies at the event level. These plots are drawn assuming the true hierarchy to be NH and different choices of representative true values of θ_{23} and δ_{CP} . In this figure, the successive rows are for $\theta_{23} = 39^\circ, 42^\circ, 48^\circ, 51^\circ$. The true δ_{CP} values chosen are $0^\circ, \pm 90^\circ$ corresponding to CP conservation and maximum CP violation respectively. It is noteworthy that the allowed area in the test $(\theta_{23} - \delta_{CP})$ plane also gives an idea about the precision of these two parameters. The blue contours correspond to the right hierarchy and magenta curves correspond to the wrong-hierarchy.

The first column of figure (4.4) shows that for $\delta_{CP} = -90^\circ$ and $\theta_{23} = 39^\circ$, apart from the true solution, RH-WO-W δ_{CP} and WH-WO-R δ_{CP} solutions are observed in the upper and lower right quadrants respectively. The RH-WO-W δ_{CP} solution is also seen for $\theta_{23} = 42^\circ$ (first pannel of second row). For this case, at $\delta_{CP} = -90^\circ$, the uppermost point of the blue band in the NO ν A neutrino probability, in figure 4.1 one can see that the same value of probability is possible for NH-HO (red band) near $\delta_{CP} = +45^\circ$ and $\pm 180^\circ$. This explains the shape of the allowed zone – wider at these values and narrower at 90° . The WH-WO-R δ_{CP} solution is seen only at a 2σ level for $\theta_{23} = 42^\circ$. This can be understood by observing that the points 42° (the upper tip of the blue band) and 48° (the lower tip of the green band) are more separated as compared to 39° (the lower tip of the blue band) and 51° (the upper tip of the green band). For θ_{23} in the higher octant (48° and 51°) there are no spurious wrong-hierarchy solutions

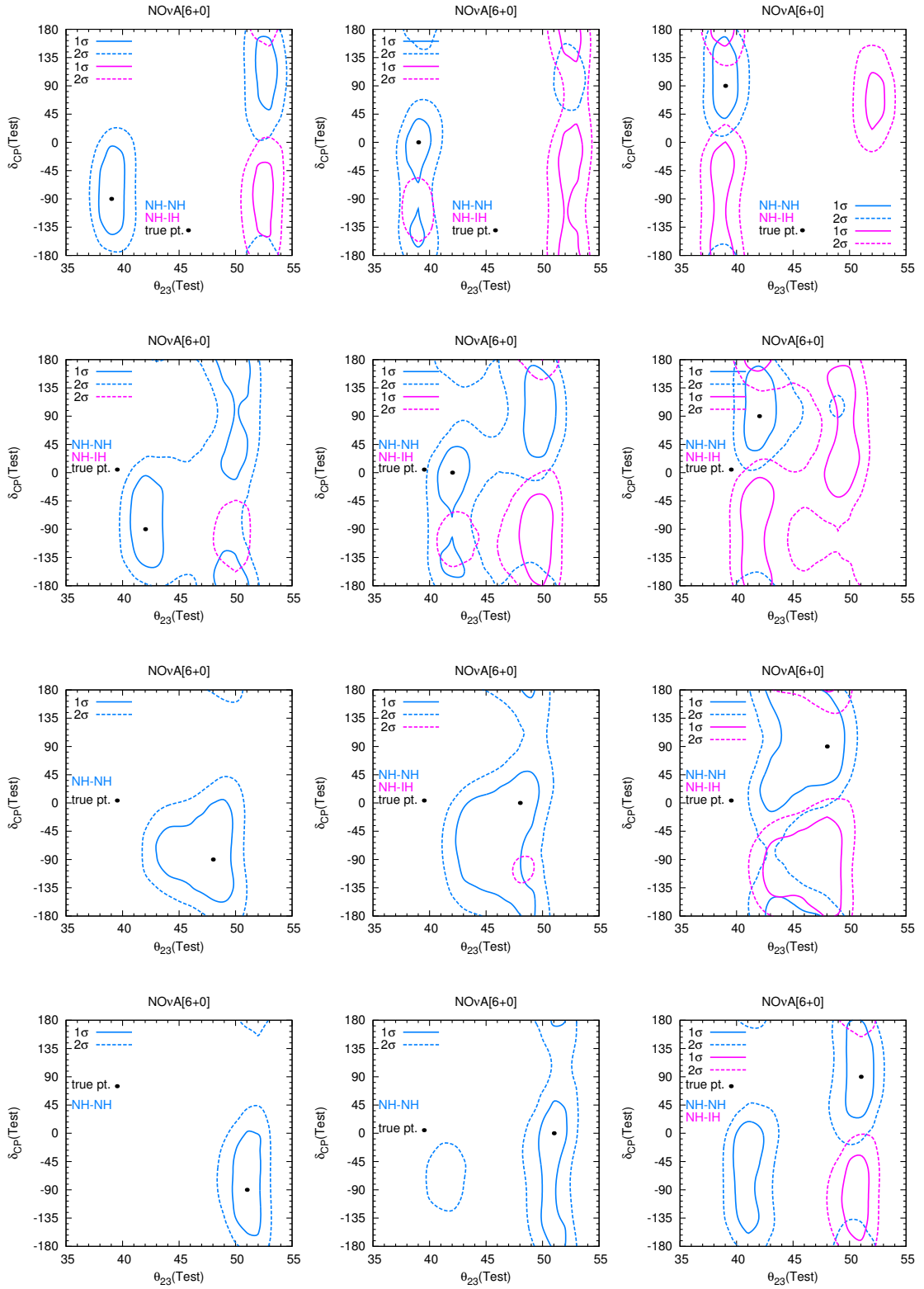


Figure 4.4: Contour plots in test ($\theta_{23} \times \delta_{CP}$) plane for $\text{NO}\nu\text{A}[6+0]$ with true values of $\theta_{23} = 39^\circ, 42^\circ, 48^\circ, 51^\circ$ in successive rows. The 3-columns correspond to $\delta_{CP} = -90^\circ, 0^\circ, +90^\circ$ respectively.

even with only neutrinos. This is because for NH, θ_{23} in the higher octant and -90° corresponds to the maximum probability for the neutrinos and this cannot be matched by any other combination of parameters. Hence, no degenerate solutions appear and only the neutrino run for NO ν A suffices to give an allowed area only near the true point. Note that the contours for 48° extend to the wrong octant also. However, (here and elsewhere) this is not due to any degenerate behavior of the $P_{\mu e}$ probability but due to the poor θ_{23} precision of the $P_{\mu\mu}$ channel near maximal mixing.

For the CP conserving case i.e. for $\delta_{CP} = 0^\circ$, a discrete RH-RO-W δ_{CP} solution is seen to be allowed at 1σ for $\theta_{23} \in \text{LO}$ and δ_{CP} around -135° . This is due to the intrinsic CP degeneracy as discussed in the context of probabilities. But at 2σ , due to the poor δ_{CP} precision this degeneracy becomes continuous and the whole LHP becomes allowed. For θ_{23} belonging to the higher octant larger statistical errors are involved as compared to $\theta_{23} \in \text{LO}$, and this degeneracy appears as continuous in the LHP even at 1σ , and at 2σ the full δ_{CP} range becomes allowed. For $\theta_{23} = 39^\circ$ and 42° , we also see wrong-hierarchy solutions appearing in the wrong octant. From the probability figure, we identify that this degeneracy occurs around $\delta_{CP} = -30^\circ, -180^\circ, 180^\circ$ for $\theta_{23} = 39^\circ$ which allows the LHP of δ_{CP} at 1σ and the whole δ_{CP} range at 2σ . For $\theta_{23} = 42^\circ$, this degeneracy is seen to occur around $\delta_{CP} = -90^\circ$ giving distinct degenerate solutions at the 1σ and 2σ levels. For $\theta_{23} = 42^\circ$, a discrete RH-WO-W δ_{CP} solution appears at 1σ . From Fig. 4.1, it is seen that $\{\text{NH}, 42^\circ, 0^\circ\}$ has the same value of probability corresponding to $\{\text{NH}, 48^\circ, 90^\circ\}$. At 2σ , this merges with the RH-RO-W δ_{CP} solution. For $\theta_{23} = 39^\circ$, this solution appears as a 2σ allowed patch around $\{\text{NH}, 51^\circ, 90^\circ\}$. From Fig. 4.1, it can be seen that the above points are not exactly degenerate in terms of probability but due to lack of precision, they become allowed. For a similar reason, the 2σ patch with wrong-hierarchy appears in the right octant for $\theta_{23} = 39^\circ$ and 42° . For $\theta_{23} = 51^\circ$ a right-hierarchy patch occurs with wrong octant. For $\theta_{23} = 48^\circ$, because of proximity to maximal mixing, the true parameter space also extends to the wrong-octant. In general, we see that the CP precision is poorer for $\delta_{CP} = 0^\circ$ at this stage. This is due to the unresolved degeneracies for $\delta_{CP} = 0^\circ$ which lead to multiple allowed regions and continuous bands at 2σ .

The third column represents $\delta_{CP} = +90^\circ$. In this case, we observe a WH-WO-

$R\delta_{CP}$ solution for both $\theta_{23} = 39^\circ$ and 42° . This can be understood from the intersection of the blue and green bands in Fig. 4.1 close to $\delta_{CP} = 90^\circ$ in the UHP. We also get a WH-RO- $W\delta_{CP}$ region in the LHP. For 42° , since the θ_{23} precision coming from the disappearance channel is worse, at 2σ both these solutions merge, and a discrete degenerate region is not obtained. For $\theta_{23} = 51^\circ$ from Fig. 4.1, we see that the point $\{\text{NH}, +90^\circ, 51^\circ\}$ in the red band intersects the blue band around $\{\text{NH}, -90^\circ, 39^\circ\}$ giving a RH-WO- $W\delta_{CP}$ solution. A WH-RO- $W\delta_{CP}$ solution is also obtained in this case in the LHP. Similar regions are also obtained for $\theta_{23} = 48^\circ$. However, the RH-WO- $W\delta_{CP}$ solution merges with the true solution at 2σ level.

4.5 Resolution of Degeneracies

4.5.1 Resolution of degeneracies using $\text{NO}\nu\text{A}[3+3]$

In this subsection, we present the role of antineutrinos to resolve various degeneracies. To address this we divide the six years of neutrino run to (3+3) years of $(\nu + \bar{\nu})$ run for $\text{NO}\nu\text{A}$. For illustrative purpose, we consider the true hierarchy as NH. Figure (4.5) shows the role of antineutrinos.

We observe the following generic features from the figure (4.5) :

- We observe that for $\theta_{23} = 39^\circ$ and 51° (first and last row), the wrong-octant regions are almost completely removed for all the three δ_{CP} values, except for the value $(51^\circ, -90^\circ)$ where we still have wrong-octant region at 2σ , whereas, for the true θ_{23} values 42° and 48° , both the right-hierarchy and wrong-hierarchy solutions extend to the wrong-octant region.
- For $\delta_{CP} = -90^\circ$ and $\theta_{23} = 51^\circ$, $\text{NO}\nu\text{A}[6+0]$ can already resolve all the degeneracies as can be seen in figure (4.4). However, the precision of θ_{23} is worse with $\text{NO}\nu\text{A}[3+3]$. This is because splitting the neutrino run into equal $(\nu + \bar{\nu})$ runs reduces the statistics and hence the precision becomes worse.
- In $\text{NO}\nu\text{A}[3+3]$, for $\delta_{CP} = 0^\circ$ and $\theta_{23} = 39^\circ, 42^\circ$ (middle panel for second and third row), comparing with the corresponding figures in figure (4.4), we see that the spurious solution appearing at -150° at 1σ due to the intrinsic degeneracy

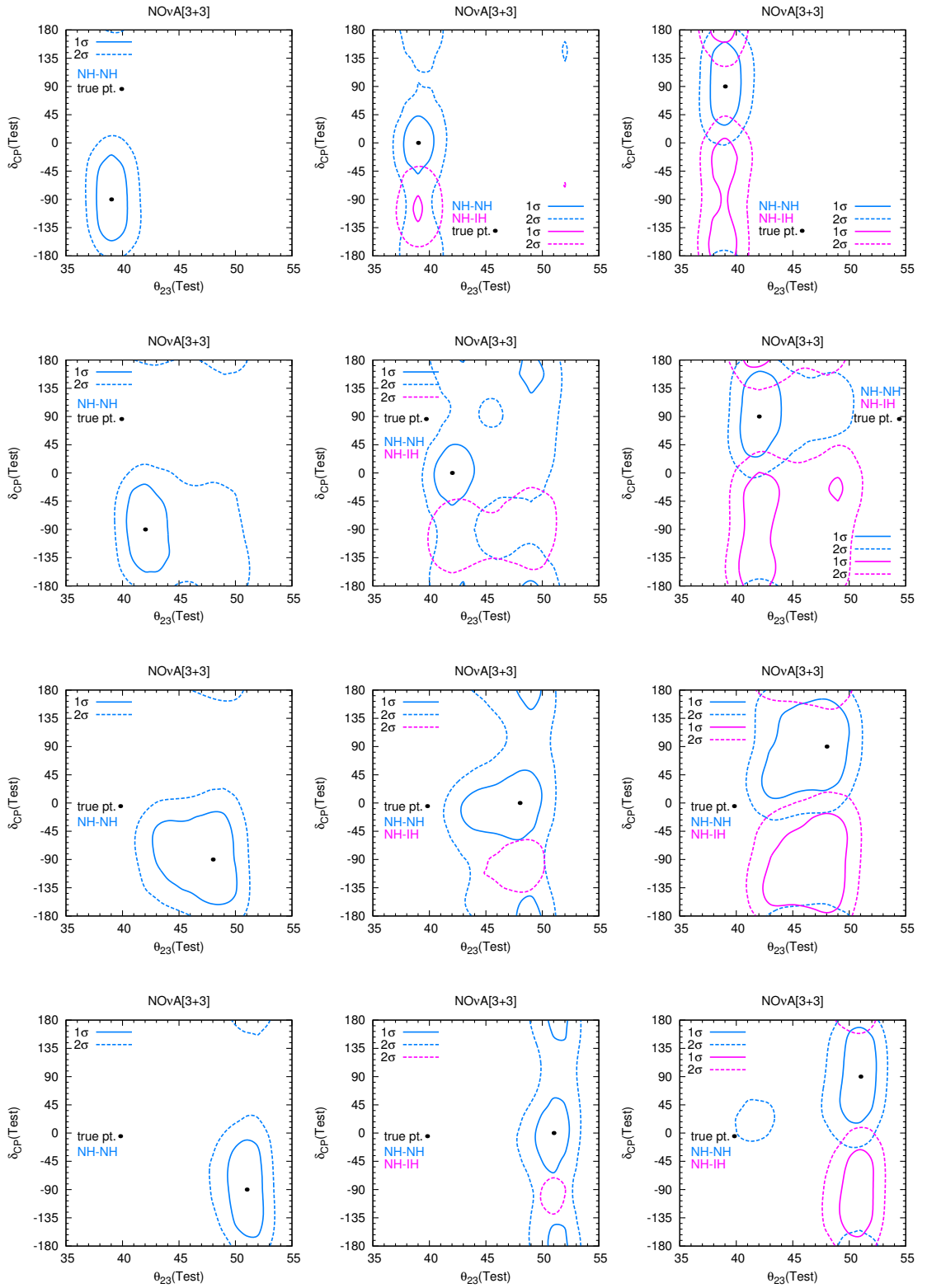


Figure 4.5: Here, columns correspond to the true $\delta_{CP} = -90^\circ, 0^\circ, 90^\circ$ respectively whereas each row correspond to the true $\theta_{23} = 39^\circ, 42^\circ, 48^\circ$ and 51° respectively for $\text{NO}\nu\text{A}[3+3]$.

is no longer present with the addition of antineutrino data, since for the antineutrino probability in $\text{NO}\nu\text{A}$ the intrinsic degeneracy is between 0° and $+150^\circ$ as discussed earlier. Thus the addition of neutrino and antineutrino data solves the intrinsic degeneracy at 1σ at both these δ_{CP} values but at 2σ both $\pm 150^\circ$ remain allowed.

- For $\text{NO}\nu\text{A}[3+3]$, among all possible cases of $(\delta_{CP}, \theta_{23})$, the combination $(-90^\circ, 39^\circ)$ best depicts the precision on the allowed parameter space.

4.5.2 Combined effects of $\text{NO}\nu\text{A}$, T2K and ICAL@INO

In figure (4.6), we illustrate the role of the combined effect of $\text{NO}\nu\text{A}[3+3]+\text{T2K}[8+0]$. From the figure (4.5), we notice that for $\theta_{23} = 39^\circ, 51^\circ$, $\text{NO}\nu\text{A}[3+3]$ was able to remove wrong-octant solutions for all the CP value except for the plot $(51^\circ, 90^\circ)$ where we still had right hierarchy-wrong octant regions at 2σ C.L. Combined effect $\text{NO}\nu\text{A}+\text{T2K}$ helps to remove this degeneracy completely at 2σ C.L and improves precision in large extent for the remaining cases. We also observe by comparing figure (4.5) with figure (4.6) that for $\theta_{23} = 39^\circ, 42^\circ$ and 51° the parameter space get largely constrained for all the three values of δ_{CP} , whereas for $\theta_{23} = 48^\circ$ because of the presence of wrong-hierarchy region a degenerate solution extends towards the LO region. Overall, we notice that addition of T2K with $\text{NO}\nu\text{A}$ helps very largely to increase the precision of the parameter space where wrong-octant solutions are already removed by $\text{NO}\nu\text{A}[3+3]$. Combined effect also constrained the parameter space including wrong-hierarchy region because of increase in statistics for $\text{NO}\nu\text{A}[3+3]+\text{T2K}[8+0]$.

Figure (4.7) shows the role of ICAL when combined with $\text{NO}\nu\text{A}[3+3]+\text{T2K}[8+0]$. We observe that when ICAL data are added to T2K and $\text{NO}\nu\text{A}$, the remaining wrong-hierarchy regions are resolved for all the true values of θ_{23} considered. The wrong-octant extensions of the right-hierarchy solutions are also reduced in size and the precision of θ_{23} improves. The combination of $\text{T2K}+\text{NO}\nu\text{A}+\text{ICAL}$ can resolve all the degeneracies at a 2σ level for true $\theta_{23} = 39^\circ, 51^\circ$ for all the three δ_{CP} values. For the θ_{23} and δ_{CP} combinations of $\{42^\circ, 0^\circ\}$ and for $48^\circ, \pm 90^\circ, 0^\circ$, there are still allowed regions in the wrong-octant. Note that some of the wrong-octant regions that are removed by the $\text{NO}\nu\text{A}$ antineutrino run could also be removed by the ICAL data.

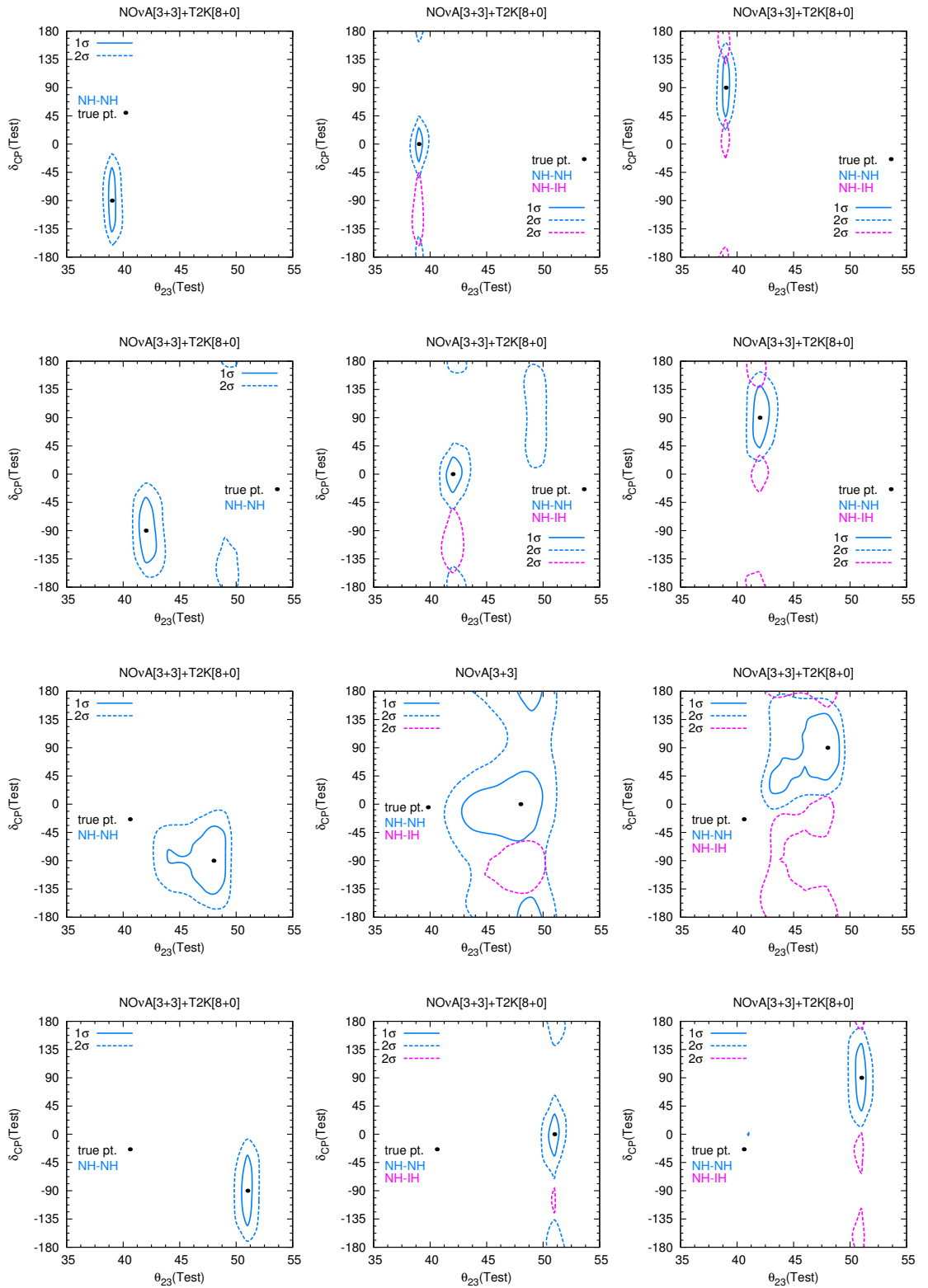


Figure 4.6: Here, columns correspond to the true $\delta_{CP} = -90^\circ, 0^\circ, 90^\circ$ respectively whereas each row correspond to the true $\theta_{23} = 39^\circ, 42^\circ, 48^\circ$ and 51° respectively for NOνA[3+3]+T2K[8+0].

The following additional observations can be made regarding alternative parameter values and running modes:

- In generating the above plots, we considered T2K running in neutrino mode with its full beam power. We find that once one includes the antineutrino run from NO ν A, running T2K in the antineutrino mode is no longer necessary for removing spurious wrong-octant solutions. Rather, running in the neutrino mode gives enhanced statistics and hence better precision. If on the other hand NO ν A runs in full neutrino mode and the antineutrino component comes from T2K, we have verified that we get similar results.
- We have presented the results for the case of true NH. If the true hierarchy is chosen to be IH, one would get a different set of allowed regions based on the degeneracies observed in Fig. 4.1. For example, for $\delta_{CP} = -90^\circ$ and $\theta_{23} = 39^\circ$ for NO ν A[6+0] in the true IH case, apart from the true solution, RH-WO- $W\delta_{CP}$ and WH-RO- $W\delta_{CP}$ solutions would be obtained. This can be predicted from Fig. 4.1 by drawing a horizontal line from the bottom of the IH-LO band at $\delta_{CP} = -90^\circ$, which cuts both the IH-HO and NH-LO bands near $\delta_{CP} = 90^\circ$.

The situation for NO ν A[3+3] and other combinations would be more complicated since the allowed regions and precision for true IH depend not only on the probability behavior but also on the statistics of neutrino and antineutrino data in the respective experiments.

- The results are significantly dependent on the true value of θ_{13} , chosen here to be $\sin^2 2\theta_{13} = 0.1$. Lower values of θ_{13} (or worse θ_{13} precision) would lead to poorer CP precision and more difficulty in removing the degeneracies. This is because δ_{CP} is coupled with θ_{13} in the oscillation probability.

4.6 Distinguishability between 0° and 180°

It will also be interesting to see how far the two CP conserving values 0° and 180° can be distinguished by the experimental setups considered. In this section, we discuss this

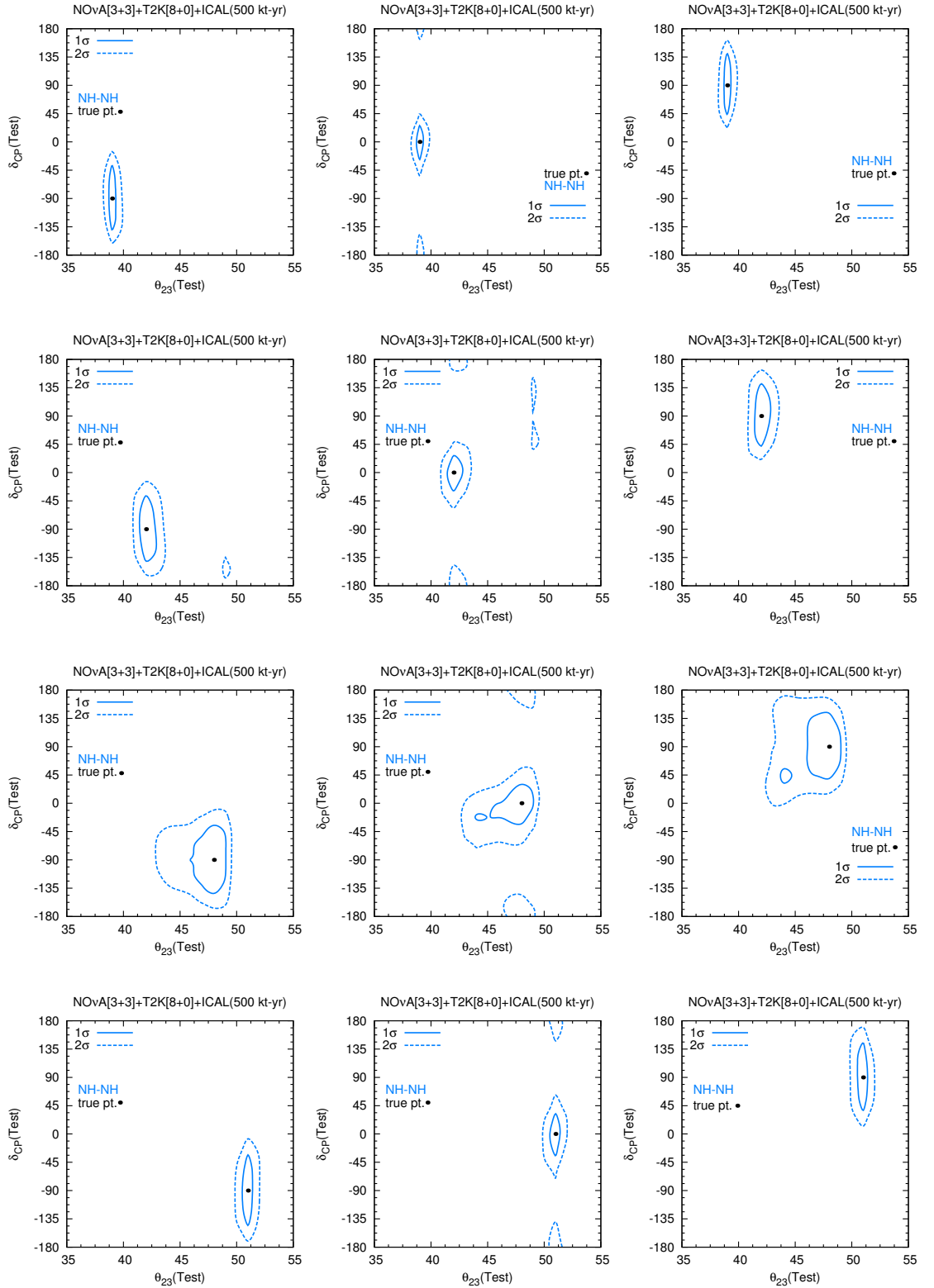


Figure 4.7: Here, columns correspond to the true $\delta_{CP} = -90^\circ, 0^\circ, 90^\circ$ respectively whereas each row correspond to the true $\theta_{23} = 39^\circ, 42^\circ, 48^\circ$ and 51° respectively for $\text{NO}\nu\text{A}[3+3]+\text{T2K}[8+0]+\text{ICAL}$.

issue. The true events are generated for $\delta_{CP} = 0^\circ$, $\theta_{23} = 39^\circ$ and normal hierarchy. In the test spectrum, we consider $\delta_{CP} = 180^\circ$ and marginalize over θ_{13} . For purposes of comparison we also give the results for test $\delta_{CP} = 90^\circ$. The results are presented in table 4.2. We observe that a 2σ sensitivity in distinguishing between $\delta_{CP} = 0^\circ$ and $\delta_{CP} = 180^\circ$ can be achieved by NO ν A+T2K. Adding ICAL data increases the sensitivity further. It is interesting to note that for beam based experiments, 0° and 90° have much larger separation than that between 0° and 180° . But for ICAL, 0° and 180° are more separated though the χ^2 values are very small. This is because ICAL itself has limited CP sensitivity due to angular smearing over all directions [231]. Note that for experiments like PINGU the CP sensitivity can be higher, and the χ^2 difference between 0° and 180° can be appreciable [232].

$\nu + \bar{\nu}$	Test $\delta_{CP} = 90^\circ$	Test $\delta_{CP} = 180^\circ$
NO ν A[3+3]	6.31	2.82
NO ν A[3+3]+T2K[8+0]	14.63	4.77
ICAL	1.21	1.60
NO ν A[3+3]+T2K[8+0]+ICAL	14.83	5.4

Table 4.2: χ^2 sensitivity for test $\delta_{CP} = 90^\circ$, 180° with true values of $\delta_{CP} = 0^\circ$ for NH-39 $^\circ$.

4.7 Summary

With the precise measurement of θ_{13} by the reactor experiments, the intrinsic degeneracy is largely removed and a 4-fold degeneracy out of the original eight [165] – involving wrong-hierarchy and wrong-octant solutions – remains to be solved by the current and upcoming experiments. In this chapter, we study these degeneracies in detail and propose that the remaining degeneracies can be studied in the most comprehensive manner by considering the generalized hierarchy– θ_{23} – δ_{CP} degeneracy. These are best visualized by contours in the test $(\theta_{23} - \delta_{CP})$ plane drawn for both right and wrong-hierarchy for different representative values of true parameters. We show that, depending on whether the wrong-hierarchy and/or wrong-octant solutions occur with right or wrong values of δ_{CP} , there can be a total of eight possibilities. We study these

possibilities at the probability level for $\text{NO}\nu\text{A}$, T2K and INO. At this level, the degeneracy is defined as the equality of the probabilities for different values of parameters. However, at the χ^2 contour level, because of the precision of the experiments, one gets finite allowed regions corresponding to degenerate solutions. We define a degenerate solution to be one which is distinct from the true solution at the 1σ level. The sample true values that we consider for obtaining the contours are $\theta_{23} = 39^\circ, 42^\circ, 48^\circ$ and 51° and $\delta_{CP} = \pm 90^\circ, 0^\circ$.

Considering only the neutrino run of $\text{NO}\nu\text{A}$, as an illustrative example, we identify which of these degenerate solutions actually occur for different representative choices of true parameters. At the present level of precision, for $\delta_{CP} = \pm 90^\circ$, the right (wrong) δ_{CP} solutions are those which occur in the same (opposite) half-plane as compared to the true solution. Since $\delta_{CP} = 0^\circ$ is common to both half-planes, for this case the right and wrong δ_{CP} solutions at a particular C.L. are inferred from the nature of the contours. The different degenerate solutions obtained are the (i) WH-WO-R δ_{CP} , (ii) RH-WO-W δ_{CP} , (iii) WH-RO-R δ_{CP} , (iv) RH-RO-W δ_{CP} and (v) WH-WO-W δ_{CP} regions. Although the options (i-iii) have been noticed in the literature earlier, the option (iv) which exists for the same true θ_{23} and hierarchy but different δ_{CP} has not been discussed extensively. A probability level discussion on this was done in Ref. [229], where it was called $\theta_{23} - \delta_{CP}$ degeneracy. However, since it can occur for the same hierarchy and same θ_{23} we call it *intrinsic CP degeneracy*. The WH-WO-W δ_{CP} solutions often appear as part of i), given the CP precision of the current experiments. Next, we present the results combining $\text{NO}\nu\text{A}[3+3]$ with T2K[8+0]. It is seen that the synergy between T2K and $\text{NO}\nu\text{A}$ helps in removing the WH-RO-W δ_{CP} solutions for true $\delta_{CP} = 0^\circ, 90^\circ$. For true $\delta_{CP} = -90^\circ$, $\text{NO}\nu\text{A}$ itself is sufficient for removing this degeneracy. The remaining degenerate solutions at 2σ can be resolved by adding ICAL data. The latter is seen to play an important role in removing the wrong-hierarchy solution for $\theta_{23} = 48^\circ$. In conclusion, we show that the combination of data from different LBL and atmospheric neutrino experiments can play a crucial role in removing the degeneracies associated with neutrino oscillation parameters, thereby improving the precision of the parameters θ_{23} and δ_{CP} . This also paves the way toward an unambiguous determination of these parameters.

Chapter 5

The Role of Antineutrinos at DUNE

*“It Is Very Easy To Defeat Someone,
But It Is Very Hard To Win Someone”*

– A. P. J. Abdul Kalam

5.1 Introduction

In the previous chapter (4), we have discussed the combined effect of $\text{NO}\nu\text{A}$, T2K and ICAL@INO to resolve the generalized “hierarchy- θ_{23} - δ_{CP} ” degeneracy in neutrino oscillation parameters. In the present chapter, our focus is on the next generation superbeam experiment DUNE (Deep Underground Neutrino Experiment). This is a 1300 km baseline experiment in which an intense neutrino beam is fired from Fermilab to Sanford Lab in South Dakota, USA. Because of longer baseline, DUNE has higher matter effect and hence it can resolve the hierarchy degeneracy at 5σ for all values of δ_{CP} with an exposure of 300 kton.MW.year as discussed in Ref. [128]. The authors in Ref. [128] also illustrated the CP sensitivity of DUNE by considering equal neutrino and antineutrino runs.

We concentrate on the determination of the octant of θ_{23} and the CP phase δ_{CP} . It is well known that the precise determination of the octant and δ_{CP} is interlinked through the octant- δ_{CP} degeneracy. As we have discussed in the last chapter (4), for $P_{\mu e}$ and $P_{\bar{\mu} \bar{e}}$ the octant- δ_{CP} degeneracy occurs at different values of δ_{CP} . Thus the combination of neutrino and antineutrino runs help to resolve this. However, in regions where neutrinos do not have octant degeneracy, adding antineutrino data is expected to de-

crease the sensitivity because of the degeneracy and reduced statistics. In the case of the DUNE baseline, we find that the antineutrino runs help even in the parameter space where the antineutrino probabilities suffer from degeneracies. We explore these in detail and point out that this happens because of the (i) broadband nature of the beam so that even if there is degeneracy at a particular energy bin, over the whole spectrum the degeneracy may not be there; (ii) enhanced matter effect due to the comparatively longer baseline which creates an increased tension between the neutrino and the antineutrino probabilities. This in turn raises the overall χ^2 in case of the combined runs. This feature is more prominent for IH since the antineutrino probabilities in this case are much higher than the neutrino probabilities due to matter effects.

The δ_{CP} sensitivity of an experiment is often understood in terms of the CP asymmetry between the neutrinos and antineutrinos.

$$A_{cp} = \frac{P_{\mu e} - P_{\bar{\mu} e}}{P_{\mu e} + P_{\bar{\mu} e}} \sim \frac{\sin \delta_{CP}}{\sin \theta_{13}} \quad (5.1.1)$$

However the diagnostics used for probing CP violation (CPV) is the sum total of the χ^2 contribution of the neutrinos and antineutrinos: $\chi_{total}^2 = \chi_{\nu}^2 + \chi_{\bar{\nu}}^2$ which does not show the same dependence as A_{cp} on the θ_{13} as given by equation (5.1.1) [233]. Hence one needs to understand the actual role played by the antineutrinos, if any, for determination of CPV. It has been observed that one of the roles of antineutrinos in enhancing CP sensitivity is their ability to remove the octant- δ_{CP} degeneracy [193, 230]. For T2K, antineutrinos do not play any role for the discovery of CP violation [234, 235]. However for the NO ν A experiment, antineutrinos seem to be playing some role even when there is no octant degeneracy [234]. In this work, it is one of our goals to understand the role of antineutrinos for enhancing CP sensitivity for the DUNE baseline. In particular we explore whether the antineutrino runs can play any non-trivial contribution to the total χ^2 if octant and hierarchy are assumed to be known and if so, then what are the physics issues involved.

The plan of this chapter is as follows : in the next section (5.2), we give the details of the experimental set-up considered in our study. In the section (5.3), we illustrate the presence of degeneracies in the appearance channel probability for DUNE. Section (5.4) is devoted to the resolutions of degeneracies, where we mainly demonstrate the broadband nature of DUNE and the role of antineutrinos to resolve the octant degen-

eracies and the capability of CPV discovery potential. We summarize our conclusions in section (5.5)

5.2 Specification of the Experiment

We use the same simulation package namely, GLOBES as used in the previous chapter for the numerical simulation of the number of events, incorporating appropriate specifications for the DUNE experiment. We consider a 10 kton LArTPC detector for detecting the neutrinos coming from the accelerator at Fermilab. In our simulation, we consider neutrino flux [236] corresponding to a proton beam of power 1.2 MW and energy 120 GeV giving 1.0×10^{21} POT/year. The systematic errors are incorporated into our analysis using the pull method [221, 222] as outlined in Ref. [203]. The systematic errors and the efficiencies corresponding to signal and background are taken from Ref. [237]. We also add 5% prior on $\sin^2 2\theta_{13}$ in our numerical simulation *. To generate the data, representative values of neutrino oscillation parameters, consistent with the global-fit of world neutrino data are used from Refs. [163, 223–225].

5.3 Identifying Degeneracies at DUNE

In figure (5.1), we present the appearance channel probability for the DUNE baseline for an energy, $E = 2$ GeV. In the previous chapter (4), we have given the probability expressions for both the appearance as well as disappearance channel which are relevant for LBL experiments. The same expressions can be used here also for the theoretical understanding of degeneracies. The bands are due to the variation of θ_{23} (see figure caption for details). Left (right) panel figure describes the oscillation probability for neutrino (antineutrino). We notice that, the neutrino oscillation probability for NH gets significant enhancement in presence of Earth’s matter as compared to IH as shown in the left panel. It is seen that the maximum probability for NH becomes 3-times more than that of IH. But in the case of antineutrinos the scenario gets reversed as A and δ_{CP} changes their sign, as can be observed in the right panel. Note that for vacuum oscil-

*Note that the detailed discussion on the inclusion of pulls for the systematic errors and the prior in our numerical simulation are discussed in appendix A

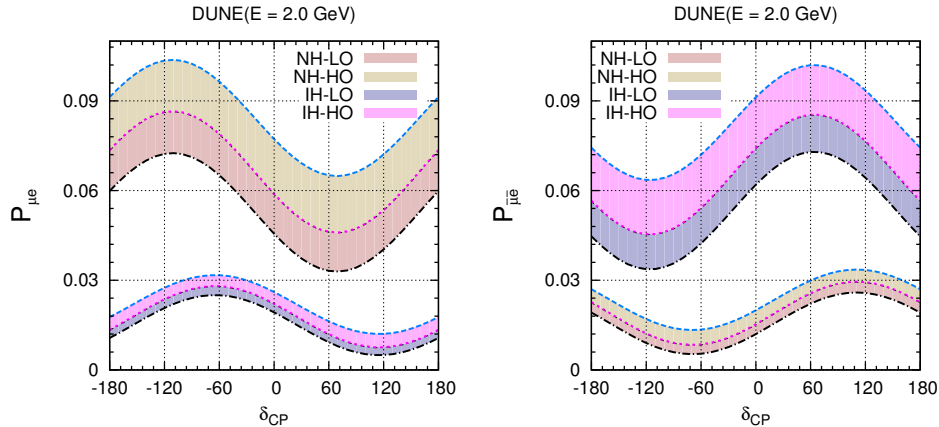


Figure 5.1: Left panel (right panel) represents $P_{\mu e}$ ($P_{\bar{\mu} e}$) for DUNE. Here the bands are over current 3σ range of θ_{23} [225]. For LO, NH (LO, IH) we consider the range of θ_{23} over $38.8^\circ - 45^\circ$ ($39.4^\circ - 55^\circ$) and for HO, NH (HO, NH) we consider the range of θ_{23} over $45^\circ - 53.3^\circ$ ($45^\circ - 53.1^\circ$).

lation maxima, Δ corresponds to 90° . Thus for the appearance channel probability (cf. Eq. 4.4.1), $\delta_{CP} = -90^\circ$ ($+90^\circ$) corresponds to maximum (minimum) point in the probability for neutrinos. For antineutrinos it is the opposite. Thus, for these values of δ_{CP} , the octant sensitivity is expected to be maximum if there is no degeneracy. Note that with the inclusion of matter effect, the appearance channel probability maxima does not coincide with the vacuum maxima and in that case the maximum and minimum points in the probability do not come exactly at $\pm 90^\circ$ but gets slightly shifted. This can be seen from figure (5.1). However for illustration, we consider $\delta_{CP} = \pm 90^\circ$ as the reference.

It is to be observed that, if we draw a horizontal line at particular probability value then the different intersection points with the given band lead to different degenerate solutions. The occurrence of octant degeneracies that can be inferred from these plots are summarized in table (5.1). From the above discussions as well as from the earlier studies it is clear that the nature of octant - δ_{CP} degeneracy is different for neutrinos and antineutrinos and therefore combined neutrino-antineutrino run is helpful for resolving the octant degeneracy [193, 230, 238]. Also note that the behaviour of octant- δ_{CP} degeneracy in neutrinos and antineutrinos is same for both NH and IH.

The probability plot as given in figure (5.1) is done for an energy of 2 GeV. However it is possible that because of the broadband nature of the beam the occurrence of degeneracy at a particular energy may not be true over the whole energy range. Thus

Octant Degeneracy	ν	$\bar{\nu}$
LHP, LO	degenerate with UHP, HO	no degeneracy
UHP, LO	no degeneracy	degenerate with LHP,HO
LHP, HO	no degeneracy	degenerate with UHP, LO
UHP, HO	degenerate with LHP,LO	no degeneracy

Table 5.1: The octant degenerate parameter space for neutrinos and antineutrinos. Here, LO = Lower octant, HO = Higher octant, UHP = Upper half plane ($0^\circ < \delta_{CP} < 180^\circ$) and LHP = Lower half plane ($-180^\circ < \delta_{CP} < 0^\circ$).

for DUNE, one can still get some amount of octant sensitivity, even in the degenerate parameter space outlined in table (5.1), when integrated over all the energy bins.

It is to be noted that figure (5.1) does not demonstrate any hierarchy degeneracy since the two bands corresponding to NH and IH remain non-overlapping. However conclusions drawn at the probability level need to be substantiated by a proper χ^2 analysis to determine with what significance the hierarchy degeneracy is actually resolved by DUNE. Therefore we will present the results of octant sensitivity either for both cases – right and wrong hierarchy or by marginalizing over the hierarchy.

5.4 Resolution of degeneracies

In this section we discuss the octant sensitivity of DUNE for a 10 kton detector volume which is the projected detector volume for DUNE in the first phase. The prescriptions regarding the generation of number of events and the χ^2 analysis are discussed in appendix (A). In figure (5.2) we show the χ^2 for octant discovery which is the combined sensitivity coming from appearance channel, disappearance channel and $\sin^2 2\theta_{13}$ prior i.e.

$$\chi^2 = \chi_{ap}^2 + \chi_{disap}^2 + \chi_{prior}^2 \quad (5.4.1)$$

as a function of true δ_{CP} .

5.4.1 Octant discovery χ^2

We consider the representative true values of $\theta_{23} = 39^\circ(51^\circ)$ for LO (HO). χ^2 is marginalized over test values of θ_{23} over the opposite octant. We give the plots sepa-

rately for true and false hierarchy. This shows for what parameters and to what extent the octant sensitivity is affected by the lack of knowledge of hierarchy. Depending on the true parameters, we get four combinations of (hierarchy–octant): NH-LO, NH-HO, IH-LO, IH-HO. For all the plots in the upper row of figure (5.2), dark-blue curves are for True(NH)-Test(NH) and magenta curves are for True(NH)-Test(IH) while for the lower row dark-blue curves correspond to True(IH)-Test(IH) and magenta curves correspond to True(IH)-Test(NH). Below we discuss the results for each true combination.

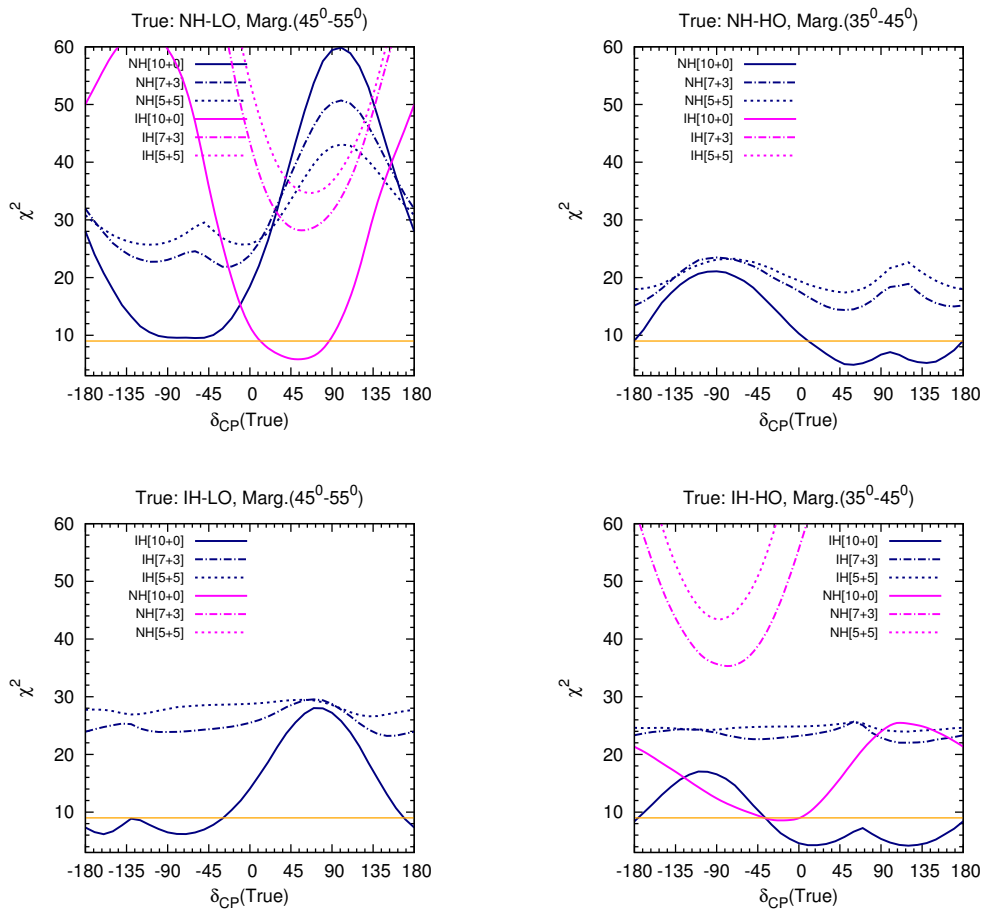


Figure 5.2: Octant discovery χ^2 for DUNE. Left (right) panel is for LO (HO), where true(θ_{23}) is considered as 39° (51°) and test(θ_{23}) is marginalized over (45° to 55°) for LO and (35° to 45°) for HO. The labels NH, IH inside the plots signifies test hierarchy.

- **NH-LO** ($\theta_{23}^{\text{true}} = 39^\circ$) : The figure for true NH-LO shows that for values of δ_{CP} in the LHP, a 10 year neutrino run of DUNE can resolve the octant degeneracy at 3σ C.L. The inclusion of antineutrino run helps in enhancing the octant

sensitivity for δ_{CP} in LHP and θ_{23} in LO since the antineutrino probability is devoid of the octant degeneracy. Note that in this case though pure neutrino run suffers from octant degeneracy, still we get χ^2 around 10. This is one of the unique features of the broadband beam where the degeneracy does not exist over the entire energy range and one can still have some octant sensitivity from the neutrino channel. For the UHP on the other hand the neutrino data gives a better octant sensitivity since antineutrinos are plagued with degeneracies for LO, as shown by the blue curves. However the scenario changes if we assume the hierarchy is not known. In that case the antineutrino run is seen to help to remove wrong hierarchy-wrong octant solutions in spite of having degeneracies, as is seen from the magenta curves. In order to understand this point we have plotted the appearance channel probability vs energy in figure (5.3).

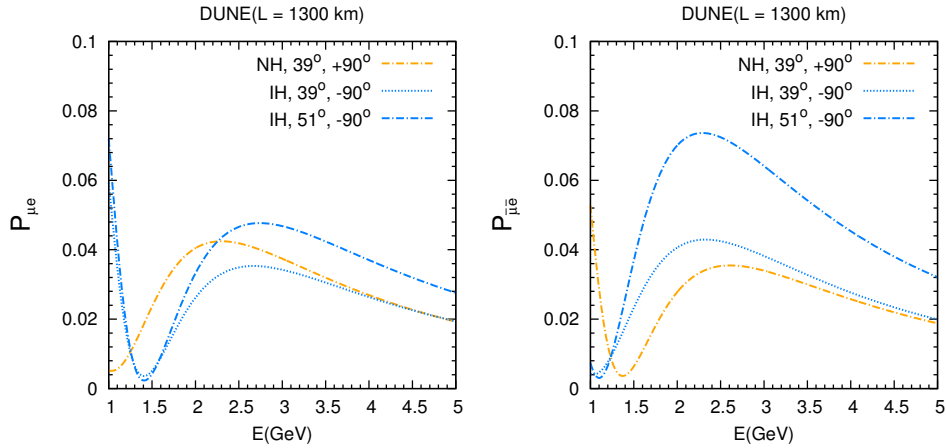


Figure 5.3: Here, left panel (right panel) represents $P_{\mu e}$ ($P_{\bar{\mu e}}$) as a function of energy for DUNE and hierarchy corresponds to orange (light blue) curve is NH (IH).

The left panel is for neutrinos and the right panel is for antineutrinos. In the left panel we see that the orange curve ($\delta_{CP} = +90^\circ$) is well separated from the dotted blue curve ($\delta_{CP} = -90^\circ$) near the oscillation maxima for $\theta_{23} = 39^\circ$. But when marginalized over θ_{23} , the dashed blue curve which corresponds to $\delta_{CP} = -90^\circ$ and $\theta_{23} = 51^\circ$, overlaps with the orange curve to give WH-WO- δ_{CP} solution[†]. On the other hand in the right panel we see that due the

[†]Due to the presence of $P_{\mu\mu}$ channel, the wrong octant minima comes around $\theta_{23} = 51^\circ$ for true $\theta_{23} = 39^\circ$.

marginalization of θ_{23} the dashed blue curve moves far away from the orange curve resolving the degeneracy. Note that if we marginalize over hierarchy then for UHP the minimum will come at the WH solution with only neutrino data and hence octant degeneracy is not resolved at 3σ for $9^\circ < \delta_{CP} < 90^\circ$, belonging to the UHP. However with 7+3 years run the octant degeneracy is resolved with a $\chi^2 > 25$ even without the knowledge of the true hierarchy for all values of δ_{CP} . With 5+5 year run in most part of UHP the minima occurs with the RH solution. But for $45^\circ < \delta_{CP} < 115^\circ$, the WH minima is below the one with RH.

- **NH-HO ($\theta_{23} = 51^\circ$)**: For this case from figure (5.1) it is seen that for $(51^\circ, -90^\circ, \text{NH})$ no octant degeneracy prevails at the probability level for neutrinos whereas antineutrinos have octant degeneracy. Also, antineutrinos have less statistics. Thus we expect that only neutrino run should give a better sensitivity. But, we notice from the top right figure of figure (5.2), that addition of antineutrino gives higher χ^2 value as compared to only neutrino mode [10+0]. In order to understand this feature in the first panel of figure (5.4) we plot the χ^2 vs test δ_{CP} .

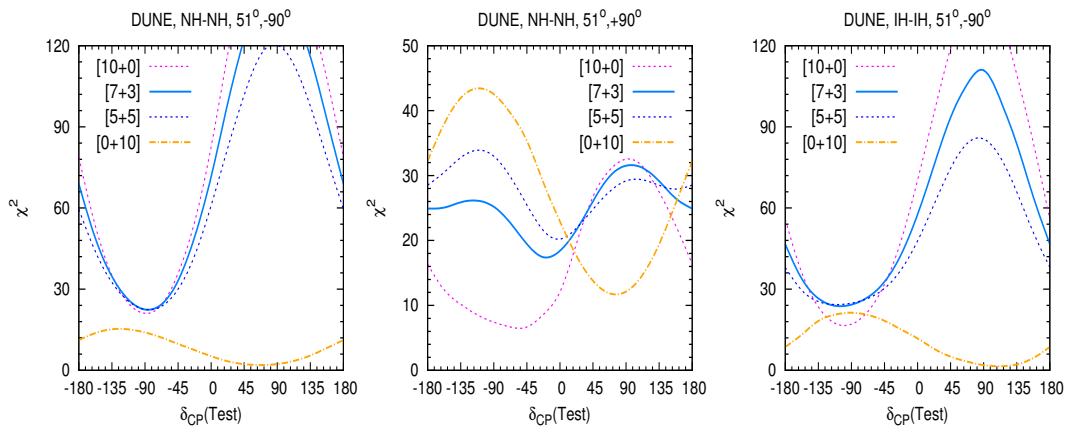


Figure 5.4: Octant χ^2 vs test(δ_{CP}) for DUNE.

The curve for only antineutrinos indeed confirms the occurrence of degeneracies close to $\delta_{CP} \sim 90^\circ$. However at that point the neutrino χ^2 is very high. Thus, when the neutrino and antineutrino data are combined the overall minima is governed by the neutrinos and so comes close to the true value of $\delta_{CP} = -90^\circ$. At this point both neutrinos and antineutrinos have octant sensitive contribu-

tion. This is shown in table 5.2 where we illustrate the contributions from the neutrinos and antineutrinos separately for the appearance channel. It is evident that as we increase the antineutrino component the contribution from neutrino channel reduces whereas that from the antineutrino channel increases. Thus although the antineutrino channel has degeneracy the minima does not come at the point of degeneracy as it is governed by the neutrinos. Even then the total $\chi^2 (= \chi_{ap,\nu}^2 + \chi_{ap,\bar{\nu}}^2)$ from appearance channel (11.13, 10.19), corresponding to [7 + 3] and [5 + 5] respectively, is less than the pure neutrino run. However, the total χ^2 for the mixed run is higher.

To understand this point we list the contribution from the disappearance χ^2 . It is seen that although for pure neutrino run the disappearance channel does not have any octant sensitive contribution to the total χ^2 , for mixed runs this channel provides some octant sensitivity. This arises because, due to matter effects the neutrino and antineutrino probabilities are different and hence the χ^2 minima comes at different places.

When one combines neutrino and antineutrino runs then this creates a synergy and hence some octant sensitivity arises from the disappearance channel also. Due to this reason when one combines appearance and disappearance channels then the addition of antineutrino runs actually gives a slight increase in χ^2 . In the UHP, on the other hand, the octant sensitivity increases with antineutrino run. This is clear, since for $P_{\mu e}$ the neutrino channel suffers from octant degeneracy whereas the antineutrino channel does not and the addition of antineutrinos help to overcome the degeneracy. To illustrate this point further in the middle panel of figure (5.4) we plot the χ^2 vs test δ_{CP} for true values (51° , 90°). In this case the pure neutrino run gives the minima in the LHP close to $\delta_{CP} \sim -45^\circ$ whereas pure antineutrino run gives minima near the true value. However when we combine neutrino and antineutrino runs then the overall minima comes in between and moves towards the antineutrino minima as the $\bar{\nu}$ component is increased. At this point there is octant sensitive contribution from both neutrinos and antineutrinos. Thus the antineutrino data helps in this case by trying to shift the minima away from the degenerate point. We also compare the χ^2 for DUNE with that

$(\nu + \bar{\nu})$	Test parameters	$\chi_{ap,\nu}^2$	$\chi_{ap,\bar{\nu}}^2$	$\chi_{disap,(\nu+\bar{\nu})}^2$	Prior	Total
NH, 51° , -90° (true)						
[10+0](8+0)	$\theta_{23}=41.5^\circ(41^\circ)$ $\sin^2 2\theta_{13} = 0.115(0.106)$	11.5(6.65)	0	0.5(0.35)	9(1.44)	21.05(8.44)
[7+3](5+3)	same as [10+0](8+0)	9.14(4.28)	1.99(1.44)	1.97(0.37)	9(1.44)	22.46(7.18)
[5+5](4+4)	same as [10+0](8+0)	7.21(3.46)	2.98(1.44)	3.34(0.37)	9(1.44)	22.52(6.72)
IH, 51° , -90° (true)						
[10+0](8+0)	$\theta_{23}=40^\circ(41^\circ), \delta_{CP} = -105^\circ(-90^\circ)$ $\sin^2 2\theta_{13} = 0.112(0.106)$	10.86(5.23)	0	0.09(1.47)	5.76(1.44)	16.71(8.14)
[7+3](5+3)	same as [10+0](8+0)	8.22(3.36)	8.10(1.33)	1.62(0.96)	5.76(1.44)	23.71(7.09)
[5+5](4+4)	$\theta_{23}=40.5^\circ(41^\circ), \delta_{CP} = -120^\circ(-90^\circ)$ $\sin^2 2\theta_{13} = 0.112(0.103)$	6.46(3.37)	9.78(2.08)	2.14(0.84)	5.76(0.36)	24.15(6.66)

Table 5.2: Here, [10+0], [7+3] and [5+5] refers to $(\nu + \bar{\nu})$ runs of DUNE, whereas (8+0), (5+3) and (4+4) refers to $(\nu + \bar{\nu})$ runs of T2K. The numbers in the parenthesis correspond to T2K. Also ‘‘Test parameters’’ refer to the test values where χ^2 minimum appears and remaining oscillation parameters are same as true parameters.

of T2K, given in parentheses in table (5.2), to understand the role of broadband beam and enhanced matter effect. It is seen from the last column that for T2K the χ^2 reduces with increasing antineutrinos as is expected. Note that this is in contrast to DUNE due to its broadband nature and enhanced matter effect.

- **IH-LO** ($\theta_{23} = 39^\circ$): In this case for LHP the antineutrino run enhances the sensitivity because they do not suffer from octant degeneracy as can be seen from table 5.1. But for the UHP the antineutrino probability has octant degeneracy. Thus again we expect that in UHP adding antineutrino data should reduce the sensitivity. But the figure shows a slight enhancement. This can again be explained by similar reasoning as for the NH, 51° and -90° case. There is also the finite contribution from the disappearance channel enhancing the octant sensitivity when the neutrino and antineutrino runs are combined. These combinations of hierarchy–octant can resolve octant degeneracy at 5σ C.L. with [5+5] years of $[\nu + \bar{\nu}]$ run for any value of true δ_{CP} as shown in figure (5.2).

- **IH-HO** ($\theta_{23} = 51^\circ$) : For this case, for δ_{CP} in LHP the octant sensitivity with pure neutrino run is seen to be above $\chi^2 = 9$ in the interval $-180^\circ < \delta_{CP} < -45^\circ$. Adding antineutrino data helps to raise the χ^2 for octant sensitivity. As before we ask the question how antineutrino data is helpful despite the presence of degeneracies in this channel. This can be explained again similar to the NH-HO case. The third panel of figure (5.4) shows that for pure antineutrinos, there is very small octant sensitivity and the minima comes in the UHP between 90° and 135° . However at the point, in the LHP, where the pure neutrino χ^2 is minimum, antineutrino χ^2 has a large non-zero value and for combined runs the minima is still governed by the neutrinos. Thus the contributions from the antineutrinos are also being added up in spite of having degeneracy. The neutrino and antineutrino contributions from the appearance channel are shown in table 5.2. It is seen that for IH, because of the enhancement of the antineutrino probability due to matter effect, a large octant sensitive contribution to the χ^2 is obtained. The disappearance channel also gives a small contribution but the contribution from the antineutrino channel is almost comparable or larger than the neutrino channel. It is also to be noted that if hierarchy is not known then for some values of δ_{CP} the minima comes in the wrong hierarchy region for pure neutrino run and the sensitivity is further reduced. Addition of antineutrinos resolves the hierarchy with $\chi^2 \geq 25$ and so the minima does not occur anymore for wrong hierarchy solution. For the UHP, only neutrino run has very poor sensitivity due to degeneracies with δ_{CP} and addition of antineutrino runs help. The UHP is more favourable for resolution of hierarchy- δ_{CP} degeneracy and even with only neutrino run hierarchy is resolved at 3σ for all values of δ_{CP} . Overall a sensitivity, close to $\chi^2 = 25$ is achieved for this combination of hierarchy and θ_{23} with 7+3 or 5+5 combination for the whole range of δ_{CP} . For this case also in table 5.2, the T2K χ^2 values are given in parentheses. It is seen from the last column that the overall χ^2 for T2K decreases with enhanced antineutrinos unlike that in DUNE. If one compares the appearance χ^2 values for the antineutrino channel for DUNE and T2K then it is seen that the contribution of this channel for DUNE is quite high and comparable or even greater than the neutrino contribution. This

is due to the enhanced matter effect associated with IH and HO for the longer baseline of DUNE.

After discussing the role of antineutrinos and disappearance channel in octant sensitivity for DUNE, in figure (5.5) we present the octant χ^2 as a function of true θ_{23} for maximal CPV. Depending on if the true hierarchy is NH or IH and true δ_{CP} is $\pm 90^\circ$ we get

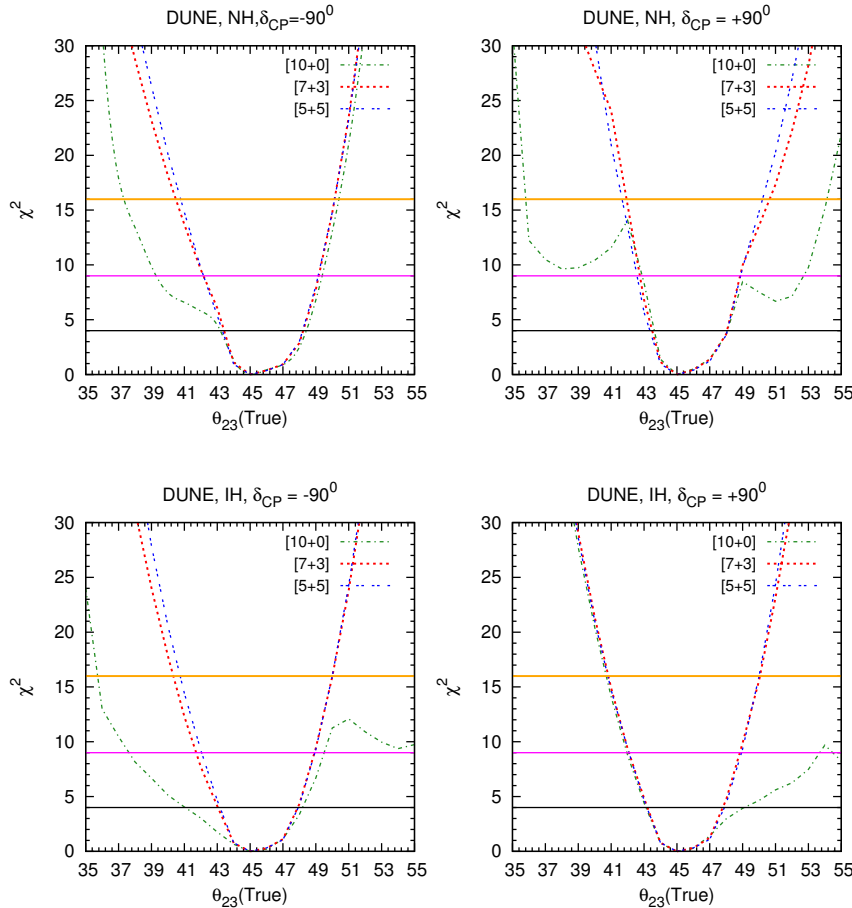


Figure 5.5: Octant sensitivity χ^2 for DUNE. Left (right) panel is for $\delta_{CP} = -90^\circ (+90^\circ)$, where true hierarchy is considered as NH(IH) for upper(lower) row. Here black, magenta and yellow lines represent χ^2 value at 2σ , 3σ and 4σ respectively.

4 possible combinations. From these figures one can read off the range of θ_{23} for which octant can be determined for $\delta_{CP} = \pm 90^\circ$ at a specified C.L. We see for all the four cases of figure (5.5) that with 7+3 years of $(\nu + \bar{\nu})$ run octant can be determined at 3σ (4σ) for $\delta_{CP} = \pm 90^\circ$ excepting for the range $41.5^\circ < \theta_{23} < 49^\circ$ ($40.5^\circ < \theta_{23} < 50.7^\circ$). From the figures we also see that 7+3 and 5+5 combinations give almost same sensitivity. However for the pure neutrino run the ranges are different and also vary depending

on the true values of δ_{CP} and hierarchy.

So far we have focused on the cases for which either true θ_{23} was fixed or true δ_{CP} was fixed. In figure (5.6) we give the 3σ exclusion plots in true($\theta_{23} - \delta_{CP}$) plane. We consider all possible true values of δ_{CP} from $(-180^\circ$ to $+180^\circ)$ and θ_{23} in lower

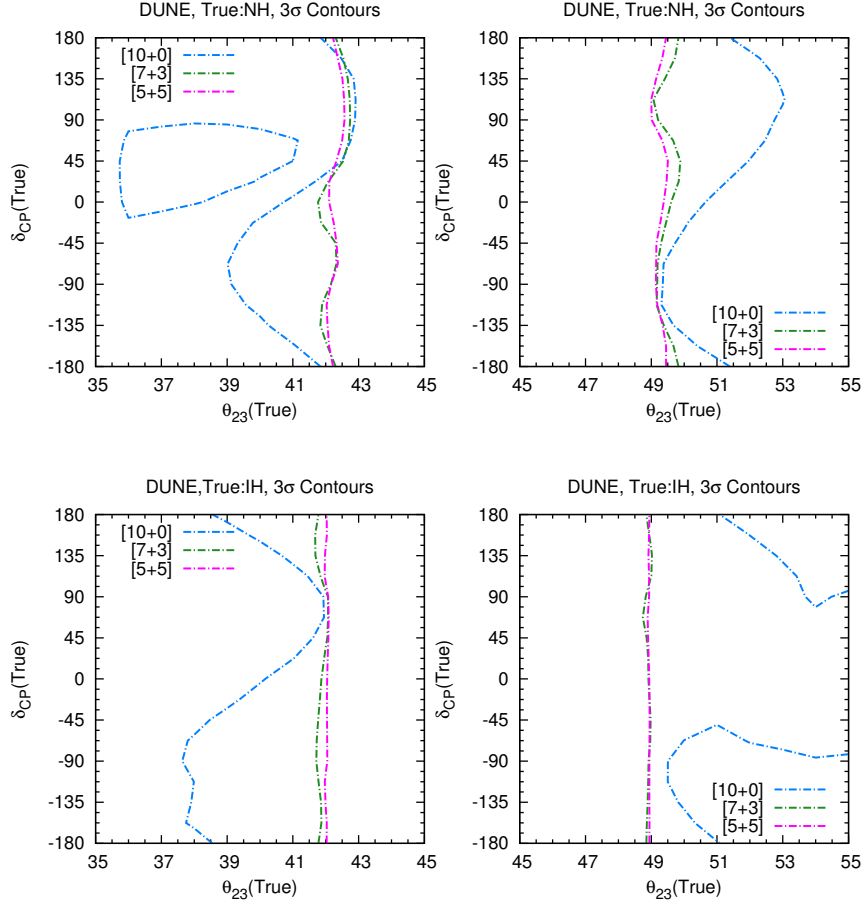


Figure 5.6: Contour plots in true $\theta_{23} \times \delta_{CP}$ -plane, here true hierarchy is NH (IH) for upper (lower) row and left(right) panel is for LO (HO). Marginalization over hierarchy is done. The allowed regions are to the right (left) side of the contours in the left (right) panel.

octant from $35^\circ - 45^\circ$ and higher octant from $45^\circ - 55^\circ$. This figure shows the role of antineutrino run in the full range of allowed δ_{CP} and θ_{23} parameter space. The allowed region for the left (right) panel is the R.H.S (L.H.S) of each curve of the true($\theta_{23} - \delta_{CP}$) plane [‡]. We observe by comparing the left and the right panels that DUNE can provide better constraints on θ_{23} parameter space in case of LO as compared to HO. For NH-LO the antineutrino run is necessary for the LHP and part of UHP. Only in the range $90^\circ <$

[‡] For NH-LO, DUNE[10+0] (top left panel of figure (5.6), the area enclosed by the blue curve also corresponds to the allowed region.

$\delta_{CP} < 135^\circ$ the only neutrino run i.e., the [10+0] configuration gives a slightly better sensitivity. On the other hand for NH-HO the antineutrinos play a more prominent role for δ_{CP} in the UHP. For IH-LO the antineutrino run is again important apart from near $\delta_{CP} \sim 90^\circ$, for which the improvement in sensitivity by adding antineutrinos is not very significant. For IH-HO the antineutrinos play important role in the full parameter space. Also the exclusion plots show that if true θ_{23} lies between $(43^\circ - 49^\circ)$ then it is not possible to resolve octant degeneracy at 3σ C.L. by DUNE using 10 kt detector. Overall one can say that antineutrino runs are necessary for most of the parameter region and 7+3 and 5+5 give similar sensitivities. Note that in the context of LBNO 75% - 25% ($\nu - \bar{\nu}$) was recommended in [239].

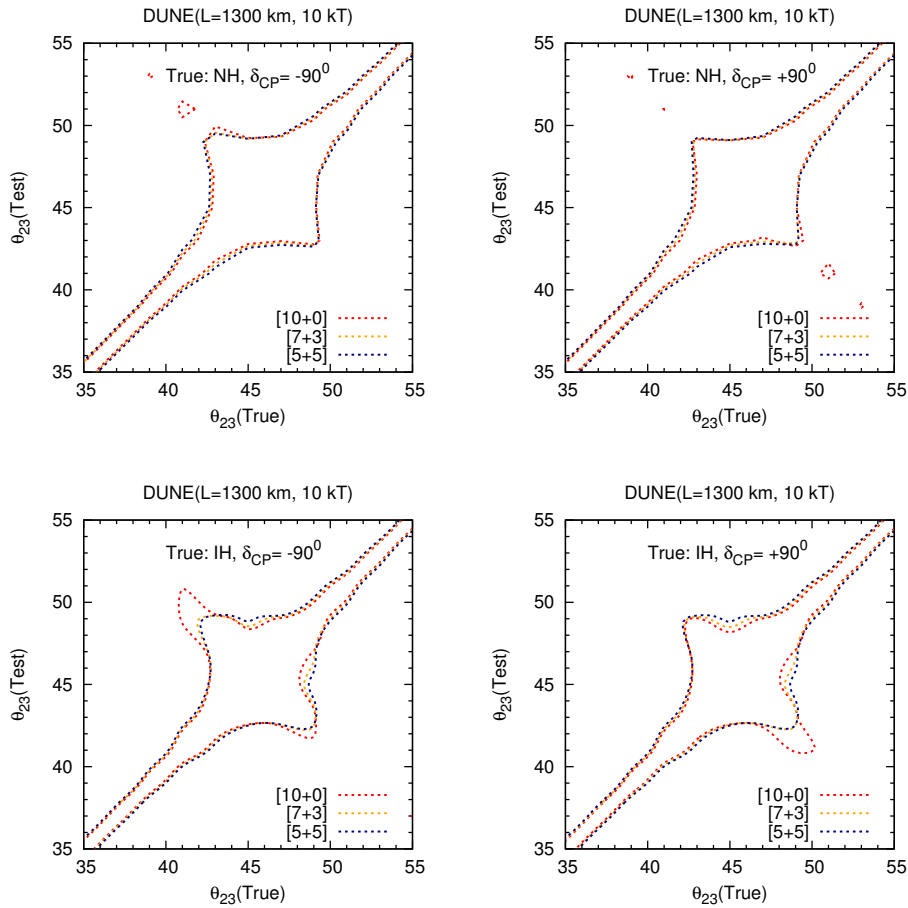


Figure 5.7: θ_{23} precision plots of DUNE in True (θ_{23}) - Test (θ_{23}) plane at 3σ (99.73%) C. L. Here top (bottom) row is for NH (IH).

Finally, in figure (5.7), we plot the 3σ precision contours in the true θ_{23} -test θ_{23} plane for $\delta_{CP} = \pm 90^\circ$. These figures reflect the relation between octant degeneracy

and precision of θ_{23} . The upper panels are for normal hierarchy and the lower panels are for inverted hierarchy. From these plots we see that for pure neutrino run there are other allowed values of θ_{23} apart from the true value, if $\theta_{23} \in \text{LO (HO)}$ at $\delta_{CP} = -90^\circ(+90^\circ)$. This happens because of the octant degeneracy. As we have already seen, for $\delta_{CP} = -90^\circ(+90^\circ)$, neutrinos suffer from octant degeneracy in LO (HO) in both the hierarchies and this in turn affects the precision of θ_{23} which is clearly seen from the figures. Adding antineutrinos help to improve the precision and both 7+3 and 5+5 give almost similar precision of θ_{23} . But as one approaches the maximal value of θ_{23} , the precision becomes worse due to the difficulty in determining the octant around those values of θ_{23} .

5.4.2 Antineutrinos, Octant Degeneracy and CPV discovery potential of DUNE

In this subsection we present the CPV discovery χ^2 of DUNE as a function of true δ_{CP} . CPV discovery potential of an experiment is defined by its capability of distinguishing a true value of δ_{CP} from the values 0° and 180° . We present these figures for the case where hierarchy and octant are assumed to be unknown and known respectively. The main aim of this section is to elucidate the role of antineutrinos in discovering δ_{CP} and the interconnection with the octant degeneracy. The figure (5.8) plots the CPV χ^2 , when hierarchy and octant are assumed to be unknown. From the different panels it is seen that:

- The $\bar{\nu}$ -runs play an important role for (i) LO near true $\delta_{CP} = -90^\circ$ and (ii) HO near true $\delta_{CP} = +90^\circ$. This is true for both NH and IH. Note from table 5.1 that these are the regions where neutrino probabilities exhibit octant degeneracy. Since antineutrino probabilities do not possess this degeneracy, addition of these helps in the removal of the degeneracy and enhancement of CP sensitivity.
- For true hierarchy as NH, $+90^\circ$ -LO and -90° -HO do not have octant degeneracy for neutrinos whereas antineutrinos have degeneracy (see table 5.1). Even then 7+3 gives almost same result as 10+0 notwithstanding the loss of statistics. In both cases this happens due to tension between the neutrino and antineutrino χ^2 s.

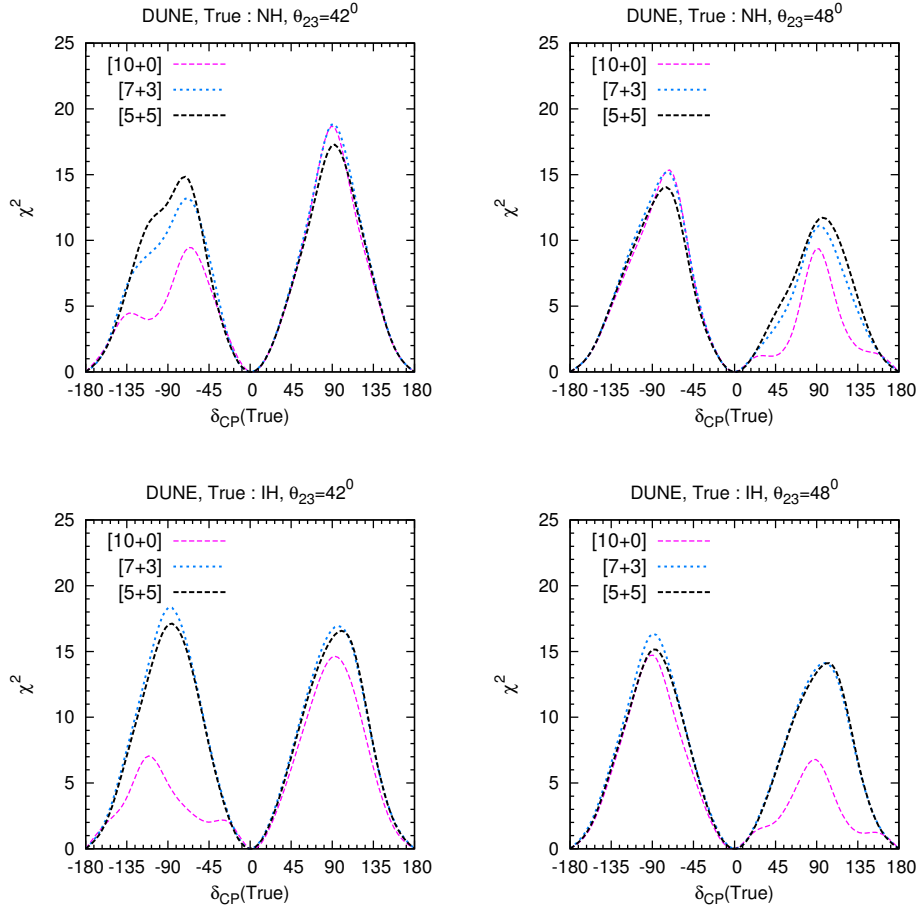


Figure 5.8: CPV χ^2 for DUNE when hierarchy and octant are unknown.

- For $+90^\circ$ -LO the minima for 10+0 comes at $\delta_{CP} = 180^\circ$ whereas replacing 3-years of ν run by $\bar{\nu}$ run shifts the χ^2_{min} at $\delta_{CP} = 0^\circ$ where the neutrino contribution is higher and thus 7+3 becomes comparable to 10+0.
- For the case of -90° -HO and neutrinos the CPV χ^2 is a falling function of θ_{13} , and the minima comes at 0.109 while for 7+3 it comes at 0.106. The neutrino contribution at $\sin^2 \theta_{13} = 0.106$ being higher the overall χ^2 for 7+3 becomes greater.
- Similarly, for true hierarchy IH, $+90^\circ$ -LO and -90° -HO are free from octant degeneracy for neutrinos. But still the CP sensitivity for these cases are slightly better for combined $\nu - \bar{\nu}$ run (for both 7+3 and 5+5 case) as compared to pure neutrino run. This happens because due to matter effects the $P_{\bar{\nu}\mu e}$ is higher than $P_{\nu\mu e}$ for IH (see Fig. 5.1). Thus addition of antineutrinos enhances the appearance χ^2 .

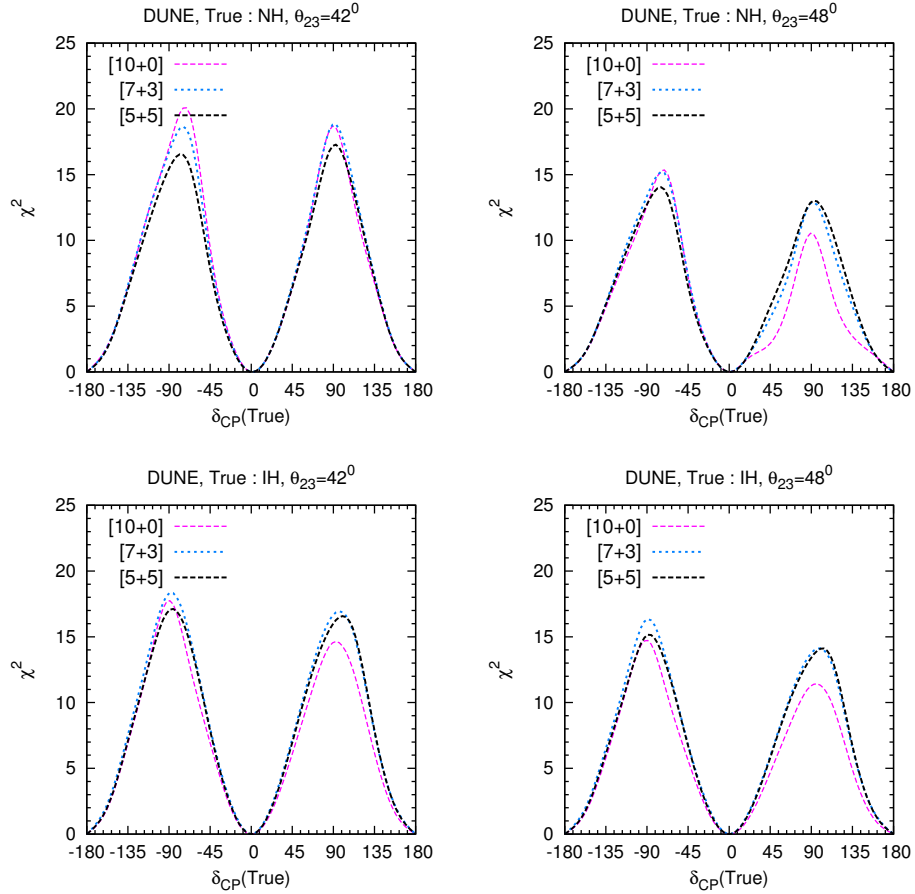


Figure 5.9: CPV χ^2 for DUNE when hierarchy and octant are known.

In figure (5.9), we present the same plots as that of figure (5.8) but assuming the hierarchy and octant to be known.

- Comparing with the plots in figure (5.8) we see that the CP sensitivity for -90° -LO is better for the 10+0 case, for both the hierarchies. In fact for -90° -LO-NH, 10+0 gives the best sensitivity if the octant is known. This establishes the fact that, the antineutrino run was instrumental for removing the wrong octant solutions.
- For $+90^\circ$ -NH-HO although there is some improvement for the 10+0 case as compared to the case of unknown octant, the CP sensitivity of 7+3 and 5+5 are still better than 10+0. This implies that though octant is known, antineutrinos play some role in enhancing the CP sensitivity.

5.4.3 Percentage of antineutrino run

In this subsection, we discuss what antineutrino fraction can give maximum CPV discovery. In the first and second panels of figure (5.10), we plot the percentage of $\bar{\nu}$ run vs percentage of δ_{CP} values for which CP violation can be discovered at 3σ C.L. in DUNE for four cases encompassing both hierarchies and octants. The first (second) panel represent when octant and hierarchy are known (unknown). From both plots it is seen that with dominant $\bar{\nu}$ or ν run a lesser CP fraction is reached. Overall 40% antineutrino run seems to be optimum in all cases. Comparing these two plots it is seen that when octant is known then greater percentage of CP fraction can be probed with less antineutrino component. The maximum CP coverage can be achieved for IH-HO and minimum for NH-HO.

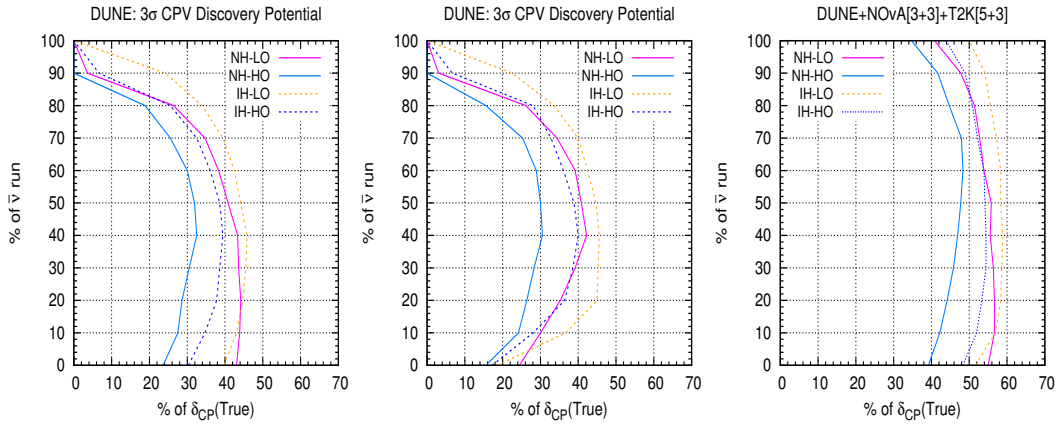


Figure 5.10: CPV discovery χ^2 at 3σ C.L. in $(\% \text{ of } \delta_{CP}(True), \% \text{ of } \bar{\nu}\text{-run})$ plane. Here, y-axis represents the $\% \text{ of } \bar{\nu}\text{-run}$ out of total 10 years of $[\nu + \bar{\nu}]$ run in DUNE.

In the third panel of figure (5.10) the same is plotted by combining $\text{NO}\nu\text{A}$ and T2K with DUNE. From the figure we can see that the percentage of δ_{CP} that can be probed is enhanced in all cases. The curves are now much flatter implying that even with pure neutrino or antineutrino runs considerable CP coverage can be obtained. This is due to the contribution from $\text{NO}\nu\text{A}$ and T2K. In figure (5.11) we show the dependence of percentage of δ_{CP} that can be probed as a function θ_{23} . This figure is drawn assuming 60% ν and 40% $\bar{\nu}$ -run which is the optimal configuration as seen in figure (5.10). The coverage of δ_{CP} for which CPV can be discovered at 3σ C.L. is better for IH. For NH specially close to 45° the coverage is less due to the poor precision of θ_{23} as discussed

earlier.

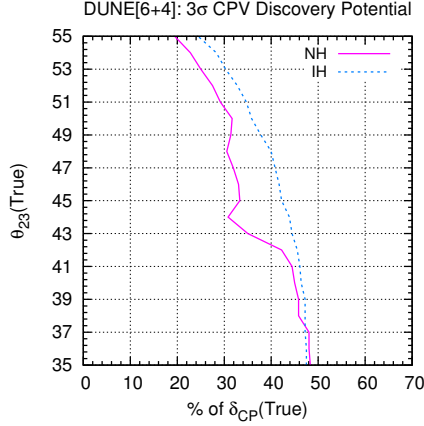


Figure 5.11: CPV discovery χ^2 at 3σ C.L. for DUNE[6+4] for all true θ_{23} when hierarchy and octant are unknown.

5.5 Summary

In this chapter we perform a detailed investigation of the octant and δ_{CP} sensitivity of the future generation superbeam experiment DUNE. We analyze in detail the physics of the antineutrinos for the DUNE baseline and what kind of synergy can be offered by the addition of antineutrinos to pure neutrino runs. We find that for the DUNE baseline the addition of antineutrinos are helpful in general. This statement holds true even when there may be some degeneracy associated with the antineutrino channel and one expects the pure neutrino run to give the best results. This occurs because of opposing tendencies of neutrino and antineutrino χ^2 s.

We consider two representative values of $\theta_{23} = 39^\circ, 51^\circ$ to study the behaviour of χ^2 with δ_{CP} for both the hierarchies. We find that although for some δ_{CP} values $(3-4)\sigma$ sensitivity can be achieved with only neutrino runs, overall adding antineutrinos is helpful. For a 7+3 year ($\nu + \bar{\nu}$) run, close to 4σ sensitivity can be achieved over all values of δ_{CP} . It is found that 7+3 and 5+5 runs do not give significantly different results. We compute the χ^2 as a function of true θ_{23} for maximum CPV. From this study we find that with 7+3 years option octant degeneracy can be resolved at 3σ for all the values of θ_{23} excepting the range $41.5^\circ < \theta_{23} < 49^\circ$. Increasing the antineutrino component and making runtime 5+5 does not make any discernible difference to the results. Finally we also study the octant sensitivity in the true($\theta_{23} - \delta_{CP}$) plane which checks the validity of the conclusions drawn earlier over the whole parameter

range. We find that including antineutrino runs, octant sensitivity can be obtained at 3σ excepting the range $43^\circ < \theta_{23} < 49^\circ$ over the whole range δ_{CP} . In this case with only the neutrino runs octant remains undetermined over a larger parameter space. We also present the 3σ precision contours in the true θ_{23} -test θ_{23} plane. These plots show that adding antineutrino runs also help in obtaining improved precision on θ_{23} .

We illustrate the results on the CPV discovery potential of DUNE emphasizing the role played by the antineutrinos. The CP sensitivity of any long-baseline experiment is affected by the occurrence of the wrong-hierarchy wrong-octant wrong- δ_{CP} solutions. Since the antineutrinos help in removing these solutions, one of the main role of the antineutrinos in enhancing CP sensitivity is to remove these wrong solutions. We present results for cases where hierarchy and octant are unknown and known and compare the role of the antineutrinos in both situations. We find that when octant is not known then in parameter spaces where octant degeneracy is manifest the antineutrino component increases CP sensitivity by removing wrong octant solutions. This is the case for instance for LO, $\delta_{CP} \sim -90^\circ$ and HO, $\delta_{CP} \sim +90^\circ$ for both hierarchies. However even when the octant is known the addition of antineutrinos can improve the result because of the tension between the two χ^2 s which raises the overall χ^2 . The contribution from the antineutrino channel is higher for IH since due to matter effects the antineutrino probability is higher than the corresponding neutrino probability. We have also explored how the addition of antineutrinos affects the fraction of δ_{CP} values for which CP sensitivity can be probed at the 3σ level. We find that when the octant is known, the same sensitivity can be achieved with a lesser fraction of antineutrinos for both hierarchies. The maximum CP fraction is achieved for IH-LO. Overall the best result comes with 60% neutrino and 40% antineutrino runs for all the four cases.

In this chapter, we have explored the role of antineutrinos in enhancing octant and CP sensitivity for DUNE experiment. We emphasize on the importance of antineutrino runs in resolving octant degeneracy and increasing CP sensitivity. Although for some specific parameters only neutrinos run can give 3σ octant sensitivity for a 10 kton detector mass of DUNE, overall a balanced neutrino-antineutrino run gives a better sensitivity. For the case of δ_{CP} discovery also, in most of the parameter space, antineutrinos play an important role due to synergistic effects between neutrinos and antineutrinos even under the assumption that the octant is known.

Chapter 6

Flavor Antisymmetry in Neutrinos

*“Science is a perception of the world around us.
Science is a place where what you find in nature pleases you.”*

– S. Chandrasekhar

6.1 Introduction

Neutrino oscillations imply neutrinos have non-zero masses and mixing angles. Earlier chapters were devoted to the study of neutrino oscillations, the presence of degeneracies in neutrino oscillation parameters and their possible resolutions using various neutrino oscillation experiments. One also needs to construct theoretical frameworks which can describe the observed values of neutrino masses and mixing angles and predict the unknown ones. Flavor symmetries provide a concrete framework to do this. In this chapter, we illustrate a framework based on flavor antisymmetry from the theoretical point of view to understand the neutrino mixing patterns. A systematic approach based on flavor symmetries has evolved in last several years, see reviews [240–244] and references therein. This is based on the observation that patterns of neutrino masses and mixing is intimately linked to the residual symmetries of the neutrino and the charged lepton mass matrices [245–247]. These residual symmetries of mass matrices can be related to the full symmetry G_f of the underlying theory by assuming that the former symmetries are contained in G_f . This provides a direct link between the group theoretical structure of G_f and the observed mixing angles. This approach has been used to predict various mixing patterns consistent with observations in large number

of cases with many different discrete symmetry groups G_f [240–244, 248].

In the *symmetry* approach, the Majorana neutrino mass matrix M_ν and the charged lepton mass matrix M_l transform as

$$S_\nu^T M_\nu S_\nu = M_\nu, \quad (6.1.1)$$

$$T_l^\dagger M_l M_l^\dagger T_l = M_l M_l^\dagger, \quad (6.1.2)$$

where S_ν and T_l are the symmetry matrices correspond to M_ν and $M_l M_l^\dagger$ respectively contained in G_f . The matrices diagonalizing this symmetry matrices can be related to the mixing matrices in each sector.

The above approach is also generalized to link both the mass and the mixing patterns of neutrinos to some underlying symmetries. Three possible neutrino mass patterns provide a good zeroth order approximation to the observed neutrino mass spectrum, fully degenerate spectrum, quasi degenerate spectrum with two degenerate neutrinos and a spectrum with two massive and one massless neutrinos. A systematic procedure is evolved to relate these patterns to underlying discrete symmetries. A general analysis is presented for three classes of groups, the discrete von-Dyck groups in the case of the degenerate and quasi degenerate spectrum [249], all possible discrete subgroups of $SU(3)$ having 3 dimensional irreducible representation in case of the quasi degenerate neutrinos [250] and a large class of discrete subgroups of $U(3)$ in case of one massless neutrino [251–253].

The basic assumption in the above approaches is that the underlying theory is invariant under some discrete group G_f but the Higgs vacuum expectation value (vev) determining neutrino mass matrix M_ν and the Hermitian combination of the charged lepton mass matrix $M_l M_l^\dagger$ remain invariant under smaller subgroups G_ν and G_l of G_f . The structure of these groups and their embedding in G_f is sufficient for the determination of mixing patterns without the knowledge of the detailed dynamics. A different dynamical possibility is studied in Ref. [254]. Here it is assumed that the Higgs vacuum expectation values breaking flavor group G_f lead to a neutrino mass matrix which displays *antisymmetry*. Specifically, M_ν satisfies

$$S_\nu^T M_\nu S_\nu = -M_\nu, \quad (6.1.3)$$

for some subgroups S_ν of G_f . This assumption was shown in Ref. [254] to constrain

not just the mixing angles but also the neutrino mass spectrum which could be determined purely from the group theoretical arguments. Detailed mixing and mass patterns allowed within the discrete subgroups $\Delta(3N^2)$ and $\Delta(6N^2)$ and a specific dynamical realization of the basic idea in case of the group $A_4 \equiv \Delta(3.2^2)$ was discussed in Ref. [254]. Also it was shown in a specific example that the antisymmetry of the mass matrix can arise from the minimization of some suitable potential. In the present chapter, we pursue this idea further and apply it to the symmetry group A_5 . We discuss the mass patterns and all the mixing patterns possible within A_5 using the idea of flavor antisymmetry of the neutrino mass matrix. A_5 has been used in the past [255–257, 257–261] to predict the neutrino mixing patterns assuming flavor symmetry. The mixing patterns predicted here are quite different compared to these cases.

A detailed analysis of A_5 also becomes interesting from a related point of view. It was shown [262] that all the discrete subgroups of $O(3)$ can lead to a universal prediction of $\theta_{23} = \frac{\pi}{4}$ and $|\delta| = \frac{\pi}{2}$ when G_ν is chosen as $Z_2 \times Z_2$ or Z_m and G_l is chosen as Z_n , $m, n \geq 3$. As we will see, the same predictions also follow when neutrino mass matrix possesses residual antisymmetry instead of symmetry.

The plan of the present chapter goes as : in next section (6.2), we demonstrate the steps which relate mixing angles with symmetry groups. In section (6.3), we discuss some of the properties of the group A_5 relevant for our study. We introduce the idea of flavor antisymmetry in section (6.4) and discuss its consequences. Section (6.5) is devoted to a detailed discussion of various mixing patterns possible within the group A_5 under the assumption of the flavor antisymmetry. Section (6.6) discusses explicit realization of the ideas discussed in the previous section. The last section (6.7) summarizes the findings.

6.2 Relating Mixing Angles with Symmetry Groups

In this section we demonstrate the steps used in relating mixing angles to symmetry groups G [245–247, 263–266]. Let U_ν and U_l diagonalize the Majorana neutrino mass

matrix M_ν and the charged lepton mass matrix M_l respectively be defined as

$$U_\nu^T M_\nu U_\nu = \text{diag}(m_{\nu_1}, m_{\nu_2}, m_{\nu_3}), \quad (6.2.1)$$

$$U_l^\dagger M_l M_l^\dagger U_l = \text{diag}(m_e^2, m_\mu^2, m_\tau^2). \quad (6.2.2)$$

Assume that M_ν ($M_l M_l^\dagger$) is invariant under some set of discrete symmetries S_ν (T_l):

$$S_\nu^T M_\nu S_\nu = M_\nu \quad \text{and} \quad T_l^\dagger M_l M_l^\dagger T_l = M_l M_l^\dagger, \quad (6.2.3)$$

where S_ν and T_l are the 3-dimensional representations of elements of some symmetry group G_f . Also it is assumed that elements within S_ν and T_l commute among themselves. Let, V_ν, V_l be unitary matrices which diagonalize S_ν and T_l as :

$$V_\nu^\dagger S_\nu V_\nu = D_S \quad \text{and} \quad V_l^\dagger T_l V_l = D_T, \quad (6.2.4)$$

where D_S and D_T correspond to diagonal matrices. Eqs. (6.2.1, 6.2.3, 6.2.4) can be used to show that [245–247, 263–266]

$$U_\nu = V_\nu P_\nu \quad \text{and} \quad U_l = V_l P_l, \quad (6.2.5)$$

where $P_{l,\nu}$ are the diagonal phase matrices. Therefore, one can write:

$$U \equiv U_{PMNS} = U_l^\dagger U_\nu = P_l^* V_l^\dagger V_\nu P_\nu. \quad (6.2.6)$$

The structure of the matrices $V_{l,\nu}$ is thus determined by group theory. The equation (6.2.6) provides a direct link between the mixing angles with the group symmetries.

6.3 A_5 and Its Abelian Subgroups

Group theory of A_5 is discussed in several papers [255–257, 257, 258, 267]. We summarize here the features which we require for subsequent analysis. The A_5 group has 60-elements and 5-conjugacy classes. The group can be represented in terms of three generators H, E, f_1 ,

$$H = \frac{1}{2} \begin{bmatrix} -1 & \mu_- & \mu_+ \\ \mu_- & \mu_+ & -1 \\ \mu_+ & -1 & \mu_- \end{bmatrix}; \quad E = \begin{bmatrix} 0 & 1 & 0 \\ 0 & 0 & 1 \\ 1 & 0 & 0 \end{bmatrix}; \quad f_1 = \begin{bmatrix} 1 & 0 & 0 \\ 0 & -1 & 0 \\ 0 & 0 & -1 \end{bmatrix}, \quad (6.3.1)$$

with $\mu_{\pm} = (-1 \pm \sqrt{5})/2$ which provides a *faithful* 3-dimensional irreducible representation*. The above equation defines the basis of the representation labeled as 3_1 and we will refer to this basis as symmetry basis. Multiple products of these generate all the sixty elements of A_5 . It is convenient for our purpose to discuss these elements in terms of the Z_n subgroups they form. We list them and their required properties below.

- Z_2 : 15 Z_2 subgroups of A_5 are generated by the elements:

$$O_2 \equiv (f_a, H, f_a H f_a, E H E^{-1}, E^{-1} H E, E f_a H f_a E^{-1}, E^{-1} f_a H f_a E), \quad (6.3.2)$$

where $a = 1, 2, 3$, $f_2 = E^2 f_1 E$, $f_3 = E^2 f_2 E$ and f_1 is given by equation (6.3.1). One also needs the matrices which diagonalize the elements in O_2 when Z_2 is used as a residual symmetry. These get determined by a matrix V_H which diagonalizes H . Let V_H be such matrix then

$$V_H^\dagger H V_H = \text{diag}(1, -1, -1). \quad (6.3.3)$$

Explicitly,

$$V_H = \begin{pmatrix} \frac{1}{2} & -\frac{\sqrt{3}}{2} & 0 \\ \frac{\mu_-}{2} & \frac{\mu_-}{2\sqrt{3}} & \frac{\mu_+}{\sqrt{3}} \\ \frac{\mu_+}{2} & \frac{\mu_+}{2\sqrt{3}} & -\frac{\mu_-}{\sqrt{3}} \end{pmatrix}. \quad (6.3.4)$$

The above V_H is arbitrary upto a unitary rotation in the 2-3 plane. We shall use the above explicit form for the subsequent analysis. We can express all the elements of A_5 in the form QPQ^{-1} . This simplifies their diagonalization since $U_{QPQ^{-1}} = QU_P$ where, U_g diagonalizes the element g . Using this, the matrices diagonalizing all the 15 elements in O_2 can be expressed in terms of V_H and are given by the following set

$$\mathcal{U}_2 \equiv (I, V_H, f_a V_H, E V_H, E^{-1} V_H, E f_a V_H, E^{-1} f_a V_H). \quad (6.3.5)$$

Respective entries of this set correspond to matrices which diagonalize the corresponding elements of O_2 .

*Note that ‘faithful’ means that the identity element is the only element whose trace will be ‘d’ for the d-dimensional representation.

- $Z_2 \times Z_2$: Not all the fifteen elements in O_2 commute among themselves. But one can find five sets of three commuting elements among O_2 . These three along with identity form a $Z_2 \times Z_2$ subgroup of A_5 . These subgroups are listed in Table 6.1. Since S_1 and S_2 in the table commute, they can be simultaneously

S_1	S_2	S_3	U_c
f_1	f_3	f_2	I
H	$E^{-1}f_2 H f_2 E$	$E f_3 H f_3 E^{-1}$	$V_H R_\mu$
$f_1 H f_1$	$E^{-1}f_1 H f_1 E$	$E f_1 H f_1 E^{-1}$	$f_1 V_H R_\mu$
$f_2 H f_2$	$E^{-1}f_3 H f_3 E$	$E H E^{-1}$	$f_2 V_H R_\mu$
$f_3 H f_3$	$E^{-1} H E$	$E f_2 H f_2 E^{-1}$	$f_3 V_H R_\mu$

Table 6.1: Elements of the five $Z_2 \times Z_2$ subgroups of A_5 along with their combined diagonalizing matrices U_c defined in the text. S_1, S_2, S_3 together with identity form a $Z_2 \times Z_2$ subgroup of A_5 .

diagonalized by a matrix U_c . We shall define U_c as

$$\begin{aligned} U_c^\dagger S_1 U_c &= f_1 = \text{diag}(1, -1, -1), \\ U_c^\dagger S_2 U_c &= f_3 = \text{diag}(-1, -1, 1). \end{aligned} \quad (6.3.6)$$

The same matrix U_c also puts $S_3 = S_1 S_2$ into a diagonal form f_2 . As before, the matrix U_c can also be expressed in terms of V_H diagonalizing H and a real rotation R_μ in the 23 plane

$$R_\mu = \begin{pmatrix} 1 & 0 & 0 \\ 0 & -\sin \theta_\mu & \cos \theta_\mu \\ 0 & \cos \theta_\mu & \sin \theta_\mu \end{pmatrix}, \quad (6.3.7)$$

where $\tan \theta_\mu = \mu_- - 1$. U_c for all five subgroups are given in table 6.1.

- Z_3 subgroups: The 20 elements generating Z_3 subgroups of A_5 are given by the set

$$O_3 = (E^m, f_a E^m f_a, A^m, E A^m E^{-1}, E^{-1} A^m E, A E^m A^{-1}, A f_{2,3} E^m f_{2,3} A^{-1}). \quad (6.3.8)$$

$m = 1, 2, a = 1, 2, 3$ and the matrix $A \equiv Hf_1$. The matrices diagonalizing these elements can be expressed in terms of the matrices U_ω and U_A which diagonalize E and A respectively:

$$\mathcal{U}_3 = (U_\omega, f_a U_\omega, U_A, EU_A, E^{-1}U_A, AU_\omega, Af_{2,3}U_\omega). \quad (6.3.9)$$

U_ω is given by

$$U_\omega = \frac{1}{\sqrt{3}} \begin{pmatrix} 1 & 1 & 1 \\ 1 & \omega & \omega^2 \\ 1 & \omega^2 & \omega \end{pmatrix}, \quad (6.3.10)$$

$\omega = e^{\frac{2\pi i}{3}}$ and U_A can be found in the Appendix of the reference [262].

- Z_5 subgroups: There are 24 different Z_5 subgroups within A_5 . Their generating elements can be expressed in terms of $T \equiv f_1EH$, E and $f_{1,2,3}$ as follows:

$$\mathcal{O}_5 = (T^p, f_2T^p f_2, ET^p E^{-1}, E^{-1}T^p E, E f_2T^p f_2 E^{-1}, E^{-1} f_2T^p f_2 E), \quad (6.3.11)$$

where $p = 1, 2, 3, 4$. This set is diagonalized by

$$\mathcal{U}_5 = (U_T, f_2U_T, EU_T, E^{-1}U_T, E f_2U_T, E^{-1} f_2U_T), \quad (6.3.12)$$

where U_T is a matrix diagonalizing T . Its explicit form is given in the Appendix of [262].

The elements in the sets $\mathcal{O}_{2,3,5}$ along with the identity constitute all the sixty elements of A_5 . We note that all the matrices diagonalizing set \mathcal{O}_3 and \mathcal{O}_5 possess the following general form as explicitly shown in Ref. [262].

$$U = \begin{pmatrix} x_1 & z_1 & z_1^* \\ x_2 & z_2 & z_2^* \\ x_3 & z_3 & z_3^* \end{pmatrix}, \quad (6.3.13)$$

where x_1, x_2, x_3 are real. We shall use this form to derive properties of the mixing matrix in the following.

6.4 Flavor Antisymmetry and Neutrino Mass Textures

We first briefly review the implications of the assumption of the flavor antisymmetry [254] represented by equation (6.1.3) where S_ν is assumed to be any 3×3 matrix belonging to a discrete subgroup of $SU(3)$. The very assumption of flavor antisymmetry implies that (at least) one of the neutrinos remains massless. This simply follows by taking the determinant of equation (6.1.3) and noting that $\text{Det}(S_\nu) = 1$. Other implications of equation (6.1.3) become clear in a basis with diagonal S_ν . Let S_ν be diagonalized by a unitary matrix V_{S_ν} as :

$$V_{S_\nu}^\dagger S_\nu V_{S_\nu} = D_S \equiv \text{diag}(\lambda_1, \lambda_2, \lambda_3), \quad (6.4.1)$$

with $\lambda_1 \lambda_2 \lambda_3 = 1$. Unitarity of S_ν implies that $\lambda_{1,2,3}$ are some roots of unity. It was argued [254] that only two possible forms of D_S can lead to a neutrino mass matrix with two massive neutrinos. These are given by

$$\begin{aligned} D_{1S} &= \text{diag}(\lambda, -\lambda^*, -1), \\ D_{2S} &= \text{diag}(\pm i, \mp i, 1), \end{aligned} \quad (6.4.2)$$

and their permutations. $\lambda^{2p} = 1$ for some integer p [†]. The group generated by the residual symmetry S_ν having diagonal form D_{1S} (D_{2S}) is Z_{2p} (Z_4). Define

$$\tilde{M}_\nu = V_{S_\nu}^T M_\nu V_{S_\nu}. \quad (6.4.3)$$

With this definition, equation (6.1.3) can be written as

$$(\tilde{M}_\nu)_{ij}(1 + \lambda_i \lambda_j) = 0 \quad (6.4.4)$$

where i, j are not summed.

Then the allowed textures of \tilde{M}_ν get determined by the allowed forms of D_S . There exists only four allowed textures for \tilde{M}_ν which correspond to one massless and a degenerate or non-degenerate pair of neutrinos. Equation (6.4.4) determines the forms of \tilde{M}_ν . Let us start the discussion by considering one of the off-diagonal terms of $\tilde{M}_\nu \neq 0$. In this case, we will have three possibilities,

[†]Note that equation (6.1.3) requires that $S_\nu^{2p} = 1$ if M_ν is not identically zero and S_ν has finite order. This translates to $\lambda^{2p} = 1$.

- For $\lambda = 1$, $D_{1S} = \text{diag}(1, -1, -1)$:

$$\tilde{M}_\nu = m_0 \begin{pmatrix} 0 & c_\nu & s_\nu e^{i\beta_\nu} \\ c_\nu & 0 & 0 \\ s_\nu e^{i\beta_\nu} & 0 & 0 \end{pmatrix}, \quad (6.4.5)$$

where $c_\nu = \cos \theta_\nu$, $s_\nu = \sin \theta_\nu$. This structure of \tilde{M}_ν describes a massless and a degenerate pair of neutrinos.

- For $\lambda = \pm i$, $D_{1S} = \text{diag}(\pm i, \pm i, -1)$:

$$\tilde{M}_\nu = \begin{pmatrix} x_1 & y & 0 \\ y & x_2 & 0 \\ 0 & 0 & 0 \end{pmatrix}, \quad (6.4.6)$$

This form of \tilde{M}_ν describes a massless and two non-degenerate pair of neutrinos.

- For $\lambda \neq \pm 1, \pm i$, $D_{1S} = \text{diag}(\lambda, -\lambda^*, -1)$:

$$\tilde{M}_\nu = m_0 \begin{pmatrix} 0 & 1 & 0 \\ 1 & 0 & 0 \\ 0 & 0 & 0 \end{pmatrix}, \quad (6.4.7)$$

This describes a massless and a degenerate pair of neutrinos[‡].

- Let us discuss the case by considering a diagonal terms of $\tilde{M}_\nu \neq 0$ (say $(\tilde{M}_\nu)_{11} \neq 0$). This implies $D_S = \text{diag}(\pm i, \tilde{\lambda}, \mp i\tilde{\lambda}^*)$ with $|\tilde{\lambda}| = 1$. We notice that the case with $\tilde{\lambda} = \pm i$ gives D_{1S} which is already discussed. $\tilde{\lambda} = \mp i$ implies the condition D_{2S} of equation (6.4.2). This gives a new structure,

For $\tilde{\lambda} = \mp i$, $D_S = \text{diag}(i, -i, 1)$:

$$\tilde{M}_\nu = m_0 \begin{pmatrix} x_1 & 0 & 0 \\ 0 & x_2 & 0 \\ 0 & 0 & 0 \end{pmatrix}, \quad (6.4.8)$$

This texture describes a massless and a non-degenerate pair of neutrinos.

For $\tilde{\lambda} = \pm 1$ one gets permutation of D_{1S} or D_{2S} whereas $\tilde{\lambda} \neq \pm 1, \pm i$ gives two massless neutrinos.

[‡]Note that we will have only these three forms of \tilde{M}_ν , permutation of the elements of D_{1S} will not give any new structures of \tilde{M}_ν .

Thus the condition given by equation (6.4.2) and its all possible permutations give all possible textures of \tilde{M}_ν which are consistent with flavor antisymmetry as given by equation (6.1.3). But in our study we observe that only the case given in equation (6.4.5) gets realized in A_5 .

6.4.1 The allowed residual symmetries in A_5

We now discuss possible residual symmetries of the leptonic mass matrices within A_5 and the resulting mixing patterns. The choices of residual antisymmetry of M_ν within A_5 are restricted. These can be obtained simply from the characters χ of all the sixty elements. χ is real for all the elements. In this case, the eigenvalues of any element are given by

$$\left(1, \frac{1}{2} \left(\chi - 1 + \sqrt{(\chi - 1)^2 - 4}\right), \frac{1}{2} \left(\chi - 1 - \sqrt{(\chi - 1)^2 - 4}\right)\right). \quad (6.4.9)$$

These eigenvalues must have the form displayed in one of the two equations given in (6.4.2) in order for an element with character χ to be able to be a viable antisymmetry operator. Elements belonging to Z_3 and Z_5 subgroups have $\chi = 0$ and $(-\mu_+, -\mu_-)$. Their eigenvalues following from above do not have these forms. Thus only viable choice for the antisymmetry operator S_ν can be any element in the set O_2 having character -1 and eigenvalues $(1, -1, -1)$. We shall require that at least one of the symmetries of M_ν acts according to equation (6.1.3). We will thus consider two possible choices of the residual neutrino symmetries (1) $S_\nu = Z_2$ as antisymmetry and (2) $S_\nu = Z_2 \times Z_2$ where one of the Z_2 transforms M_ν into it's negative and the other leaves it invariant. In contrast, the eigenvalues of the residual symmetry of $M_l M_l^\dagger$ is not restricted and we can take any of the Z_n of A_5 as the residual symmetry T_l . We shall consider the following choices for T_l (a) (Z_3, Z_5) groups generated by (O_3, O_5) (b) five $Z_2 \times Z_2$ subgroups or (c) elements of the Z_2 subgroups contained in O_2 . Possible choices of S_ν and T_l determine the leptonic mixing matrix.

Elements in O_2 when used as antisymmetry operator lead to a unique form for the neutrino mass matrix \tilde{M}_ν given in equation (6.4.5). This texture describes a pair of degenerate and one massless neutrino. Residual antisymmetry in this case is Z_2 . The

neutrino mass matrix in equation (6.4.5) can be diagonalized by a matrix V_ν :

$$V_\nu^T \tilde{M}_\nu V_\nu = \text{diag}(m_0, m_0, 0) \quad (6.4.10)$$

where,

$$V_\nu = \begin{pmatrix} \frac{1}{\sqrt{2}} & -\frac{i}{\sqrt{2}} & 0 \\ c_\nu & \frac{ic_\nu}{\sqrt{2}} & -s_\nu \\ \frac{s_\nu}{\sqrt{2}} e^{-i\beta_\nu} & \frac{is_\nu}{\sqrt{2}} e^{-i\beta_\nu} & c_\nu e^{-i\beta_\nu} \end{pmatrix} \begin{pmatrix} \cos \psi & -\sin \psi & 0 \\ \sin \psi & \cos \psi & 0 \\ 0 & 0 & 1 \end{pmatrix}. \quad (6.4.11)$$

The arbitrary rotation by an angle ψ originates due to degeneracy in masses. It follows from equations (6.4.3,6.4.10) that the matrix M_ν is diagonalized by the product $V_{S_\nu} V_\nu$. Thus the neutrino mixing matrix with the residual antisymmetry Z_2 in the symmetry basis is given by

$$U_\nu^I = V_{S_\nu} V_\nu. \quad (6.4.12)$$

Note that the U_ν^I gets determined by the structure of S_ν and essentially two unknown angles θ_ν and β_ν . The unknowns can be fixed if the residual symmetry is chosen as $Z_2 \times Z_2$. Consider the $Z_2 \times Z_2$ groups generated by $S_{1\nu} = S_1$ and $S_{2\nu} = S_2$ where S_1, S_2 are as in table 6.1. They satisfy

$$S_1^T M_\nu S_1 = -M_\nu \quad ; \quad S_2^T M_\nu S_2 = M_\nu. \quad (6.4.13)$$

As discussed in the previous section, both S_1 and S_2 are diagonalized by U_c as given in table 6.1. The structure of the neutrino mass matrix in this case becomes transparent in the basis with diagonal S_1, S_2 . Let

$$M'_\nu = U_c^T M_\nu U_c. \quad (6.4.14)$$

Equation (6.4.13) reduces in the prime basis to

$$f_1^T M'_\nu f_1 = -M'_\nu \quad , \quad f_3^T M'_\nu f_3 = M'_\nu. \quad (6.4.15)$$

The first of this equation implies the form (6.4.5) for M'_ν . The second imposed on this then leads to the restriction $s_\nu = 0, c_\nu = 1$. The final M'_ν is determined by an overall scale m_0 and is diagonalized by $U_{12} \equiv R_{12}(\frac{\pi}{4}) \text{diag}(1, i, 1)$. It follows from this and equation (6.4.14) that M_ν is diagonalized by

$$U_\nu^{II} = U_c U_{12} = U_c R_{12}(\frac{\pi}{4}) \text{diag}(1, i, 1). \quad (6.4.16)$$

The matrix U_l diagonalizing $M_l M_l^\dagger$ also gets determined by its symmetry. Assume that

$$T_l^\dagger M_l M_l^\dagger T_l = M_l M_l^\dagger . \quad (6.4.17)$$

This implies that T_l commutes with $M_l M_l^\dagger$. Hence the matrix U_{T_l} diagonalizing T_l can be taken to be the matrix which diagonalizes $M_l M_l^\dagger$ also. Three possible choices of T_l referred as (a),(b),(c) above lead to specific forms of U_l :

$$\begin{aligned} U_l^a &= U_{3,5} , \\ U_l^b &= U_c , \\ U_l^c &= U_2 U_{23} . \end{aligned} \quad (6.4.18)$$

Here, $U_{3,5}$ are given by any matrix in the set, \mathcal{U}_3 , equation (6.3.9) and \mathcal{U}_5 , equation (6.3.12) when T_l belongs to O_3 or O_5 respectively. U_c is given in Table 6.1 for T_l belonging to $Z_2 \times Z_2$. There is some arbitrariness in the choice of U_l when T_l is chosen as any of the element O_2 forming a Z_2 . These elements have eigenvalues $(1, -1, -1)$ and matrix diagonalizing T_l is arbitrary up to a unitary rotation in the 23 plane. This rotation can be taken without the loss of generality to $U_{23} \equiv \text{diag}(1, 1, e^{i\beta_l}) R_{23}(\theta_l)$. Various combinations of $U_l^{a,b,c}$ and $U_\nu^{I,II}$ give all possible $U \equiv U_l^\dagger U_\nu$ in A_5 .

6.5 Mixing Patterns in A_5

As discussed, all possible structure of the PMNS matrix U in A_5 with flavor antisymmetry are given by

$$U \sim U_l^{\dagger a,b,c} U_\nu^{I,II} . \quad (6.5.1)$$

Not all of these give viable mixing pattern for neutrinos as we will show. Before discussing individual choices, we first derive a fairly general property of the mixing matrix with flavor antisymmetry. If (a) the neutrino mass matrix shows flavor antisymmetry equation (6.1.3), with $S_\nu^2 = 1$ and a real mixing matrix V_ν or (b) if it has residual symmetry structure $Z_2 \times Z_2$ as in equation (6.4.13) and if the charged lepton matrix $M_l M_l^\dagger$ is invariant under a residual symmetry Z_3 or Z_5 within A_5 then the mixing matrix can be chosen to have the property

$$|U_{\mu i}| = |U_{\tau i}| , \quad (i = 1, 2, 3) . \quad (6.5.2)$$

This property known as the $\mu-\tau$ reflection symmetry [268] or generalized $\mu-\tau$ symmetry was derived [269] using a generalized definition of CP. The same result was derived from more general assumptions in case of the non-degenerate neutrinos [262, 270] as well as for a pair of degenerate neutrinos [249, 262]. The basic assumption in these cases was the existence of a real residual symmetry. The same result also follows when the symmetry is replaced by antisymmetry as we discuss below.

The equality $|U_{\mu 3}| = |U_{\tau 3}|$ implies atmospheric mixing angle to be maximal. The equality $|U_{\mu 2}| = |U_{\tau 2}|$ then leads to the maximal CP phase $|\delta| = \frac{\pi}{2}$ if neutrinos are non-degenerate and $s_{13} \neq 0$. For the degenerate solar pair, the first two columns of U depend on an unknown mixing angle ψ as given in equation (6.4.11). But by considering ψ invariant combination of the observables, it was argued [249] that one instead gets $|\delta - \kappa| = \frac{\pi}{2}$ where κ is the Majorana phase.

The proof of equation (6.5.2) is straightforward and follows the proof given in [262] in case of the flavor symmetry. Assume that neutrino mass matrix \tilde{M}_ν has the structure (6.4.5) with $\beta_\nu = 0$. Then it is diagonalized by $U_\nu^I = U_2 V_\nu$. Here U_2 belonging to the set \mathcal{U}_2 is real. For $\beta_\nu = 0$, one therefore gets $U_\nu^I = O_\nu P$, with O_ν being a real orthogonal matrix and $P = \text{diag.}(1, i, 1)$. A similar structure of U_ν also holds in case II with $Z_2 \times Z_2$ symmetry since in this case, the neutrino mixing matrix U_ν is given by U_ν^{II} , equation (6.4.16) which also can be written as an orthogonal matrix times a phase matrix because of the reality of U_c . The charged lepton mixing matrix on the other hand has a general structure specified by equation (6.3.13) when the residual charge lepton symmetry is either Z_3 or Z_5 . It is then easy to see that U_l as in equation (6.3.13) and U_ν as O_ν times a diagonal phase matrix leads to equation (6.5.2). This result does not follow when the residual symmetry of the charged leptons is Z_2 or $Z_2 \times Z_2$ since in this case U_l does not have the form given in equation (6.3.13).

Let us now discuss individual choices of residual symmetries and their viability or otherwise. We will work out various mixing patterns for different choices and confront them with the results of the global fits as given in [223, 271, 272]. For definiteness, we shall use the results given in [272]. The structures of $U^{I,II}$ appearing in equation (6.5.1) are determined only up to a rotation in the 12 plane and the solar angle remains undetermined at the leading order. The third column of U is however inde-

pendent of the unknown angle and can be predicted group theoretically at the zeroth order. We shall thus concentrate on the prediction of θ_{13} and θ_{23} determined by the third column of $|U|$. Also, the ordering of eigenvalues of T_l cannot be determined group theoretically. Change in this ordering permutes the rows of U . Thus any of the entries of the third column $|U_{i3}|$ may be identified with the physical mixing elements $|U_{\alpha 3}|$ ($\alpha = e, \mu, \tau$). In view of this, we shall consider different orderings which can give viable mixing patterns.

6.5.1 $S_\nu = Z_2$ and $T_l = Z_3$ or Z_5

There are 15 different choices of Z_2 and 20+24 choices of the $Z_3 + Z_5$ symmetry within A_5 . Specific forms of U_l and U_ν as discussed before can be used to obtain $|U_{i3}|$ in all these cases. They are determined by the unknown angles θ_ν and β_ν . While the dependence of $|U_{i3}|$ on these are different for different choices of residual symmetries all the choices share the following features

- If $\beta_\nu = 0$ then equation (6.3.13) holds for the specific ordering of eigenvectors of T_l as given in equation (6.5.2). The atmospheric mixing angle is predicted to be maximal for all the values of θ_ν . In this case, $|U_{e3}|$ is to be identified with the 13 element of $|U|$ since $|U_{23}| = |U_{33}|$. In all these cases, $|U_{e3}|$ depends on θ_ν which can be chosen to obtain the correct s_{13}^2 .
- If $\beta_\nu \neq 0$ then any of $|U_{i3}|$ can be identified with $|U_{e3}|$. It is possible in this case to choose two unknowns θ_ν and β_ν to obtain correct θ_{13} and θ_{23} . Let us discuss a specific example with $S_\nu = E^2 f_1 H f_1 E$ and $T_l = E$ as illustration. They respectively generate Z_2 antisymmetry in M_ν and Z_3 symmetry in $M_l M_l^\dagger$. The mixing matrix is given by $U = U_\omega^\dagger E^2 f_1 V_H V_\nu$ with V_H as in equation (6.3.4) and U_ω as in (6.3.10). The third column of the mixing matrix is then given by

$$\begin{aligned} |U_{13}|^2 &= \frac{1}{9} |c_\nu(1 + 2\mu_+) - s_\nu e^{i\beta_\nu}|^2, \\ |U_{23}|^2 &= \frac{1}{36} |-2c_\nu(1 - \omega\mu_+) + s_\nu e^{i\beta_\nu}(\mu_+ + 3\omega + \omega^2\mu_-)|^2, \\ |U_{33}|^2 &= \frac{1}{36} |-2c_\nu(1 - \omega^2\mu_+) + s_\nu e^{i\beta_\nu}(\mu_+ + 3\omega^2 + \omega\mu_-)|^2. \end{aligned} \quad (6.5.3)$$

For $\beta_\nu = 0$, one gets $|U_{23}|^2 = |U_{33}|^2$ in accordance with the general result

discussed above. In this case, identification of $|U_{13}|^2$ with $|U_{e3}|^2$ leads to the result $\theta_{23} = \frac{\pi}{4}$. $\theta_\nu = 0.959$ then leads to $s_{13}^2 \sim 0.024$. Any of $|U_{i3}|^2$ can be identified with $|U_{e3}|^2$ when β_ν is non-zero, e.g. the choice $\beta_\nu = -1.076, \theta_\nu = -0.801$ leads to $|U_{i3}|^2 = (0.444, 0.024, 0.532)$. In this case, $|U_{23}|^2$ plays the role of $|U_{e3}|^2$. This specific ordering in U can be obtained by exchanging the first and the second column of U_ω .

6.5.2 $S_\nu = Z_2 \times Z_2$ and $T_l = Z_3$ or Z_5

In this case, S_ν can be chosen in five different ways corresponding to five different $Z_2 \times Z_2$ subgroups. The corresponding neutrino mixing matrix U_ν is given by equation (6.4.16). As before T_l can be chosen in 44 different ways with U_l either in \mathcal{U}_3 or \mathcal{U}_5 . Unlike in the previous case, both U_ν and U_l get completely fixed group theoretically. This case also predicts the maximal atmospheric mixing angle as already outlined. Possible values of θ_{13} are also fixed. Explicit evaluation of various cases reveal that in all the cases one either gets $\theta_{13} = 0$ or $s_{13}^2 > 0.1$. The zero value for θ_{13} occurs for example when $S_1 = H, S_2 = E^2 f_2 H f_2 E$ and $T_l = f_3 E f_3$. One would require relatively large perturbations in this case to get θ_{13} within its 3σ range.

6.5.3 $S_\nu = Z_2 \times Z_2$ and $T_l = Z_2$

This case is characterized by completely determined $U_\nu = U_\nu^{II}$ and $U_l = U_l^c$ containing two unknowns θ_l, β_l . The explicit form of U_l^c is given in equation (6.4.18) while U_c can be any of the five forms given in table 6.1. U_l in this case does not have the general form given in equation (6.3.13). As a result, one does not obtain equation (6.5.2) corresponding to the μ - τ reflection symmetry and the atmospheric mixing angle is not predicted to be maximal. But this case has the following interesting feature. Explicit evaluation of $U = U_l^{c\dagger} U_\nu^{II}$ reveals that one of the entries in the third column of U is independent of the unknown angles θ_l, β_l and can be predicted group theoretically. The third column of the mixing matrix U in this case is given by

$$\begin{aligned} |U_{13}|^2 &= |(U_{T_l}^\dagger U_\nu^{II})_{13}|^2, \\ |U_{23}|^2 &= |c_l (U_{T_l}^\dagger U_\nu^{II})_{23} + s_l e^{-i\beta_l} (U_{T_l}^\dagger U_\nu^{II})_{33}|^2, \\ |U_{33}|^2 &= |-s_l (U_{T_l}^\dagger U_\nu^{II})_{23} + c_l e^{-i\beta_l} (U_{T_l}^\dagger U_\nu^{II})_{33}|^2 \end{aligned} \quad (6.5.4)$$

where T_l belongs to the set O_2 and U_{T_l} to \mathcal{U}_2 . We get interesting pattern when we identify T_l with $S_{1\nu} = S_1$ residing in $Z_2 \times Z_2$. There exists five such choices and in all these cases, the mixing matrix U is independent of the explicit form of U_{T_l} . One gets from equation (6.4.16) and equation (6.4.18)

$$U = U_{23}^\dagger R_\mu R_{12} \left(\frac{\pi}{4} \right) \text{diag.}(1, i, 1).$$

The neutrino mass matrix $M_{\nu f} \equiv U_l^T M_\nu U_l$ in the flavor basis has the following form in this case:

$$M_{\nu f} = m_0 \begin{pmatrix} 0 & e^{i\beta_l} c_\mu s_l - c_l s_\mu & e^{i\beta_l} c_l c_\mu + s_l s_\mu \\ e^{i\beta_l} c_\mu s_l - c_l s_\mu & 0 & 0 \\ e^{i\beta_l} c_l c_\mu + s_l s_\mu & 0 & 0 \end{pmatrix}, \quad (6.5.5)$$

where $c_l = \cos \theta_l$, $c_\mu = \cos \theta_\mu \dots$ etc. This form can be obtained by imposing $L_e - L_\mu - L_\tau$ symmetry on $M_{\nu f}$ as has been done in the past. Here, this symmetry arises as an effective symmetry of $M_{\nu f}$ from a very different set of basic symmetries. This symmetry leads to a degenerate pair of neutrinos and vanishing θ_{13} . The atmospheric mixing angle is determined as $\sin^2 \theta_{23} = |e^{i\beta_l} c_l c_\mu + s_l s_\mu|^2$. Perturbations to this symmetry have been studied in the past [273–275]. It is possible to simultaneously generate the correct solar scale, solar angle and θ_{13} with suitable but relatively large perturbations. Consider perturbing the zero entries in equation (6.5.5) by,

$$\delta M_{\nu f} = m_0 \begin{pmatrix} \epsilon_1 & 0 & 0 \\ 0 & \epsilon_2 & \epsilon_4 \\ 0 & \epsilon_4 & \epsilon_3 \end{pmatrix}. \quad (6.5.6)$$

Parameters $|\epsilon|$ are assumed less than the dominant entry of $M_{\nu f}$. We give here one example of perturbations which reproduces the observed spectrum within 3σ :

$$\{\epsilon_1, \epsilon_2, \epsilon_3, \epsilon_4\} = \{-0.284497, 0.284497, -0.0748816, 0.182915\} \quad (6.5.7)$$

leading to

$$\left\{ \frac{\Delta m_{\text{sol}}^2}{\Delta m_{\text{atm}}^2}, s_{12}^2, s_{13}^2, s_{23}^2 \right\} = \{0.0339706, 0.358739, 0.0243674, 0.443736\}. \quad (6.5.8)$$

We have taken $\beta_l = 0$ and $\cos(\theta_l - \theta_\mu) \approx -0.69$. The values of parameters required to get above values is quite large and the solar angle is also near to its 3σ limit. We have

verified by randomly varying the parameters over a large range that this is a general feature of this case. Relatively large perturbation to the basic symmetry may come from some soft breaking as discussed for example in [275].

We get a non-zero $|U_{13}|^2$ when T_l is not identified with S_1 . One could determine these values for different choices of T_l . The predicted $|U_{13}|^2$ is found from the explicit evaluation of various cases to take one of the three values (0.095, 0.25, 0.65). Of these, only the last value provides a good leading order prediction. $|U_{13}|^2 \sim 0.65$ can be identified in this case either with $|U_{\mu 3}|^2$ or $|U_{\tau 3}|^2$ as this gives s_{23}^2 close to its 3σ range 0.38 – 0.64. [272]. This amounts to reordering of the eigenvectors of T_l . An example of this choice is provided by $S_1 = f_3 H f_3$, $S_2 = E^{-1} H E$ and $T_l = f_1 H f_1$. $|U_{i3}|^2$ are given in this case by

$$\begin{aligned} |U_{13}|^2 &= \frac{1}{4}(2 + \mu_+) \approx 0.654, \\ |U_{23}|^2 &= \frac{|\mu_+ c_l + 2(1 + \mu_+) s_l e^{-i\beta_l}|^2}{12(2 + \mu_+)}, \\ |U_{33}|^2 &= \frac{|-\mu_+ s_l + 2(1 + \mu_+) c_l e^{-i\beta_l}|^2}{12(2 + \mu_+)}, \end{aligned} \quad (6.5.9)$$

One could identify either the second or the third entries with s_{13}^2 and determine θ_l accordingly, e.g. $\theta_l \sim 1.6488$, $\beta_l = 0$ leads to $s_{13}^2 \equiv |U_{33}|^2 \sim 0.024$ giving $s_{23}^2 c_{13}^2 \equiv |U_{13}|^2 \sim 0.654$. The resulting $\sin^2 \theta_{23}$ is given by 0.67. Small perturbation to this case can lead to θ_{23} within 3σ range and also split the degeneracy.

6.5.4 $S_\nu = Z_2$ and $T_l = Z_2 \times Z_2$

In this case, the Z_2 can be generated by any of the fifteen elements in O_2 while T_l is generated by $T_{1l} \equiv S_1$ and $T_{2l} \equiv S_2$, where S_1, S_2 form any of the five $Z_2 \times Z_2$ subgroups listed in table 6.1. The PMNS matrix in this case is given by $U = U_l^{b\dagger} U_{S_\nu} V_\nu$. Just as in the previous case, the atmospheric mixing angle is not predicted to be maximal but now unlike it, both the angles s_{13}^2 and s_{23}^2 depend on the unknown parameters θ_ν, β_ν . Not all the choices of the residual symmetries leads to a viable values of θ_{13}, θ_{23} in spite of the presence of the two unknowns. We determine the allowed patterns by fitting θ_ν, β_ν to the observed values of θ_{13}, θ_{23} . This allows us to identify cases which provide viable patterns of the mixing angles. One finds essentially

three patterns this way. Examples of the residual symmetries, the patterns and best fit values of θ_ν, β_ν in each of these cases are listed below.

$$\begin{aligned} S_\nu = f_3 H f_3 & : \theta_\nu = 1.42417, \beta_\nu = 1.84521, s_{13}^2 = 0.024, s_{23}^2 = 0.455, \\ S_\nu = f_2 H f_2 & : \theta_\nu = -0.487, \beta_\nu = 0, s_{13}^2 = 0.0244, s_{23}^2 = 0.676, \\ S_\nu = H & : \theta_\nu = -0.6716, \beta_\nu = -1.1620, s_{13}^2 = 0, s_{23}^2 = 0.455. \end{aligned} \quad (6.5.10)$$

All the above cases occur for the choice $T_{1l} = H$ and $T_{2l} = E^{-1} f_2 H f_2 E$. Similar results follow for different choices of $Z_2 \times Z_2$ as T_l but with alternative choices of S_ν . The first case given above reproduces the observed values of the mixing angles θ_{13}, θ_{23} . The second choice gives a θ_{23} on the verge of its 3σ value but correct s_{13}^2 . Thus small perturbation to this case can lead to a viable pattern. The third choice corresponding to $s_{13}^2 = 0$ would need significant corrections from the perturbations and is analogous to the case already discussed in section (III C).

6.5.5 $S_\nu = Z_2 \times Z_2$ and $T_l = Z_2 \times Z_2$

In this case, the residual symmetries of neutrinos and the charged leptons correspond to (different) $Z_2 \times Z_2$ groups. Due to the presence of two Z_2 groups, there are no undetermined parameters and the mixing angles θ_{13}, θ_{23} get predicted group theoretically. Since we have five different $Z_2 \times Z_2$ subgroups, there are twenty different choices which would lead to a non-trivial mixing matrix U . None of these correspond to even a good zeroth order values. The predicted third column of $|U|^2$ in all these cases is

$$|U_{i3}|^2 = (0.0954915, 0.25, 0.654508)^T. \quad (6.5.11)$$

and its permutations. These predictions are quite far from the observed mixing angles.

6.6 Explicit Realization with $A_5 \times Z_3$ Symmetry

In this section we discuss a realization of the above group theoretical discussion choosing specific examples of S_ν and T_l . We discuss the necessary Higgs fields and vacuum structure needed to implement above the symmetries. Implementation of antisymmetry needs imposition of an additional discrete symmetry which we choose as Z_3 . We use supersymmetry as the basic ingredient.

Irreducible representations (IR) of A_5 are : $1 + 3_1 + 3_2 + 4 + 5$ where 3_1 and 3_2 are non-equivalent IR. We assign l_L, l^c to 3_1 which is explicitly generated by E, H, f_1 given in equation (6.3.1). It follows from the product rule

$$3_1 \times 3_1 = (1 + 5)_{symm} + 3_{antisym}$$

that the symmetric neutrino mass matrix can arise from $1 + 5$ and the charged lepton masses can arise from all three IR. The neutrino masses are generated from a 5-plet $\eta_{5\nu}$ of flavon. Various fields transform under Z_3 as

$$(l_L, \eta_\nu) \rightarrow \omega(l_L, \eta_{5\nu}) \quad , \quad l^c \rightarrow \omega^2 l^c \quad .$$

The standard Higgs fields H_u, H_d and Higgs triplet Δ are singlets of $A_5 \times Z_3$.

The neutrino masses are generated from the following superpotential using the type-II seesaw mechanism:

$$W_\nu = \frac{1}{2\Lambda} (l_L \Delta l_L)_5 h_{5\nu} \eta_{5\nu} \quad . \quad (6.6.1)$$

Note that the singlet term $(l_L \Delta l_L)_1$ allowed by A_5 is prevented above due to the Z_3 symmetry. The charged lepton masses are generated by three additional flavons, a singlet η_{1l} , a 5-plet η_{5l} and a 3-plet η_{3l} all transforming trivially under Z_3 . The relevant superpotential is

$$W_l = \frac{1}{\Lambda} [h_{sl} (l_L H_d l^c)_1 \eta_{1l} + h_{5l} (l_L H_d l^c)_5 \eta_{5l} + h_{3l} (l_L H_d l^c)_3 \eta_{3l}] \quad . \quad (6.6.2)$$

The Z_3 symmetry separates the neutrino and the charged lepton sectors and does not allow flavons of one sector to couple to the other sector at the leading order.

We specialize to a particular choice of symmetries already discussed in section (IIIA). This corresponds to $T_l = E$ and $S_\nu = E^2 f_1 H f_1 E$. The above S_ν can serve as an antisymmetry of the neutrino mass matrix if the 5-plet $\eta_{5\nu}$ has antisymmetric vacuum expectation value:

$$S_\nu(5) \langle \eta \rangle_{5\nu} = - \langle \eta \rangle_{5\nu} \quad . \quad (6.6.3)$$

$S_\nu(5)$ in equation (6.6.3) corresponds to the five dimensional representation of S_ν . This representation can be obtained from the basic generators defined as a, b, c in [258] by

noting the correspondence $E = b$, $f_3 = a$ and $H = bc$. This leads to

$$S_\nu(5) = \begin{pmatrix} \frac{1}{2} & 0 & -\frac{1}{2} & \frac{1}{2\sqrt{2}} & \frac{\sqrt{\frac{3}{2}}}{2} \\ 0 & \frac{1}{2} & -\frac{1}{2} & -\frac{1}{\sqrt{2}} & 0 \\ -\frac{1}{2} & -\frac{1}{2} & 0 & -\frac{1}{2\sqrt{2}} & \frac{\sqrt{\frac{3}{2}}}{2} \\ \frac{1}{2\sqrt{2}} & -\frac{1}{\sqrt{2}} & -\frac{1}{2\sqrt{2}} & -\frac{1}{4} & -\frac{\sqrt{3}}{4} \\ \frac{\sqrt{\frac{3}{2}}}{2} & 0 & \frac{\sqrt{\frac{3}{2}}}{2} & -\frac{\sqrt{3}}{4} & \frac{1}{4} \end{pmatrix}. \quad (6.6.4)$$

Antisymmetry of $\langle \eta_{5\nu} \rangle$ together with A_5 symmetry in W_ν results in the flavor antisymmetric mass matrix. It is worth noting that unlike in the case of symmetry, equation (6.6.3) breaks the symmetry S_ν completely and it does not remain as a residual symmetry. But just as in the case with symmetry, a broken solution given in equation (6.6.3) may also arise from the minimization of suitable superpotential but would need enlargement in the model. This is explicitly demonstrated [254] in a simpler case of the group A_4 .

Denoting the vev $\langle \eta_{5\nu} \rangle$ as $(s_1, s_2, s_3, s_4, s_5)^T$, equation (6.6.3) is solved for

$$s_2 = s_3 - s_1, \quad s_4 = \sqrt{2}s_3 - \frac{3s_1}{\sqrt{2}}, \quad s_5 = -\sqrt{\frac{3}{2}}s_1. \quad (6.6.5)$$

Inserting this solution in equation (6.6.1), we get the neutrino mass matrix

$$M_\nu^0 = m_0 \begin{pmatrix} \frac{-3 + \sqrt{5} + y(1 - \sqrt{5})}{2\sqrt{2}} & \frac{1}{\sqrt{2}} & \frac{y}{\sqrt{2}} \\ \frac{1}{\sqrt{2}} & \frac{-2\sqrt{5} + y(1 + \sqrt{5})}{2\sqrt{2}} & \frac{y-1}{\sqrt{2}} \\ \frac{y}{\sqrt{2}} & \frac{y-1}{\sqrt{2}} & \frac{3 + \sqrt{5} - 2y}{2\sqrt{2}} \end{pmatrix}, \quad (6.6.6)$$

which satisfies the flavor antisymmetry, equation (6.1.3) with respect to $S_\nu = E^2 f_1 H f_1 E$.

This matrix has only one complex parameter $y \equiv \frac{s_3}{s_1}$ apart from an overall scale. In particular, $\tilde{M}_\nu \equiv V_{S_\nu}^T M_\nu V_{S_\nu}$ has the form given in equation (6.4.5) with

$$\tan \theta_\nu e^{i\beta_\nu} = -\frac{1 + \mu_+ \frac{s_3}{s_1}}{(\mu_+ - \mu_-) + \mu_- \frac{s_3}{s_1}}, \quad (6.6.7)$$

where $V_{S_\nu} = E^2 f_1 V_H$ diagonalizes $S_\nu = E^2 f_1 H f_1 E$. The neutrino mixing matrix is then given by $U_\nu = E^2 f_1 V_H V_\nu$ with V_ν as given in equation (6.4.11) and θ_ν, β_ν

given by equation (6.6.7) in terms of $\frac{s_3}{s_1}$. The charged lepton mixing matrix is analogously determined by the form of M_l obtained from W_l . W_l and the residual symmetry $T_l = E$ coincide with the one already discussed in [262]. The T_l invariant vacuum configuration discussed in [262] leads to the following charged lepton mass matrix

$$M_l = \begin{pmatrix} m_0 & m_1 - m_2 & m_1 + m_2 \\ m_1 + m_2 & m_0 & m_1 - m_2 \\ m_1 - m_2 & m_1 + m_2 & m_0 \end{pmatrix}, \quad (6.6.8)$$

where $m_{0,1,2}$ respectively label the singlet, triplet and 5-plet contributions to M_l . $M_l M_l^\dagger$ is diagonalized by the matrix (6.3.10) which also diagonalizes T_l :

$$U_\omega^\dagger M_l M_l^\dagger U_\omega = \text{diag}(m_1^2, m_2^2, m_3^2)$$

with eigenvalues

$$\begin{aligned} \lambda_1^2 &= m_0^2 + 4|m_1|^2 + 4m_{1R}m_0, \\ \lambda_2^2 &= m_0^2 + |m_1|^2 + 3|m_2|^2 + 2\sqrt{3} \text{Im}(m_1 m_2^*) - 2m_0(m_{1R} + \sqrt{3}m_{2I}), \\ \lambda_3^2 &= m_0^2 + |m_1|^2 + 3|m_2|^2 - 2\sqrt{3} \text{Im}(m_1 m_2^*) - 2m_0(m_{1R} - \sqrt{3}m_{2I}) \end{aligned} \quad (6.6.9)$$

Here, $m_{1R,2R}$ and $m_{1I,2I}$ respectively denote the real and imaginary parts of $m_{1,2}$. m_0 is assumed real without loss of generality.

The identification of eigenvalues $\lambda_{1,2,3}^2$ with the physical charged lepton masses $m_{e,\mu,\tau}^2$ depends on the choice of parameters $m_{0,1,2}$. In particular, one can choose these parameters in a way that gives $\lambda_2^2 = m_e^2$, $\lambda_1^2 = m_\mu^2$ and $\lambda_3^2 = m_\tau^2$. With this identification,

$$U_l = \frac{1}{\sqrt{3}} \begin{pmatrix} 1 & 1 & 1 \\ \omega & 1 & \omega^2 \\ \omega^2 & 1 & \omega \end{pmatrix}. \quad (6.6.10)$$

This U_l together with $U_\nu = E^2 f_1 V_H V_\nu$ gives the mixing matrix U which is already worked out in equation (6.5.3). The above form of U_l leads to the identification $|U_{23}|^2 = s_{13}^2$, $|U_{13}|^2 = c_{13}^2 s_{23}^2$. Values of θ_ν, β_ν giving correct s_{13}^2, s_{23}^2 were already determined in section IIIA. This translates to the following values of the model parameter $\frac{s_3}{s_1}$ when equation (6.6.7) is used:

$$\frac{s_3}{s_1} \approx 0.9979 \exp(-i 0.7181). \quad (6.6.11)$$

Non-zero neutrino masses remain degenerate at the leading order. They can be split and the solar angle can be determined by perturbations which break antisymmetry at the non-leading order. A simple perturbation can be generated by introducing a singlet flavon $\eta_{1\nu}$ transforming as $\eta_{1\nu} \rightarrow \omega^2 \eta_{1\nu}$ under Z_3 . This flavon leads to a non-leading term

$$\frac{h_{1\nu}}{2\Lambda^2} (l_i \Delta l_L)_1 \eta_{1\nu}^2$$

in W_ν . This generates a diagonal perturbation which can be parameterized as

$$M_\nu = m_0 (\hat{M}_\nu^0 + \epsilon I)$$

with $\hat{M}_\nu^0 \equiv \frac{M_\nu^0}{m_0}$ and $|\epsilon| \ll 1$. This simple perturbation is enough to generate the solar splitting without disturbing the zeroth order values of s_{13}^2, s_{23}^2 significantly. One could vary $\frac{s_3}{s_1}$ around the zeroth order value determined in equation (6.6.11) and find the region of parameters which fits the data with $|\epsilon| < 0.1$. This procedure leads to a solution close to the best fit values of all parameters. For example, $\frac{s_3}{s_1} = 1.00019 \exp(-i 0.711498)$ and $\epsilon = 0.0168241$ leads to

$$\begin{aligned} \sin^2 \theta_{12} &= 0.295455 & , & & \sin^2 \theta_{13} &= 0.0235172 & , \\ \sin^2 \theta_{23} &= 0.449634 & , & & \frac{\Delta m_{\text{sol}}^2}{\Delta m_{\text{atm}}^2} &= 0.0285398 & . \end{aligned} \quad (6.6.12)$$

6.7 Summary

In this chapter, we have studied the consequences of an ansatz of flavor antisymmetry in the context of the flavor group A_5 assuming that S_ν in equation (6.1.3) and T_l in equation (6.4.17) are contained in the group A_5 . These assumptions constrain the mixing patterns which we have determined in various cases. The use of flavor antisymmetry in the context of the A_5 group necessarily leads to a degenerate pair of neutrinos in addition to a massless one. This is a good zeroth order prediction. Small perturbations splitting the degeneracy can lead to a viable neutrino masses. The predicted neutrino mass hierarchy is inverted.

We have considered discrete subgroups Z_2 and $Z_2 \times Z_2$ of A_5 as residual symmetries of M_ν and discrete groups Z_3, Z_5, Z_2 and $Z_2 \times Z_2$ contained in A_5 as symmetries

of $M_l M_l^\dagger$ and worked out the resulting mixing patterns at the leading order in all the cases. The third column of the mixing matrix and hence the angles θ_{13}, θ_{23} get determined at this order. Various predictions discussed in section (6.5) can be summarized as follows :

- It is possible to get a universal prediction of the maximal atmospheric mixing angle with the choice S_ν as Z_2 or $Z_2 \times Z_2$ and T_l as any element in Z_3, Z_5 . For $S_\nu = Z_2$, one can also get the correct θ_{13} at the leading order while the case of $S_\nu = Z_2 \times Z_2$ predicts either $\theta_{13} = 0$ or large $s_{13}^2 \geq 0.1$.
- The case $T_l = Z_2$ and $S_\nu = Z_2 \times Z_2$ does not predict maximal θ_{23} but can be used to predict one of the entries of the third column. The other entry gets determined by an unknown angle inherent with the use of the Z_2 groups. The viable predictions within this case are either $\theta_{13} = 0$ or $s_{23}^2 c_{13}^2 = 0.65$. The former requires large perturbation and we have presented a typical set of such perturbation which lead to correct description of masses and mixing angles.
- The case $S_\nu = Z_2$ and $T_l = Z_2 \times Z_2$ involves an unknown angle and a phase. Not all possible choices of S_ν, T_l in this category can lead to correct mixing in spite of the presence of two unknowns. We have identified cases which lead to the correct description of the mixing angles θ_{13}, θ_{23} .
- The case of both S_ν and T_l belonging to different $Z_2 \times Z_2$ subgroups of A_5 is fully predictive without any unknowns. But none of the possible cases within this category lead even to a good zeroth order prediction.

We have supplemented the group theoretical predictions of neutrino mixing angles and mass patterns using the hypothesis of flavour antisymmetry in the context of the discrete subgroup A_5 of $SO(3)$. We have determined the Higgs content and the required vacuum pattern which realizes one of the viable cases discussed group theoretically. The use of a concrete model also allows a systematic discussion of possible perturbations and we have given an example of a perturbation within the model which can be used to split the degeneracy of neutrinos and which can give the correct descriptions of all mixing angles and masses.

Chapter 7

Texture Zero Studies in the Minimal Extended type-I Seesaw Model

*“...failure is not about not succeeding. Rather it is about not putting in your bet effort
and not contributing, however modestly, to the common good.”*

– V. Sarabhai

7.1 Introduction

In the previous chapters, we have discussed about the neutrino oscillation mechanism by considering three active neutrinos. Another very interesting aspect in neutrino physics is the search for the existence of light sterile neutrinos in neutrino oscillation experiments. These neutrinos do not carry any charge under the SM gauge group and thus, they do not take part in the weak interactions. But they can mix with the active neutrinos and hence their existence can be probed in neutrino oscillation experiments. As discussed in chapter (1) the sterile neutrino hypothesis gained popularity in the context of the LSND results which reported oscillations governed by a $\Delta m^2 \sim \text{eV}^2$ [53–55]. The latest data of the MiniBooNE experiment [56] also have some overlap with the allowed regions of the LSND experiment and hence support the existence of the sterile neutrino hypothesis. Indication for sterile neutrinos also came from Gallium anomaly [57] and the anomaly in reactor antineutrino flux studies [58] with the recalculated fluxes. Both these anomalies showed a deficit in the observed rate as compared to the predicted rates. Recent analysis of the Planck data can also accommodate

the possibility of light sterile neutrino in the eV scale if one deviates slightly from the base Λ CDM model [37]. In short, the scenario with a light sterile neutrino is quite riveting at present and many future experiments are proposed to test this [63]. Although it is possible to have a better fit of neutrino oscillation data with more than one light sterile neutrinos [276–278], the 3+1 scheme i.e., three active neutrinos and one sterile neutrino in the sub-eV and eV scale respectively, is considered to be minimal. There are three different ways to add sterile neutrino in the standard mass patterns and these are, (i) 3+1 scheme in which three active neutrinos are of sub-eV scale and sterile neutrino is of eV scale [279]. (ii) 2+2 scheme in which two different pairs of neutrino mass states differ by eV^2 [280]. The latter scheme was disfavored by solar and atmospheric data [281]. (iii) 1+3 scheme in which three active neutrinos are in eV scale and sterile neutrino is lighter than the active neutrinos. This scenario is however disfavored from cosmology [282, 283]. Hence, we focus on the 3+1 scenario in our study.

Theoretically it is challenging to construct models with light sterile neutrinos. Flavor symmetry models giving rise to eV sterile neutrinos have been studied in the literature [60–62]. These models might require modifications to usual seesaw framework [284, 285]. In the explicit seesaw models, the eV scale sterile neutrinos with their mass suppressed by Froggatt - Nielsen mechanism can be naturally accommodated in non Abelian A_4 flavor symmetry [61, 286, 287]. S_3 bimodel or schizophrenic models for light sterile neutrinos are also widely studied in Refs. [288, 289]. In order to have a theoretical understanding of the origin of eV scale sterile neutrino as well as admixtures between sterile and active neutrinos, the authors of Refs. [61, 286, 287] have studied an extension to the canonical type-I seesaw model. This model is known as “minimal extended type - I seesaw” (MES) model. In the MES model a fermion singlet, S , is added along with three right handed neutrinos. This extension results into an eV scale sterile neutrino naturally, without imposing tiny mass scale or Yukawa term for this neutrino.

In this chapter, we study the various possible textures of the Dirac neutrino mass matrix, M_D , Majorana neutrino mass matrix, M_R and the mass matrix M_S that originate from the Yukawa interaction between right handed neutrinos with the gauge singlet within the framework of MES model and classify the allowed possibilities. It has

been noted by many authors [290–294] that the zeros of the Dirac neutrino mass matrix M_D and the right handed Majorana mass matrix M_R are the progenitors of zeros in the effective Majorana mass matrix m_ν through the type - I seesaw mechanism. This motivates us to look for zeros in various neutrino mass matrices in the MES model which can lead to viable texture zeros in neutrino mass matrix. We also seek extra correlations connecting the parameters of the active and sterile sector which can put further constraints on the allowed possibilities.

We classify different structures of M_D , M_R and M_S that can give allowed textures for the light neutrino mass matrix m_ν . Interestingly, the only phenomenologically allowed form of m_ν that we obtain are the two one zero textures – namely $m_{e\tau} = 0$ and $m_{\tau\tau} = 0$. In the MES model, because of extra correlations connecting active and sterile sector, not all Yukawa matrices that give $m_{e\tau} = 0$ or $m_{\tau\tau} = 0$ for m_ν are allowed. We study these additional correlations and tabulate the allowed textures. We also include a discussion on the impact of NLO corrections in this model. In this context it is also important to study the origin of zero textures. Here, we show that it is possible to obtain various zero entries in lepton mass matrices with an Abelian discrete symmetry group $Z_8 \times Z_2$. An alternative approach to obtain lepton mixing is discussed in Ref. [295] by considering non-Abelian symmetry group. We follow the method discussed in Ref. [296] to obtain Abelian discrete symmetry group which can generate viable zero textures in m_ν . Their method is based on the type - I seesaw and we extend it to apply on the MES model.

This chapter is organized in the following manner. In next section (7.2) a brief review of the MES model is given. In section (7.3) and its subsections, we present the formalism of this study. We discuss the implication of the allowed forms of one zero textures in m_ν , in section (7.4). The following section (7.5) discusses the results obtained from the comparison of low energy and high energy neutrino mass matrices and the extra correlations connecting active and sterile sector. We also describe the importance of NLO corrections in section (7.5.1). Symmetry realizations for the allowed zero textures are discussed in section (7.6). The summary of our findings and conclusions are presented in section (7.7).

7.2 Minimal Extended type-I Seesaw Mechanism

In this section, we illustrate the basic structure of the MES model. In this model, the fermion content of the SM is extended by three right handed neutrinos together with a gauge singlet field S . One can get a natural eV scale sterile neutrino without inserting any small Yukawa coupling in this model [61, 286]. The Lagrangian containing the neutrino masses can be written as

$$-\mathcal{L}_{\mathcal{M}} = \bar{\nu}_L M_D \nu_R + \bar{S}^c M_S \nu_R + \frac{1}{2} \bar{\nu}_R^c M_R \nu_R + h.c. \quad (7.2.1)$$

Here, M_D, M_R are the (3×3) Dirac and Majorana mass matrices respectively and M_S is a (1×3) coupling matrix between right handed neutrinos with the gauge singlet. In the basis (ν_L, ν_R^c, S^c) , the (7×7) neutrino mass matrix can be expressed as

$$M_{\nu}^{7 \times 7} = \begin{pmatrix} 0 & M_D & 0 \\ M_D^T & M_R & M_S^T \\ 0 & M_S & 0 \end{pmatrix}. \quad (7.2.2)$$

We consider the following hierarchical mass spectrum in these mass matrices i.e. $M_R \gg M_S > M_D$, in analogy with the type - I seesaw. The right handed neutrinos are much heavier compared to the electroweak scale and thus they will decouple at the low scale. Therefore, equation (7.2.2) can be block diagonalized using the seesaw approximation and the effective neutrino mass matrix in the basis (ν_L, S^c) can be written as

$$M_{\nu}^{4 \times 4} = - \begin{pmatrix} M_D M_R^{-1} M_D^T & M_D M_R^{-1} M_S^T \\ M_S (M_R^{-1})^T M_D^T & M_S M_R^{-1} M_S^T \end{pmatrix}. \quad (7.2.3)$$

Note that the rank of $M_{\nu}^{4 \times 4}$ is three and hence one of the light neutrino always remains massless.

Considering $M_S > M_D$, one can apply seesaw approximation once again on equation (7.2.3) to obtain the active neutrino mass matrix as *

$$m_{\nu}^{3 \times 3} \simeq M_D M_R^{-1} M_S^T (M_S M_R^{-1} M_S^T)^{-1} M_S (M_R^{-1})^T M_D^T - M_D M_R^{-1} M_D^T, \quad (7.2.4)$$

whereas the mass of the sterile neutrino is given by,

$$m_s \simeq -M_S M_R^{-1} M_S^T. \quad (7.2.5)$$

*Note that RHS of equation (7.2.4) does not vanish since $(M_S)_{1 \times 3}$ is a vector rather than a square matrix.

Note that the zero textures of fermion mass matrices in the context of the type - I seesaw mechanism studied in Refs. [290–292, 294], leading to viable texture zeros in $m_\nu^{3\times 3}$ can be different from that of the MES model because of the presence of the first term of equation (7.2.4). The active-sterile neutrino mixing matrix is given by,

$$V \simeq \begin{pmatrix} (1 - \frac{1}{2}RR^\dagger)U' & R \\ -R^\dagger U' & 1 - \frac{1}{2}R^\dagger R \end{pmatrix}, \quad (7.2.6)$$

where $R_{3\times 1}$ governs the strength of active-sterile mixing and can be expressed as

$$R_{3\times 1} = M_D M_R^{-1} M_S^T (M_S M_R^{-1} M_S^T)^{-1}. \quad (7.2.7)$$

Additionally in our formalism we assume $|V_{\tau 4}| = 0$, which is allowed by the current active sterile neutrino mixing data. Thus, $R_{3\times 1} = (V_{e4}, V_{\mu 4}, 0)^T$ which is suppressed by the ratio $\mathcal{O}(M_D)/\mathcal{O}(M_S)$.

	SNH	SIH
m_1	0	$\sqrt{\Delta m_{31}^2}$
m_2	$\sqrt{\Delta m_{21}^2}$	$\sqrt{\Delta m_{21}^2 + \Delta m_{31}^2}$
m_3	$\sqrt{\Delta m_{21}^2 + \Delta m_{32}^2}$	0
m_4	$\sqrt{\Delta m_{41}^2}$	$\sqrt{\Delta m_{43}^2}$

Table 7.1: Neutrino mass spectrum for normal and inverted hierarchies. Δm_{12}^2 , Δm_{31}^2 (Δm_{32}^2) are the solar and atmospheric mass squared differences and Δm_{41}^2 (Δm_{43}^2) is the active sterile mass squared difference. The allowed ranges of these three mass squared differences are given in table (7.2).

We consider two different mass hierarchies in 3+1 framework. We denote 3+1 scenario as (SNH) when the three active neutrinos follow normal hierarchy ($m_1 < m_2 \ll m_3$) and the second choice is (SIH) when the three active neutrinos follow inverted hierarchy ($m_3 \ll m_1 \approx m_2$) as shown in figure (7.1). These masses can be expressed in terms of the mass squared differences obtained from oscillation experiments as given in table (7.1). In the next section we systematically explore the various zero texture structures of M_D , M_R and M_S which can give rise to viable zero textures of $m_\nu^{3\times 3}$. The best fit values along with 3σ ranges of neutrino oscillation parameters used in our numerical analysis are given in table (7.2).

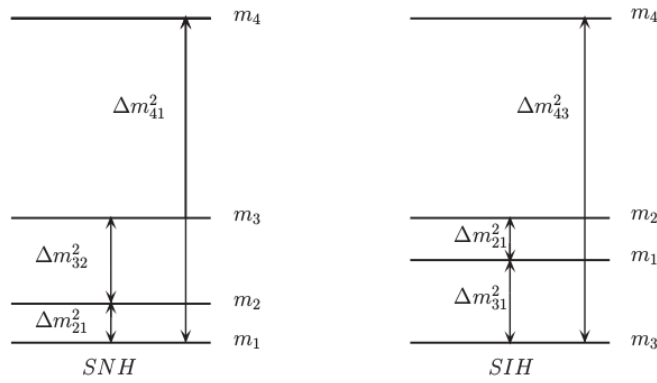


Figure 7.1: Left (right) panel corresponds to allowed mass spectrum in 3+1 scheme for SNH (SIH).

7.3 Formalism

In our formalism, the charged lepton mass matrix, M_l , is considered to be diagonal. For the right handed Majorana neutrino mass matrix, we consider four different structures:

(i) Diagonal M_R having three zeros i.e.,

$$M_R = \begin{pmatrix} r_1 & 0 & 0 \\ 0 & r_2 & 0 \\ 0 & 0 & r_3 \end{pmatrix}. \quad (7.3.1)$$

(ii) Non-diagonal minimal form of M_R having four zeros with $\text{Det}(M_R) \neq 0$ i.e.,

$$M_R = \begin{pmatrix} 0 & r_2 & 0 \\ r_2 & 0 & 0 \\ 0 & 0 & r_1 \end{pmatrix}; \quad \begin{pmatrix} 0 & 0 & r_2 \\ 0 & r_1 & 0 \\ r_2 & 0 & 0 \end{pmatrix}; \quad \begin{pmatrix} r_1 & 0 & 0 \\ 0 & 0 & r_2 \\ 0 & r_2 & 0 \end{pmatrix}. \quad (7.3.2)$$

These three non-diagonal forms of M_R correspond to $L_e - L_\mu$, $L_e - L_\tau$ and $L_\mu - L_\tau$ flavor symmetry respectively. Such forms of M_R in the context of zero textures in the type-I seesaw model have been considered for instance in Ref. [301]. The mass matrix, $M_S = (s_1, s_2, s_3)$ being a 1×3 matrix can have one zero or two zeros. In Ref. [286], an A_4 based model was considered with 2 zeros in M_S and 3 zeros in M_D to obtain the $m_\nu^{3 \times 3}$ as given by equation (7.2.4). In our analysis, we find that the maximum number of zeros of M_D that can give phenomenologically allowed zero textures in m_ν is five.

Parameter	Best Fit	3σ Range
$\Delta m_{21}^2 [10^{-5} \text{ eV}^2]$	7.37	6.93 – 7.97
$\Delta m_{31}^2 [10^{-3} \text{ eV}^2]$ (NH)	2.50	2.37 – 2.63
$\Delta m_{31}^2 [10^{-3} \text{ eV}^2]$ (IH)	2.46	2.33 – 2.60
$\sin^2 \theta_{12}/10^{-1}$	2.97	2.50 – 3.54
$\sin^2 \theta_{13}/10^{-2}$ (NH)	2.14	1.85 – 2.46
$\sin^2 \theta_{13}/10^{-2}$ (IH)	2.18	1.86 – 2.48
$\sin^2 \theta_{23}/10^{-1}$ (NH)	4.37	3.79 – 6.16
$\sin^2 \theta_{23}/10^{-1}$ (IH)	5.69	3.83 – 6.37
δ_{13}/π (NH)	1.35	0 – 2
δ_{13}/π (IH)	1.32	0 – 2
R_ν (NH)	0.0295	0.0263 – 0.0336
R_ν (IH)	0.0299	0.0266 – 0.0342
$\Delta m_{\text{LSND}}^2 (\Delta m_{41}^2 \text{ or } \Delta m_{43}^2) \text{ eV}^2$	1.63	0.87 – 2.04
$ V_{e4} ^2$	0.027	0.012 – 0.047
$ V_{\mu 4} ^2$	0.013	0.005 – 0.03
$ V_{\tau 4} ^2$	–	< 0.16

Table 7.2: The latest best-fit and 3σ ranges of active ν oscillation parameters from [297]. The current constraints on sterile neutrino parameters are from the global analysis [298–300]. Here R_ν is the solar to atmospheric mass squared difference ratio.

For such cases, two zeros in M_S do not lead to any viable textures in m_ν . The only allowed possibility therefore is one zero in M_S result in three possible structures. The possible combinations of M_D , M_R and M_S that lead to phenomenologically viable textures of m_ν are discussed in the following subsections.

7.3.1 5 zeros in M_D and diagonal M_R

First let us assume M_R to be diagonal. As M_D is a non-symmetric 3×3 matrix, 5 zeros can be arranged in ${}^9C_5 = 126$ ways. Thus considering 126 cases of M_D together with 3 cases of M_S and 1 case of M_R , we obtain total 378 possible structures of m_ν . Out of

all possible combinations of these matrices the only allowed texture that we obtain is the one zero texture in m_ν with $m_{e\tau} = 0$. Here, we have three possible forms of M_S and these are,

$$M_S^{(1)} = (0, s_2, s_3), M_S^{(2)} = (s_1, 0, s_3), \text{ and } M_S^{(3)} = (s_1, s_2, 0). \quad (7.3.3)$$

The various forms of M_D which lead to viable texture $m_{e\tau} = 0$ are presented below:

$$M_S^{(1)}, M_D^{(1)} = \begin{pmatrix} 0 & 0 & a_3 \\ b_1 & 0 & b_3 \\ c_1 & 0 & 0 \end{pmatrix}, M_D^{(2)} = \begin{pmatrix} 0 & a_2 & 0 \\ b_1 & 0 & b_3 \\ c_1 & 0 & 0 \end{pmatrix}, M_D^{(3)} = M_D^{(1)} Z_{23}, M_D^{(4)} = M_D^{(2)} Z_{23}. \quad (7.3.4)$$

$$M_S^{(2)}, M_D^{(5)} = \begin{pmatrix} 0 & 0 & a_3 \\ 0 & b_2 & b_3 \\ 0 & c_2 & 0 \end{pmatrix}, M_D^{(6)} = \begin{pmatrix} a_1 & 0 & 0 \\ 0 & b_2 & b_3 \\ 0 & c_2 & 0 \end{pmatrix}, M_D^{(7)} = M_D^{(5)} Z_{13}, M_D^{(8)} = M_D^{(6)} Z_{13}. \quad (7.3.5)$$

$$M_S^{(3)}, M_D^{(9)} = \begin{pmatrix} a_1 & 0 & 0 \\ 0 & b_2 & b_3 \\ 0 & 0 & c_3 \end{pmatrix}, M_D^{(10)} = \begin{pmatrix} 0 & a_2 & 0 \\ 0 & b_2 & b_3 \\ 0 & 0 & c_3 \end{pmatrix}, M_D^{(11)} = M_D^{(9)} Z_{12}, M_D^{(12)} = M_D^{(10)} Z_{12}. \quad (7.3.6)$$

Here, Z_{12} , Z_{13} and Z_{23} are the permutation matrices that exchange first and second columns, first and third columns and second and third columns respectively. Therefore, we observe that out of 126 cases only 12 above forms of $M_D^{(i)}$, $i = 1 - 12$ give the allowed texture $m_{e\tau} = 0$ of m_ν when M_R is diagonal.

7.3.2 5 zeros in M_D and non-diagonal M_R corresponding to $L_e - L_\mu$ flavor symmetry

The form of M_R that we consider here corresponds to flavor symmetry $L_e - L_\mu$ as given in equation (7.3.2). Among the 378 possibilities we obtain two allowed one zero textures of m_ν , namely $m_{e\tau} = 0$ and $m_{\tau\tau} = 0$. We observe that out of total 126 forms of M_D , only four structures give rise to $m_{e\tau} = 0$ while eight structures give rise to $m_{\tau\tau} = 0$. We list them below:

Textures leading to $m_{e\tau} = 0$

$$M_S^{(3)}, M_D^{(13)} = \begin{pmatrix} a_1 & 0 & 0 \\ 0 & b_2 & b_3 \\ 0 & 0 & c_3 \end{pmatrix}, M_D^{(14)} = \begin{pmatrix} 0 & a_2 & 0 \\ 0 & b_2 & b_3 \\ 0 & 0 & c_3 \end{pmatrix}, M_D^{(15)} = M_D^{(13)} Z_{12}, M_D^{(16)} = M_D^{(14)} Z_{12}. \quad (7.3.7)$$

Textures leading to $m_{\tau\tau} = 0$

$$M_S^{(1)}, M_D^{(17)} = \begin{pmatrix} a_1 & a_2 & 0 \\ b_1 & 0 & 0 \\ 0 & c_2 & 0 \end{pmatrix}, M_D^{(18)} = \begin{pmatrix} a_1 & 0 & a_3 \\ b_1 & 0 & 0 \\ 0 & c_2 & 0 \end{pmatrix}, \quad (7.3.8)$$

$$M_D^{(19)} = \begin{pmatrix} a_1 & 0 & 0 \\ b_1 & b_2 & 0 \\ 0 & c_2 & 0 \end{pmatrix}, M_D^{(20)} = \begin{pmatrix} a_1 & 0 & 0 \\ b_1 & 0 & b_3 \\ 0 & c_2 & 0 \end{pmatrix}.$$

$$M_S^{(2)}, M_D^{(21)} = \begin{pmatrix} 0 & a_2 & a_3 \\ 0 & b_2 & 0 \\ c_1 & 0 & 0 \end{pmatrix}, M_D^{(22)} = \begin{pmatrix} a_1 & a_2 & 0 \\ 0 & b_2 & 0 \\ c_1 & 0 & 0 \end{pmatrix}, \quad (7.3.9)$$

$$M_D^{(23)} = \begin{pmatrix} 0 & a_2 & 0 \\ b_1 & b_2 & 0 \\ c_1 & 0 & 0 \end{pmatrix}, M_D^{(24)} = \begin{pmatrix} 0 & a_2 & 0 \\ 0 & b_2 & b_3 \\ c_1 & 0 & 0 \end{pmatrix}.$$

7.3.3 5 zeros in M_D and non-diagonal M_R corresponding to $L_e - L_\tau$ flavor symmetry

The form of M_R that we consider in this subsection corresponds to flavor symmetry $L_e - L_\tau$ as given in equation (7.3.2). In this case also we observe that out of total 126 cases of M_D , only four structures of M_D give rise to $m_{e\tau} = 0$ and eight forms of M_D give rise to texture $m_{\tau\tau} = 0$. We list them below. Note that these forms of M_D are different from those obtained in the earlier subsection.

Textures leading to $m_{e\tau} = 0$

$$M_S^{(2)}, M_D^{(25)} = \begin{pmatrix} 0 & 0 & a_3 \\ 0 & b_2 & b_3 \\ 0 & c_2 & 0 \end{pmatrix}, M_D^{(26)} = \begin{pmatrix} 0 & 0 & a_3 \\ b_1 & b_2 & 0 \\ 0 & c_2 & 0 \end{pmatrix}, M_D^{(27)} = M_D^{(25)} Z_{13}, M_D^{(28)} = M_D^{(26)} Z_{13}. \quad (7.3.10)$$

Textures leading to $m_{\tau\tau} = 0$

$$M_S^{(1)}, M_D^{(29)} = \begin{pmatrix} a_1 & a_2 & 0 \\ b_1 & 0 & 0 \\ 0 & 0 & c_3 \end{pmatrix}, M_D^{(30)} = \begin{pmatrix} a_1 & 0 & a_3 \\ b_1 & 0 & 0 \\ 0 & 0 & c_3 \end{pmatrix}, \quad (7.3.11)$$

$$M_D^{(31)} = \begin{pmatrix} a_1 & 0 & 0 \\ b_1 & b_2 & 0 \\ 0 & 0 & c_3 \end{pmatrix}, M_D^{(32)} = \begin{pmatrix} a_1 & 0 & 0 \\ b_1 & 0 & b_3 \\ 0 & 0 & c_3 \end{pmatrix}.$$

$$M_S^{(3)}, M_D^{(33)} = \begin{pmatrix} 0 & a_2 & a_3 \\ 0 & 0 & b_3 \\ c_1 & 0 & 0 \end{pmatrix}, M_D^{(34)} = \begin{pmatrix} a_1 & 0 & a_3 \\ 0 & 0 & b_3 \\ c_1 & 0 & 0 \end{pmatrix}, \quad (7.3.12)$$

$$M_D^{(35)} = \begin{pmatrix} 0 & 0 & a_3 \\ 0 & b_2 & b_3 \\ c_1 & 0 & 0 \end{pmatrix}, M_D^{(36)} = \begin{pmatrix} 0 & 0 & a_3 \\ b_1 & 0 & b_3 \\ c_1 & 0 & 0 \end{pmatrix}.$$

7.3.4 5 zeros in M_D and non-diagonal M_R corresponding to $L_\mu - L_\tau$ flavor symmetry

The form of M_R that we consider here corresponds to flavor symmetry $L_\mu - L_\tau$ as given in equation (7.3.2). Here also we observe that out of 126 cases of M_D only four structures of M_D give rise to texture $M_{e\tau} = 0$ and 8 forms of M_D give rise to texture $M_{\tau\tau} = 0$. But these forms of M_D are different from those obtained in the earlier two subsections:

Structures leading to $m_{e\tau} = 0$

$$M_S^{(1)}, M_D^{(37)} = \begin{pmatrix} 0 & a_2 & 0 \\ b_1 & 0 & b_3 \\ c_1 & 0 & 0 \end{pmatrix}, M_D^{(38)} = \begin{pmatrix} 0 & 0 & a_3 \\ b_1 & 0 & b_3 \\ c_1 & 0 & 0 \end{pmatrix}, M_D^{(39)} = M_D^{(37)} Z_{23}, M_D^{(40)} = M_D^{(38)} Z_{23}. \quad (7.3.13)$$

Structures leading to $m_{\tau\tau} = 0$

$$M_S^{(2)}, M_D^{(41)} = \begin{pmatrix} a_1 & a_2 & 0 \\ 0 & b_2 & 0 \\ 0 & 0 & c_3 \end{pmatrix}, M_D^{(42)} = \begin{pmatrix} 0 & a_2 & a_3 \\ 0 & b_2 & 0 \\ 0 & 0 & c_3 \end{pmatrix}, \quad (7.3.14)$$

$$M_D^{(43)} = \begin{pmatrix} 0 & a_2 & 0 \\ 0 & b_2 & b_3 \\ 0 & 0 & c_3 \end{pmatrix}, M_D^{(44)} = \begin{pmatrix} 0 & a_2 & 0 \\ b_1 & b_2 & 0 \\ 0 & 0 & c_3 \end{pmatrix}.$$

$$M_S^{(3)}, M_D^{(45)} = \begin{pmatrix} 0 & a_2 & a_3 \\ 0 & 0 & b_3 \\ 0 & c_2 & 0 \end{pmatrix}, M_D^{(46)} = \begin{pmatrix} a_1 & 0 & a_3 \\ 0 & 0 & b_3 \\ 0 & c_2 & 0 \end{pmatrix},$$

$$M_D^{(47)} = \begin{pmatrix} 0 & 0 & a_3 \\ b_1 & 0 & b_3 \\ 0 & c_2 & 0 \end{pmatrix}, M_D^{(48)} = \begin{pmatrix} 0 & 0 & a_3 \\ 0 & b_2 & b_3 \\ 0 & c_2 & 0 \end{pmatrix}. \quad (7.3.15)$$

Note that in general the entries of the Yukawa matrices M_D , M_R and M_S are complex (of the form $pe^{i\theta}$). However some of the phases can be absorbed by redefinition of the leptonic fields. For the case when M_R is diagonal, the number of un-absorbed phases is two – one each in M_D and M_S whereas for the off-diagonal M_R only one phase remains in M_S . In this section we do not explicitly write the phases. However in section (7.5) where we discuss specific cases, the phases are explicitly included.

7.4 Active Neutrino Mass Matrix with 1-Zero Texture

In this section, we discuss the implications of the one-zero textures $m_{e\tau} = 0$ and $m_{\tau\tau} = 0$ for the light neutrino mass matrix without taking recourse to any model. The (3×3) light neutrino mass matrix, m_ν , being symmetric, there are 6 possible cases of one zero textures with a vanishing lowest mass and these are studied in detail in Refs. [302–305]. In the above section, we observed that in context of the MES model only viable textures of m_ν that we obtain are $m_{e\tau} = 0$ and $m_{\tau\tau} = 0$. According to the recent studies [304–306], both these textures are ruled out for normal hierarchy when the lowest mass m_1 is zero but they can be allowed for the inverted hierarchy even

when then lowest mass m_3 is zero [†].

This kind of mass pattern can be obtained completely from group theoretical point of view if one assumes that Majorana neutrino mass matrix displays flavor antisymmetry under some discrete subgroup of SU(3) as discussed in Refs. [254, 307].

In this section we re-analyse the textures $m_{e\tau} = 0$ and $m_{\tau\tau} = 0$ for the inverted hierarchical mass spectrum assuming $m_3 = 0$ in the light of recent neutrino oscillation data as given in table (7.2). In our analysis we find that correlations among various oscillation parameters become highly constrained as compared to the earlier studies. This is due to the recent constraints on the 3σ ranges of the mass squared differences and θ_{13} as compared to earlier results [303–305] [‡].

In three neutrino paradigm, low energy Majorana neutrino mass matrix can be diagonalized as,

$$m_\nu^{3\times 3} = U' \text{diag}(m_1, m_2, m_3) U'^T. \quad (7.4.1)$$

Here, $U' = U.P$ ($P = \text{diag}(1, e^{i\alpha}, e^{i(\beta+\delta_{13})})$) is a lepton mixing matrix in the basis where M_l is diagonal. The PMNS matrix U has 3 mixing angles and a CP phase δ_{13} .

The elements of neutrino mass matrix can be calculated from equation (7.4.1) are,

$$(m_\nu^{3\times 3})_{ab} = m_1 U_{a1} U_{b1} + m_2 U_{a2} U_{b2} e^{2i\alpha} + m_3 U_{a3} U_{b3} e^{2i(\beta+\delta_{13})}, \quad (7.4.2)$$

where, $a, b = e, \mu$ and τ and $m_i (i = 1, 2, 3)$ are given in table (7.1). We express elements of m_ν as m_{ab} in the text.

Imposing the condition of zero texture for IH with $m_3 = 0$ in the above equation we get,

$$m_1 U_{a1} U_{b1} + m_2 U_{a2} U_{b2} e^{2i\alpha} = 0, \quad (7.4.3)$$

which can be simplified to obtain the mass ratio

$$\frac{m_1}{m_2} e^{-2i\alpha} = -\frac{U_{a2} U_{b2}}{U_{a1} U_{b1}}. \quad (7.4.4)$$

Let, $q = \frac{m_1}{m_2} e^{-2i\alpha}$ we get

[†]We also observed that both these textures are disallowed for NH with the most recent data.

[‡] The latest constraint on $|\Delta m_{31}^2|$ comes from T2K and NO ν A including both appearance and disappearance modes [17, 18, 308, 309]. Whereas reanalysis of KamLAND data shows decrease in the value of Δm_{21}^2 and $\sin^2 \theta_{12}$ as discussed in Refs. [297].

$$\alpha = -\frac{1}{2} \text{Arg}(q), \quad (7.4.5)$$

$$|q| = \frac{m_1}{m_2} = \left| -\frac{U_{a2}U_{b2}}{U_{a1}U_{b1}} \right|. \quad (7.4.6)$$

Let us define the ratio of the two mass squared differences as

$$R_\nu = \frac{\Delta m_{21}^2}{|\Delta m_{31}^2|} = \frac{1 - |q|^2}{|q|^2}. \quad (7.4.7)$$

The R_ν defined above can be calculated either using the current neutrino mass squared differences as given in table (7.2) or by calculating $|q|$. If the value of R_ν calculated using $|q|$ falls in the allowed 3σ range of R_ν from the current data, then we say the texture under consideration is allowed by the current data. As given in table (7.2) we vary the Dirac CP phase δ_{13} from $0^\circ < \delta_{13} < 360^\circ$ while the relevant Majorana phase α in the range $0^\circ < \alpha < 180^\circ$ and find the correlations among different parameters, specially the predictions for α and δ_{13} .

We also study the effective Majorana neutrino mass, m_{ee} , governing neutrinoless double beta decay ($0\nu\beta\beta$) for these allowed textures. In three flavor paradigm this can be written as

$$\begin{aligned} m_{ee} &= |\Sigma U_{ei}^2 m_i| \\ &= |m_1 c_{12}^2 c_{13}^2 + m_2 e^{2i\alpha} c_{13}^2 s_{12}^2 + m_3 e^{2i\beta} s_{13}^2|. \end{aligned} \quad (7.4.8)$$

where $c_{ij}(s_{ij}) = \cos \theta_{ij}(\sin \theta_{ij})$, ($i < j$, $i, j = 1, 2, 3$). From the above equation we understand that m_{ee} depends on the Majorana phases but not on the Dirac phase. Various experiments such as CUORE [33], GERDA [34], SuperNEMO [35], KamLAND-ZEN [32] and EXO [36] are looking for signatures for neutrinoless double beta decay ($0\nu\beta\beta$). The current experiments provide bounds on the effective Majorana mass m_{ee} from the non-observation of $0\nu\beta\beta$. For instance, the combined results from KamLAND-ZEN and EXO-200 [32] give the upper bound on the effective Majorana neutrino mass as $m_{ee} < (0.12 - 0.25)$ eV where the range signifies the uncertainty in the nuclear matrix elements. The future experiments can improve this limit by one order of magnitude. Below we discuss the various correlations that we obtain for the allowed textures.

7.4.1 Case I: $m_{e\tau} = 0$

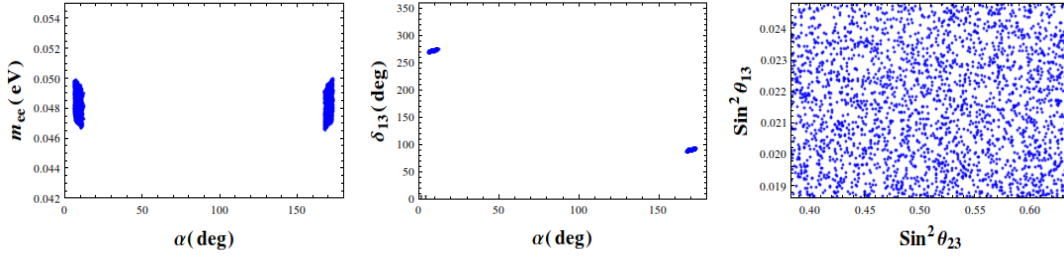


Figure 7.2: Correlation plots of $m_{e\tau} = 0$ for IH with vanishing m_3 in 3 neutrino paradigm.

The Majorana mass matrix element $m_{e\tau}$ in 3-flavor case can be written as

$$m_{e\tau} = m_1 U_{e1} U_{\tau 1} + m_2 U_{e2} U_{\tau 2} e^{2i\alpha} + m_3 U_{e3} U_{\tau 3} e^{2i(\beta + \delta_{13})}. \quad (7.4.9)$$

Imposing the condition of zero texture with vanishing lowest mass ($m_3 = 0$) for IH, we get,

$$\begin{aligned} |m_1 U_{e1} U_{\tau 1} + m_2 U_{e2} U_{\tau 2} e^{2i\alpha}| &= 0, \\ |m_1 c_{12} c_{13} (s_{12} s_{23} - c_{12} c_{23} s_{13} e^{i\delta}) + m_2 s_{12} c_{13} (-c_{12} s_{23} - s_{12} c_{23} s_{13} e^{i\delta})^2 e^{2i\alpha}| &= 0. \end{aligned} \quad (7.4.10)$$

From the above equation we obtain the mass ratio as below

$$\frac{m_2}{m_1} \approx 1 - \frac{s_{13} \cos \delta_{13}}{\tan \theta_{23} s_{12} c_{12}} + \mathcal{O}(s_{13}^2). \quad (7.4.11)$$

The mass ratio $\frac{m_2}{m_1}$ should be greater than 1. For this to happen $\cos \delta_{13}$ should be negative. We find that due to the interplay of the terms $\mathcal{O}(s_{13})$ and $\mathcal{O}(s_{13}^2)$ the phase δ_{13} is restricted to the range $[85^\circ - 95^\circ]$ and $[265^\circ - 275^\circ]$. The effective mass, m_{ee} as function of Majorana phase α is constrained due to very small allowed range of α ($5^\circ < \alpha < 10^\circ$, $170^\circ < \alpha < 175^\circ$) as shown in equation (7.4.8). The allowed range of m_{ee} for this texture is $0.046 \text{ eV} < m_{ee} < 0.05 \text{ eV}$ and which can be probed in future experiments. Also, this texture predicts Dirac CP phase $\sim 270^\circ$ which is in agreement with the indications from the current ongoing oscillation experiments like T2K and NO ν A. There is however no constrain on the values of the neutrino mixing angles θ_{13} and θ_{23} seen in right panel of figure (7.2) for this texture.

7.4.2 Case II: $m_{\tau\tau} = 0$

The Majorana mass matrix element $m_{\tau\tau}$ in 3-flavor case can be written as,

$$m_{\tau\tau} = m_1 U_{\tau 1}^2 + m_2 U_{\tau 2}^2 e^{2i\alpha} + m_3 U_{\tau 3}^2 e^{2i(\beta+\delta_{13})}. \quad (7.4.12)$$

Imposing the condition of texture zero with vanishing lowest mass ($m_3 = 0$) for IH, we get,

$$\begin{aligned} |m_1 U_{\tau 1}^2 + m_2 U_{\tau 2}^2 e^{2i\alpha}| &= 0, \\ |m_1 (s_{12}s_{23} - c_{12}c_{23}s_{13}e^{i\delta})^2 + m_2 (-c_{12}s_{23} - s_{12}c_{23}s_{13}e^{i\delta})^2 e^{2i\alpha}| &= 0. \end{aligned} \quad (7.4.13)$$

The mass ratio from the above equation can be written as

$$\frac{m_2}{m_1} \approx \frac{s_{12}^2}{c_{12}^2} \left[1 - \frac{2 \cot \theta_{23} s_{13} \cos \delta_{13}}{c_{12} s_{12}} \right] + \mathcal{O}(s_{13}^2). \quad (7.4.14)$$

Since this mass ratio $\frac{m_2}{m_1}$ is always greater than 1 from oscillation data, we find that

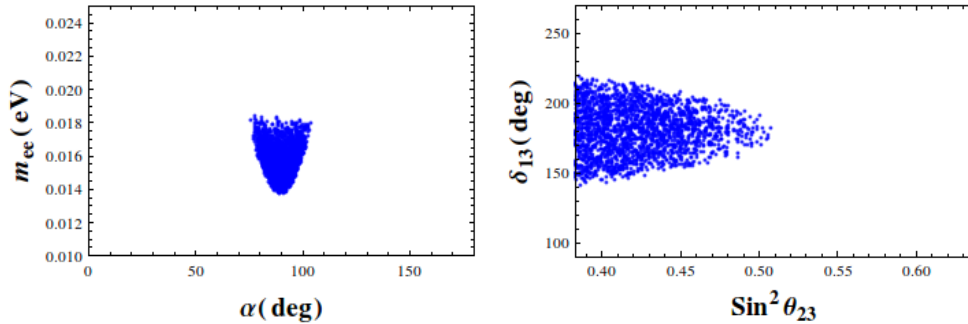


Figure 7.3: Correlation plots of $m_{\tau\tau} = 0$ for IH with vanishing m_3 in 3 neutrino paradigm.

$\cos \delta_{13}$ should be negative for this texture as well. As can be seen from figure 7.3 that δ_{13} is constrained in the range $140^\circ < \delta_{13} < 220^\circ$. We observe that, due to the more constrained values of mass squared differences and θ_{13} from present data, as considered in our analysis, the atmospheric mixing angle θ_{23} is restricted to be below maximal. In the earlier analysis [303–305] there was no preferred octant of θ_{23} . The values of $\theta_{23} > 45^\circ$ are disallowed for this texture as can be seen in figure 7.3. The effective mass, m_{ee} , being function of unknown Majorana phase α as seen in equation (7.4.8) is constrained due to very small allowed range of α ($80^\circ < \alpha < 110^\circ$). The allowed range of m_{ee} for this texture is $0.014 \text{ eV} < m_{ee} < 0.018 \text{ eV}$ which is smaller

compared to the case $m_{e\tau}=0$ where a vanishing element is off-diagonal. The allowed values of the effective mass m_{ee} for diagonal texture $m_{\tau\tau}$ are on the lower side having no overlap with non-diagonal texture zero $m_{e\tau}$. Thus, m_{ee} can be used to distinguish between diagonal and off-diagonal one texture zero classes with a vanishing neutrino mass. Note that allowed ranges of δ_{13} and m_{ee} are more constrained in our analysis as compared to Refs. [303, 304] again due to the recent improved constraints on the mass squared differences and θ_{13} at 3σ . In the next section, we discuss how these correlations can change if we assume specific textures in the MES model giving rise to these forms.

7.5 Comparison of low and high energy neutrino mass matrix elements

In this section, we obtain explicitly the light neutrino neutrino mass matrix (m_ν) (equation 7.2.4), sterile mixing matrix (m_s) (equation 7.2.5) and the active sterile mixing matrix (R) (equation 7.2.7) using the different forms of M_D , M_S and M_R given in section (III) of the MES model. Since in the MES model both the active neutrino mass matrix m_ν and the active sterile mixing matrix R depends on the parameters of M_S , M_D and M_R , this can induce additional correlations between active and sterile sector. Similarly, the mass of the sterile neutrino m_s depends on M_S and M_R . Hence expressing the various variables in terms of the parameters of these matrices one can get some interrelations.

For illustrative purposes, we will discuss three specific cases. In case I and II we discuss $m_{e\tau} = 0$ assuming diagonal structure of M_R and in the case III, we study about $m_{\tau\tau} = 0$ by considering the off diagonal form of M_R . Note that here we consider the complex phases in our calculation. We compare the high energy mass matrix with low energy mass matrix after the decoupling of the eV sterile neutrino as discussed in section II.

- Case I : Considering the forms of $M_S^{(1)}$, $M_D^{(1)}$ and diagonal M_R from equation (7.3.4),

$$M_S^{(1)} = (0, s_2, s_3 e^{i\rho_2}), M_D^{(1)} = \begin{pmatrix} 0 & 0 & a_3 \\ b_1 & 0 & b_3 e^{i\rho_1} \\ c_1 & 0 & 0 \end{pmatrix}, M_R = \text{diag}(r_1, r_2, r_3) \quad (7.5.1)$$

and using them in equations(7.2.4, 7.2.5 and 7.2.7) we get the low energy neutrino mass matrix, the sterile mass and the active sterile mixing matrix as

$$m_\nu^{3 \times 3} = \begin{pmatrix} -\frac{a_3^2 s_2^2}{(r_3 s_2^2 + r_2 s_3^2 e^{2i\rho_2})} & -\frac{a_3 b_3 e^{i\rho_1} s_2^2}{(r_3 s_2^2 + r_2 s_3^2 e^{2i\rho_2})} & 0 \\ \cdot & -\frac{b_1^2}{r_1} - \frac{b_3^2 s_2^2 e^{2i\rho_1}}{(r_3 s_2^2 + r_2 s_3^2 e^{2i\rho_2})} & -\frac{b_1 c_1}{r_1} \\ \cdot & \cdot & -\frac{c_1^2}{r_1} \end{pmatrix}, \quad (7.5.2)$$

$$m_s = -\left(\frac{s_2^2}{r_2} + \frac{s_3^2 e^{2i\rho_2}}{r_3}\right), \quad R = \begin{pmatrix} \frac{a_3 r_2 s_3 e^{i\rho_2}}{(r_3 s_2^2 + r_2 s_3^2 e^{2i\rho_2})} \\ \frac{b_3 r_2 s_3 e^{i(\rho_1 + \rho_2)}}{(r_3 s_2^2 + r_2 s_3^2 e^{2i\rho_2})} \\ 0 \end{pmatrix} = \begin{pmatrix} V_{e4} \\ V_{\mu 4} \\ 0 \end{pmatrix}. \quad (7.5.3)$$

From equation (7.5.2) and (7.5.3) it can be seen that

$$\frac{m_{\mu\tau}}{m_{\tau\tau}} = \frac{b_1}{c_1}, \quad \frac{V_{e4}}{V_{\mu 4}} = \frac{a_3}{b_3} e^{-i\rho_1} = \frac{m_{ee}}{m_{e\mu}} \quad (7.5.4)$$

Here m_{ab} , ($a, b = e, \mu, \tau$) are the low energy neutrino mass matrix elements. The eigenvalues of $m_\nu^{3 \times 3}$ will give the masses of the three active neutrinos. Note that, only allowed hierarchy in our case is IH and hence $m_3 = 0$ and $m_s = m_4 = \sqrt{\Delta m_{43}^2}$. From equation (7.5.4) we get,

$$\left| \frac{V_{e4}}{V_{\mu 4}} \right| = \left| \frac{m_{ee}}{m_{e\mu}} \right|. \quad (7.5.5)$$

We find that the LHS of equation (7.5.5) lies in the range (0.63 – 3.06) whereas RHS lies in (3.9 - 5.9) in their 3σ range. This shows that there is no overlapping between lhs and rhs of equation (7.5.5) and hence disallowed from current neutrino oscillation data. We observe that out of 12 forms of $M_D^{(i)}$, ($i = 1, 2, \dots, 12$) as given in equation (7.3.4 - 7.3.6), 6 of them ($M_D^{(2)}$, $M_D^{(4)}$, $M_D^{(6)}$, $M_D^{(8)}$, $M_D^{(9)}$ and $M_D^{(11)}$) do not lead to the correlation given in equation (7.5.5) and these $M_D^{(i)}$'s are not ruled out. Hence a detail analysis of one of these $M_D^{(i)}$'s is discussed below in Case II.

- Case II : Considering the form of $M_S^{(1)}$, $M_D^{(2)}$ and diagonal M_R given in equation (7.3.4),

$$M_S^{(1)} = (0, s_2, s_3 e^{i\rho_2}), \quad M_D^{(2)} = \begin{pmatrix} 0 & a_2 & 0 \\ b_1 & 0 & b_3 e^{i\rho_1} \\ c_1 & 0 & 0 \end{pmatrix}, \quad M_R = \text{diag}(r_1, r_2, r_3) \quad (7.5.6)$$

and using them in equations (7.2.4, 7.2.5 and 7.2.7) we get the texture $m_{e\tau} = 0$,

$$m_\nu^{3 \times 3} = \begin{pmatrix} -\frac{a_2^2 s_3^2 e^{2i\rho_2}}{(r_3 s_2^2 + r_2 s_3^2 e^{2i\rho_2})} & \frac{a_2 b_3 s_2 s_3 e^{i(\rho_1 + \rho_2)}}{(r_3 s_2^2 + r_2 s_3^2 e^{2i\rho_2})} & 0 \\ \cdot & -\frac{b_1^2}{r_1} - \frac{b_3^2 s_3^2 e^{2i\rho_1}}{(r_3 s_2^2 + r_2 s_3^2 e^{2i\rho_2})} & -\frac{b_1 c_1}{r_1} \\ \cdot & \cdot & -\frac{c_1^2}{r_1} \end{pmatrix}. \quad (7.5.7)$$

The sterile mass and active sterile mixing becomes

$$m_s = -\left(\frac{s_2^2}{r_2} + \frac{s_3^2 e^{2i\rho_2}}{r_3}\right), \quad R = \begin{pmatrix} \frac{a_2 r_3 s_2}{(r_3 s_2^2 + r_2 s_3^2 e^{2i\rho_2})} \\ \frac{b_3 r_2 s_3 e^{i(\rho_1 + \rho_2)}}{(r_3 s_2^2 + r_2 s_3^2 e^{2i\rho_2})} \\ 0 \end{pmatrix} = \begin{pmatrix} V_{e4} \\ V_{\mu 4} \\ 0 \end{pmatrix}. \quad (7.5.8)$$

It can be seen from the above equations that

$$\frac{m_{\mu\tau}}{m_{\tau\tau}} = \frac{b_1}{c_1}, \quad \frac{m_{ee}}{m_{e\mu}} = -\frac{a_2 s_3}{b_3 s_2} e^{i(\rho_2 - \rho_1)}. \quad (7.5.9)$$

From equation (7.5.7) we get the following relation between the light neutrino mass matrix elements,

$$m_{\mu\mu} = \frac{b_1}{c_1} m_{\mu\tau} - \frac{b_3 s_2}{a_2 s_3} e^{i(\rho_1 - \rho_2)} m_{e\mu} = \frac{m_{e\mu}^2}{m_{ee}} + \frac{m_{\mu\tau}^2}{m_{\tau\tau}},$$

which implies,

$$m_{ee} = \frac{m_{e\mu}^2 m_{\tau\tau}}{m_{\mu\mu} m_{\tau\tau} - m_{\mu\tau}^2}. \quad (7.5.10)$$

To obtain equation (7.5.10) we have used the correlations of equation (7.5.9). Now to test the viability of these structures of M_D , M_R and M_S , we look for the parameter space in which both the conditions $m_{e\tau} = 0$ and equation (7.5.10) are satisfied simultaneously. In the upper panels of figure (7.4), we have plotted the correlations obtained between different low energy parameters in this scenario. Comparing these correlations with figure (7.2) (which corresponds to only $m_{e\tau} = 0$), we find that the MES model disfavours a large area in the $\sin^2 \theta_{23} - \sin^2 \theta_{13}$ plane and allows θ_{23} values in the lower octant : $0.383 < \sin^2 \theta_{23} < 0.42$ whereas the admissible values of θ_{13} ($0.021 < \sin^2 \theta_{13} < 0.0248$) are near the higher side of it's allowed range. However the values of α and m_{ee} which are predicted by the two cases are similar. The prediction of the texture with $m_{e\tau} = 0$

is $6^\circ < \alpha < 13^\circ$ and $167^\circ < \alpha < 174^\circ$ while the MES model predicts a slightly constrained range $11.7^\circ < \alpha < 13^\circ$ and $167^\circ < \alpha < 168.1^\circ$. In this case we also obtain another correlation for sterile neutrino mass from this model of the form,

$$m_s = \left| -\frac{m_{e\mu}}{V_{e4}V_{\mu4}} \right|. \quad (7.5.11)$$

In the lower panels of figure (7.4), we have plotted the prediction of m_s as

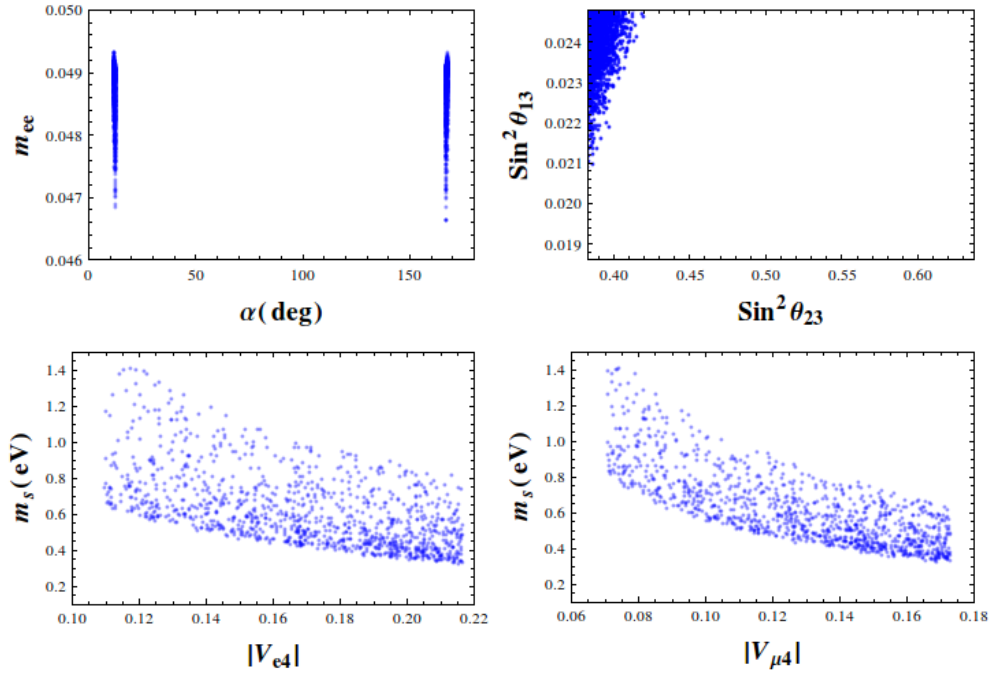


Figure 7.4: Correlation plots for case II.

given by equation (7.5.11) by varying V_{e4} and $V_{\mu4}$ within their allowed range as given in table (7.2). This is obtained when both the conditions i.e., $m_{e\tau} = 0$ and equation (7.5.10) is satisfied simultaneously. From the figures we see that the prediction of m_s by this model is consistent with data coming from the SBL experiments.

- Case III : Considering the cases for the off-diagonal forms of M_R given in Eqs.(7.3.7-7.3.15), we find that out of the 36 $M_D^{(i)}$, ($i = 13, 14, \dots, 48$), 19 cases lead to exactly the same correlation depicted by equation (7.5.5). This is not allowed from current oscillation data as discussed earlier. Among the remaining 17 cases 11 $M_D^{(i)}$ (for $i = 17, 19, 22, 23, 30, 32, 34, 42, 43, 44$ and 45) lead to a

correlation of the form,

$$\left| \frac{V_{e4}}{V_{\mu4}} \right| = \left| \frac{m_{e\tau}}{m_{\mu\tau}} \right|. \quad (7.5.12)$$

This is also not satisfied by current neutrino oscillation data as the RHS of equation (7.5.12) lies in the range (3.8 – 4.7) showing no overlapping with LHS. The remaining six forms of $M_D^{(i)}$ are $M_D^{(18)}$, $M_D^{(21)}$, $M_D^{(29)}$, $M_D^{(33)}$, $M_D^{(41)}$ and $M_D^{(46)}$. All these forms of M_D and the corresponding forms of M_R and M_S lead to neutrino mass matrix with $m_{\tau\tau} = 0$. We found that, all these M_D 's lead a correlation of the form,

$$\left| \frac{V_{e4}}{V_{\mu4}} \right| = \left| \frac{m_{e\mu}}{m_{\mu\mu}} \right| \quad (7.5.13)$$

which is satisfied by current oscillation data. The RHS of equation (7.5.12) lies in the range (1.8 – 2.3) which shows complete overlap with LHS (0.63- 3.06). For illustration, we consider $M_D^{(18)}$ with corresponding M_R and $M_S^{(1)}$ and using them in equations (7.2.4, 7.2.5 and 7.2.7) we get ,

$$m_\nu^{3 \times 3} = \begin{pmatrix} \frac{a_1 s_2 (a_1 s_2 r_1 + 2 a_3 s_3 r_2 e^{i\rho_2})}{r_2^2 s_3^2 e^{2i\rho_2}} & \frac{b_1 s_2 (a_1 s_2 r_1 + a_3 s_3 r_2 e^{i\rho_2})}{r_2^2 s_3^2 e^{2i\rho_2}} & -\frac{a_1 c_2}{r_2} \\ \cdot & \frac{b_1^2 s_2^2 r_1}{r_2^2 s_3^2} e^{-2i\rho_2} & -\frac{b_1 c_2}{r_2} \\ \cdot & \cdot & 0 \end{pmatrix}, \quad (7.5.14)$$

$$m_s = -\frac{s_3^2}{r_1} e^{2i\rho_2}, \quad R = \begin{pmatrix} \frac{a_1 s_2 r_1 + a_3 s_3 r_2 e^{i\rho_2}}{r_2 s_3^2 e^{2i\rho_2}} \\ \frac{b_1 s_2 r_1}{r_2 s_3^2 e^{2i\rho_2}} \\ 0 \end{pmatrix} = \begin{pmatrix} V_{e4} \\ V_{\mu4} \\ 0 \end{pmatrix}. \quad (7.5.15)$$

From the above matrices we find the following correlation,

$$m_s = \left| -\frac{m_{e\mu}}{V_{e4} V_{\mu4}} \right|. \quad (7.5.16)$$

Also the correlation mentioned by equation (7.5.13). We find that both the equations (7.5.13 and 7.5.16) are consistent with the current oscillation data. The simultaneous validity of equations (7.5.13 and 7.5.16) lead to light sterile neutrino mass in the range $1.4 \text{ eV} < m_s < 3.5 \text{ eV}$ which is marginally allowed by global analysis as seen from figure (7.5). However, individual experiments (MINOS, IceCube, Daya Bay) still allow higher value of sterile neutrino mass [310–313].

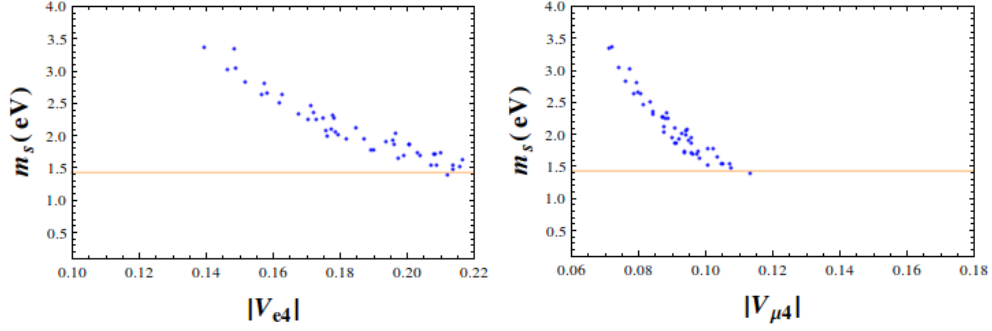


Figure 7.5: Sterile neutrino mass from Eqs.(7.5.16) for $m_{\tau\tau} = 0$. The yellow line is the current upper bound on m_s as given by global analysis of 3+1 neutrino oscillation data.

7.5.1 NLO correction for MES model

In section (7.3), the structures of various mass matrices are obtained using the leading order expression of $m_\nu^{3\times 3}$ as given by equation (7.2.4) which give rise to texture zeros with exact cancellation. However, if $M_D/M_S \sim 0.1$, NLO corrections can be important. In this section, we discuss the effect of NLO correction terms for the MES model corresponding to the allowed texture zeros. The NLO correction term can be calculated following the standard algorithm given in Ref. [39]. To calculate the NLO term, let us rewrite equation (7.2.3) in the form,

$$M_\nu^{4\times 4} = \begin{pmatrix} \mathcal{M}_L & \mathcal{M}_D^T \\ \mathcal{M}_D & \mathcal{M}_R \end{pmatrix} \quad (7.5.17)$$

where,

$$\mathcal{M}_L = M_D M_R^{-1} M_D^T, \quad \mathcal{M}_D = M_S (M_R^{-1})^T M_D^T, \quad \mathcal{M}_R = M_S M_R^{-1} M_S^T \quad (7.5.18)$$

$$\begin{aligned} (m_\nu^{3\times 3})_{NLO} &= \frac{1}{2} [\mathcal{M}_D^T \mathcal{M}_R^{-1} \mathcal{M}_R^{-1*} \mathcal{M}_D^* \mathcal{M}_L + (\text{last term})^T] \\ &\quad - \frac{1}{2} \mathcal{M}_D^T \mathcal{M}_R^{-1} [\mathcal{M}_D \mathcal{M}_D^\dagger \mathcal{M}_R^{-1*} + (\text{last term})^T] \mathcal{M}_R^{-1} \mathcal{M}_D \\ &= \frac{1}{2} [M_D M_R^{-1} M_S^T (M_S M_R^{-1} M_S^T)^{-1} (M_S^* M_R^{-1*} M_S^\dagger)^{-1} M_S^* (M_R^{-1})^\dagger M_D^\dagger M_D M_R^{-1} M_D^T \\ &\quad + (\text{last term})^T] \\ &\quad - \frac{1}{2} M_D M_R^{-1} M_S^T (M_S M_R^{-1} M_S^T)^{-1} [M_S (M_R^{-1})^T M_D^T M_D^* (M_R^{-1})^* M_S^\dagger \\ &\quad (M_S M_R^{-1} M_S^T)^{-1*} + (\text{last term})^T] (M_S M_R^{-1} M_S^T)^{-1} M_D M_R^{-1} M_S^T \end{aligned} \quad (7.5.19)$$

In the second line we use the form of \mathcal{M}_L , \mathcal{M}_D and \mathcal{M}_R as given by equation (7.5.18) to obtain the final form given by equation (7.5.19). We see that the contribution of the

NLO terms of equation (7.5.19) are proportional to $M_D^4/M_R M_S^2$. This implies that a term of the order $M_D^4/M_R M_S^2$ will add to every term of $m_\nu^{3 \times 3}$ as given by the equation (7.5.7). To get the specific form of NLO correction term, in equation (7.5.19), we use the specific forms of M_D , M_R and M_S used for obtaining equation (7.5.7). The NLO correction term we obtain for (1,3) element of equation (7.5.7) is $\sim \frac{a_3 b_3 b_1 c_1 r_2^2 s_3^2}{2r_1(r_3 s_2^2 + r_2 s_3^2)^2}$, which is of the order of $M_D^4/M_R M_S^2$, where a_3 , b_3 , b_1 , c_1 are elements of M_D , r_1 , r_2 are elements of M_R and s_2 , s_3 are elements of M_S . We see here that because of NLO corrections, we no longer have exact cancellation leading to $m_{e\tau} = 0$, unlike the leading order case. But, if we consider representative values of parameters say, $M_D \sim 80$ GeV, $M_R \sim 6 \times 10^{14}$ GeV and $M_S \sim 1000$ GeV then we find that $m_\nu \sim 0.011$ eV, $m_s \sim 1.6$ eV, $R \sim 0.1$ and $\text{NLO} \sim 10^{-5}$ eV. In figure (7.6) we show the allowed parameter spaces of M_D , M_R and M_S which can lead to NLO correction term $\sim 10^{-5}$ eV or less.[§] Hence, there exist a parameter space where we can safely neglect NLO correction terms in our analysis compared to leading order terms and consider the texture zero even with the inclusion of the NLO term.[¶] Thus, all the model predictions corresponding to leading order terms remain unchanged. Note that similar conclusions can also be obtained for the texture $m_{\tau\tau} = 0$.

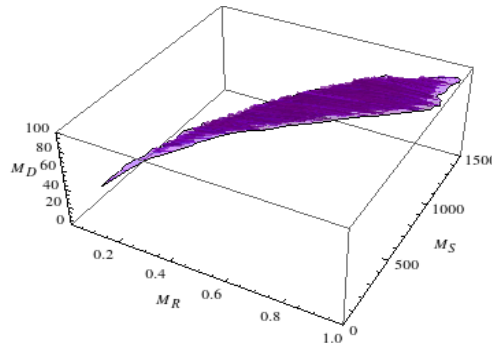


Figure 7.6: This plot shows the allowed parameter spaces of M_D (GeV), M_R (in units of 10^{15} GeV) and M_S (GeV) which lead to NLO correction term $\sim 10^{-5}$ eV or less.

7.6 Symmetry realization

Singular one zero neutrino mass matrices can be realized using a discrete Abelian flavor symmetry within the context of the MES mechanism. Earlier in Ref. [296] authors

[§]In our numerical analysis texture zero (say, $m_{e\tau} = 0$) corresponds to $m_{e\tau} = 10^{-5}$ eV.

[¶]We notice that the set of M_D , M_R and M_S which do not give $\text{NLO} \sim 10^{-5}$ eV do not give the one zero textures.

studied the possibilities to enforce zero textures in arbitrary entries of the fermion mass matrices by means of Abelian symmetries in the context of the type - I seesaw mechanism. We adopt the same approach to probe the zero textures of m_ν in the context of the MES mechanism. We observe that one zero textures of m_ν with a vanishing mass can be realized by $Z_8 \times Z_2$ symmetry. To realize the texture structures we extend the SM particle composition by three right handed neutrinos ($\nu_{eR}, \nu_{\mu R}, \nu_{\tau R}$) as required in the MES model and two more Higgs doublets (ϕ', ϕ'') in addition to the SM one (ϕ). Few $SU(2)_L$ scalar singlets ($\chi_i, i = 1, 2$) are required to realize diagonal M_R whereas two singlets $\lambda_i, i = 1, 2$ helps in realizing one zero texture structure of M_S . Note that the model that we discuss here to get the zero texture structure is general, flexible and in no way unique. The additional discrete group Z_2 is introduced to restrict some of the unwanted terms in the Lagrangian. For illustration, we present the detailed symmetry realization of our two viable textures of m_ν ($m_{e\tau}, m_{\tau\tau} = 0$). The particle assignments for ($m_{e\tau} = 0$ which is allowed by current data (case II) under the action of $Z_8 \times Z_2$ symmetry are given in table (7.3). According to the charge assignments of the lep-

Lepton doublet	$(Z_8 \times Z_2)$	RH Singlet	$(Z_8 \times Z_2)$	ν fields	$(Z_8 \times Z_2)$	Higgs doublet	$(Z_8 \times Z_2)$
\bar{D}_{L_e}	$(\omega^6, -1)$	e_R	$(\omega^2, -1)$	ν_{eR}	$(\omega^5, 1)$	ϕ	$(1, 1)$
\bar{D}_{L_μ}	$(\omega^3, 1)$	μ_R	$(\omega^5, 1)$	$\nu_{\mu R}$	$(\omega^2, -1)$	ϕ'	$(\omega^3, 1)$
\bar{D}_{L_τ}	$(\omega^5, 1)$	τ_R	$(1, 1)$	$\nu_{\tau R}$	$(1, 1)$	ϕ''	$(\omega^2, 1)$

Table 7.3: Here, \bar{D}_{L_l} denote $SU(2)_L$ doublets and l_R, ν_{l_R} ($l = e, \mu, \tau$) are the right-handed (RH) $SU(2)_L$ singlet for charged lepton and neutrino fields respectively. Also, ϕ, ϕ' and ϕ'' are the Higgs doublets.

tonic field given in table (7.3) the bilinears $\bar{D}_{L_l} l_R, \bar{D}_{L_l} \nu_{l_R}$ and $\nu_{l_R}^T C^{-1} \nu_{l_R}$ relevant for M_l, M_D and M_R transform as

$$\bar{D}_{L_l} l_R \sim \begin{pmatrix} 1 & \omega^3 & \omega^6 \\ \omega^5 & 1 & \omega^3 \\ \omega^7 & \omega^2 & \omega^5 \end{pmatrix}, \bar{D}_{L_l} \nu_{l_R} \sim \begin{pmatrix} \omega^3 & 1 & \omega^6 \\ 1 & \omega^5 & \omega^3 \\ \omega^2 & \omega^7 & \omega^5 \end{pmatrix}, \nu_{l_R} \nu_{l_R}^T \sim \begin{pmatrix} \omega^2 & \omega^7 & \omega^5 \\ \omega^7 & \omega^4 & \omega^2 \\ \omega^5 & \omega^2 & 1 \end{pmatrix}, \quad (7.6.1)$$

where $\omega = e^{\pi i/4}, \omega^8 = 1$. We introduce three $SU(2)_L$ doublet Higgs (ϕ, ϕ', ϕ''). One of these Higgs doublet ϕ , is invariant under Z_8 while the other two fields transforms as: $\phi' \rightarrow \omega^3 \phi'$ ($\tilde{\phi}' \rightarrow \omega^5 \tilde{\phi}'$) and $\phi'' \rightarrow \omega^2 \phi''$ ($\tilde{\phi}'' \rightarrow \omega^6 \tilde{\phi}''$). The $(Z_8 \times Z_2)$ invariant

Yukawa Lagrangian than becomes

$$\begin{aligned}
 -\mathcal{L}_Y = & Y_{ee}\bar{D}_{L_e}e_R\phi + Y_{\mu\mu}\bar{D}_{L_\mu}\mu_R\phi + Y_{\tau\tau}\bar{D}_{L_\tau}\tau_R\phi' + \\
 & Y_{e\mu}\bar{D}_{L_e}\nu_{\mu R}\tilde{\phi} + Y_{\mu e}\bar{D}_{L_\mu}\nu_{e R}\tilde{\phi} + Y_{\mu\tau}\bar{D}_{L_\mu}\nu_{\tau R}\tilde{\phi}' + Y_{\tau e}\bar{D}_{L_\tau}\nu_{e R}\tilde{\phi}'' + h.c.
 \end{aligned} \tag{7.6.2}$$

Here all $\tilde{\phi} = i\tau_2\phi^*$. The Higgs fields acquires the vacuum expectation values $\langle\phi\rangle_o \neq 0$ and results in the M_l and M_D of the following form,

$$M_l = \begin{pmatrix} m_e & 0 & 0 \\ 0 & m_\mu & 0 \\ 0 & 0 & m_\tau \end{pmatrix}, M_D = \begin{pmatrix} 0 & a_2 & 0 \\ b_1 & 0 & b_3 \\ c_1 & 0 & 0 \end{pmatrix}. \tag{7.6.3}$$

Here $m_e = Y_{ee}\langle\phi\rangle_o$, $m_\mu = Y_{\mu\mu}\langle\phi\rangle_o$, $m_\tau = Y_{\tau\tau}\langle\phi'\rangle_o$. The elements of M_D are $a_2 = Y_{e\mu}\langle\phi^*\rangle_o$, $b_1 = Y_{\mu e}\langle\phi^*\rangle_o$, $b_3 = Y_{\mu\tau}\langle\phi'^*\rangle_o$ and $c_1 = Y_{\tau e}\langle\phi''^*\rangle_o$. For the right-handed Majorana mass matrix (M_R) and for the mass matrix M_S , we introduce few $SU(2)_L$ scalar singlets and their transformation under $Z_8 \times Z_2$ is given in the table (7.4). Thus

Scalar singlet	$(Z_8 \times Z_2)$	Scalar singlet	$(Z_8 \times Z_2)$
χ_1	$(\omega^6, 1)$	λ_1	$(1, 1)$
χ_2	$(\omega^4, 1)$	λ_2	$(\omega^2, -1)$

Table 7.4: Here, scalar singlet χ_1 and χ_2 give M_R whereas λ_1 and λ_2 give M_S .

the mass matrices M_R and M_S becomes,

$$M_R = \begin{pmatrix} r_1 & 0 & 0 \\ 0 & r_2 & 0 \\ 0 & 0 & r_3 \end{pmatrix}, M_S = \begin{pmatrix} 0 & s_2 & s_3 \end{pmatrix}. \tag{7.6.4}$$

We also give the transformation to the singlet field S as $(\omega^6, -1)$ under $(Z_8 \times Z_2)$ which will prevent the term of the form $\bar{S}^c S$ as demand by the MES model will still give the correct form of M_S . Using the minimal extended type I seesaw given in equation (7.2.4) with the mass matrices M_D , M_R and M_S as discussed above leads to effective neutrino mass matrix m_ν with a texture zero at (1,3) position.

Similarly, one can assign the various fields transformation under the action of $(Z_8 \times Z_2)$ to obtain the texture with $m_{\tau\tau} = 0$. The form of $M_D^{(18)}$, M_R and M_S used to get $m_{\tau\tau} = 0$ are given in equation (7.3.8). We summarize the fields transformations in the table (7.5). Here, no extra scalar singlet is needed to obtain the mass structure of

M_R which has $L_e - L_\mu$ symmetry and for M_S we need two scalar singlets (λ_1, λ_2) which transform under $Z_8 \times Z_2$ as $(\omega^2, 1)$ and $(\omega^7, -1)$ respectively. We also give transformation to singlet field S as $(\omega, 1)$ under $(Z_8 \times Z_2)$ which will prevent the term $\overline{S^c}S$. Note that symmetry realization of this texture is more economical than the $m_{e\tau} = 0$ texture.

Lepton doublet	$(Z_8 \times Z_2)$	RH Singlet	$(Z_8 \times Z_2)$	ν fields	$(Z_8 \times Z_2)$	Higgs doublet	$(Z_8 \times Z_2)$
\bar{D}_{L_e}	(1, 1)	e_R	(1, 1)	ν_{eR}	$(\omega^3, 1)$	ϕ	(1, 1)
\bar{D}_{L_μ}	$(\omega^5, -1)$	μ_R	$(\omega^3, -1)$	$\nu_{\mu R}$	$(\omega^5, 1)$	ϕ'	$(\omega^3, 1)$
\bar{D}_{L_τ}	$(\omega^3, 1)$	τ_R	$(\omega^2, 1)$	$\nu_{\tau R}$	(1, -1)		

Table 7.5: The fields descriptions are same as given in table (7.3).

7.7 Summary

In this chapter we describe the low energy phenomenology of the minimal extended type-I seesaw model which can accommodate an eV scale light sterile neutrino. This model is motivated by the recent experimental evidences which support the existence of light sterile neutrinos in addition to three active neutrinos. To formulate the MES model, apart from three right handed neutrinos, an extra gauge singlet S is added to the SM. This model gives rise to one massless, two active neutrinos in the sub-eV scale and one sterile neutrino in the eV scale.

We obtain different textures of fermion mass matrices, M_D , M_R and M_S that give rise to phenomenologically allowed zero textures in the low energy neutrino mass matrix, m_ν . The maximum number of zeros in M_D that results in viable m_ν are found to be five. Thus, there are 126 different possible structures of M_D to be probed. We consider four possible structures of M_R with one diagonal and three non diagonal forms. The maximum number of zeros in M_S is one as two zeros do not result in phenomenologically viable textures of m_ν . This leads to three possible structures of M_S . After analysing all the different combinations we obtain only two viable one zero textures of m_ν ($m_{e\tau} = 0$ and $m_{\tau\tau} = 0$) with different possible structures of M_D , M_R and M_S . We study these textures of m_ν in the light of the current oscillation data. Both these textures have inverted hierarchical mass spectrum and we get constraints on observables

like effective Majorana neutrino mass m_{ee} and Dirac CP phase δ_{13} .

Next we studied the predictions of the MES model for the Yukawa matrices that gave viable forms of m_ν and check whether any extra correlations can come from the model. We find that some of the Yukawa matrices which can generate allowed one zero textures $m_{e\tau} = 0$ and $m_{\tau\tau} = 0$ in the active neutrino mass matrix, m_ν , cannot satisfy the extra correlations coming from the predictions of the MES model. Our analysis reveals that due to these additional correlations among the $126 \times 4 \times 3 = 1512$ possible combinations of M_D , M_R and M_S , only 6 combinations giving $m_{e\tau} = 0$ and other 6 combinations giving $m_{\tau\tau} = 0$ are allowed from the current oscillation data. The 6 allowed combinations which give $m_{e\tau} = 0$, reveal severe restrictions on the values of θ_{23} and θ_{13} due to the extra correlations in the MES model and only the lower octant of θ_{23} and relatively higher values of θ_{13} remains allowed. In addition an interesting correlation is obtained, connecting the mass of the sterile neutrino to the active sterile mixing parameters, which also involves the light neutrino masses and mixing. For $m_{e\tau} = 0$ the prediction for the sterile neutrino mass obtained from the MES model is in complete agreement with what is obtained from global analysis. The texture, $m_{\tau\tau} = 0$ also predicts a correlation for sterile neutrino mass. This however is in marginal agreement with the global analysis.

We also explored the consequences of NLO correction terms in our analysis and depicted the parameter space in M_D , M_R and M_S for which the NLO corrections can be neglected as compared to the leading order term. Finally, working within the framework of the MES mechanism, we present a discrete Abelian symmetry model based on $Z_8 \times Z_2$ group leading to the two phenomenologically allowed zero textures of m_ν .

In this chapter, we analysed the low energy predictions of the minimal extended seesaw model that can give an eV scale sterile neutrino. The results described in our analysis shows the compatibility of this model with the neutrino oscillation data. We also find correlations that can be tested in future experiments. This kind of study is indispensable to test the viability of a given model in the context of present and forthcoming neutrino oscillation experiments.

Chapter 8

Summary

In this doctoral work, we have addressed some interesting aspects of neutrino physics from the phenomenological as well as theoretical point of view. These are mainly,

1. Study of degeneracies in neutrino oscillation parameters and their resolutions using neutrino oscillation experiments.
2. Flavor antisymmetric models with respect to A_5 discrete group, which predicts inverted neutrino mass ordering and mixing angles consistent with experimental data.
3. Sterile neutrino phenomenology considering “minimal extended type-I seesaw” mechanism.

The parameters involved in three flavor neutrino oscillations are : two mass squared differences (Δm_{j1}^2 , $j = 2, 3$), three mixing angles (θ_{ij} , $i < j = 1, 2, 3$) and the CP phase δ_{CP} . At the present era, the major unknown neutrino oscillation parameters are the mass hierarchy, the octant of the mixing angle θ_{23} and the CP phase δ_{CP} . Determination of these unknowns using various neutrino oscillation experiments and exploring the synergy between different experiments constitute a dominant part of the thesis. In this respect, we concentrate on four neutrino oscillation experiments namely, T2K, NO ν A, DUNE and ICAL@INO^{*}. It is well known that presence of parameter degeneracies are the major drawbacks that these experiments can come across to determine

^{*}Note that T2K and NO ν A are the currently operating long baseline (LBL) experiments whereas DUNE and ICAL@INO are the next generation LBL and atmospheric neutrino experiments respectively.

these unknowns. We study the synergy between the different LBL experiments and the combined effect of LBL and atmospheric neutrino experiments to resolve these degeneracies. In this thesis, the first three chapters are introductory whereas in the next four chapters, we have discussed the work that has been accomplished during the doctoral period.

We start the thesis with a discussion of the history of the discovery of neutrino in chapter (1). Later, we briefly discuss neutrinos in the SM, neutrino oscillation which implies neutrinos have non-zero masses and mixing angles and hence physics beyond the SM. We also briefly describe the generation of neutrino masses via seesaw mechanism. Next, we present a brief overview regarding neutrinos beyond three flavors and mention some of the unresolved issues in neutrino physics. In chapter (2), we discuss the different sources of neutrinos. We also give brief descriptions about the various detector technologies. We end this chapter with a discussion on the specifications of different experiments that we have considered in this thesis. In chapter (3), we present the formalism of neutrino oscillations and give the neutrino oscillation probabilities for both vacuum as well as matter. We also mention the current status of the neutrino oscillation parameters and various unknowns in neutrino oscillation physics.

In chapter (4), we focus on the physics reach of T2K, NO ν A and ICAL@INO experiments to resolve the presence of degeneracies in neutrino oscillation parameters. We study these degeneracies in detail and propose that different degeneracies can be studied in a most comprehensive manner by considering the generalized “hierarchy– $\theta_{23} - \delta_{CP}$ ” degeneracy. We show that, depending on whether the wrong-hierarchy and/or wrong-octant solutions occur with right or wrong values of δ_{CP} , there can be a total of eight possibilities. We describe the presence of parameter degeneracies at the probability level for T2K, NO ν A and INO. Considering six years of neutrino runs for NO ν A, we identify which of these degenerate solutions actually occur for different representative choices of true parameters at the χ^2 -level. We discuss the role of antineutrinos, considering NO ν A[3+3], for the resolution of different degenerate solutions. Next, we present the results combining NO ν A[3+3] with T2K[8+0]. It is seen that the synergy between T2K and NO ν A helps in removing the wrong hierarchy-right octant-wrong δ_{CP} solutions for true $\delta_{CP} = 0^\circ, 90^\circ$ at 1σ C.L. For true $\delta_{CP} = -90^\circ$,

$\text{NO}\nu\text{A}$ itself is sufficient for removing this degeneracy at 2σ C.L. The remaining degenerate solutions at 2σ can be resolved by adding INO data with $\text{NO}\nu\text{A}$ and T2K. Addition of INO also helps to improve the precision of the parameters θ_{23} and δ_{CP} .

We illustrate the potential and proficiency of the next generation superbeam experiment DUNE (L=1300 km) to determine the unknowns in neutrino oscillation parameters in chapter (5). In particular, we focus on the study of octant and δ_{CP} sensitivity. We analyze in detail the physics of the antineutrinos for the DUNE baseline and what kind of synergy can be offered by the addition of antineutrinos with the pure neutrino runs. We also illustrate to what extent the broad-band nature of the beam and enhanced matter effect influences the octant sensitivity. We observe that for the DUNE baseline addition of antineutrinos are helpful in general. We find that when antineutrinos are combined with neutrinos then the overall χ^2 minimum is still governed by the neutrinos because of higher statistics. At this point the antineutrino contribution to χ^2 is higher and hence adding these enhances octant sensitivity in spite of the associated octant degeneracy. We also describe how addition of antineutrinos affect the fraction of δ_{CP} values for which CP sensitivity can be probed at 3σ level.

From a theoretical point of view, it is always challenging to formulate a model which can explain the neutrino mixing pattern. In this context, we illustrate consequences of an ansatz of flavor antisymmetry in the context of the flavor group A_5 in chapter (6). We assume that the Majorana neutrino mass matrix M_ν and the charged lepton mass matrix M_l satisfy, $S_\nu^T M_\nu S_\nu = -M_\nu$, $T_l^\dagger M_l M_l^\dagger T_l = M_l M_l^\dagger$ with respect to some discrete groups S_ν, T_l contained in A_5 group. These assumptions constrain the leptonic mixing pattern and lead to a degenerate pair of neutrinos in addition to a massless one i.e. flavors inverted mass ordering. This is a good zeroth order prediction. Small perturbations splitting the degeneracy can lead to viable neutrino masses. We consider discrete subgroups Z_2 and $Z_2 \times Z_2$ of A_5 as residual symmetries of the neutrino mass matrix, M_ν and discrete groups Z_3, Z_5, Z_2 and $Z_2 \times Z_2$ contained in A_5 as symmetries of the charged lepton mass matrix, $M_l M_l^\dagger$ and calculate the resulting mixing patterns at the leading order in all the cases. The third column of the mixing matrix and hence the angles θ_{13}, θ_{23} get determined at this order. We also provide the group theoretical derivation of the mixing patterns in A_5 with a concrete example.

In chapter (7), we consider the low energy phenomenology of the “minimal extended type-I seesaw” (MES) model which can give an eV scale light sterile neutrino. In this model, Standard Model is extended with 3-right handed neutrinos and an extra gauge singlet S . The lightest active neutrino always remains massless whereas the remaining two are in the sub-eV scale and the sterile neutrino is in the eV scale. After scrutinizing all the possible combinations of fermion mass matrices, remarkably, we find the only phenomenological allowed possibilities are— two one-zero textures of m_ν ($m_{e\tau} = 0$ and $m_{\tau\tau} = 0$). We study these textures of m_ν in light of the current oscillation data and notice that both these textures predict inverted mass ordering. Next, we discuss the predictions of the MES model and obtain extra correlations among neutrino oscillation parameters which can be tested in future oscillation experiments. We also illustrate the importance of next-to-leading order correction terms in this model. Finally, working within the framework of the MES model, we present a simple discrete Abelian symmetry group $Z_8 \times Z_2$ which explains allowed zero textures of m_ν .

Neutrino physics has now entered an era of precision studies. During the last two decades, tremendous growth has happened in the area of experimental neutrino physics. This has also contributed immensely to the advancement of our knowledge about neutrino properties. The worldwide effort now is to determine the remaining unknown parameters and to understand the origin of neutrino masses and mixings which is also the task undertaken in this thesis. It is expected that the ongoing neutrino oscillation experiments will be able to shed light on the above unknowns and set the agenda for the future experiments. Some of the noteworthy future experiments are, DUNE, T2HK, T2HKK, INO, PINGU, etc. Apart from the determination of the oscillation parameters, the prospect of probing new physics like, non-standard interactions, sterile neutrinos, CPT violation, etc. has also been studied widely in the literature. Once there is some definite knowledge about the three unknowns, the exploration of new physics studies may gain momentum in the future. Also a better knowledge of the unknown oscillation parameters can provide further insight into allowed theoretical scenarios. In this direction, sufficient theoretical progress has been made already. Therefore, in coming times with new experimental results from the ambitious neutrino projects, the study of neutrino physics will be even more exciting and challenging.

Appendix A

Numerical Details

A.1 Event calculation

In the present appendix, we illustrate the calculation of the number of neutrino events that are detected in a neutrino detector. We also explain the χ^2 analysis procedure that has been performed in our study. Let us consider a neutrino oscillation experiment where we are interested to look for the oscillation probability $P_{\mu e}(\{s\})$ i.e. the probability that a neutrino with an initial flavor ν_μ is converted to a final flavor ν_e *. Let us denote Φ_μ as the ν_μ flux at the detector. Then the number of ν_e events at the detector can be written as

$$N \simeq \Phi_\mu P_{\mu e}(\{s\}) \sigma_e, \quad (\text{A.1.1})$$

where σ_e denotes the cross section of the ν_e .

Equation (A.1.1) provides the schematic form for the calculation of number of neutrino events. However, this is not a simple task because of the process of reconstruction of the neutrino energy. We like to mention here that in any neutrino oscillation experiment the detector does not detect neutrinos directly. When neutrinos pass through a medium, their interactions produce charged leptons corresponding to the given flavor of neutrino. The energy of these particles are measured from which the neutrino energy is reconstructed using some definite algorithm. In our work, we parameterize this using a simple Gaussian resolution or smearing function involving true and reconstructed

*Note that $\{s\} = \{\Delta m_{21}^2, \Delta m_{31}^2, \theta_{12}, \theta_{13}, \theta_{23}, \delta_{CP}\}$ denotes the set of oscillation parameters.

neutrino energy,

$$\mathcal{R}(E_t, E_m) = N_e e^{-\left[\frac{(E_t - E_m)^2}{2\sigma_E^2}\right]}, \quad (\text{A.1.2})$$

where $\mathcal{R}(E_t, E_m)$ is the *smearing function*, E_t, E_m are the *true* and *measured* energy of the neutrinos respectively. N_e is the normalization coefficient and σ_E is the width of $\mathcal{R}(E_t, E_m)$. This σ_E can be expressed as

$$\sigma_E = \alpha E + \beta\sqrt{E} + \gamma. \quad (\text{A.1.3})$$

where the coefficients α, β and γ depend on the detector specifications. Using these measured neutrino energy information, the number of neutrino events can be expressed as a function of *measured* energy E_m and is given by,

$$N(E_m) = \int \Phi_\mu(E_t) P_{\mu e}(\{s\}, E_t) \mathcal{R}(E_t, E_m) \sigma_e(E_t) \varepsilon dE_t, \quad (\text{A.1.4})$$

where ε denotes the detector efficiency and the integration is done over the entire true energy range.

We also incorporate the binning information of the measured neutrino events. We can express the measured neutrino events for the i^{th} bin as

$$N_i = \int \int \Phi_\mu(E_t) P_{\mu e}(\{s\}, E_t) \mathcal{R}(E_t, E_m) \sigma_e(E_t) \varepsilon dE_t dE_m \quad (\text{A.1.5})$$

Expression (A.1.5) can be used for the long baseline superbeam neutrino oscillation experiments. In the case of atmospheric neutrino experiments, the oscillation probability and the flux of the initial neutrino flavor not only depend on the true energy but also on the direction of the neutrinos (i.e. on the zenith angle θ). This angular dependence brings a new smearing function named as *angular smearing* and it is given by [203],

$$\mathcal{R}(\Omega_t, \Omega_m) = N_a e^{-\left[\frac{(\theta_t - \theta_m)^2 + \sin^2 \theta_t (\phi_t - \phi_m)^2}{2\sigma_\Omega^2}\right]}, \quad (\text{A.1.6})$$

where N_a is the normalization constant, ϕ is the azimuthal angle, ‘t’ and ‘m’ represent the ‘true’ and ‘measured’ values respectively.

Thus the events for atmospheric neutrino experiments considering i^{th} energy bin and j^{th} zenith angle bin can be expressed as

$$N_{ij} = \int \int \int \int \Phi_\mu(E_t, \Omega_t) P_{\mu e}(\{s\}, E_t, \Omega_t) \mathcal{R}(E_t, E_m) \mathcal{R}(\Omega_t, \Omega_m) \sigma_e(E_t) \varepsilon \\ \times dE_t dE_m d\Omega_t d\Omega_m, \quad (\text{A.1.7})$$

As mentioned earlier, integration is done by considering the full spectrum of E_t and Ω_t whereas for E_m and Ω_m , the integration is done only by considering i^{th} and j^{th} bins respectively. In the above framework, we consider $\nu_\mu \rightarrow \nu_e$ channel as an example. However, similar procedure can be followed for other channels also. There are various background events which can also be mis-identified as an event in a detector. Therefore, while simulating total number of events at the detector one considers the sum of both signal and background events.

A.2 χ^2 Analysis

In our analysis, we use simulated data in lieu of real data. The experimental events, N_i^{ex} (say i^{th} bin) are generated for some specific set of parameter values. These are called true parameters. Similarly, we also generate the number of events by considering test set of parameters for a given bin and name them as test or theoretical events N_i^{th} .

For the χ^2 analysis, one uses the Gaussian formula in the analysis when the number of events per bin is greater than five and in this case the statistical χ^2 can be expressed as

$$\chi_{\text{stat}}^2 = \sum_i \frac{(N_i^{th} - N_i^{ex})^2}{N_i^{ex}}, \quad (\text{A.2.1})$$

whereas one can use Poisson formula if the number of events per bin are less than five i.e.,

$$\chi_{\text{stat}}^2 = \sum_i 2 \left[N_i^{th} - N_i^{ex} - N_i^{ex} \log \left(\frac{N_i^{th}}{N_i^{ex}} \right) \right]. \quad (\text{A.2.2})$$

where, N_{ex} is the total number of simulated experimental or true events, and N^{th} is the total number of simulated theoretical or test events.

The formalism discussed above gives us the statistical χ^2 for a given oscillation experiment. However, one needs to consider the various systematic uncertainties in the experiment [†].

In order to incorporate the systematic errors, we use the method of pull [221, 222]. Let us consider the systematic uncertainties in terms of cross-sections. Suppose when

[†]Note that the systematic errors for an experiment can come from uncertainties in the cross-sections, neutrino flux, directional uncertainties, etc.

the cross-section deviates from its central value by 1σ , then let c_i be the change in the number of events in the i^{th} bin. Now for a $\xi\sigma$ change from the central value will lead to ξc_i change in the total number of events (note here that ξ is the pull variable.). Therefore, the number of events due to this pull variable will change as follows :

$$N_i^{th} \rightarrow N_i^{th} + \xi c_i. \quad (\text{A.2.3})$$

This will change total χ^2 as

$$\begin{aligned} \chi_{total}^2 &= \chi_{stat}^2 + \chi_{syst}^2, \\ &= \chi_{stat}^2 + \xi^2. \end{aligned} \quad (\text{A.2.4})$$

We can also generalize this for multiple number of systematic errors and the final expression can be written as

$$\chi_{total}^2 = \sum_i \frac{(N_i^{th} - N_i^{ex})^2}{N_i^{ex}} + \sum_k \xi_k^2 \quad (\text{A.2.5})$$

where k runs over the number of pull variables.

The final χ_{pull}^2 is obtained by varying ξ_k in their 3σ ranges and by minimizing over the total χ^2 as

$$\chi_{pull}^2 = \text{Min} [\chi_{total}^2]. \quad (\text{A.2.6})$$

Finally, we discuss about the uncertainties in the oscillation parameters. We consider these uncertainties by varying all the parameters in their 3σ range in the test events and then we minimize the resultant χ^2 with respect to these test parameters [‡].

$$\chi^2 = \text{Min}\{x_{th}\} [\chi_{pull}^2 + \chi_{prior}^2], \quad (\text{A.2.7})$$

here χ_{prior}^2 is the prior or penalty term arising due to the deviation of the oscillation parameters from their true values. In our numerical analysis we add prior only for θ_{13} . This is because the solar parameters (θ_{12} , Δ_{21}) are measured very precisely. Also for the atmospheric parameters (θ_{23} , Δ_{31}) we have not considered any prior because the disappearance channel itself is capable of measuring these parameters. The form of the prior for the parameter θ_{13} can be written as

$$\chi_{prior}^2 = \left[\frac{\sin^2 2\theta_{13}^{ex} - \sin^2 2\theta_{13}^{th}}{\sigma(\sin^2 2\theta_{13})} \right]^2. \quad (\text{A.2.8})$$

where $\sigma(\sin^2 2\theta_{13})$ is the error in the measurement of $\sin^2 2\theta_{13}$.

[‡]Note that the true events are calculated by considering a set of true oscillation parameters.

Appendix B

Synergy between the oscillation probabilities and the role of antineutrinos

In this appendix, we discuss the origin of discrete degenerate regions in the test $\delta_{CP} - \theta_{23}$ -plane from the combination of appearance and disappearance channels for $\text{NO}\nu\text{A}$. We demonstrate the role of antineutrinos in resolving the degeneracies. The reference true point chosen, in generating the data, is $\delta_{CP} = -90^\circ$ and $\theta_{23} = 39^\circ$. In the upper row of figure B.1, we plot the sensitivity of $\text{NO}\nu\text{A}[6+0]$. The serpentine curves in the top-left panel of figure B.1 represent the allowed area at 90% C.L. from only the appearance channel. The area inside the vertical curves represents the allowed area from only the disappearance channel at the same C.L. The area between the blue dotted (magenta dotted) curves denotes the region obtained for the right (wrong) hierarchy. For the appearance channel, the allowed region is continuous and no discrete degenerate solutions appear. This can be understood in the following manner. In the neutrino appearance channel, $\delta_{CP} = -90^\circ$ corresponds to the maximum value in the probability. As one moves away from -90° , the probability decreases and reaches its minimum value at $+90^\circ$. On the other hand, the probability increases(decreases) as θ_{23} increases(decreases). So if we draw an imaginary horizontal line and an imaginary vertical line at the true point, then the allowed region is expected to come along the diagonal of the rectangle obtained by the intersection of these two imaginary lines and

the X,Y axes for $\theta_{23} > 39^\circ$ and $\delta_{CP} \leq +90^\circ$. For $\delta_{CP} > +90^\circ$, the probability starts to increase, so θ_{23} has to fall to keep the probability same. This explains the serpentine nature of the allowed area. The width of the band corresponds to the θ_{23} precision of the experiment. For the disappearance channel, the allowed region is in the vicinity of θ_{23} and $\pi/2 - \theta_{23}$ and parallel to the δ_{CP} axis since the $P_{\mu\mu}$ probability has a very weak dependence on δ_{CP} . However, the combination of the disappearance and appearance channels gives discrete regions in the parameter space due to the excellent θ_{23} precision of the disappearance channel near $\theta_{23} = 39^\circ$ and 51° . This helps to exclude the other wrong values of θ_{23} . This is shown in the top right panel of figure B.1. Apart from the allowed regions around the true value, one can identify the distinct degenerate solutions corresponding to wrong hierarchy-wrong octant-right δ_{CP} (WH-WO-R δ_{CP}) and right hierarchy-wrong octant-wrong δ_{CP} (RH-WO-W δ_{CP}) regions.

To show the exact synergy between the appearance and disappearance channels, in the middle panel of the top row we plot the χ^2 as a function of $\theta_{23}(\text{test})$ for a fixed δ_{CP} value of -90° for the same hierarchy (NH). This figure shows that, though the disappearance channel suffers from the intrinsic octant degeneracy and does not have any octant sensitivity itself ($\chi^2 \sim 0$), when added to the appearance channel, the channel is responsible for that of δ_{CP} .

Next, we discuss the role of antineutrino runs in NO ν A. In the bottom row of figure B.1, we plot the same figures as the top row but for the 3 year neutrino + 3 year antineutrino run. In the bottom left panel, we see that when antineutrino information is added to neutrino data, the allowed region from the appearance channel is significantly reduced. The reason is as follows: as δ_{CP} changes its sign for antineutrinos, the serpentine shape of the allowed region gets flipped with respect to δ_{CP} . This excludes the right hierarchy-wrong octant regions of $\delta_{CP} \in \text{UHP}$ (i.e. RH-WO-W δ_{CP}) and the wrong hierarchy-wrong octant regions of $\delta_{CP} \in \text{LHP}$ (i.e. WH-WO-R δ_{CP}). Thus, after adding the antineutrino data only the RH-RO-R δ_{CP} solution remains, as can be seen from the third panel in the bottom row. From the NO ν A antineutrino probability figure in the top right panel of figure 4.1, it is seen that the probability of the true point cannot be matched by any points in the NH-HO or IH-HO bands. This means that for this true point antineutrinos are free from the degeneracies that appear with the wrong

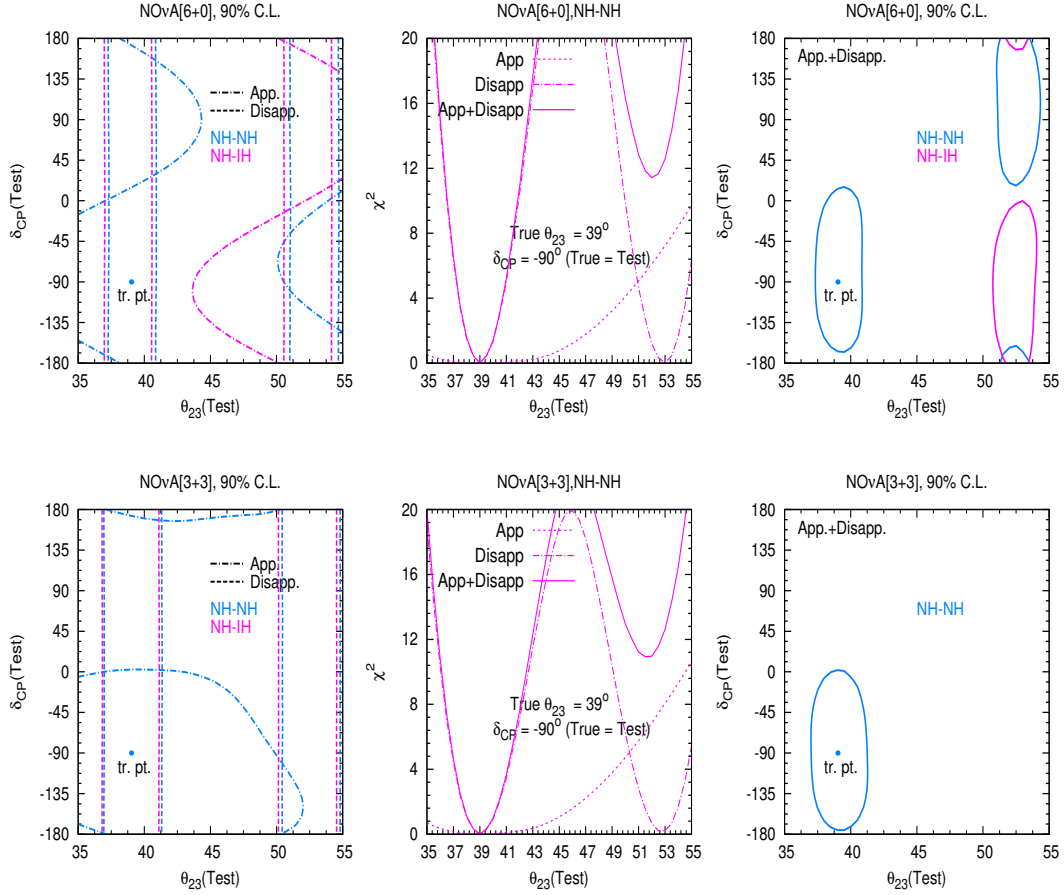


Figure B.1: The plots in the upper row are for $\text{NO}\nu\text{A}$ running only in the neutrino mode i.e. $\text{NO}\nu\text{A}[6+0]$. Those in the lower row are for $\text{NO}\nu\text{A}$ running in equal neutrino and antineutrino mode i.e. $\text{NO}\nu\text{A}[3+3]$. To generate these plots, we have assumed true $\theta_{23} = 39^\circ$, true $\delta_{CP} = -90^\circ$ and true hierarchy = NH, whereas test parameters are marginalized over the range given in table 3.2. The plots in the middle panel are generated for a fixed value of the test $\delta_{CP} (= -90^\circ)$.

octant in neutrinos. Thus, the addition of antineutrino information removes the wrong octant solutions of $\text{NO}\nu\text{A}[6+0]$ that appear in the top right panels of figure B.1.

The nature of the disappearance channel contours are seen to remain unaltered but now the allowed area is slightly broader. This is because of a reduction in the overall statistics due to the smaller cross sections of the antineutrinos. This is also seen in the middle panels where the widths of the χ^2 contours increase.

Bibliography

- [1] J. Chadwick Verh. Phys. Gesell. **16** (1914) 383–391.
- [2] C. L. Cowan, F. Reines, F. B. Harrison, H. W. Kruse, and A. D. McGuire.
<http://science.sciencemag.org/content/124/3212/103>.
- [3] G. Danby, J. M. Gaillard, K. A. Goulianos, L. M. Lederman, N. B. Mistry, M. Schwartz, and J. Steinberger *Phys. Rev. Lett.* **9** (1962) 36–44.
- [4] **DONUT**, K. Kodama *et al.* *Phys. Lett.* **B504** (2001) 218–224,
[arXiv:hep-ex/0012035](http://arxiv.org/abs/hep-ex/0012035).
- [5] R. Davis, Jr., D. S. Harmer, and K. C. Hoffman *Phys. Rev. Lett.* **20** (1968) 1205–1209.
- [6] J. N. Bahcall, N. A. Bahcall, and G. Shaviv *Phys. Rev. Lett.* **20** (1968) 1209–1212.
- [7] B. Pontecorvo *Sov. Phys. JETP* **6** (1957) 429. [*Zh. Eksp. Teor. Fiz.*33,549(1957)].
- [8] B. Pontecorvo *Sov. Phys. JETP* **7** (1958) 172–173. [*Zh. Eksp. Teor. Fiz.*34,247(1957)].
- [9] **SNO**, Q. R. Ahmad *et al.* *Phys. Rev. Lett.* **87** (2001) 071301,
[arXiv:nucl-ex/0106015](http://arxiv.org/abs/nucl-ex/0106015).
- [10] **SNO**, Q. R. Ahmad *et al.* *Phys. Rev. Lett.* **89** (2002) 011301,
[arXiv:nucl-ex/0204008](http://arxiv.org/abs/nucl-ex/0204008).

- [11] **Super-Kamiokande**, Y. Fukuda *et al.* *Phys. Rev. Lett.* **82** (1999) 2644–2648, [arXiv:hep-ex/9812014](#).
- [12] **KamLAND**, K. Eguchi *et al.* *Phys. Rev. Lett.* **92** (2004) 071301, [arXiv:hep-ex/0310047](#).
- [13] **K2K**, S. H. Ahn *et al.* *Phys. Lett.* **B511** (2001) 178–184, [arXiv:hep-ex/0103001](#).
- [14] **K2K**, M. H. Ahn *et al.* *Phys. Rev. Lett.* **90** (2003) 041801, [arXiv:hep-ex/0212007](#).
- [15] **MINOS**, D. G. Michael *et al.* *Phys. Rev. Lett.* **97** (2006) 191801, [arXiv:hep-ex/0607088](#).
- [16] **T2K**, K. Abe *et al.* *Phys. Rev. Lett.* **107** (2011) 041801, [arXiv:1106.2822](#).
- [17] **NOvA**, P. Adamson *et al.* *Phys. Rev. Lett.* **116** (2016) no. 15, 151806, [arXiv:1601.05022](#).
- [18] **NOvA**, P. Adamson *et al.* *Phys. Rev.* **D93** (2016) no. 5, 051104, [arXiv:1601.05037](#).
- [19] **SLD Electroweak Group, DELPHI, ALEPH, SLD, SLD Heavy Flavour Group, OPAL, LEP Electroweak Working Group, L3**, S. Schael *et al.* *Phys. Rept.* **427** (2006) 257–454, [arXiv:hep-ex/0509008](#).
- [20] T. D. Lee and C.-N. Yang *Phys. Rev.* **104** (1956) 254–258.
- [21] C. S. Wu, E. Ambler, R. W. Hayward, D. D. Hoppes, and R. P. Hudson *Phys. Rev.* **105** (1957) 1413–1414.
- [22] M. Goldhaber, L. Grodzins, and A. W. Sunyar *Phys. Rev.* **109** (1958) 1015–1017.
- [23] P. W. Higgs *Phys. Rev. Lett.* **13** (1964) 508–509.
- [24] P. W. Higgs *Phys. Lett.* **12** (1964) 132–133.

- [25] P. W. Higgs *Phys. Rev.* **145** (1966) 1156–1163.
- [26] T. W. B. Kibble *Phys. Rev.* **155** (1967) 1554–1561.
- [27] G. S. Guralnik, C. R. Hagen, and T. W. B. Kibble *Phys. Rev. Lett.* **13** (1964) 585–587.
- [28] F. Englert and R. Brout *Phys. Rev. Lett.* **13** (1964) 321–323.
- [29] **ATLAS**, G. Aad *et al.* *Phys. Lett.* **B716** (2012) 1–29, [arXiv:1207.7214](https://arxiv.org/abs/1207.7214).
- [30] **CMS**, S. Chatrchyan *et al.* *Phys. Lett.* **B716** (2012) 30–61, [arXiv:1207.7235](https://arxiv.org/abs/1207.7235).
- [31] J. Schechter and J. W. F. Valle *Phys. Rev.* **D25** (1982) 2951.
- [32] **KamLAND-Zen**, A. Gando *et al.* *Phys.Rev.Lett.* **110** (2013) no. 6, 062502, [arXiv:1211.3863](https://arxiv.org/abs/1211.3863).
- [33] **CUORE**, P. Gorla *J.Phys.Conf.Ser.* **375** (2012) 042013.
- [34] J. Wilkerson, E. Aguayo, F. Avignone, H. Back, A. Barabash, *et al.* *J.Phys.Conf.Ser.* **375** (2012) 042010.
- [35] **SuperNEMO**, A. Barabash *J.Phys.Conf.Ser.* **375** (2012) 042012.
- [36] **EXO**, M. Auger *et al.* *Phys.Rev.Lett.* **109** (2012) 032505, [arXiv:1205.5608](https://arxiv.org/abs/1205.5608).
- [37] **Planck**, P. A. R. Ade *et al.* *Astron. Astrophys.* **594** (2016) A13, [arXiv:1502.01589](https://arxiv.org/abs/1502.01589).
- [38] M. Sturm in *Proceedings, 31st International Conference on Physics in collisions (PIC 2011): Vancouver, Canada, August 28-September 1, 2011*. 2011. [arXiv:1111.4773](https://arxiv.org/abs/1111.4773).
<http://inspirehep.net/record/946800/files/arXiv:1111.4773.pdf>.
- [39] W. Grimus and L. Lavoura *JHEP* **11** (2000) 042, [arXiv:hep-ph/0008179](https://arxiv.org/abs/hep-ph/0008179).

- [40] S. Weinberg *Phys. Rev. Lett.* **43** (1979) 1566–1570.
- [41] S. Weinberg *Phys. Rev.* **D22** (1980) 1694.
- [42] P. Minkowski *Phys. Lett.* **B67** (1977) 421–428.
- [43] T. Yanagida *Conf. Proc.* **C7902131** (1979) 95–99.
- [44] M. Gell-Mann, P. Ramond, and R. Slansky *Conf. Proc.* **C790927** (1979) 315–321, [arXiv:1306.4669](https://arxiv.org/abs/1306.4669).
- [45] R. N. Mohapatra and G. Senjanovic *Phys. Rev. Lett.* **44** (1980) 912.
- [46] M. Magg and C. Wetterich *Phys. Lett.* **B94** (1980) 61–64.
- [47] G. Lazarides, Q. Shafi, and C. Wetterich *Nucl. Phys.* **B181** (1981) 287–300.
- [48] R. N. Mohapatra and G. Senjanovic *Phys. Rev.* **D23** (1981) 165.
- [49] J. Schechter and J. W. F. Valle *Phys. Rev.* **D25** (1982) 774.
- [50] R. Foot, H. Lew, X. G. He, and G. C. Joshi *Z. Phys.* **C44** (1989) 441.
- [51] E. Ma and D. P. Roy *Nucl. Phys.* **B644** (2002) 290–302, [arXiv:hep-ph/0206150](https://arxiv.org/abs/hep-ph/0206150).
- [52] B. Bajc and G. Senjanovic *JHEP* **08** (2007) 014, [arXiv:hep-ph/0612029](https://arxiv.org/abs/hep-ph/0612029).
- [53] **LSND**, C. Athanassopoulos *et al.* *Phys.Rev.Lett.* **77** (1996) 3082–3085, [arXiv:nucl-ex/9605003](https://arxiv.org/abs/nucl-ex/9605003).
- [54] **LSND**, C. Athanassopoulos *et al.* *Phys. Rev. Lett.* **81** (1998) 1774–1777, [arXiv:nucl-ex/9709006](https://arxiv.org/abs/nucl-ex/9709006).
- [55] **LSND**, A. Aguilar-Arevalo *et al.* *Phys.Rev.* **D64** (2001) 112007, [arXiv:hep-ex/0104049](https://arxiv.org/abs/hep-ex/0104049).
- [56] **MiniBooNE**, A. A. Aguilar-Arevalo *et al.* *Phys. Rev. Lett.* **110** (2013) 161801, [arXiv:1207.4809](https://arxiv.org/abs/1207.4809).

- [57] C. Giunti and M. Laveder *Phys.Rev.* **C83** (2011) 065504,
[arXiv:1006.3244](#).
- [58] G. Mention, M. Fechner, T. Lasserre, T. Mueller, D. Lhuillier, *et al.* *Phys.Rev.*
D83 (2011) 073006, [arXiv:1101.2755](#).
- [59] C. Giunti, M. Laveder, Y. F. Li, Q. Y. Liu, and H. W. Long *Phys. Rev.* **D86**
(2012) 113014, [arXiv:1210.5715](#).
- [60] E. J. Chun, A. S. Joshipura, and A. Yu. Smirnov *Phys. Rev.* **D54** (1996)
4654–4661, [arXiv:hep-ph/9507371](#).
- [61] J. Barry, W. Rodejohann, and H. Zhang *JHEP* **1107** (2011) 091,
[arXiv:1105.3911](#).
- [62] C.-S. Chen and R. Takahashi *Eur. Phys. J.* **C72** (2012) 2089,
[arXiv:1112.2102](#).
- [63] K. N. Abazajian *et al.* hep-ph/1204.5379 (2012) , [arXiv:1204.5379](#).
- [64] C. Spiering *Eur. Phys. J.* **H37** (2012) 515–565, [arXiv:1207.4952](#).
- [65] A. Faessler, R. Hodak, S. Kovalenko, and F. imkovic *Rom. J. Phys.* **58** (2013)
no. 9-10, 1221–1231, [arXiv:1304.5632](#).
- [66] S. Betts *et al.* in *Proceedings, 2013 Community Summer Study on the Future of
U.S. Particle Physics: Snowmass on the Mississippi (CSS2013): Minneapolis,
MN, USA, July 29-August 6, 2013*. 2013. [arXiv:1307.4738](#).
[http://www.slac.stanford.edu/econf/C1307292/docs/
submittedArxivFiles/1307.4738.pdf](http://www.slac.stanford.edu/econf/C1307292/docs/submittedArxivFiles/1307.4738.pdf).
- [67] R. Mohammadi *Eur. Phys. J.* **C74** (2014) no. 10, 3102, [arXiv:1312.2199](#).
- [68] B. T. Cleveland, T. Daily, R. Davis, Jr., J. R. Distel, K. Lande, C. K. Lee, P. S.
Wildenhain, and J. Ullman *Astrophys. J.* **496** (1998) 505–526.
- [69] **Kamiokande**, Y. Fukuda *et al.* *Phys. Rev. Lett.* **77** (1996) 1683–1686.
- [70] **GALLEX**, W. Hampel *et al.* *Phys. Lett.* **B447** (1999) 127–133.

- [71] **SAGE**, J. N. Abdurashitov *et al.* *J. Exp. Theor. Phys.* **95** (2002) 181–193,
[arXiv:astro-ph/0204245](#). [*Zh. Eksp. Teor. Fiz.*122,211(2002)].
- [72] **GNO**, M. Altmann *et al.* *Phys. Lett.* **B490** (2000) 16–26,
[arXiv:hep-ex/0006034](#).
- [73] **SNO**, S. N. Ahmed *et al.* *Phys. Rev. Lett.* **92** (2004) 181301,
[arXiv:nucl-ex/0309004](#).
- [74] **BOREXINO**, R. Tartaglia *Nucl. Instrum. Meth.* **A461** (2001) 327–328.
- [75] **KamLAND**, A. Gando *et al.* *Nature Geo.* **4** (2011) 647–651.
- [76] **Borexino**, L. Miramonti *et al.* *Phys. Procedia* **61** (2015) 340–344.
- [77] H. Duan and J. P. Kneller *J. Phys.* **G36** (2009) 113201, [arXiv:0904.0974](#).
- [78] H. Duan, G. M. Fuller, and Y.-Z. Qian *Ann. Rev. Nucl. Part. Sci.* **60** (2010)
569–594, [arXiv:1001.2799](#).
- [79] K. S. Hirata *et al.* *Phys. Rev.* **D38** (1988) 448–458.
- [80] **IMB**, C. B. Bratton *et al.* *Phys. Rev.* **D37** (1988) 3361.
- [81] **Daya Bay**, F. P. An *et al.* *Phys. Rev. Lett.* **108** (2012) 171803,
[arXiv:1203.1669](#).
- [82] **RENO**, J. K. Ahn *et al.* *Phys. Rev. Lett.* **108** (2012) 191802,
[arXiv:1204.0626](#).
- [83] **Double Chooz**, Y. Abe *et al.* *Phys. Rev. Lett.* **108** (2012) 131801,
[arXiv:1112.6353](#).
- [84] S. E. Kopp in *Particle accelerator. Proceedings, Conference, PAC’05, Knoxville, USA, May 16-20, 2005*. http://lss.fnal.gov/cgi-bin/find_paper.pl?conf-05-093.
- [85] **OPERA**, R. Acquafredda *et al.* *New J. Phys.* **8** (2006) 303,
[arXiv:hep-ex/0611023](#).

- [86] **OPERA**, A. G. Cocco *Nucl. Phys. Proc. Suppl.* **85** (2000) 125–128.
- [87] E. Aprile, K. L. Giboni, and C. Rubbia *Nucl. Instrum. Meth.* **A241** (1985) 62–71.
- [88] S. Amoruso *et al.* *Nucl. Instrum. Meth.* **A516** (2004) 68–79.
- [89] **T2K**, Y. Itow *et al.* in *Neutrino oscillations and their origin. Proceedings, 3rd International Workshop, NOON 2001, Kashiwa, Tokyo, Japan, December 508, 2001*, pp. 239–248. 2001. [arXiv:hep-ex/0106019](https://arxiv.org/abs/hep-ex/0106019).
<http://alice.cern.ch/format/showfull?sysnb=2258620>.
- [90] **Hyper-Kamiokande Working Group**, T. Ishida in *15th International Workshop on Neutrino Factories, Super Beams and Beta Beams (NuFact2013) Beijing, China, August 19-24, 2013*. 2013.
<http://inspirehep.net/record/1265508/files/arXiv:1311.5287.pdf>.
- [91] **Hyper-Kamiokande proto-**, K. Abe *et al.* [arXiv:1611.06118](https://arxiv.org/abs/1611.06118).
- [92] **MiniBooNE**, A. A. Aguilar-Arevalo *et al.* *Phys. Rev. Lett.* **98** (2007) 231801, [arXiv:0704.1500](https://arxiv.org/abs/0704.1500).
- [93] **K2K**, E. Aliu *et al.* *Phys. Rev. Lett.* **94** (2005) 081802, [arXiv:hep-ex/0411038](https://arxiv.org/abs/hep-ex/0411038).
- [94] **NOvA**, D. S. Ayres *et al.* [arXiv:hep-ex/0503053](https://arxiv.org/abs/hep-ex/0503053).
- [95] T. K. Gaisser and M. Honda *Ann. Rev. Nucl. Part. Sci.* **52** (2002) 153–199, [arXiv:hep-ph/0203272](https://arxiv.org/abs/hep-ph/0203272).
- [96] C. V. Achar *et al.* *Phys. Lett.* **18** (1965) 196–199.
- [97] C. V. Achar *et al.* *Phys. Lett.* **19** (1965) 78–80.
- [98] F. Reines, M. F. Crouch, T. L. Jenkins, W. R. Kropp, H. S. Gurr, G. R. Smith, J. P. F. Sellschop, and B. Meyer *Phys. Rev. Lett.* **15** (1965) 429–433.
- [99] **Kamiokande**, Y. Fukuda *et al.* *Phys. Lett.* **B335** (1994) 237–245.

- [100] R. Becker-Szendy *et al.* *Phys. Rev. Lett.* **69** (1992) 1010–1013.
- [101] **Soudan 2**, M. C. Sanchez *et al.* *Phys. Rev.* **D68** (2003) 113004,
[arXiv:hep-ex/0307069](#).
- [102] **Super-Kamiokande**, Y. Ashie *et al.* *Phys. Rev. Lett.* **93** (2004) 101801,
[arXiv:hep-ex/0404034](#).
- [103] D. Eichler *Astrophys. J.* **232** (1979) 106–112.
- [104] E. Waxman and J. N. Bahcall *Phys. Rev. Lett.* **78** (1997) 2292–2295,
[arXiv:astro-ph/9701231](#).
- [105] T. K. Gaisser, F. Halzen, and T. Stanev *Phys. Rept.* **258** (1995) 173–236,
[arXiv:hep-ph/9410384](#). [Erratum: *Phys. Rept.*271,355(1996)].
- [106] P. O. Hulth *Int. J. Mod. Phys.* **A21** (2006) 1914–1924. [,339(2006)].
- [107] **ANITA**, A. Silvestri *et al.* *NATO Sci. Ser. II* **209** (2005) 297–306,
[arXiv:astro-ph/0411007](#). [,297(2004)].
- [108] **IceCube**, M. G. Aartsen *et al.* *Science* **342** (2013) 1242856,
[arXiv:1311.5238](#).
- [109] R. M. Bionta *et al.* *Phys. Rev.* **D38** (1988) 768–775.
- [110] **Super-Kamiokande**, S. Fukuda *et al.* *Phys. Lett.* **B539** (2002) 179–187,
[arXiv:hep-ex/0205075](#).
- [111] **SNO**, J. Boger *et al.* *Nucl. Instrum. Meth.* **A449** (2000) 172–207,
[arXiv:nucl-ex/9910016](#).
- [112] F. Ardellier *et al.* [arXiv:hep-ex/0405032](#).
- [113] **Daya Bay**, X. Guo *et al.* [arXiv:hep-ex/0701029](#).
- [114] **RENO**, S.-B. Kim *AIP Conf. Proc.* **981** (2008) 205–207. [*J. Phys. Conf. Ser.*120,052025(2008)].

- [115] A. Bueno, Z. Dai, Y. Ge, M. Laffranchi, A. J. Melgarejo, A. Meregaglia, S. Navas, and A. Rubbia *JHEP* **04** (2007) 041, [arXiv:hep-ph/0701101](#).
- [116] G. Karagiorgi *AIP Conf. Proc.* **1663** (2015) 100001, [arXiv:1304.2083](#).
- [117] **Soudan-2**, W. W. M. Allison *et al.* *Nucl. Instrum. Meth.* **A376** (1996) 36–48.
- [118] W. W. M. Allison *et al.* *Phys. Lett.* **B391** (1997) 491–500, [arXiv:hep-ex/9611007](#).
- [119] **MINOS**, P. Adamson *et al.* *IEEE Trans. Nucl. Sci.* **49** (2002) 861–863.
- [120] **INO**, M. S. Athar *et al.* 2006. <http://www.imsc.res.in/~ino/OpenReports/INOReport.pdf>.
- [121] **ICAL**, S. Ahmed *et al.* [arXiv:1505.07380](#).
- [122] K. T. McDonald [arXiv:hep-ex/0111033](#).
- [123] **T2K**, K. Abe *et al.* *Nucl. Instrum. Meth.* **A659** (2011) 106–135, [arXiv:1106.1238](#).
- [124] **T2K**, K. Abe *et al.* *Phys. Rev. Lett.* **118** (2017) no. 15, 151801, [arXiv:1701.00432](#).
- [125] **T2K**, K. Abe *et al.* [arXiv:1607.08004](#).
- [126] **NOvA**, D. S. Ayres *et al.*
- [127] **NuMI, NOvA, LBNE**, S. Childress and J. Strait *J. Phys. Conf. Ser.* **408** (2013) 012007, [arXiv:1304.4899](#).
- [128] **DUNE**, R. Acciarri *et al.* [arXiv:1512.06148](#).
- [129] **DUNE**, R. Acciarri *et al.* [arXiv:1601.05471](#).
- [130] **DUNE**, J. Strait *et al.* [arXiv:1601.05823](#).
- [131] L. S. Mohan and D. Indumathi *Eur. Phys. J.* **C77** (2017) no. 1, 54, [arXiv:1605.04185](#).

- [132] A. Chatterjee, K. K. Meghna, K. Rawat, T. Thakore, V. Bhatnagar, R. Gandhi, D. Indumathi, N. K. Mondal, and N. Sinha *JINST* **9** (2014) P07001, [arXiv:1405.7243](https://arxiv.org/abs/1405.7243).
- [133] R. Kanishka, K. K. Meghna, V. Bhatnagar, D. Indumathi, and N. Sinha *JINST* **10** (2015) no. 03, P03011, [arXiv:1503.03369](https://arxiv.org/abs/1503.03369).
- [134] M. M. Devi, T. Thakore, S. K. Agarwalla, and A. Dighe *JHEP* **10** (2014) 189, [arXiv:1406.3689](https://arxiv.org/abs/1406.3689).
- [135] Z. Maki, M. Nakagawa, and S. Sakata *Prog. Theor. Phys.* **28** (1962) 870–880.
- [136] S. Eliezer and A. R. Swift *Nucl. Phys.* **B105** (1976) 45–51.
- [137] H. Fritzsch and P. Minkowski *Phys. Lett.* **B62** (1976) 72–76.
- [138] S. M. Bilenky and B. Pontecorvo *Yad. Fiz.* **24** (1976) 603–608. [*Sov. J. Nucl. Phys.*24,316(1976)].
- [139] S. M. Bilenky and B. Pontecorvo *Lett. Nuovo Cim.* **17** (1976) 569.
- [140] S. Nussinov *Phys. Lett.* **B63** (1976) 201–203.
- [141] C. Kim and A. Pevsner. *Contemporary concepts in physics*. Harwood Academic, 1993.
<https://books.google.co.in/books?id=TNrvAAAAMAAJ>.
- [142] Y. Zhang, X. Zhang, and B.-Q. Ma *Phys. Rev.* **D86** (2012) 093019, [arXiv:1211.3198](https://arxiv.org/abs/1211.3198).
- [143] **Particle Data Group**, C. Patrignani *et al.* *Chin. Phys.* **C40** (2016) no. 10, 100001.
- [144] L. Wolfenstein *Phys. Rev.* **D17** (1978) 2369–2374.
- [145] S. P. Mikheev and A. Yu. Smirnov *Sov. J. Nucl. Phys.* **42** (1985) 913–917. [*Yad. Fiz.*42,1441(1985)].
- [146] S. P. Mikheev and A. Yu. Smirnov *Nuovo Cim.* **C9** (1986) 17–26.

- [147] C. Giunti and C. Kim. OUP Oxford, 2007.
<https://books.google.co.in/books?id=2faTXKIDnfgC>.
- [148] P. B. Pal *Int. J. Mod. Phys. A* **7** (1992) 5387–5460.
- [149] T.-K. Kuo and J. T. Pantaleone *Rev. Mod. Phys.* **61** (1989) 937.
- [150] A. Cervera, A. Donini, M. B. Gavela, J. J. Gomez Cadenas, P. Hernandez, O. Mena, and S. Rigolin *Nucl. Phys.* **B579** (2000) 17–55,
[arXiv:hep-ph/0002108](https://arxiv.org/abs/hep-ph/0002108). [Erratum: *Nucl. Phys.*B593,731(2001)].
- [151] M. Freund *Phys. Rev.* **D64** (2001) 053003, [arXiv:hep-ph/0103300](https://arxiv.org/abs/hep-ph/0103300).
- [152] E. K. Akhmedov, R. Johansson, M. Lindner, T. Ohlsson, and T. Schwetz *JHEP* **04** (2004) 078, [arXiv:hep-ph/0402175](https://arxiv.org/abs/hep-ph/0402175).
- [153] G. L. Fogli, E. Lisi, A. Marrone, and G. Scioscia *Phys. Rev.* **D59** (1999) 033001, [arXiv:hep-ph/9808205](https://arxiv.org/abs/hep-ph/9808205).
- [154] R. Gandhi, P. Ghoshal, S. Goswami, P. Mehta, and S. U. Sankar *Phys. Rev. Lett.* **94** (2005) 051801, [arXiv:hep-ph/0408361](https://arxiv.org/abs/hep-ph/0408361).
- [155] A. M. Dziewonski and D. L. Anderson *Phys. Earth Planet. Interiors* **25** (1981) 297–356.
- [156] **Kamiokande-II**, K. S. Hirata *et al.* *Phys. Rev.* **D44** (1991) 2241. [Erratum: *Phys. Rev.*D45,2170(1992)].
- [157] **SNO**, B. Aharmim *et al.* *Phys. Rev.* **C72** (2005) 055502,
[arXiv:nucl-ex/0502021](https://arxiv.org/abs/nucl-ex/0502021).
- [158] **KamLAND**, T. Araki *et al.* *Phys. Rev. Lett.* **94** (2005) 081801,
[arXiv:hep-ex/0406035](https://arxiv.org/abs/hep-ex/0406035).
- [159] R. Foot, R. R. Volkas, and O. Yasuda *Phys. Rev.* **D58** (1998) 013006,
[arXiv:hep-ph/9801431](https://arxiv.org/abs/hep-ph/9801431).
- [160] **Super-Kamiokande**, K. Abe *et al.* *Phys. Rev. Lett.* **110** (2013) no. 18, 181802,
[arXiv:1206.0328](https://arxiv.org/abs/1206.0328).

- [161] **Super-Kamiokande**, J. Hosaka *et al.* *Phys. Rev.* **D74** (2006) 032002,
[arXiv:hep-ex/0604011](#).
- [162] **MINOS**, P. Adamson *et al.* *Phys. Rev. Lett.* **107** (2011) 181802,
[arXiv:1108.0015](#).
- [163] I. Esteban, M. C. Gonzalez-Garcia, M. Maltoni, I. Martinez-Soler, and
T. Schwetz *JHEP* **01** (2017) 087, [arXiv:1611.01514](#).
- [164] P. Adamson *et al.* [arXiv:1703.03328](#).
- [165] V. Barger, D. Marfatia, and K. Whisnant *Phys.Rev.* **D65** (2002) 073023,
[arXiv:hep-ph/0112119](#).
- [166] J. Burguet-Castell, M. Gavela, J. Gomez-Cadenas, P. Hernandez, and O. Mena
Nucl.Phys. **B646** (2002) 301–320, [arXiv:hep-ph/0207080](#).
- [167] H. Minakata and H. Nunokawa *JHEP* **0110** (2001) 001,
[arXiv:hep-ph/0108085](#).
- [168] G. L. Fogli and E. Lisi *Phys.Rev.* **D54** (1996) 3667–3670,
[arXiv:hep-ph/9604415](#).
- [169] T. Kajita, H. Minakata, S. Nakayama, and H. Nunokawa *Phys.Rev.* **D75** (2007)
013006, [arXiv:hep-ph/0609286](#).
- [170] **T2K**, K. Abe *et al.* *Phys. Rev. Lett.* **107** (2011) 041801, [arXiv:1106.2822](#).
- [171] **Double Chooz**, Y. Abe *et al.* *JHEP* **1410** (2014) 086, [arXiv:1406.7763](#).
- [172] **Daya Bay**, F. An *et al.* *Nucl.Instrum.Meth.* **A773** (2015) 8–20,
[arXiv:1407.0275](#).
- [173] **RENO collaboration**, J. Ahn *et al.* *Phys.Rev.Lett.* **108** (2012) 191802,
[arXiv:1204.0626](#).
- [174] A. Donini, D. Meloni, and P. Migliozzi *Nucl.Phys.* **B646** (2002) 321–349,
[arXiv:hep-ph/0206034](#).

- [175] V. Barger, D. Marfatia, and K. Whisnant *Phys. Rev.* **D66** (2002) 053007, [arXiv:hep-ph/0206038](#).
- [176] O. Mena, S. Palomares-Ruiz, and S. Pascoli *Phys.Rev.* **D73** (2006) 073007, [arXiv:hep-ph/0510182](#).
- [177] M. Narayan and S. U. Sankar *Phys.Rev.* **D61** (2000) 013003, [arXiv:hep-ph/9904302](#).
- [178] M. Ishitsuka, T. Kajita, H. Minakata, and H. Nunokawa *Phys. Rev.* **D72** (2005) 033003, [arXiv:hep-ph/0504026](#).
- [179] K. Hagiwara, N. Okamura, and K. ichi Senda *Phys.Lett.* **B637** (2006) 266–273, [arXiv:hep-ph/0504061](#).
- [180] V. Barger, D. Marfatia, and K. Whisnant *Phys.Lett.* **B560** (2003) 75–86, [arXiv:hep-ph/0210428](#).
- [181] P. Huber, M. Lindner, and W. Winter *Nucl.Phys.* **B654** (2003) 3–29, [arXiv:hep-ph/0211300](#).
- [182] P. Huber, M. Lindner, T. Schwetz, and W. Winter *Nucl.Phys.* **B665** (2003) 487–519, [arXiv:hep-ph/0303232](#).
- [183] O. Mena and S. J. Parke *Phys.Rev.* **D70** (2004) 093011, [arXiv:hep-ph/0408070](#).
- [184] O. Mena *Mod.Phys.Lett.* **A20** (2005) 1–17, [arXiv:hep-ph/0503097](#).
- [185] H. Minakata and H. Sugiyama *Phys.Lett.* **B580** (2004) 216–228, [arXiv:hep-ph/0309323](#).
- [186] S. Prakash, S. K. Raut, and S. U. Sankar *Phys.Rev.* **D86** (2012) 033012, [arXiv:1201.6485](#).
- [187] S. K. Agarwalla, S. Prakash, S. K. Raut, and S. U. Sankar *JHEP* **1212** (2012) 075, [arXiv:1208.3644](#).

- [188] M. Blennow, P. Coloma, A. Donini, and E. Fernandez-Martinez *JHEP* **1307** (2013) 159, [arXiv:1303.0003](#).
- [189] K. Hiraide, H. Minakata, T. Nakaya, H. Nunokawa, H. Sugiyama, *et al.* *Phys.Rev.* **D73** (2006) 093008, [arXiv:hep-ph/0601258](#).
- [190] H. Minakata, H. Sugiyama, O. Yasuda, K. Inoue, and F. Suekane *Phys.Rev.* **D68** (2003) 033017, [arXiv:hep-ph/0211111](#).
- [191] S. Prakash, S. K. Raut, and S. U. Sankar *Phys.Rev.* **D86** (2012) 033012, [arXiv:1201.6485](#).
- [192] A. Chatterjee, P. Ghoshal, S. Goswami, and S. K. Raut *JHEP* **1306** (2013) 010, [arXiv:1302.1370](#).
- [193] S. K. Agarwalla, S. Prakash, and S. U. Sankar *JHEP* **1307** (2013) 131, [arXiv:1301.2574](#).
- [194] P. Machado, H. Minakata, H. Nunokawa, and R. Z. Funchal [arXiv:1307.3248](#).
- [195] M. Ghosh, S. Goswami, and S. K. Raut [arXiv:1409.5046](#).
- [196] M. Banuls, G. Barenboim, and J. Bernabeu *Phys.Lett.* **B513** (2001) 391–400, [arXiv:hep-ph/0102184](#).
- [197] J. Bernabeu, S. Palomares-Ruiz, A. Perez, and S. Petcov *Phys.Lett.* **B531** (2002) 90–98, [arXiv:hep-ph/0110071](#).
- [198] J. Bernabeu, S. Palomares Ruiz, and S. Petcov *Nucl.Phys.* **B669** (2003) 255–276, [arXiv:hep-ph/0305152](#).
- [199] R. Gandhi, P. Ghoshal, S. Goswami, P. Mehta, and S. U. Sankar *Phys.Rev.* **D73** (2006) 053001, [arXiv:hep-ph/0411252](#).
- [200] S. Palomares-Ruiz and S. Petcov *Nucl.Phys.* **B712** (2005) 392–410, [arXiv:hep-ph/0406096](#).

- [201] D. Indumathi and M. Murthy *Phys.Rev.* **D71** (2005) 013001,
[arXiv:hep-ph/0407336](#).
- [202] S. Petcov and T. Schwetz *Nucl.Phys.* **B740** (2006) 1–22,
[arXiv:hep-ph/0511277](#).
- [203] R. Gandhi *et al.* *Phys. Rev.* **D76** (2007) 073012, [arXiv:0707.1723](#).
- [204] A. Samanta *Phys.Lett.* **B673** (2009) 37–46, [arXiv:hep-ph/0610196](#).
- [205] M. M. Devi, T. Thakore, S. K. Agarwalla, and A. Dighe *JHEP* **1410** (2014) 189, [arXiv:1406.3689](#).
- [206] A. Ghosh, T. Thakore, and S. Choubey *JHEP* **1304** (2013) 009,
[arXiv:1212.1305](#).
- [207] A. Ghosh and S. Choubey [arXiv:1306.1423](#).
- [208] R. Gandhi, P. Ghoshal, S. Goswami, and S. U. Sankar *Phys.Rev.* **D78** (2008) 073001, [arXiv:0807.2759](#).
- [209] V. Barger, R. Gandhi, P. Ghoshal, S. Goswami, D. Marfatia, *et al.* *Phys.Rev.Lett.* **109** (2012) 091801, [arXiv:1203.6012](#).
- [210] M. Gonzalez-Garcia, M. Maltoni, and A. Y. Smirnov *Phys.Rev.* **D70** (2004) 093005, [arXiv:hep-ph/0408170](#).
- [211] S. Choubey and P. Roy *Phys.Rev.* **D73** (2006) 013006,
[arXiv:hep-ph/0509197](#).
- [212] P. Huber, M. Maltoni, and T. Schwetz *Phys.Rev.* **D71** (2005) 053006,
[arXiv:hep-ph/0501037](#).
- [213] M. Blennow and T. Schwetz *JHEP* **1208** (2012) 058, [arXiv:1203.3388](#).
- [214] S. Choubey and A. Ghosh *JHEP* **1311** (2013) 166, [arXiv:1309.5760](#).
- [215] P. Huber, M. Lindner, and W. Winter *Comput. Phys. Commun.* **167** (2005) 195,
[arXiv:hep-ph/0407333](#).

- [216] P. Huber, J. Kopp, M. Lindner, M. Rolinec, and W. Winter *Comput. Phys. Commun.* **177** (2007) 432–438, [arXiv:hep-ph/0701187](#).
- [217] M. D. Messier Ph.D. Thesis, Boston University Graduate School of Arts and Science, 1999 (1999) .
- [218] E. Paschos and J. Yu *Phys.Rev.* **D65** (2002) 033002, [arXiv:hep-ph/0107261](#).
- [219] **NO ν A**, R. Patterson 2012. Talk given at the Neutrino 2012 Conference, June 3-9, 2012, Kyoto, Japan, <http://neu2012.kek.jp/>.
- [220] A. Chatterjee, K. Meghna, K. Rawat, T. Thakore, V. Bhatnagar, *et al.* *JINST* **9** (2014) P07001, [arXiv:1405.7243](#).
- [221] M. C. Gonzalez-Garcia and M. Maltoni *Phys. Rev.* **D70** (2004) 033010, [arXiv:hep-ph/0404085](#).
- [222] G. Fogli, E. Lisi, A. Marrone, D. Montanino, and A. Palazzo *Phys.Rev.* **D66** (2002) 053010, [arXiv:hep-ph/0206162](#).
- [223] M. C. Gonzalez-Garcia, M. Maltoni, and T. Schwetz *JHEP* **11** (2014) 052, [arXiv:1409.5439](#).
- [224] F. Capozzi, G. Fogli, E. Lisi, A. Marrone, D. Montanino, *et al.* *Phys.Rev.* **D89** (2014) 093018, [arXiv:1312.2878](#).
- [225] D. Forero, M. Tortola, and J. Valle [arXiv:1405.7540](#).
- [226] E. K. Akhmedov, R. Johansson, M. Lindner, T. Ohlsson, and T. Schwetz *JHEP* **04** (2004) 078, [arXiv:hep-ph/0402175](#).
- [227] A. Cervera *et al.* *Nucl. Phys.* **B579** (2000) 17–55, [arXiv:hep-ph/0002108](#).
- [228] M. Freund *Phys. Rev.* **D64** (2001) 053003, [arXiv:hep-ph/0103300](#).
- [229] H. Minakata and S. J. Parke *Phys.Rev.* **D87** (2013) no. 11, 113005, [arXiv:1303.6178](#).

- [230] P. Coloma, H. Minakata, and S. J. Parke *Phys. Rev.* **D90** (2014) 093003, [arXiv:1406.2551](#).
- [231] M. Ghosh, P. Ghoshal, S. Goswami, and S. K. Raut *Phys. Rev. D* **89** (Jan, 2014) 011301.
- [232] S. Razzaque and A. Yu. Smirnov *JHEP* **05** (2015) 139, [arXiv:1406.1407](#).
- [233] M. Ghosh, P. Ghoshal, S. Goswami, and S. K. Raut *Nucl.Phys.* **B884** (2014) 274–304, [arXiv:1401.7243](#).
- [234] M. Ghosh *Phys. Rev.* **D93** (2016) no. 7, 073003, [arXiv:1512.02226](#).
- [235] J. Evslin, S.-F. Ge, and K. Hagiwara *JHEP* **02** (2016) 137, [arXiv:1506.05023](#).
- [236] D. Cherdack.
- [237] **LBNE Collaboration**, C. Adams *et al.* [arXiv:1307.7335](#).
- [238] S. K. Agarwalla, S. Prakash, and S. Uma Sankar *JHEP* **1403** (2014) 087, [arXiv:1304.3251](#).
- [239] C. R. Das, J. Maalampi, J. Pulido, and S. Vihonen *JHEP* **02** (2015) 048, [arXiv:1411.2829](#).
- [240] G. Altarelli and F. Feruglio *Rev.Mod.Phys.* **82** (2010) 2701–2729, [arXiv:1002.0211](#).
- [241] G. Altarelli, F. Feruglio, and L. Merlo *Fortsch.Phys.* **61** (2013) 507–534, [arXiv:1205.5133](#).
- [242] A. Y. Smirnov *J.Phys.Conf.Ser.* **335** (2011) 012006, [arXiv:1103.3461](#).
- [243] H. Ishimori, T. Kobayashi, H. Ohki, Y. Shimizu, H. Okada, *et al.* *Prog.Theor.Phys.Suppl.* **183** (2010) 1–163, [arXiv:1003.3552](#).
- [244] S. F. King and C. Luhn *Rept.Prog.Phys.* **76** (2013) 056201, [arXiv:1301.1340](#).

- [245] C. Lam *Phys.Lett.* **B656** (2007) 193–198, [arXiv:0708.3665](#).
- [246] C. Lam *Phys.Rev.Lett.* **101** (2008) 121602, [arXiv:0804.2622](#).
- [247] C. Lam *Phys.Rev.* **D78** (2008) 073015, [arXiv:0809.1185](#).
- [248] R. M. Fonseca and W. Grimus [arXiv:1410.4133](#).
- [249] D. Hernandez and A. Y. Smirnov *Phys.Rev.* **D88** (2013) no. 9, 093007, [arXiv:1304.7738](#).
- [250] A. S. Joshipura and K. M. Patel *Phys.Rev.* **D90** (2014) no. 3, 036005, [arXiv:1405.6106](#).
- [251] A. S. Joshipura and K. M. Patel *Phys.Lett.* **B727** (2013) 480–487, [arXiv:1306.1890](#).
- [252] A. S. Joshipura and K. M. Patel *JHEP* **1404** (2014) 009, [arXiv:1401.6397](#).
- [253] S. F. King and P. O. Ludl [arXiv:1605.01683](#).
- [254] A. S. Joshipura *JHEP* **11** (2015) 186, [arXiv:1506.00455](#).
- [255] L. L. Everett and A. J. Stuart *Phys.Rev.* **D79** (2009) 085005, [arXiv:0812.1057](#).
- [256] F. Feruglio and A. Paris *JHEP* **1103** (2011) 101, [arXiv:1101.0393](#).
- [257] G.-J. Ding, L. L. Everett, and A. J. Stuart *Nucl.Phys.* **B857** (2012) 219–253, [arXiv:1110.1688](#).
- [258] I. de Medeiros Varzielas and L. Lavoura *J.Phys.* **G41** (2014) 055005, [arXiv:1312.0215](#).
- [259] J. Gehrlein, S. T. Petcov, M. Spinrath, and X. Zhang *Nucl. Phys.* **B899** (2015) 617–630, [arXiv:1508.07930](#).
- [260] J. Gehrlein, S. T. Petcov, M. Spinrath, and X. Zhang *Nucl. Phys.* **B896** (2015) 311–329, [arXiv:1502.00110](#).

- [261] J. Gehrlein, J. P. Oppermann, D. Schfer, and M. Spinrath *Nucl. Phys.* **B890** (2014) 539–568, [arXiv:1410.2057](#).
- [262] A. S. Joshipura and K. M. Patel *Phys. Lett.* **B749** (2015) 159–166, [arXiv:1507.01235](#).
- [263] R. d. A. Toorop, F. Feruglio, and C. Hagedorn *Phys.Lett.* **B703** (2011) 447–451, [arXiv:1107.3486](#).
- [264] D. Hernandez and A. Y. Smirnov *Phys.Rev.* **D86** (2012) 053014, [arXiv:1204.0445](#).
- [265] D. Hernandez and A. Y. Smirnov *Phys.Rev.* **D87** (2013) no. 5, 053005, [arXiv:1212.2149](#).
- [266] M. Holthausen, K. S. Lim, and M. Lindner *Phys.Lett.* **B721** (2013) 61–67, [arXiv:1212.2411](#).
- [267] W. Grimus and P. O. Ludl *J.Phys.* **A45** (2012) 233001, [arXiv:1110.6376](#).
- [268] P. Harrison and W. Scott *Phys.Lett.* **B547** (2002) 219–228, [arXiv:hep-ph/0210197](#).
- [269] W. Grimus and L. Lavoura *Phys.Lett.* **B579** (2004) 113–122, [arXiv:hep-ph/0305309](#).
- [270] H.-J. He, W. Rodejohann, and X.-J. Xu *Phys. Lett.* **B751** (2015) 586–594, [arXiv:1507.03541](#).
- [271] D. V. Forero, M. Tortola, and J. W. F. Valle *Phys. Rev.* **D90** (2014) no. 9, 093006, [arXiv:1405.7540](#).
- [272] F. Capozzi, G. L. Fogli, E. Lisi, A. Marrone, D. Montanino, and A. Palazzo *Phys. Rev.* **D89** (2014) 093018, [arXiv:1312.2878](#).
- [273] H. S. Goh, R. N. Mohapatra, and S.-P. Ng *Phys. Lett.* **B542** (2002) 116–122, [arXiv:hep-ph/0205131](#).

- [274] G. Altarelli and R. Franceschini *JHEP* **03** (2006) 047,
[arXiv:hep-ph/0512202](#).
- [275] W. Grimus and L. Lavoura *J. Phys.* **G31** (2005) 683–692,
[arXiv:hep-ph/0410279](#).
- [276] J. Kopp, M. Maltoni, and T. Schwetz *Phys. Rev. Lett.* **107** (2011) 091801,
[arXiv:1103.4570](#).
- [277] J. M. Conrad, C. M. Ignarra, G. Karagiorgi, M. H. Shaevitz, and J. Spitz *Adv. High Energy Phys.* **2013** (2013) 163897, [arXiv:1207.4765](#).
- [278] C. Giunti and M. Laveder *Phys. Rev.* **D84** (2011) 073008,
[arXiv:1107.1452](#).
- [279] S. Goswami *Phys. Rev.* **D55** (1997) 2931–2949, [arXiv:hep-ph/9507212](#).
- [280] J. J. Gomez-Cadenas and M. C. Gonzalez-Garcia *Z. Phys.* **C71** (1996) 443–454, [arXiv:hep-ph/9504246](#).
- [281] M. Maltoni, T. Schwetz, M. A. Tortola, and J. W. F. Valle *Phys. Rev.* **D67** (2003) 013011, [arXiv:hep-ph/0207227](#).
- [282] J. Hamann, S. Hannestad, G. G. Raffelt, I. Tamborra, and Y. Y. Y. Wong *Phys. Rev. Lett.* **105** (2010) 181301, [arXiv:1006.5276](#).
- [283] E. Giusarma, M. Corsi, M. Archidiacono, R. de Putter, A. Melchiorri, O. Mena, and S. Pandolfi *Phys. Rev.* **D83** (2011) 115023, [arXiv:1102.4774](#).
- [284] A. de Gouvea, J. Jenkins, and N. Vasudevan *Phys. Rev.* **D75** (2007) 013003,
[arXiv:hep-ph/0608147](#).
- [285] P. S. Bhupal Dev and A. Pilaftsis *Phys. Rev.* **D87** (2013) no. 5, 053007,
[arXiv:1212.3808](#).
- [286] H. Zhang *Phys. Lett.* **B714** (2012) 262–266, [arXiv:1110.6838](#).
- [287] J. Heeck and H. Zhang *JHEP* **05** (2013) 164, [arXiv:1211.0538](#).

- [288] R. Allahverdi, B. Dutta, and R. N. Mohapatra *Phys. Lett.* **B695** (2011) 181–184, [arXiv:1008.1232](#).
- [289] A. C. B. Machado and V. Pleitez *Phys. Lett.* **B698** (2011) 128–130, [arXiv:1008.4572](#).
- [290] G. C. Branco, D. Emmanuel-Costa, M. N. Rebelo, and P. Roy *Phys. Rev.* **D77** (2008) 053011, [arXiv:0712.0774](#).
- [291] S. Goswami and A. Watanabe *Phys. Rev.* **D79** (2009) 033004, [arXiv:0807.3438](#).
- [292] S. Goswami, S. Khan, and A. Watanabe *Phys. Lett.* **B693** (2010) 249–254, [arXiv:0811.4744](#).
- [293] S. Choubey, W. Rodejohann, and P. Roy *Nucl. Phys.* **B808** (2009) 272–291, [arXiv:0807.4289](#). [Erratum: *Nucl. Phys.*B818,136(2009)].
- [294] L. Lavoura *J. Phys.* **G42** (2015) 105004, [arXiv:1502.03008](#).
- [295] R. M. Fonseca and W. Grimus *JHEP* **09** (2014) 033, [arXiv:1405.3678](#).
- [296] W. Grimus, A. S. Joshipura, L. Lavoura, and M. Tanimoto *Eur. Phys. J.* **C36** (2004) 227–232, [arXiv:hep-ph/0405016](#).
- [297] F. Capozzi, E. Lisi, A. Marrone, D. Montanino, and A. Palazzo *Nucl. Phys.* **B908** (2016) 218–234, [arXiv:1601.07777](#).
- [298] S. Gariazzo, C. Giunti, M. Laveder, Y. F. Li, and E. M. Zavanin *J. Phys.* **G43** (2016) 033001, [arXiv:1507.08204](#).
- [299] C. Giunti 2016. Talk given at Proceedings of Neutrino 2016, London, UK.
- [300] T. Schwetz 2011. Talk given at Proceedings of Sterile Neutrino Crossroads, 2011, Virginia Tech, USA.
- [301] S. Goswami, S. Khan, and W. Rodejohann *Phys. Lett.* **B680** (2009) 255–262, [arXiv:0905.2739](#).

- [302] A. Merle and W. Rodejohann *Phys. Rev.* **D73** (2006) 073012,
[arXiv:hep-ph/0603111](#).
- [303] E. I. Lashin and N. Chamoun *Phys. Rev.* **D85** (2012) 113011,
[arXiv:1108.4010](#).
- [304] R. R. Gautam, M. Singh, and M. Gupta *Phys. Rev.* **D92** (2015) no. 1, 013006,
[arXiv:1506.04868](#).
- [305] L. Lavoura, W. Rodejohann, and A. Watanabe *Phys. Lett.* **B726** (2013)
352–355, [arXiv:1307.6421](#).
- [306] K. Harigaya, M. Ibe, and T. T. Yanagida *Phys. Rev.* **D86** (2012) 013002,
[arXiv:1205.2198](#).
- [307] A. S. Joshipura and N. Nath *Phys. Rev.* **D94** (2016) no. 3, 036008,
[arXiv:1606.01697](#).
- [308] **T2K**, K. Abe *et al.* *Phys. Rev.* **D91** (2015) no. 7, 072010,
[arXiv:1502.01550](#).
- [309] **T2K**, M. Ravonel Salzgeber [arXiv:1508.06153](#).
- [310] **Daya Bay**, F. P. An *et al.* [arXiv:1607.01174](#).
- [311] **IceCube**, M. G. Aartsen *et al.* *Phys. Rev. Lett.* **117** (2016) no. 7, 071801,
[arXiv:1605.01990](#).
- [312] **MINOS**, P. Adamson *et al.* Submitted to: *Phys. Rev. Lett.* (2016) ,
[arXiv:1607.01176](#).
- [313] **MINOS, Daya Bay**, P. Adamson *et al.* Submitted to: *Phys. Rev. Lett.* (2016) ,
[arXiv:1607.01177](#).

List of Publications

Publications in Refreed Journals

1. **Newton Nath**, Monojit Ghosh, Srubabati Goswami and Shivani Gupta :
Phenomenological study of extended seesaw model for light sterile neutrino,
JHEP03(2017)075, arXiv: 1610.09090 [hep-ph].
2. Anjan S. Joshipura and **Newton Nath** :
Neutrino masses and mixing in A_5 with flavour antisymmetry,
Phys.Rev. D94, 036008 (2016), arXiv: 1606.01697[hep-ph].
3. **Newton Nath**, Monojit Ghosh, and Shivani Gupta :
Understanding the masses and mixings of one-zero textures in $3 + 1$ scenario,
Int. J. Mod. Phys. A 31, 1650132 (2016), arXiv: 1512.00635 [hep-ph].
4. **Newton Nath**, Monojit Ghosh and Srubabati Goswami :
The Physics of antineutrinos in DUNE and resolution of octant degeneracy,
Nucl.Phys. B913 (2016) 381-404, arXiv : 1511.07496[hep-ph].
5. Monojit Ghosh, Pomita Ghoshal, Srubabati Goswami, **Newton Nath** and Sushant K. Raut :
A new look to the degeneracies in the neutrino oscillation parameters and their resolution by T2K, NO ν A and ICAL,
Phys. Rev. D 93, 013013 (2016), arXiv : 1504.06283[hep-ph].

Preprints under review

1. Srubabati Goswami and **Newton Nath** :
Implications of the latest NO ν A results,
arXiv:1705.01274 [hep-ph].

2. K. N. Deepthi, Srubabati Goswami and **Newton Nath** :
Nonstandard interactions jeopardizing the hierarchy sensitivity of DUNE,
arXiv:1612.00784 [hep-ph].

Conference Proceedings :

1. **Newton Nath**, Srubabati Goswami and K. N. Deepthi :
Generalized degeneracies and their resolution in neutrino oscillation experiments,
arXiv:1703.00245 [hep-ph] for **XXII DAE-BRNS SYMPOSIUM 2016.**
2. **Newton Nath**, Monojit Ghosh and Srubabati Goswami :
What antineutrinos can tell about octant and δ_{CP} in DUNE? ,
PoS(ICHEP2016)979, arXiv:1611.03635 [hep-ph] for **ICHEP2016.**
3. **Newton Nath**, Monojit Ghosh and Srubabati Goswami :
The Physics of antineutrinos in DUNE and resolution of octant degeneracy,
arXiv:1610.01183 [hep-ex] for **Neutrino2016.**

Publications Attached with Thesis

1. Monojit Ghosh, Pomita Ghoshal, Srubabati Goswami, **Newton Nath** and Sushant K. Raut :
A new look to the degeneracies in the neutrino oscillation parameters and their resolution by T2K, NO ν A and ICAL,
Phys. Rev. D 93, 013013 (2016), arXiv : 1504.06283[hep-ph],
doi : [10.1103/PhysRevD.93.013013](https://doi.org/10.1103/PhysRevD.93.013013).
2. **Newton Nath**, Monojit Ghosh and Srubabati Goswami :
The Physics of antineutrinos in DUNE and resolution of octant degeneracy,
Nucl.Phys. B913 (2016) 381-404, arXiv : 1511.07496[hep-ph],
doi : [10.1016/j.nuclphysb.2016.09.017](https://doi.org/10.1016/j.nuclphysb.2016.09.017).
3. Anjan S. Joshipura and **Newton Nath** :
Neutrino masses and mixing in A_5 with flavour antisymmetry,
Phys.Rev. D94, 036008 (2016), arXiv: 1606.01697[hep-ph],
doi : [10.1103/PhysRevD.94.036008](https://doi.org/10.1103/PhysRevD.94.036008).
4. **Newton Nath**, Monojit Ghosh, Srubabati Goswami and Shivani Gupta :
Phenomenological study of extended seesaw model for light sterile neutrino,
JHEP03(2017)075, arXiv: 1610.09090 [hep-ph],
doi : [10.1007/JHEP03\(2017\)075](https://doi.org/10.1007/JHEP03(2017)075).

New look at the degeneracies in the neutrino oscillation parameters, and their resolution by T2K, NO ν A and ICAL

Monojit Ghosh,^{1,*} Pomita Ghoshal,^{2,†} Srubabati Goswami,^{1,‡} Newton Nath,^{1,3,§} and Sushant K. Raut^{4,||}

¹*Physical Research Laboratory, Navrangpura, Ahmedabad, Gujarat 380 009, India*

²*Department of Physics, LNM Institute of Information Technology (LNMIIT), Rupa-ki-Nangal, post-Sumel, via-Jamdoli, Jaipur, Rajasthan 302 031, India*

³*Indian Institute of Technology, Gandhinagar, Ahmedabad, Gujarat 382424, India*

⁴*Department of Theoretical Physics, School of Engineering Sciences,*

KTH Royal Institute of Technology AlbaNova University Center,

Roslagstullsbacken 21, 106 91 Stockholm, Sweden

(Received 7 August 2015; published 14 January 2016)

The three major unknown neutrino oscillation parameters at the present juncture are the mass hierarchy, the octant of the mixing angle θ_{23} and the CP phase δ_{CP} . It is well known that the presence of hierarchy- δ_{CP} and octant degeneracies affects the unambiguous determination of these parameters. In this paper, we show that a comprehensive way to study the remaining parameter degeneracies is in the form of a generalized hierarchy- θ_{23} - δ_{CP} degeneracy. This is best depicted as contours in the test $(\theta_{23} - \delta_{CP})$ plane for different representative true values of parameters. We show that the wrong-hierarchy and/or wrong-octant solutions can be further classified into eight different solutions depending on whether they occur with the wrong or right value of δ_{CP} . These eight solutions are different from the original eightfold degenerate solutions and can exist, in principle, even if θ_{13} is known. These multiple solutions, apart from affecting the determination of the true hierarchy and octant, also affect the accurate estimation of δ_{CP} . We identify which of these eight different degenerate solutions can occur in the test $(\theta_{23} - \delta_{CP})$ parameter space, taking the long-baseline experiment NO ν A running in the neutrino mode as an example. The inclusion of the NO ν A antineutrino run removes the wrong-octant solutions appearing with both right and wrong hierarchy. Adding T2K data to this resolves the wrong hierarchy-right octant solutions to a large extent. The remaining wrong-hierarchy solutions can be removed by combining NO ν A + T2K with atmospheric neutrino data. We demonstrate this using ICAL@INO as the prototype atmospheric neutrino detector. We find that the degeneracies can be resolved at the 2σ level by the combined data set, for the true parameter space considered in the study.

DOI: [10.1103/PhysRevD.93.013013](https://doi.org/10.1103/PhysRevD.93.013013)

I. INTRODUCTION

The standard three-flavor neutrino oscillation probability is described by six parameters, namely three mixing angles $(\theta_{12}, \theta_{23}, \theta_{13})$, two mass squared differences $[\Delta m_{31}^2, \Delta m_{21}^2]$ ($\Delta m_{ij}^2 = m_i^2 - m_j^2$) and the Dirac CP phase δ_{CP} . The neutrino oscillation data from solar, atmospheric, reactor and accelerator experiments have so far given information about each of these oscillation parameters except δ_{CP} [1–3]. At present, the unknowns in neutrino oscillation physics are (i) the sign of Δm_{31}^2 [$\Delta m_{31}^2 > 0$ known as normal hierarchy (NH) and $\Delta m_{31}^2 < 0$ known as inverted hierarchy (IH)], (ii) the octant of θ_{23} [$\theta_{23} > 45^\circ$ known as a higher octant (HO) and $\theta_{23} < 45^\circ$ known as a lower octant (LO)] and (iii) the CP phase δ_{CP} ; any value of this parameter other than 0° and $\pm 180^\circ$ would signal CP violation in the lepton

sector. In this case, it is often useful to talk in terms of the lower half-plane (LHP) with $-180^\circ < \delta_{CP} < 0^\circ$ and upper half-plane (UHP) with $0^\circ < \delta_{CP} < 180^\circ$.

The appearance channel $P_{\mu e}$ often known as the “golden channel” can measure all the three unknown parameters described above.¹ However, the measurement is complicated by the fact that different sets of values of parameters can give the same oscillation probability. This gives rise to degeneracies that render an unambiguous determination of true parameters difficult. It was discussed in Ref. [4] that there can be eight-fold degeneracies in neutrino oscillation probabilities which are (a) the intrinsic or $\theta_{13} - \delta_{CP}$ degeneracy [5], (b) the hierarchy- δ_{CP} degeneracy [6] and (c) the intrinsic octant degeneracy [7]. The intrinsic degeneracy refers to clone solutions occurring due to a different θ_{13} and δ_{CP} value. This degeneracy can be removed to a large extent by using spectral information [8]. Moreover, the current precision determination of θ_{13}

* monojit@prl.res.in
 † pomita.ghoshal@gmail.com
 ‡ sruba@prl.res.in
 § newton@prl.res.in
 || raut@kth.se

¹Originally, $P_{\mu e}$ was termed as the golden channel because of its sensitivity to θ_{13} , hierarchy and δ_{CP} .

[9–12] has removed this degeneracy to a great extent. The hierarchy- δ_{CP} degeneracy leads to wrong-hierarchy solutions occurring for a different value of δ_{CP} other than the true value. The intrinsic octant degeneracy refers to duplicate solutions occurring for θ_{23} and $\pi/2 - \theta_{23}$.

Many papers have discussed possibilities of the resolution of these degeneracies by using different detectors in the same experiment [13–15]. The synergistic combination of data from different experiments was also discussed as an effective means of removing such degeneracies by virtue of the fact that the oscillation probabilities offer different combinations of parameters at varying baselines and energies [8,16–23]. In particular, the synergy between long-baseline (LBL) experiments $\text{NO}\nu\text{A}$ and T2K in resolving the hierarchy- δ_{CP} degeneracy has been discussed recently in Refs. [24–27].

It has been shown in Refs. [21,28,29] that a precise measurement of the mixing angle θ_{13} is helpful for the removal of octant degeneracy. Octant sensitivity in the T2K and $\text{NO}\nu\text{A}$ experiments has been studied recently in Refs. [30,31] in view of the measurement of a nonzero θ_{13} . The octant degeneracy is different for neutrinos and antineutrinos, and hence a combination of these two data sets can be conducive for the removal of this degeneracy for most values of δ_{CP} [32–34].

Since atmospheric neutrino baselines experience strong Earth matter effects, these effectively remove the overlap between right- and wrong-hierarchy solutions [35–38]. In particular, atmospheric neutrino experiments capable of distinguishing neutrinos and antineutrinos can be very useful in resolving degeneracies related to the mass hierarchy [38–48]. The octant sensitivity of the atmospheric neutrinos comes from both the appearance [49] and disappearance channels [50] and also benefits from significant matter effects, especially facilitated by the large value of θ_{13} measured by reactor experiments. Atmospheric neutrinos also provide a synergy with LBL experiments in terms of probability behavior with respect to parameters, so that the combination of atmospheric neutrino data with LBL data exhibits a reduced effect of the hierarchy and octant degeneracies [31,45,51–53].

Recently, it has been realized that for the appearance channel, the octant degeneracy can be generalized to the octant- δ_{CP} degeneracy corresponding to any value of θ_{23} in the opposite octant [31,54]. A continuous generalized degeneracy in the three-dimensional $\theta_{23} - \theta_{13} - \delta_{CP}$ plane has been studied in Ref. [54]. In this work, we show that with the high precision measurement of θ_{13} by reactor experiments, the degeneracies can be discussed in an integrated manner in terms of a generalized hierarchy- $\theta_{23} - \delta_{CP}$ degeneracy. A good way to visualize the different degenerate solutions is in terms of contours in the test $(\theta_{23} - \delta_{CP})$ plane for different choices of true values of parameters.² These

²Note that prior to the discovery of a nonzero value of θ_{13} , the degeneracies were studied mainly in $\theta_{13} - \delta_{CP}$ plane.

TABLE I. Various possibilities of degeneracy in the probability $P_{\mu e}$. Here, R = right, W = wrong, H = hierarchy and O = octant.

Solution with right δ_{CP}	Solution with wrong δ_{CP}
I. RH-RO-R δ_{CP}	V. WH-WO-W δ_{CP}
II. RH-WO-R δ_{CP}	VI. RH-RO-W δ_{CP}
III. WH-RO-R δ_{CP}	VII. RH-WO-W δ_{CP}
IV. WH-WO-R δ_{CP}	VIII. WH-RO-W δ_{CP}

plots also give an indication regarding the precision of the parameters δ_{CP} and θ_{23} . Although hierarchy degeneracy is discrete, the $\theta_{23} - \delta_{CP}$ degeneracy is continuous for the appearance channel probability $P_{\mu e}$. Inclusion of the information from the disappearance channel $P_{\mu\mu}$ restricts θ_{23} , and discrete degenerate solutions are generated. We classify, for the first time, the wrong-hierarchy and wrong-octant solutions with respect to right or wrong δ_{CP} values. This also allows us to understand how the hierarchy and octant degeneracies can affect the precision in δ_{CP} . We observe that since the wrong-hierarchy and wrong-octant solutions can occur for wrong values of δ_{CP} as well, there can exist, in principle, a total of eight degenerate solutions corresponding to different combinations of hierarchy, octant and δ_{CP} . This is summarized in Table I.³ Note that these solutions are different from the eight-fold degenerate solutions that have been discussed in the literature. To the best of our knowledge, the parameter degeneracies have not been studied in this generalized form in the literature prior to this. We identify which degenerate solutions among the eight possibilities listed in Table I exist in the neutrino oscillation probabilities for typical baselines and energies corresponding to the LBL experiments T2K and $\text{NO}\nu\text{A}$.

For representative true values of these parameters, we demonstrate to what extent the degenerate solutions can be removed by $\text{NO}\nu\text{A}$, $\text{NO}\nu\text{A} + \text{T2K}$ and $\text{NO}\nu\text{A} + \text{T2K} + \text{ICAL}$. Note that, although the combined capability of $\text{NO}\nu\text{A}$, T2K and ICAL in the hierarchy octant and δ_{CP} determination have been investigated, a comprehensive study for the removal of degeneracies using these three facilities together has not been done before.

The paper is organized as follows. In Sec. II, we give the experimental details of the LBL and atmospheric neutrino experiments being considered. In Sec. III, first we summarize the parameter degeneracies and identify degenerate solutions at the level of neutrino oscillation probabilities. Then, we show their occurrence at the event level considering $\text{NO}\nu\text{A}$ and discuss the resolution of the different kinds of degeneracies by combinations of the given

³It is to be noted in this connection that if the δ_{CP} precision is not good, then there can be continuous regions connecting right and wrong δ_{CP} solutions, and hence it may not always be possible to identify discrete wrong δ_{CP} solutions.

experiments. We also present the precision of the parameters θ_{23} and δ_{CP} from the combined analysis with NO ν A + T2K + ICAL data. The conclusions are presented in Sec. IV. The Appendix outlines the synergy between the disappearance and appearance channels and the role of antineutrinos.

II. EXPERIMENTAL DETAILS

We use the GLoBES package [55,56] (along with the required auxiliary files [57,58]) to simulate the data of the two long-baseline neutrino oscillation experiments T2K (Tokai to Kamioka, Japan) and NO ν A (NuMI Off-Axis ν_e Appearance, Fermilab). The source to detector distance, L , for T2K is 295 km. In the T2K experiment [59], muon neutrinos are directed from J-PARC, making an off-axis angle of 2.5° toward the Super-Kamiokande detector, which is a Water Čerenkov detector of mass 22.5 kt. T2K has been proposed to run for a total luminosity of 7.8×10^{21} protons on target (POT), and it has already collected 10% of the total data in the neutrino mode. At present it is running in the antineutrino mode, and the first results have been reported [60]. The recently operational NO ν A experiment is also sending muon neutrinos through two detectors, one at Fermilab (the near detector) and one in northern Minnesota (the far detector), making an off-axis angle of 0.8° and traveling a distance of 810 km to reach the far detector, which is a 14 kt totally active scintillator detector (TASD). The beam power of NO ν A is planned to be 700 kW which corresponds to 6×10^{20} POT/year which will run for $3(\nu) + 3(\bar{\nu})$ years. In our simulation of NO ν A data, we considered the reoptimized NO ν A set up from Refs. [26,61].

For the simulation of an atmospheric neutrino experiment, we consider a magnetized iron calorimeter detector (ICAL) planned by the India-based Neutrino Observatory (INO), the primary goal of which is to study atmospheric muon neutrinos. ICAL@INO has an advantage over other detectors because it has a magnetic field which allows charge discrimination, thus providing the facility to distinguish between μ^+ and μ^- . Here, we consider the 50 kt detector for ICAL@INO with a runtime of 10 years. In our numerical analysis, we have used constant detector angular and energy resolutions of 10° and 10% respectively and 85% overall efficiency. The muon resolutions from INO simulations can be found in Ref. [62]. We have checked that the constant resolutions used in this paper give results similar to those obtained using resolutions from INO simulation codes [44,45]. In our analysis of atmospheric neutrinos, we used the Gaussian formula to compute the statistical χ^2 . Systematic errors are taken into account using the method of pulls [63,64] as outlined in Ref. [42]. We have added a 5% prior on $\sin^2 2\theta_{13}$.

We use the following representative values for the oscillation parameters in our numerical simulation as given in Table II, Refs. [1–3].

TABLE II. Values of neutrino oscillation parameters used in our simulations. Here, the second column gives the true values of the parameters, and the third column represents the parameter range over which we have marginalized the test values.

Oscillation parameters	True value	Test value
$\sin^2 2\theta_{13}$	0.1	0.085–0.115
$\sin^2 \theta_{12}$	0.31	–
θ_{23}	LO = $39^\circ, 42^\circ$, HO = $48^\circ, 51^\circ$	35° – 55°
Δm_{21}^2	$7.60 \times 10^{-5} \text{ eV}^2$	–
Δm_{31}^2	$2.40 \times 10^{-3} \text{ eV}^2$	$(2.15$ – $2.65) \times 10^{-3} \text{ eV}^2$
δ_{CP}	$90^\circ, 0^\circ, -90^\circ$	-180° to $+180^\circ$

III. IDENTIFYING DEGENERACIES IN NEUTRINO OSCILLATION PARAMETERS AND THEIR RESOLUTION

For the baselines relevant for the experiments NO ν A and T2K, the Earth matter density is in the range (2.3 – 3.0 g/cc), well below the matter resonance. Therefore, oscillation probabilities computed assuming constant matter density can be used for these experiments. Such probabilities calculated using perturbative expansion of the small leptonic mixing angle θ_{13} (in terms of s_{13}) and the mass hierarchy parameters $\alpha (\equiv \Delta m_{21}^2 / \Delta m_{31}^2)$ are given as follows [65–67],

$$P_{\mu\mu} = 1 - \sin^2 2\theta_{23} \sin^2 \Delta + \mathcal{O}(\alpha, s_{13}) \quad (1)$$

$$P_{\mu e} = 4s_{13}^2 s_{23}^2 \frac{\sin^2(A-1)\Delta}{(A-1)^2} + \alpha^2 \cos^2 \theta_{23} \sin^2 2\theta_{12} \frac{\sin^2 A\Delta}{A^2} + \alpha s_{13} \sin 2\theta_{12} \sin 2\theta_{23} \cos(\Delta + \delta_{cp}) \times \frac{\sin(A-1)\Delta \sin A\Delta}{(A-1)A}, \quad (2)$$

where $s_{ij}(c_{ij}) = \sin \theta_{ij}(\cos \theta_{ij})$ for $j > i$ ($i, j = 1, 2, 3$). We use the following notation: $\Delta \equiv \Delta m_{31}^2 L / 4E$, $A \equiv 2EV / \Delta m_{31}^2 = VL / 2\Delta$, where $V = \sqrt{2}G_F n_e$ is the Wolfenstein matter term. The antineutrino oscillation probability can be obtained by replacing $\delta_{CP} \rightarrow -\delta_{CP}$ and $V \rightarrow -V$. Hence, in the neutrino oscillation probability, A is positive for NH and negative for IH, and for antineutrinos, the sign of A gets reversed. We observe the following salient features from the probability formulas:

- (i) The leading order term in the muon neutrino survival probability $P_{\mu\mu}$, also known as the disappearance channel, is proportional to $\sin^2 2\theta_{23} \sin^2 \Delta$. This gives rise to the intrinsic hierarchy and octant degeneracies:

$$P_{\mu\mu}(\Delta) = P_{\mu\mu}(-\Delta) \quad (3)$$

$$P_{\mu\mu}(\theta_{23}) = P_{\mu\mu}(\pi/2 - \theta_{23}). \quad (4)$$

This leads to a loss of sensitivity to the hierarchy and octant, when the measurement is performed using this channel.

- (ii) The appearance channel $P_{\mu e}$ does not have intrinsic degeneracies but suffers from the combined effect of different parameters, which leads to the following set of degeneracies:

$$P_{\mu e}(\theta_{13}, \delta_{CP}) = P_{\mu e}(\theta'_{13}, \delta'_{CP}) \quad (5)$$

$$P_{\mu e}(\Delta, \delta_{CP}) = P_{\mu e}(-\Delta, \delta'_{CP}). \quad (6)$$

Equations (4)–(6) constitute the eight-fold degeneracy discussed in Ref. [4].

Recently, it has been discussed that in the context of probabilities which are dependent on $\sin^2 \theta_{23}$, the octant degeneracy can be generalized to include all values of θ_{23} in the second octant [31] and can also be correlated with δ_{CP} [31,68]. The pattern of parameter degeneracies in the three-dimensional $\theta_{23} - \theta_{13} - \delta_{CP}$ space arising from the appearance probability $P_{\mu e}$ has been discussed in Ref. [54]. This is a continuous degeneracy and can be expressed as

$$\begin{aligned} P_{\mu e}(\theta_{23}, \theta_{13}, \delta_{CP}) &= P_{\mu e}(\theta'_{23}, \theta'_{13}, \delta'_{CP}) \\ &\Rightarrow \text{generalized octant degeneracy.} \end{aligned} \quad (7)$$

However, the reactor experiments have measured $\sin^2 \theta_{13}$ with a high degree of accuracy, and future measurements are expected to improve it further. This has reduced the impact of θ_{13} uncertainty on octant degeneracy to a large extent [31]. In this paper, we consider another generalized degeneracy which is the hierarchy- $\theta_{23} - \delta_{CP}$ degeneracy:

$$\begin{aligned} P_{\mu e}(\theta_{23}, \Delta, \delta_{CP}) &= P_{\mu e}(\theta'_{23}, -\Delta', \delta'_{CP}) \\ &\Rightarrow \text{generalized hierarchy} \\ &\quad - \theta_{23} - \delta_{CP} \text{ degeneracy.} \end{aligned} \quad (8)$$

This degeneracy can be observed best in the test $\theta_{23} - \delta_{CP}$ plane. Studying it in this fashion allows us to view the degeneracies arising out of the remaining unknown parameters in a comprehensive manner. We note that while the hierarchy degeneracy is always discrete, the $\theta_{23} - \delta_{CP}$ degeneracy arising out of the appearance channel is continuous. On the other hand, the intrinsic octant degeneracy arising from the $P_{\mu\mu}$ channel is independent of δ_{CP} and discrete in θ_{23} except for θ_{23} values close to maximal. Thus, combining the survival and conversion probabilities gives rise to disconnected degenerate regions in the $\theta_{23} - \delta_{CP}$ plane. We have elaborated on this point in the Appendix.

In the next subsection, we study the occurrence of the above degeneracies in terms of probabilities for NO ν A and T2K and identify the different possible degenerate solutions at the probability level.

A. Identifying degeneracies at the probability level

Figure 1 shows the probability $P_{\mu e}$ for neutrinos (left panel) and antineutrinos (right panel) as a function of δ_{CP} for both NH and IH. The plots in the upper panel correspond to NO ν A, while those in the lower panel are for T2K. These probabilities are plotted for the energy where the neutrino flux peaks. The hatched area denotes variation over θ_{23} . For the lower (higher) octant, we vary θ_{23} between 39° – 42° (48° – 51°). This is a good assumption for θ_{23} not too close to its maximal value, for the purpose of illustrating the physics, since for a given $\theta_{23}(\text{true})$, the disappearance channel anyway excludes values away from $\theta_{23}(\text{true})$ and $\pi/2 - \theta_{23}(\text{true})$. Thus, these plots implicitly assume information from the disappearance channel. From Fig. 1, the following points can be noted:

For neutrinos—

- (i) The NH probabilities are higher than the IH probabilities. This is because of the enhanced matter effect for neutrinos for NH in the Earth's matter.
- (ii) For both NH and IH, the probabilities are higher in the LHP.
- (iii) The probabilities for a higher octant are higher for both NH and IH.

While, for antineutrinos—

- (i) “A” changes its sign, and IH probabilities become higher than NH.
- (ii) The flip in sign of δ_{CP} makes both the NH and IH probabilities higher in the UHP.
- (iii) Like neutrinos, the probabilities for a higher octant remain higher for both NH and IH. For both neutrinos and antineutrinos, the lowest line in the LO (HO) band corresponds to 39° (48°), while the highest point corresponds to 42° (51°), due to the $\sin^2 \theta_{23}$ dependence of the leading order term.

The overlapping regions between various curves at a specific value of δ_{CP} indicate the degeneracy occurring for the right value of δ_{CP} , while the same value of the probability for different δ_{CP} values denotes degeneracy occurring at wrong values of δ_{CP} . Clearly, the former would correspond to solutions with the wrong hierarchy and/or octant with right δ_{CP} , while the latter would correspond to the solutions with the wrong hierarchy and/or octant and wrong δ_{CP} . The wrong- CP degenerate solutions corresponding to a given true value of θ_{23} and δ_{CP} can be obtained from the probability figures by drawing a horizontal line through this point. The different intersection points of this line with the probability bands are degenerate as they share the same value of probability. However, the degenerate solutions occurring for a particular θ_{23} (true) which is not in the vicinity of $\pi/2 - \theta_{23}$ (true) in the opposite octant will be excluded by the disappearance channel, and the occurrence of these solutions in the test $\theta_{23} - \delta_{CP}$ plane will depend on the θ_{23} precision of the disappearance channel.

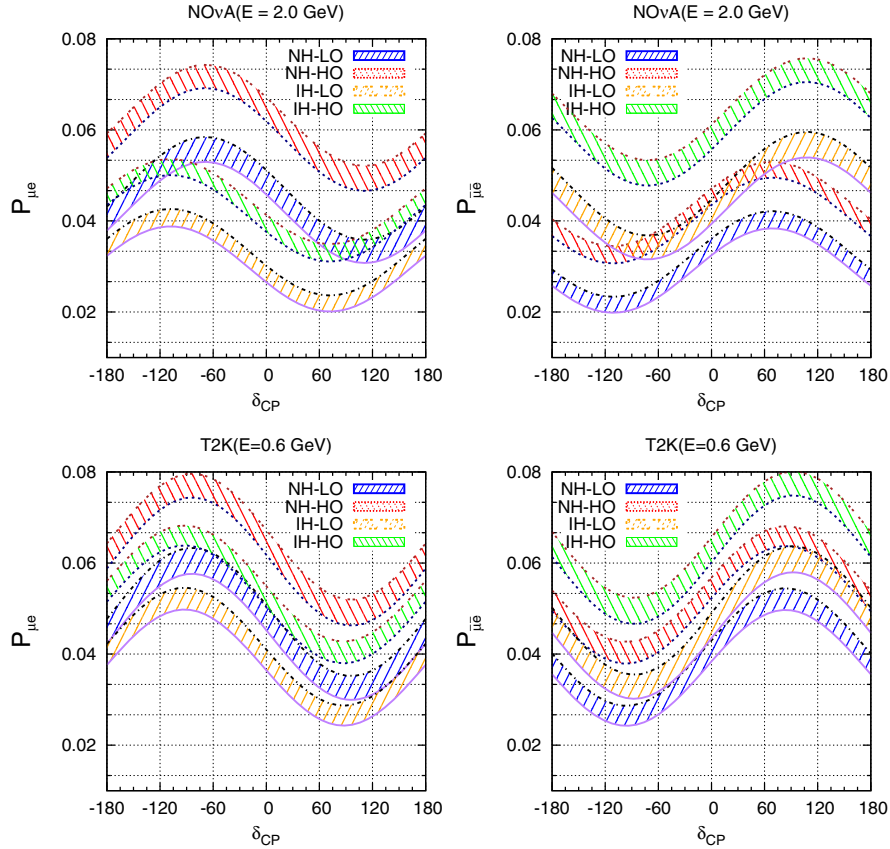


FIG. 1. The oscillation probability $P_{\mu e}$ as a function of δ_{CP} . Here, the upper row represents oscillation probability for $\text{NO}\nu\text{A}$ [$L = 810$ km], and the lower row represents probability for T2K [$L = 295$ km]. The left panel is for neutrinos, while the right panel is for antineutrinos.

Below, we explain the occurrence of the different degenerate combinations of $\{\text{hierarchy}, \theta_{23}, \delta_{CP}\}$ taking the $\text{NO}\nu\text{A}$ neutrino probabilities (the top-left panel) as reference unless otherwise mentioned:

- (1) The overlapping regions between the NH-LO (blue) and IH-HO (green) bands around $\delta_{CP} = -120^\circ$ and 90° give rise to WH-WO- $R\delta_{CP}$ degenerate solutions in the probability. However, for antineutrinos, these bands are well separated. Thus, combining $\text{NO}\nu\text{A}$ neutrino and antineutrino data can help in removing these solutions.
- (2) The probability corresponding to UHP of the NH-LO (blue) band can be the same as those for the LHP of the IH-LO (yellow) band for $\theta_{23} = 39^\circ$. This can give rise to WH-RO- $W\delta_{CP}$ solutions. Note that this degeneracy is present in the antineutrinos for the same values of δ_{CP} . Thus, for true NH, UHP (i.e. $0^\circ < \delta_{CP} < 180^\circ$) is the unfavorable half-plane of δ_{CP} , and this degeneracy cannot be resolved by using $\text{NO}\nu\text{A}$ data alone. For T2K, the probability exhibits a sharper variation with δ_{CP} , and hence this degeneracy is less pronounced between the UHP and LHP. Hence, the addition of T2K data to $\text{NO}\nu\text{A}$ can be

helpful in removing this degeneracy. For LHP (i.e. $-180^\circ < \delta_{CP} < 0^\circ$), which is the favorable half-plane of δ_{CP} in NH, there is no WH-RO- $W\delta_{CP}$ solution for both $\text{NO}\nu\text{A}$ and T2K.

- (3) For $\delta_{CP} \in \text{UHP}$, the NH-HO (red) band can share same value of probability with NH-LO (blue) band for $\delta_{CP} \in \text{LHP}$. This is the reason for the RH-WO- $W\delta_{CP}$ solution. For antineutrinos, the degeneracy is seen to be between NH-HO-LHP and NH-LO-UHP. Thus, a combination of neutrinos and antineutrinos helps to remove this degeneracy.
- (4) The WH-WO- $W\delta_{CP}$ solution can be observed along the isoprobability line that intersects the NH-LO (blue) and IH-HO (green) bands at different values of δ_{CP} . This degeneracy can be seen for instance between $\{\text{NH}, 39^\circ, -180^\circ\}$ and $\{\text{IH}, 51^\circ, 0^\circ\}$. Again, the antineutrino probability does not suffer from this degeneracy, and thus combining neutrino and antineutrino data can be helpful in removing these solutions.
- (5) One can also have RH-RO- $W\delta_{CP}$ solutions as a result of a so-called ‘‘intrinsic CP degeneracy’’ that occurs for the same hierarchy and same value of θ_{23} but at a different value of δ_{CP} . This is due to the

harmonic dependence of the probability on δ_{CP} . For instance, within the NH-HO (blue) band, $\delta_{CP} = 0^\circ$ and $\delta_{CP} \approx -135^\circ$ have the same value of probability for $\theta_{23} = 39^\circ$. However, for antineutrinos, this occurs for $\delta_{CP} = 0^\circ$ and $\delta_{CP} = +135^\circ$. Thus, a combination of neutrino and antineutrino data can help to get rid of this degeneracy. This can also be seen to occur for T2K, for $\{\text{NH}, 48^\circ, -180^\circ\}$ and $\{\text{NH}, 48^\circ, 0^\circ\}$. For T2K, since the flux peak coincides with the probability peak, the CP -dependent term is proportional to $\sin \delta_{CP}$, and thus this degeneracy occurs for δ_{CP} and $\pi - \delta_{CP}$ [68]. For $\text{NO}\nu\text{A}$, since the flux and the probability peak are not at the same energy, the degeneracy does not correspond exactly to δ_{CP} and $\pi - \delta_{CP}$. It is interesting to note that this degeneracy does not occur for $\delta_{CP} = \pm 90^\circ$.

Thus, among the eight solutions listed above, only the WH-RO- $R\delta_{CP}$ and RH-WO- $R\delta_{CP}$ solutions do not exist even at the probability level. The above description is in terms of probabilities without including any experimental errors. At the event level, many of these may not appear as discrete degeneracies. In particular, for a C.L. beyond the reach of a particular experiment's precision, the different discrete degenerate solutions merge, and the degeneracy becomes continuous.

Note that another way to understand the degeneracies is the biprobability ellipses in the $P_{\mu e} - P_{\bar{\mu} e}$ plane [6]. This requires a single plot for neutrinos and antineutrinos. However, each point on these ellipses corresponds to different values of δ_{CP} which cannot be read off from the plots. The probability band plots presented in this paper provide a complementary way to visualize the occurrence of the degeneracies at different CP values, and one can readily identify the wrong and right δ_{CP} solutions which are the main focus of this work.

B. Identifying degeneracies at the event level

To show the occurrence of the different degeneracies at the event level, in Fig. 2 we present a set of contour plots in the $\theta_{23} - \delta_{CP}$ test-parameter plane assuming only neutrino run (6 years) of $\text{NO}\nu\text{A}$, which is denoted as $[6 + 0]$. We note that the proposed run time of $\text{NO}\nu\text{A}$ is $3 + 3$. However, in this section, we intend to identify which of the different degenerate solutions discussed in Table I can arise in the $\theta_{23} - \delta_{CP}$ plane. Since the wrong-octant solutions disappear including the antineutrino run, the $6 + 0$ case is the best option for visualizing all the possible degenerate solutions. The $3 + 3$ case is discussed in the next section. These sets of plots also show the role of statistics which can give enhanced precision *vis-à-vis* the antineutrino run which helps in resolving degeneracies. Similar plots can also be drawn for the T2K $8 + 0$ case. However, for T2K, since the hierarchy sensitivity is much less, the possibility of getting continuous regions instead of

discrete degenerate solutions is more. Thus, the different degenerate solutions cannot be visualized so distinctly, and in this section, our main aim is to identify the different degenerate solutions in the $\theta_{23} - \delta_{CP}$ plane. This can be done better with $\text{NO}\nu\text{A } 6 + 0$ as the illustrative example. These plots are drawn assuming true hierarchy to be NH and different choices of true values of θ_{23} and δ_{CP} . In this and all the other subsequent figures, the successive rows are for $\theta_{23} = 39^\circ, 42^\circ, 48^\circ, 51^\circ$. The true δ_{CP} values chosen are $\pm 90^\circ$ corresponding to maximum CP violation and 0° corresponding to CP conservation. The blue contours correspond to the right hierarchy, and magenta curves correspond to the wrong hierarchy.

The first column of Fig. 2 shows the degenerate solutions for $\delta_{CP} = -90^\circ$ for $\text{NO}\nu\text{A}$ running only in the neutrino mode. For $\theta_{23} = 39^\circ$, apart from the true solution, RH-WO- $W\delta_{CP}$ and WH-WO- $R\delta_{CP}$ solutions are observed in the upper and lower right quadrants respectively. The RH-WO- $W\delta_{CP}$ solution is also seen for $\theta_{23} = 42^\circ$. For this case, at $\delta_{CP} = -90^\circ$, the uppermost point of the blue band in the $\text{NO}\nu\text{A}$ neutrino probability, in Fig. 1 one can see that the same value of probability is possible for NH-HO (red band) near $\delta_{CP} = +45^\circ$ and $\pm 180^\circ$. This explains the shape of the allowed zone—wider at these values and narrower at 90° . The WH-WO- $R\delta_{CP}$ solution is seen only at a 2σ level for $\theta_{23} = 42^\circ$. This can be understood by observing that the points 42° (the upper tip of the blue band) and 48° (the lower tip of the green band) are more separated as compared to 39° (the lower tip of the blue band) and 51° (the upper tip of the green band). For θ_{23} in the higher octant (48° and 51°), there are no spurious wrong-hierarchy solutions even with only neutrinos. This is because for NH, θ_{23} in the higher octant and -90° correspond to the maximum probability for neutrinos, and this cannot be matched by any other combination of parameters. Hence, no degenerate solutions appear, and only the neutrino run for $\text{NO}\nu\text{A}$ suffices to give an allowed area only near the true point. Note that the contours for 48° extend to the wrong octant also. However, (here and elsewhere) this is not due to any degenerate behavior of the $P_{\mu e}$ probability but due to the poor θ_{23} precision of the $P_{\mu\mu}$ channel near maximal mixing.

The second column represents $\delta_{CP} = +90^\circ$. In this case, we observe a WH-WO- $R\delta_{CP}$ solution for both $\theta_{23} = 39^\circ$ and 42° . This can be understood from the intersection of the blue and green bands in Fig. 1 close to $\delta_{CP} = 90^\circ$ in the UHP. We also get a WH-RO- $W\delta_{CP}$ region in the LHP. For 42° , since the θ_{23} precision coming from the disappearance channel is worse, at 2σ both these solutions merge, and a discrete degenerate region is not obtained. For $\theta_{23} = 51^\circ$ from Fig. 1, we see that the point $\{\text{NH}, +90^\circ, 51^\circ\}$ in the red band intersects the blue band around $\{\text{NH}, -90^\circ, 39^\circ\}$ giving a RH-WO- $W\delta_{CP}$ solution.

A WH-RO- $W\delta_{CP}$ solution is also obtained in this case in the LHP. Similar regions are also obtained for $\theta_{23} = 48^\circ$.

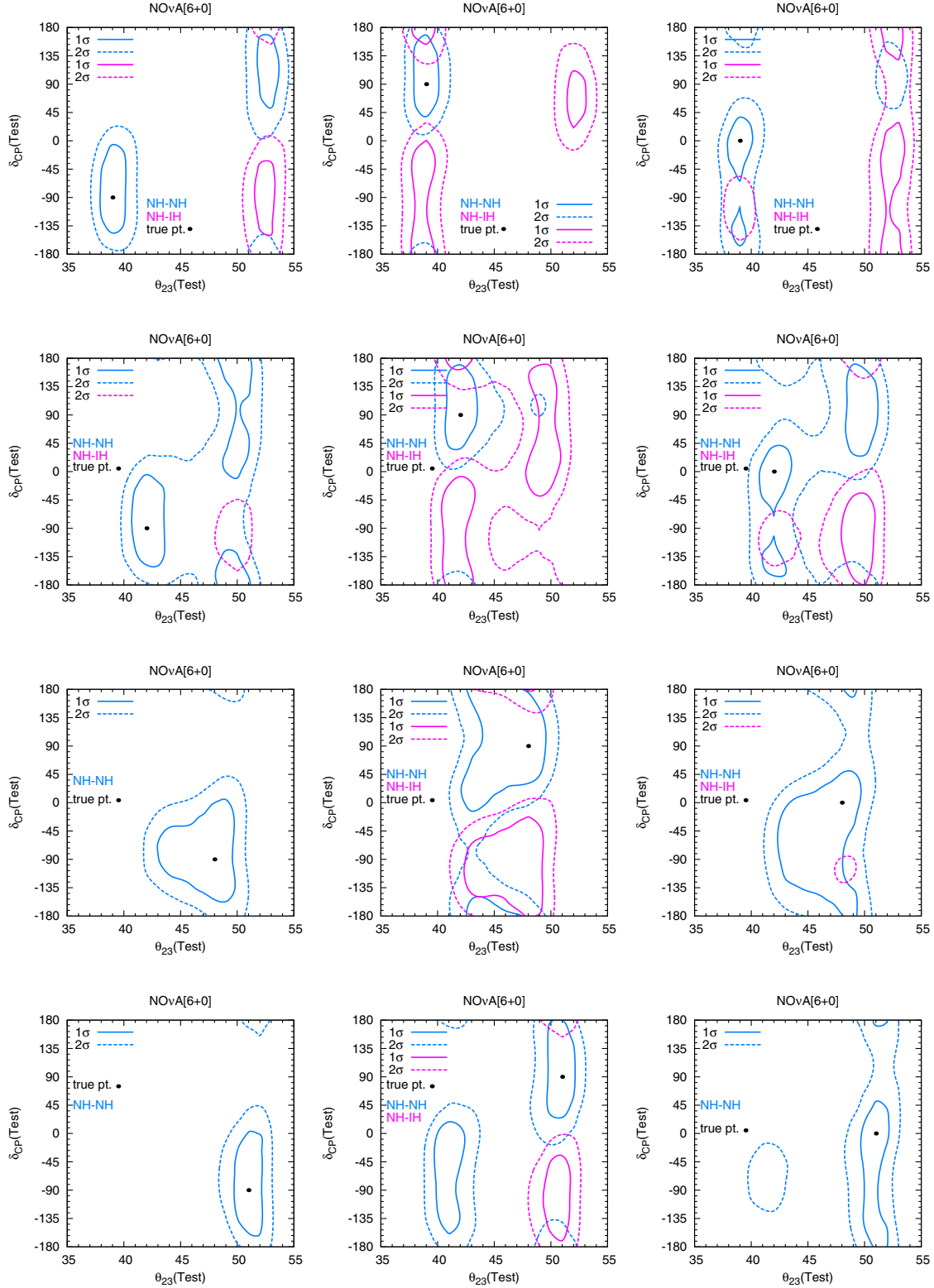


FIG. 2. Contour plots for $\text{NOvA}[6+0]$ with true values of $\theta_{23} = 39^\circ, 42^\circ, 48^\circ, 51^\circ$ in successive rows. The three columns correspond to $\delta_{CP} = -90^\circ, 90^\circ, 0^\circ$ respectively.

However, the RH-WO-W δ_{CP} solution merges with the true solution at 2σ level.

For $\delta_{CP} = 0^\circ$, a discrete RH-RO-W δ_{CP} solution is seen to be allowed at 1σ for $\theta_{23} \in \text{LO}$. This is due to the intrinsic CP degeneracy as discussed in the context of probabilities. But at 2σ , due to the poor δ_{CP} precision, this degeneracy becomes continuous, and the whole LHP becomes allowed. For θ_{23} belonging to the higher octant, larger statistical errors are involved as compared to $\theta_{23} \in \text{LO}$, and this degeneracy appears as continuous in the LHP even at 1σ , and at 2σ the full δ_{CP} range becomes allowed. For $\theta_{23} = 39^\circ$ and 42° , we also see wrong-hierarchy solutions appearing in the wrong octant. From the probability figure, we identify that this degeneracy occurs around $\delta_{CP} = -30^\circ, -180^\circ, 180^\circ$ for $\theta_{23} = 39^\circ$ which allows the LHP of δ_{CP} at 1σ and the whole δ_{CP} range at 2σ . For $\theta_{23} = 42^\circ$, this degeneracy is seen to occur around $\delta_{CP} = -90^\circ$ giving distinct degenerate solutions at the 1σ and 2σ levels. For $\theta_{23} = 42^\circ$, a discrete RH-WO-W δ_{CP} solution appears at 1σ . From Fig. 1, it is seen that $\{\text{NH}, 42^\circ, 0^\circ\}$ has the same value of probability corresponding to $\{\text{NH}, 48^\circ, 90^\circ\}$. At 2σ , this merges with the RH-RO-W δ_{CP} solution. For $\theta_{23} = 39^\circ$, this solution appears as a 2σ allowed patch around $\{\text{NH}, 51^\circ, 90^\circ\}$. From Fig. 1, it can be seen that the above points are not exactly degenerate in terms of probability, but due to lack of precision, they become allowed. For a similar reason, the 2σ patch with wrong hierarchy appears in the right octant for $\theta_{23} = 39^\circ$ and 42° . For $\theta_{23} = 51^\circ$, a right-hierarchy patch occurs with the wrong octant. For $\theta_{23} = 48^\circ$, because of the proximity to maximal mixing, the true parameter space also extends to the wrong octant. In general, we see that the CP precision is poorer for $\delta_{CP} = 0^\circ$ at this stage. This is due to the unresolved degeneracies for $\delta_{CP} = 0^\circ$ which lead to multiple allowed regions and continuous bands at 2σ .

C. Successive resolution of degeneracies with data from different experiments

In this section, first we show the status of the above degenerate regions when $\text{NO}\nu\text{A}$ runs in $[3+3]$ configuration. We then study the combined potential of $\text{NO}\nu\text{A}[3+3]$ and $\text{T2K}[8+0]$ in resolving the degeneracies. Finally, we add the atmospheric neutrino data from ICAL and show its impact.

It is well known that due to Earth matter effects and the presence of an antineutrino component in the atmospheric neutrino flux, ICAL can play a prominent role in resolving the hierarchy and octant degeneracies [44,62]. Since there is no δ_{CP} dependence in ICAL, the hierarchy and octant sensitivities are independent of δ_{CP} . This δ_{CP} -independent χ^2 adds to the χ^2 for $\text{NO}\nu\text{A}$ and T2K in the degenerate region, and the wrong-hierarchy and wrong-octant solutions can be resolved. This aids in improving both the octant and δ_{CP} sensitivities of T2K and $\text{NO}\nu\text{A}$ [31,69,70]. Note that this is a synergistic effect and the combined

sensitivity is better than that obtained by adding individual χ^2 values.

The advantage offered by the atmospheric neutrino detector ICAL and the synergy between the various experiments in removing the degeneracies can be seen from these plots. It is noteworthy that the allowed area in the test $\theta_{23} - \delta_{CP}$ plane also gives an idea about the precision of these two parameters.

Our results are presented in Figs. 3–5 which correspond to true $\delta_{CP} = -90^\circ, 90^\circ$ and 0° respectively. In each figure, the successive columns represent $\text{NO}\nu\text{A}[3+3]$, $\text{NO}\nu\text{A}[3+3] + \text{T2K}[8+0]$ and $\text{NO}\nu\text{A}[3+3] + \text{T2K}[8+0] + \text{ICAL}$ respectively. In these figures, the following generic features can be noted:

- (i) Comparing with the $\text{NO}\nu\text{A}[6+0]$ panels, in all the $\text{NO}\nu\text{A}[3+3]$ figures, we note that the addition of antineutrino information removes the wrong-octant degenerate regions. This also includes the wrong-hierarchy regions occurring with the wrong octant. For $\theta_{23} = 39^\circ$ and 51° , the wrong-octant regions are almost completely removed. But for the true θ_{23} values 42° and 48° , both the right-hierarchy and wrong-hierarchy solutions extend to the wrong-octant region.
- (ii) When T2K data is added to $\text{NO}\nu\text{A}[3+3]$, it helps in removing these wrong-octant extensions. The wrong hierarchy-right octant regions also get significantly reduced in size by adding T2K data to $\text{NO}\nu\text{A}[3+3]$. This is due to the fact that for T2K , these solutions occur at different δ_{CP} values than $\text{NO}\nu\text{A}$. Addition of T2K data also improves the precision of θ_{23} and δ_{CP} .
- (iii) When ICAL data are added to T2K and $\text{NO}\nu\text{A}$, the remaining wrong-hierarchy regions are resolved for all the true values of θ_{23} considered. The wrong-octant extensions of the right-hierarchy solutions are also reduced in size, and the precision of θ_{23} improves. The combination of $\text{T2K} + \text{NO}\nu\text{A} + \text{ICAL}$ can resolve all the degeneracies at a 2σ level for true $\theta_{23} = 39^\circ, 51^\circ$ for all the three δ_{CP} values. For the θ_{23} and δ_{CP} combinations of $\{42^\circ, 0^\circ\}$ and for $48^\circ, \pm 90^\circ, 0^\circ$, there are still allowed regions in the wrong octant. Note that some of the wrong-octant regions that are removed by the $\text{NO}\nu\text{A}$ antineutrino run could also be removed by the ICAL data.

Apart from the above features, the following important points can be observed from the figures:

- (i) For $\delta_{CP} = -90^\circ$, there are no wrong-hierarchy solutions in $\text{NO}\nu\text{A}[3+3]$, and the addition of T2K helps in improving the θ_{23} precision. This feature is particularly prominent for $\theta_{23} = 42^\circ$ and 48° where T2K data help in removing the wrong-octant extensions for the right-hierarchy solutions. With the addition of ICAL data, the wrong-octant

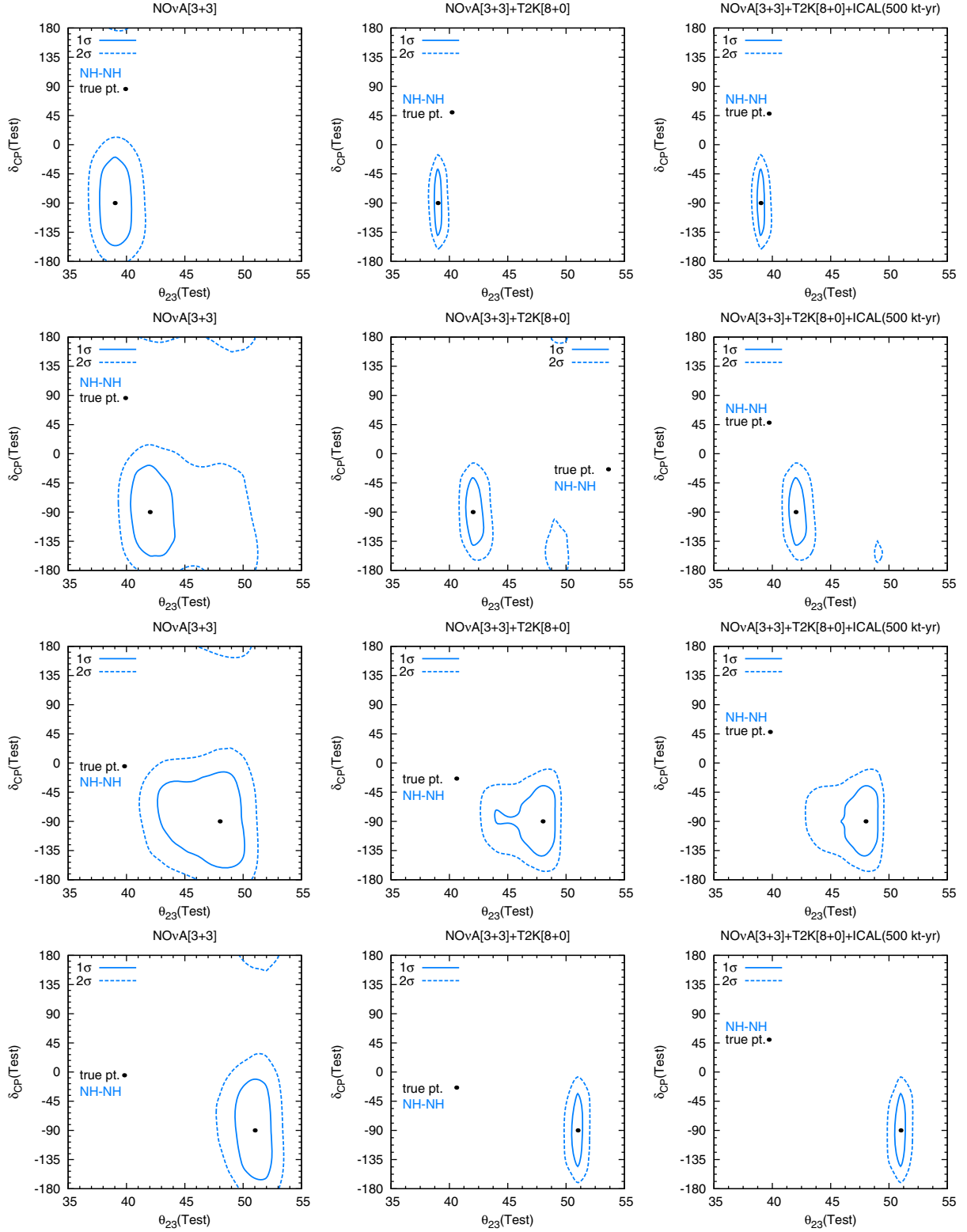
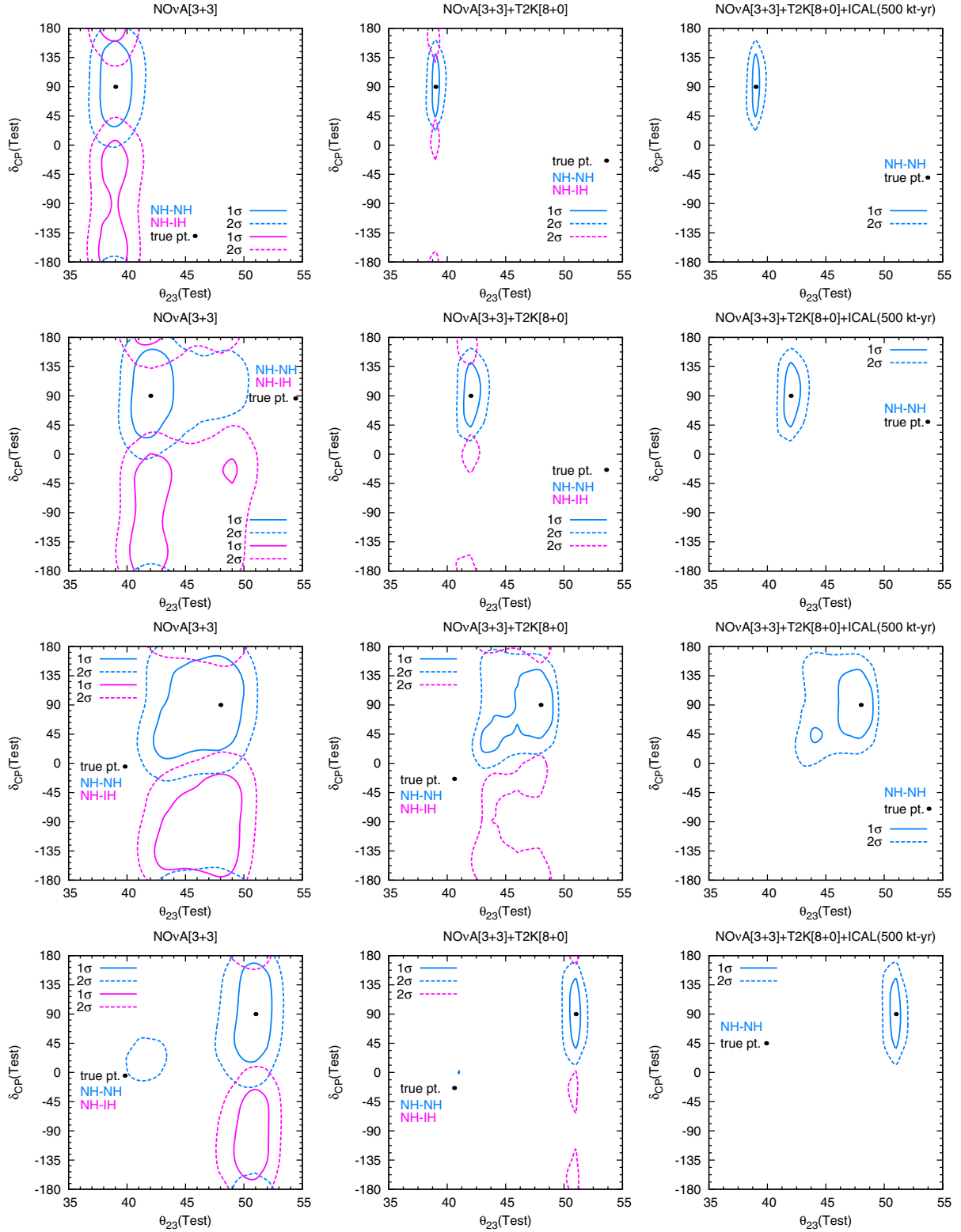


FIG. 3. Contour plots in the test $\theta_{23} - \delta_{CP}$ plane for true $\delta_{CP} = -90^\circ$ and true $\theta_{23} = 39^\circ, 42^\circ, 48^\circ$ and 51° in successive rows. The first column is for $\text{NO}\nu\text{A}[3+3]$. The second and third columns are for $\text{NO}\nu\text{A}[3+3] + \text{T2K}[8+0]$ and $\text{NO}\nu\text{A}[3+3] + \text{T2K}[8+0] + \text{ICAL}$ respectively.

FIG. 4. Same as in Fig. 3 but for true $\delta_{CP} = +90^\circ$.

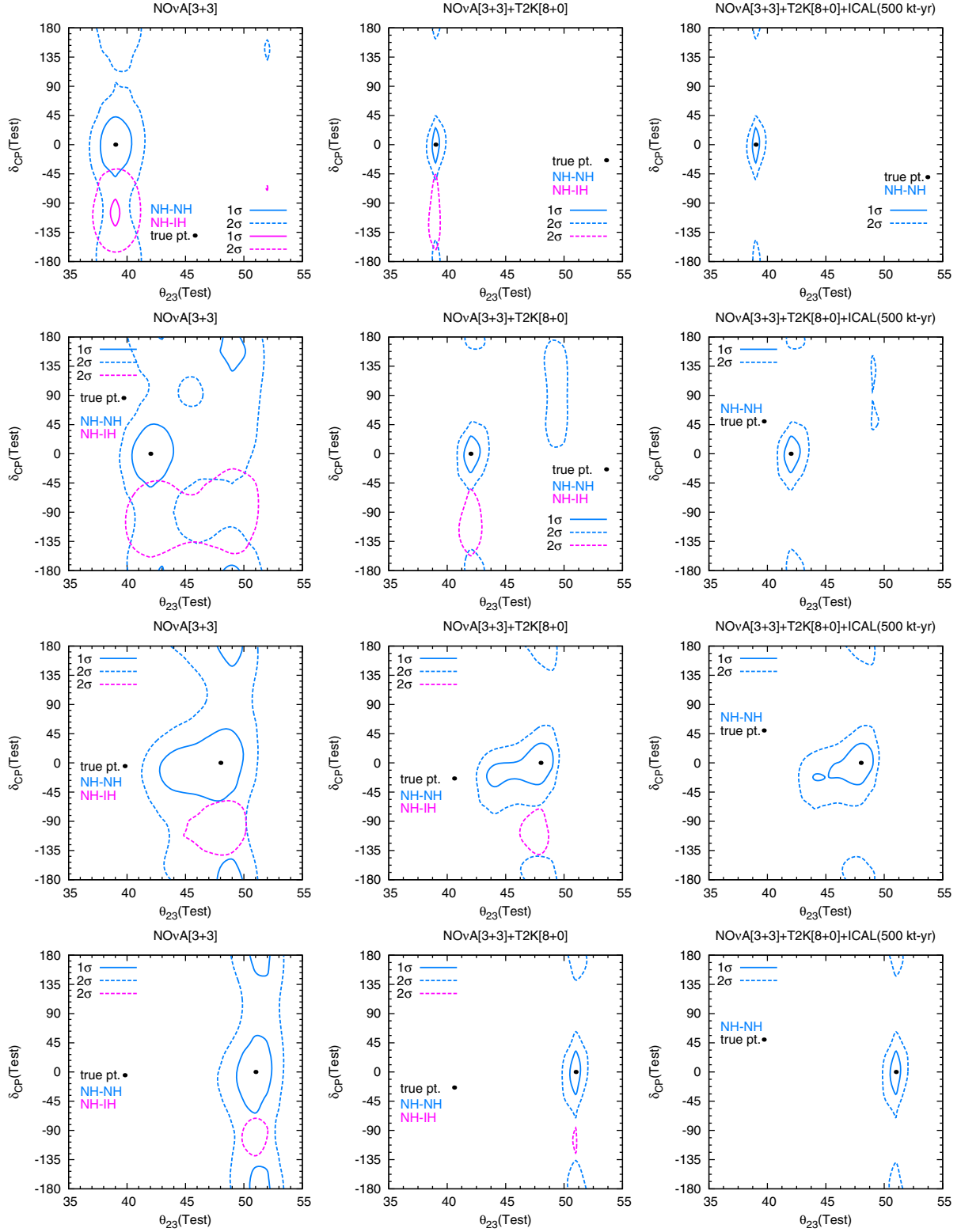


FIG. 5. Same as in Fig. 3 but for true $\delta_{CP} = 0^\circ$.

solution is almost resolved for $\theta_{23} = 42^\circ$, while for $\theta_{23} = 48^\circ$, the same is resolved at 1σ .

- (ii) For $\delta_{CP} = -90^\circ$ and $\theta_{23} = 51^\circ$, $\text{NO}\nu\text{A}$ can already resolve all the degeneracies with 6 years of neutrino run only as can be seen in Fig. 2. However, the precision of θ_{23} is worse with $\text{NO}\nu\text{A}[3+3]$. This is because splitting the neutrino run into equal neutrino and antineutrino runs reduces the statistics, and hence the precision becomes worse.
- (iii) For $\delta_{CP} = 90^\circ$, we also see that for $\theta_{23} = 48^\circ$, the wrong-hierarchy region in $\text{NO}\nu\text{A}[3+3] + \text{T2K}[8+0]$ is still quite large, and this is where ICAL has a remarkable role to play. We see that when ICAL data are added, the large wrong-hierarchy region corresponding to $\theta_{23} = 48^\circ$ completely vanishes.
- (iv) The small 1σ wrong hierarchy-wrong octant allowed zone for $\delta_{CP} = 90^\circ$ and $\theta_{23} = 42^\circ$ in $\text{NO}\nu\text{A}[3+3]$ can be identified as the part of the WH-WO-R δ_{CP} solution of $\text{NO}\nu\text{A}[6+0]$ by comparing with Fig. 2.
- (v) For $\delta_{CP} = 0^\circ$, adding T2K data to $\text{NO}\nu\text{A}[3+3]$ improves the precision considerably and also removes the wrong-hierarchy solutions to a large extent. The precision of θ_{23} and δ_{CP} around the true solution also improves. The enhanced precision due to adding T2K is also responsible for reducing the continuous allowed regions to discrete degenerate solutions for θ_{23} values near 45° . Adding ICAL data removes the remaining wrong-hierarchy regions and further help to pinpoint the allowed zones at a 2σ level.
- (vi) In $\text{NO}\nu\text{A}[3+3]$, for $\delta_{CP} = 0^\circ$ and $\theta_{23} = 39^\circ, 42^\circ$, comparing with the corresponding figures in Fig. 2, we see that the spurious solution appearing at -150° at 1σ due to the intrinsic degeneracy is no longer present with the addition of antineutrino data, since for the antineutrino probability in $\text{NO}\nu\text{A}$ the intrinsic degeneracy is between 0° and $+150^\circ$ as discussed earlier. Thus, the addition of neutrino and antineutrino data solves the intrinsic degeneracy at 1σ at both these δ_{CP} values, but at 2σ , both $\pm 150^\circ$ remain allowed. The allowed area near the true value increases in size because replacing half the neutrino run with antineutrinos reduces the statistics, and hence the precision becomes worse.

The following additional observations can be made regarding alternative parameter values and running modes:

- (i) In generating the above plots, we considered T2K running in the neutrino mode with its full beam power. We find that once one includes the antineutrino run from $\text{NO}\nu\text{A}$, running T2K in the antineutrino mode is no longer necessary for removing spurious wrong-octant solutions. Rather, running in the neutrino mode gives enhanced statistics and hence better precision. If on the other hand $\text{NO}\nu\text{A}$ runs in full neutrino mode and the antineutrino

component comes from T2K, we have verified that we get similar results.

- (ii) We have presented the results for the case of true NH. If the true hierarchy is chosen to be IH, one would get a different set of allowed regions based on the degeneracies observed in Fig. 1. For example, for $\delta_{CP} = -90^\circ$ and $\theta_{23} = 39^\circ$ for $\text{NO}\nu\text{A}[6+0]$ in the true IH case, apart from the true solution, RH-WO-W δ_{CP} and WH-RO-W δ_{CP} solutions would be obtained. This can be predicted from Fig. 1 (top left panel) by drawing a horizontal line from the bottom of the IH-LO band at $\delta_{CP} = -90^\circ$, which cuts both the IH-HO and NH-LO bands near $\delta_{CP} = 90^\circ$.

The situation for $\text{NO}\nu\text{A}[3+3]$ and other combinations would be more complicated since the allowed regions and precision for true IH depend not only on the probability behavior but also on the statistics of neutrino and antineutrino data in the respective experiments.

- (iii) The results are significantly dependent on the true value of θ_{13} , chosen here to be $\sin^2 2\theta_{13} = 0.1$. Lower values of θ_{13} (or worse θ_{13} precision) would lead to poorer CP precision and more difficulty in removing the degeneracies. This is because δ_{CP} is coupled with θ_{13} in the oscillation probability.

D. Distinguishability between 0° and 180°

It will also be interesting to see how far the two CP conserving values 0° and 180° can be distinguished by the experimental setups considered. In this section, we discuss this issue. The true events are generated for $\delta_{CP} = 0^\circ$, $\theta_{23} = 39^\circ$ and normal hierarchy. In the test spectrum, we consider $\delta_{CP} = 180^\circ$ and marginalize over θ_{13} . For purposes of comparison, we also give the results for test $\delta_{CP} = 90^\circ$. The results are presented in Table III. We observe that a 2σ sensitivity in distinguishing between $\delta_{CP} = 0^\circ$ and $\delta_{CP} = 180^\circ$ can be achieved by $\text{NO}\nu\text{A} + \text{T2K}$. Adding ICAL data increases the sensitivity further. It is interesting to note that for beam based experiments, 0° and 90° have much larger separation than that between 0° and 180° . But for ICAL, 0° and 180° are more separated though the χ^2 values are very small. This is because ICAL itself has limited CP sensitivity due to angular smearing over all directions [69]. Note that for experiments like PINGU, the CP sensitivity can be

TABLE III. χ^2 sensitivity for test $\delta_{CP} = 90^\circ, 180^\circ$ with true $\delta_{CP} = 0^\circ$, true hierarchy as NH and true θ_{23} as 39° .

$\nu + \bar{\nu}$	Test $\delta_{CP} = 90^\circ$	Test $\delta_{CP} = 180^\circ$
$\text{NO}\nu\text{A}[3+3]$	6.31	2.82
$\text{NO}\nu\text{A}[3+3] + \text{T2K}[8+0]$	14.63	4.77
ICAL	1.21	1.60
$\text{NO}\nu\text{A}[3+3] + \text{T2K}[8+0] + \text{ICAL}$	14.83	5.4

TABLE IV. Percentage precision of parameters θ_{23} and δ_{CP} around the true value using NO ν A + T2K + ICAL.

True value		LO precision				True value		HO precision			
θ_{23}	δ_{CP}	1σ		2σ		θ_{23}	δ_{CP}	1σ		2σ	
		θ_{23}	δ_{CP}	θ_{23}	δ_{CP}			θ_{23}	δ_{CP}	θ_{23}	δ_{CP}
39°	+90°	1.02	26.63	2.17	39.50	48°	+90°	3.15	28.45	7.70	48.27
	-90°	0.89	34.52	2.17	41.52		-90°	3.15	30.00	7.35	43.22
	0°	0.64	15.83	2.04	28.33		0°	4.03	17.50	7.59	35.80
42°	+90°	1.6	27.00	3.32	38.52	51°	+90°	0.88	30.32	2.16	43.33
	-90°	1.7	29.77	3.31	41.52		-90°	0.98	34.48	2.16	45.00
	0°	1.66	15.83	3.08	29.16		0°	0.88	19.16	2.16	37.50

higher, and the χ^2 difference between 0° and 180° can be appreciable [71].

E. Precision of θ_{23} and δ_{CP}

As stated earlier, the contour plots also give information about the precision of θ_{23} and δ_{CP} . In general the presence of degenerate solutions leads to a worse precision (a larger width of the allowed area) in these parameters. For most values of true δ_{CP} and θ_{23} , there is a negligible difference between the δ_{CP} precision of NO ν A[6 + 0] and NO ν A[3 + 3] around the true point. While there is a qualitative advantage to including both neutrinos and antineutrinos because of their different dependences on δ_{CP} , this advantage is squandered by the lower cross section of antineutrinos. The precision in these parameters can be quantified using the following formulas:

$$CP \text{ precision} = \frac{\delta_{CP}^{\text{Max}} - \delta_{CP}^{\text{Min}}}{360^\circ} \times 100\% \quad (9)$$

$$\theta_{23} \text{ precision} = \frac{\theta_{23}^{\text{Max}} - \theta_{23}^{\text{Min}}}{\theta_{23}^{\text{Max}} + \theta_{23}^{\text{Min}}} \times 100\%. \quad (10)$$

In Table IV, we list the values of the 1σ and 2σ precision of θ_{23} and δ_{CP} using these expressions for the case of NO ν A[3 + 3] + T2K[8 + 0] + ICAL. The CP precision is seen to be better for $\delta_{CP} = 0^\circ$ as compared to $\delta_{CP} = \pm 90^\circ$ for a given true value of θ_{23} . This is because in the absence of degeneracies the precision simply follows from the probability expression, where $dP_{\mu e}/d\delta_{CP}$ is smallest at 0° [25]. On the other hand, for a given value of δ_{CP} , the CP precision is seen to become worse with increasing θ_{23} . The θ_{23} precision is worse near maximal mixing and improves as one moves away.

IV. CONCLUSION

In the era when the value of θ_{13} was unknown, an eight-fold degeneracy of neutrino oscillation parameters was identified, which included the intrinsic θ_{13} , hierarchy- δ_{CP} and octant degeneracies. With the precise measurement of θ_{13} , the intrinsic degeneracy is largely removed, and a

four-fold degeneracy out of the original eight—involving wrong-hierarchy and wrong-octant solutions—remains to be solved by the current and upcoming experiments. In this paper, we study these degeneracies in detail and propose that the remaining degeneracies can be studied in the most comprehensive manner by considering the generalized hierarchy- $\theta_{23} - \delta_{CP}$ degeneracy. This degeneracy is continuous for the $P_{\mu e}$ channel. The addition of information on the measurement of θ_{23} by the $P_{\mu\mu}$ channel gives rise to discrete solutions. These are best visualized by contours in the test $(\theta_{23} - \delta_{CP})$ plane drawn for both right and wrong hierarchy for different representative values of true parameters. We show that, depending on whether the wrong-hierarchy and/or wrong-octant solutions occur with right or wrong values of δ_{CP} , there can be a total of eight possibilities. We study these possibilities at the probability level for T2K and NO ν A. At this level, the degeneracy is defined as the equality of the probabilities for different values of parameters. However, at the χ^2 contour level, because of the precision of the experiments, one gets finite allowed regions corresponding to degenerate solutions. We define a degenerate solution to be one which is distinct from the true solution at the 1σ level.

Taking only the neutrino run of NO ν A as an illustrative example, we identify which of these degenerate solutions actually occur for different representative choices of true parameters. The sample true values that we consider for obtaining the contours are $\theta_{23} = 39^\circ, 42^\circ, 48^\circ$ and 51° and $\delta_{CP} = \pm 90^\circ, 0^\circ$. At the present level of precision, for $\delta_{CP} = \pm 90^\circ$, the right (wrong) δ_{CP} solutions are those which occur in the same (opposite) half-plane as compared to the true solution. Since $\delta_{CP} = 0^\circ$ is common to both half-planes, for this case, the right and wrong δ_{CP} solutions at a particular C.L. are inferred from the nature of the contours. The different degenerate solutions obtained are the (i) WH-WO-R δ_{CP} , (ii) RH-WO-W δ_{CP} , (iii) WH-RO-R δ_{CP} , (iv) RH-RO-W δ_{CP} and (v) WH-WO-W δ_{CP} regions. Although the options i–iii have been noticed in the literature earlier, the option iv which exists for the same true θ_{23} but different δ_{CP} has not been discussed extensively. A probability level discussion was done in Ref. [68], where it was called $\theta_{23} - \delta_{CP}$

degeneracy. However, since it can occur for the same hierarchy and same θ_{23} , we call it “intrinsic CP degeneracy.” The WH-WO-W δ_{CP} solutions often appear as part of *i*, given the CP precision of the current experiments. We identify a few points in the true parameter space where this solution appears as a distinct degenerate solution. Note that for a true value of θ_{23} in the range 48° – 51° and δ_{CP} in the lower half-plane ($-180^\circ < \delta_{CP} < 0^\circ$), the $NO\nu A$ neutrino probability being highest cannot be matched by any other combination, and hence no degenerate solutions appear. In this case, only the neutrino run is better as it gives a better precision. In all other cases that we have studied, 3 years of the neutrino and 3 years of the antineutrino run of $NO\nu A$ are helpful in removing the wrong-octant solutions *i*, *ii* and *v* to a large extent. This also improves the CP precision since the wrong δ_{CP} solutions occurring with the wrong octant are resolved. Next, we present the results combining $NO\nu A[3 + 3]$ with T2K[8 + 0]. It is seen that the synergy between T2K and $NO\nu A$ helps in removing the WH-RO-W δ_{CP} solutions for true $\delta_{CP} = 0^\circ, 90^\circ$. For true $\delta_{CP} = -90^\circ$, $NO\nu A$ itself is sufficient for removing this degeneracy. The precision of both parameters also improves when these two sets of information are compounded together. The remaining degenerate solutions at 2σ can be resolved by adding ICAL data. The latter is seen to play an important role in removing the wrong-hierarchy solution for $\theta_{23} = 48^\circ$. In conclusion, we show that the combination of data from different LBL and atmospheric neutrino experiments can play a crucial role in removing the degeneracies associated with neutrino oscillation parameters, thereby improving the precision of the parameters θ_{23} and δ_{CP} . This also paves the way toward an unambiguous determination of these parameters.

APPENDIX: SYNERGY BETWEEN APPEARANCE AND DISAPPEARANCE CHANNEL AND ROLE OF ANTINEUTRINOS

In this Appendix, we discuss the origin of discrete degenerate regions in the test ($\delta_{CP} - \theta_{23}$) plane from the combination of appearance and disappearance channels for $NO\nu A$. We demonstrate the role of antineutrinos in resolving the degeneracies. The reference true point chosen in generating the data is $\delta_{CP} = -90^\circ$ and $\theta_{23} = 39^\circ$. In the upper row of Fig. 6, we plot the sensitivity of $NO\nu A[6 + 0]$. The serpentine curves in the top-left panel of Fig. 6 represent the allowed area at 90% C.L. from only the appearance channel. The area inside the vertical curves represents the allowed area from only the disappearance channel at the same C.L. The area between the blue dotted (magenta dotted) curves denotes the region obtained for the right (wrong) hierarchy. For the appearance channel, the allowed region is continuous, and no discrete degenerate solutions appear. This can be understood in the following manner. In the neutrino appearance channel, $\delta_{CP} = -90^\circ$ corresponds

to the maximum value in the probability. As one moves away from -90° , the probability decreases and reaches its minimum value at $+90^\circ$. On the other hand, the probability increases (decreases) as θ_{23} increases (decreases). So if we draw an imaginary horizontal line and an imaginary vertical line at the true point, then the allowed region is expected to come along the diagonal of the rectangle obtained by the intersection of these two imaginary lines and the X, Y axes for $\theta_{23} > 39^\circ$ and $\delta_{CP} \leq +90^\circ$. For $\delta_{CP} > +90^\circ$, the probability starts to increase, so θ_{23} has to fall to keep the probability same. This explains the serpentine nature of the allowed area. The width of the band corresponds to the θ_{23} precision of the experiment. For the disappearance channel, the allowed region is in the vicinity of θ_{23} and $\pi/2 - \theta_{23}$ and parallel to the δ_{CP} axis since the $P_{\mu\mu}$ probability has a very weak dependence on δ_{CP} . However, the combination of the disappearance and appearance channels gives discrete regions in the parameter space due to the excellent θ_{23} precision of the disappearance channel near $\theta_{23} = 39^\circ$ and 51° . This helps to exclude the other wrong values of θ_{23} . This is shown in the top right panel of Fig. 6. Apart from the allowed regions around the true value, one can identify the distinct degenerate solutions corresponding to wrong hierarchy-wrong octant-right δ_{CP} (WH-WO-R δ_{CP}) and right hierarchy-wrong octant-wrong δ_{CP} (RH-WO-W δ_{CP}) regions.

To show the exact synergy between the appearance and disappearance channels, in the middle panel of the top row, we plot the χ^2 as a function of θ_{23} (test) for a fixed δ_{CP} value of -90° for the same hierarchy (NH). This figure shows that, though the disappearance channel suffers from the intrinsic octant degeneracy and does not have any octant sensitivity itself ($\chi^2 \sim 0$), when added to the appearance channel, the channel is responsible for that of δ_{CP} .

Next, we discuss the role of antineutrino runs in $NO\nu A$. In the bottom row of Fig. 6, we plot the same figures as the top row but for the 3 year neutrino + 3 year antineutrino run. In the bottom left panel, we see that when antineutrino information is added to neutrino data, the allowed region from the appearance channel is significantly reduced. The reason is as follows: as δ_{CP} changes its sign for antineutrinos, the serpentine shape of the allowed region gets flipped with respect to δ_{CP} . This excludes the right hierarchy-wrong octant regions of $\delta_{CP} \in \text{UHP}$ (i.e. RH-WO-W δ_{CP}) and the wrong hierarchy-wrong octant regions of $\delta_{CP} \in \text{LHP}$ (i.e. WH-WO-R δ_{CP}). Thus, after adding the antineutrino data, only the RH-RO-R δ_{CP} solution remains, as can be seen from the third panel in the bottom row. From the $NO\nu A$ antineutrino probability figure in the top right panel of Fig. 1, it is seen that the probability of the true point cannot be matched by any points in the NH-HO or IH-HO bands. This means that for this true point, antineutrinos are free from the degeneracies that appear with the wrong octant in neutrinos. Thus, the addition of antineutrino information removes the wrong-octant solutions of $NO\nu A[6 + 0]$ that appear in the top right panels of Fig. 6.

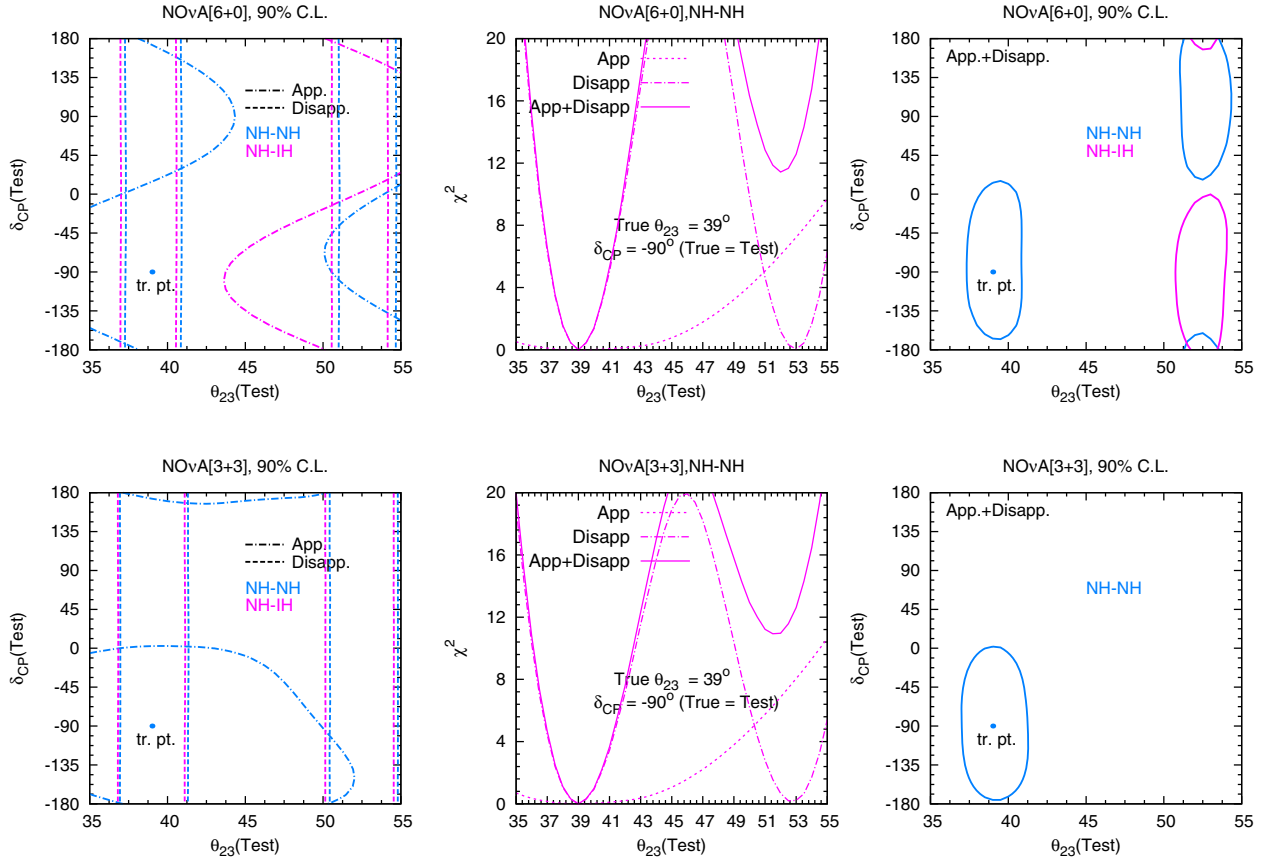


FIG. 6. The plots in the upper row are for $\text{NO}\nu\text{A}$ running only in the neutrino mode i.e. $\text{NO}\nu\text{A}[6+0]$. Those in the lower row are for $\text{NO}\nu\text{A}$ running in equal neutrino and antineutrino mode i.e. $\text{NO}\nu\text{A}[3+3]$. To generate these plots, we have assumed true $\theta_{23} = 39^\circ$, true $\delta_{CP} = -90^\circ$ and true hierarchy = NH, whereas test parameters are marginalized over the range given in Table II. The plots in the middle panel are generated for a fixed value of the test $\delta_{CP} (= -90^\circ)$.

The nature of the disappearance channel contours are seen to remain unaltered, but now the allowed area is slightly broader. This is because of a reduction in the

overall statistics due to the smaller cross sections of the antineutrinos. This is also seen in the middle panels where the widths of the χ^2 contours increase.

- | | |
|--|--|
| <p>[1] M. Gonzalez-Garcia, M. Maltoni, and T. Schwetz, <i>J. High Energy Phys.</i> 11 (2014) 052.</p> <p>[2] F. Capozzi, G. L. Fogli, E. Lisi, A. Marrone, D. Montanino, and A. Palazzo, <i>Phys. Rev. D</i> 89, 093018 (2014).</p> <p>[3] D. Forero, M. Tortola, and J. Valle, <i>Phys. Rev. D</i> 90, 093006 (2014).</p> <p>[4] V. Barger, D. Marfatia, and K. Whisnant, <i>Phys. Rev. D</i> 65, 073023 (2002).</p> <p>[5] J. Burguet-Castell, M. Gavela, J. Gomez-Cadenas, P. Hernandez, and O. Mena, <i>Nucl. Phys.</i> B646, 301 (2002).</p> <p>[6] H. Minakata and H. Nunokawa, <i>J. High Energy Phys.</i> 10 (2001) 001.</p> <p>[7] G. L. Fogli and E. Lisi, <i>Phys. Rev. D</i> 54, 3667 (1996).</p> | <p>[8] T. Kajita, H. Minakata, S. Nakayama, and H. Nunokawa, <i>Phys. Rev. D</i> 75, 013006 (2007).</p> <p>[9] K. Abe <i>et al.</i> (T2K Collaboration), <i>Phys. Rev. Lett.</i> 107, 041801 (2011).</p> <p>[10] Y. Abe <i>et al.</i> (Double Chooz Collaboration), <i>J. High Energy Phys.</i> 10 (2014) 086.</p> <p>[11] F. An <i>et al.</i> (Daya Bay Collaboration), <i>Nucl. Instrum. Methods Phys. Res., Sect. A</i> 773, 8 (2015).</p> <p>[12] J. Ahn <i>et al.</i> (RENO Collaboration), <i>Phys. Rev. Lett.</i> 108, 191802 (2012).</p> <p>[13] A. Donini, D. Meloni, and P. Migliozzi, <i>Nucl. Phys.</i> B646, 321 (2002).</p> <p>[14] V. Barger, D. Marfatia, and K. Whisnant, <i>Phys. Rev. D</i> 66, 053007 (2002).</p> |
|--|--|

- [15] O. Mena, S. Palomares-Ruiz, and S. Pascoli, *Phys. Rev. D* **73**, 073007 (2006).
- [16] M. Narayan and S. U. Sankar, *Phys. Rev. D* **61**, 013003 (1999).
- [17] M. Ishitsuka, T. Kajita, H. Minakata, and H. Nunokawa, *Phys. Rev. D* **72**, 033003 (2005).
- [18] K. Hagiwara, N. Okamura, and K. ichi Senda, *Phys. Lett. B* **637**, 266 (2006).
- [19] V. Barger, D. Marfatia, and K. Whisnant, *Phys. Lett. B* **560**, 75 (2003).
- [20] P. Huber, M. Lindner, and W. Winter, *Nucl. Phys.* **B654**, 3 (2003).
- [21] P. Huber, M. Lindner, T. Schwetz, and W. Winter, *Nucl. Phys.* **B665**, 487 (2003).
- [22] O. Mena and S. J. Parke, *Phys. Rev. D* **70**, 093011 (2004).
- [23] O. Mena, *Mod. Phys. Lett. A* **20**, 1 (2005).
- [24] H. Minakata and H. Sugiyama, *Phys. Lett. B* **580**, 216 (2004).
- [25] S. Prakash, S. K. Raut, and S. U. Sankar, *Phys. Rev. D* **86**, 033012 (2012).
- [26] S. K. Agarwalla, S. Prakash, S. K. Raut, and S. U. Sankar, *J. High Energy Phys.* **12** (2012) 075.
- [27] M. Blennow, P. Coloma, A. Donini, and E. Fernandez-Martinez, *J. High Energy Phys.* **07** (2013) 159.
- [28] K. Hiraide, H. Minakata, T. Nakaya, H. Nunokawa, H. Sugiyama, W. J. C. Teves, and R. Z. Funchal, *Phys. Rev. D* **73**, 093008 (2006).
- [29] H. Minakata, H. Sugiyama, O. Yasuda, K. Inoue, and F. Suekane, *Phys. Rev. D* **68**, 033017 (2003).
- [30] S. Prakash, S. K. Raut, and S. U. Sankar, *Phys. Rev. D* **86**, 033012 (2012).
- [31] A. Chatterjee, P. Ghoshal, S. Goswami, and S. K. Raut, *J. High Energy Phys.* **06** (2013) 010.
- [32] S. K. Agarwalla, S. Prakash, and S. U. Sankar, *J. High Energy Phys.* **07** (2013) 131.
- [33] P. Machado, H. Minakata, H. Nunokawa, and R. Z. Funchal, *J. High Energy Phys.* **05** (2014) 109.
- [34] M. Ghosh, S. Goswami, and S. K. Raut, [arXiv:1409.5046](https://arxiv.org/abs/1409.5046).
- [35] M. Banuls, G. Barenboim, and J. Bernabeu, *Phys. Lett. B* **513**, 391 (2001).
- [36] J. Bernabeu, S. Palomares-Ruiz, A. Perez, and S. Petcov, *Phys. Lett. B* **531**, 90 (2002).
- [37] J. Bernabeu, S. Palomares-Ruiz, and S. Petcov, *Nucl. Phys.* **B669**, 255 (2003).
- [38] R. Gandhi, P. Ghoshal, S. Goswami, P. Mehta, and S. U. Sankar, *Phys. Rev. D* **73**, 053001 (2006).
- [39] S. Palomares-Ruiz and S. Petcov, *Nucl. Phys.* **B712**, 392 (2005).
- [40] D. Indumathi and M. Murthy, *Phys. Rev. D* **71**, 013001 (2005).
- [41] S. Petcov and T. Schwetz, *Nucl. Phys.* **B740**, 1 (2006).
- [42] R. Gandhi, P. Ghoshal, S. Goswami, P. Mehta, S. U. Sankar, and S. Shalgar, *Phys. Rev. D* **76**, 073012 (2007).
- [43] A. Samanta, *Phys. Lett. B* **673**, 37 (2009).
- [44] M. M. Devi, T. Thakore, S. K. Agarwalla, and A. Dighe, *J. High Energy Phys.* **10** (2014) 189.
- [45] A. Ghosh, T. Thakore, and S. Choubey, *J. High Energy Phys.* **04** (2013) 009.
- [46] A. Ghosh and S. Choubey, *J. High Energy Phys.* **10** (2013) 174.
- [47] R. Gandhi, P. Ghoshal, S. Goswami, and S. U. Sankar, *Phys. Rev. D* **78**, 073001 (2008).
- [48] V. Barger, R. Gandhi, P. Ghoshal, S. Goswami, D. Marfatia, S. Prakash, S. K. Raut, and S. U. Sankar, *Phys. Rev. Lett.* **109**, 091801 (2012).
- [49] M. Gonzalez-Garcia, M. Maltoni, and A. Y. Smirnov, *Phys. Rev. D* **70**, 093005 (2004).
- [50] S. Choubey and P. Roy, *Phys. Rev. D* **73**, 013006 (2006).
- [51] P. Huber, M. Maltoni, and T. Schwetz, *Phys. Rev. D* **71**, 053006 (2005).
- [52] M. Blennow and T. Schwetz, *J. High Energy Phys.* **08** (2012) 058.
- [53] S. Choubey and A. Ghosh, *J. High Energy Phys.* **11** (2013) 166.
- [54] P. Coloma, H. Minakata, and S. J. Parke, *Phys. Rev. D* **90**, 093003 (2014).
- [55] P. Huber, M. Lindner, and W. Winter, *Comput. Phys. Commun.* **167**, 195 (2005).
- [56] P. Huber, J. Kopp, M. Lindner, M. Rolinec, and W. Winter, *Comput. Phys. Commun.* **177**, 432 (2007).
- [57] M. D. Messier, Ph.D. Thesis, Boston University Graduate School of Arts and Science, 1999.
- [58] E. Paschos and J. Yu, *Phys. Rev. D* **65**, 033002 (2002).
- [59] Y. Itow *et al.* (T2K Collaboration), [arXiv:hep-ex/0106019](https://arxiv.org/abs/hep-ex/0106019).
- [60] <http://t2k-experiment.org/2015/05/t2k-releases-its-first-measurement-of-muon-antineutrino-disappearance/>.
- [61] R. Patterson (NO ν A Collaboration), *Neutrino 2012 Conference*, Kyoto, Japan, 2012 (unpublished).
- [62] A. Chatterjee, K. K. Meghna, R. Kanishka, T. Thakore, V. Bhatnagar, R. Gandhi, D. Indumathi, N. K. Mondal, and N. Sinha, *J. Instrum.* **9**, P07001 (2014).
- [63] M. C. Gonzalez-Garcia and M. Maltoni, *Phys. Rev. D* **70**, 033010 (2004).
- [64] G. Fogli, E. Lisi, A. Marrone, D. Montanino, and A. Palazzo, *Phys. Rev. D* **66**, 053010 (2002).
- [65] E. K. Akhmedov, R. Johansson, M. Lindner, T. Ohlsson, and T. Schwetz, *J. High Energy Phys.* **04** (2004) 078.
- [66] A. Cervera, A. Donini, M. B. Gavela, J. J. G. Cádenas, P. Hernández, O. Mena, and S. Rigolin, *Nucl. Phys.* **B579**, 17 (2000).
- [67] M. Freund, *Phys. Rev. D* **64**, 053003 (2001).
- [68] H. Minakata and S. J. Parke, *Phys. Rev. D* **87**, 113005 (2013).
- [69] M. Ghosh, P. Ghoshal, S. Goswami, and S. K. Raut, *Phys. Rev. D* **89**, 011301 (2014).
- [70] M. Ghosh, P. Ghoshal, S. Goswami, and S. K. Raut, *Nucl. Phys.* **B884**, 274 (2014).
- [71] S. Razzaque and A. Yu. Smirnov, *J. High Energy Phys.* **05** (2015) 139.



The physics of antineutrinos in DUNE and determination of octant and δ_{CP}

Newton Nath ^{a,b,*}, Monojit Ghosh ^a, Srubabati Goswami ^a

^a Physical Research Laboratory, Navrangpura, Ahmedabad 380 009, India

^b Indian Institute of Technology, Gandhinagar, Ahmedabad–382424, India

Received 23 June 2016; received in revised form 21 September 2016; accepted 22 September 2016

Available online 28 September 2016

Editor: Tommy Ohlsson

Abstract

The octant of the leptonic mixing angle θ_{23} and the CP phase δ_{CP} are the two major unknowns (apart from neutrino mass hierarchy) in neutrino oscillation physics. It is well known that the precise determination of octant and δ_{CP} is interlinked through the octant- δ_{CP} degeneracy. In this paper we study the proficiency of the DUNE experiment to determine these parameters scrutinizing, in particular, the role played by the antineutrinos, the broadband nature of the beam and the matter effect. It is well known that for $P_{\mu e}$ and $P_{\bar{\mu} \bar{e}}$ the octant- δ_{CP} degeneracy occurs at different values of δ_{CP} , combination of neutrino and antineutrino runs help to resolve this. However, in regions where neutrinos do not have octant degeneracy adding antineutrino data is expected to decrease the sensitivity because of the degeneracy and reduced statistics. However we find that in case of DUNE baseline, the antineutrino runs help even in parameter space where the antineutrino probabilities suffer from degeneracies. We explore this point in detail and point out that this happens because of the (i) broad-band nature of the beam so that even if there is degeneracy at a particular energy bin, over the whole spectrum the degeneracy may not be there; (ii) the enhanced matter effect due to the comparatively longer baseline which creates an increased tension between the neutrino and the antineutrino probabilities which raises the overall χ^2 in case of combined runs. This feature is more prominent for IH since the antineutrino probabilities in this case are much higher than the neutrino probabilities due to matter effects. The main role of antineutrinos in enhancing CP sensitivity is their ability to remove the octant- δ_{CP} degeneracy. However even if one assumes octant to be known the addition of antineutrinos can give enhanced CP sensitivity in some parameter regions due to the tension between the neutrino and antineutrino χ^2 s.

* Corresponding author at: Physical Research Laboratory, Navrangpura, Ahmedabad 380 009, India.

E-mail addresses: newton@prl.res.in (N. Nath), monojit@prl.res.in (M. Ghosh), sruba@prl.res.in (S. Goswami).

© 2016 The Author(s). Published by Elsevier B.V. This is an open access article under the CC BY license (<http://creativecommons.org/licenses/by/4.0/>). Funded by SCOAP³.

1. Introduction

The discovery of a non-zero value of the 1–3 leptonic mixing angle θ_{13} by the reactor experiments have established the paradigm of oscillations of the neutrinos amongst three flavours on a firm footing. The parameters involved are: two mass squared differences – Δm_{21}^2 , Δm_{31}^2 , three mixing angles θ_{12} , θ_{23} and θ_{13} and the CP violating phase δ_{CP} . Among these Δm_{21}^2 and θ_{12} are measured by the solar neutrino and the KamLAND reactor neutrino experiments [1]. The information on Δm_{31}^2 and θ_{23} has come from Super-Kamiokande (SK) [2] atmospheric neutrino data, as well as from the data of the beam based experiments MINOS [3] and T2K [4]. The best-fit values and 3σ ranges of these parameters are given in [5,6] by analyzing the global neutrino data. The remaining unknown oscillation parameters are (i) the sign of $|\Delta m_{31}^2|$ or the neutrino mass ordering. If we assume the neutrinos to be hierarchical then there can be two types of ordering – the normal hierarchy (NH) corresponding to $m_1 \ll m_2 \ll m_3$ and $\Delta m_{31}^2 > 0$ and the inverted hierarchy (IH) corresponding to $m_2 \approx m_1 \gg m_3$ and $\Delta m_{31}^2 < 0$, (ii) the octant of θ_{23} – with $\theta_{23} < 45^\circ$ corresponding to lower octant (LO) and $\theta_{23} > 45^\circ$ corresponding to higher octant (HO) and (iii) the CP violating phase δ_{CP} for which the full range from $-180^\circ < \delta_{CP} < 180^\circ$ is still allowed at 3σ C.L. [5,6]. Information on these parameters can come from the currently running superbeam experiments T2K [7] and NO ν A [8,9]. However this is possible only for favourable values of parameters. The main problem which these experiments can face is due to parameter degeneracies by which it is meant that different parameters giving equally good fit to the data. With θ_{13} unknown, an eight-fold degeneracy was identified which would make the precise determination of parameters difficult [10]. These were intrinsic θ_{13} degeneracy [11], hierarchy- δ_{CP} degeneracy [12] and octant degeneracy [13]. With the precise determination of θ_{13} [14–17] and inclusion of spectral information the intrinsic degeneracy is now solved. However the lack of knowledge of hierarchy, octant and δ_{CP} can still give rise to degenerate solutions which can affect the sensitivities of these experiments towards these parameters [18–22].

In this paper our focus is on the determination of the octant of θ_{23} and the CP phase δ_{CP} . Currently the most precise measurements of the parameter θ_{23} comes from the T2K experiment. The primary channel for this is the survival probability $P_{\mu\mu}$. For baselines shorter than 1000 km this probability is a function of $\sin^2 2\theta_{23}$ to the leading order and suffers from an intrinsic octant degeneracy which refers to the same value of probability for θ_{23} and $\pi/2 - \theta_{23}$. The leading order term of the appearance channel probability $P_{\mu e}$ depends on the combination $\sin^2 \theta_{23} \sin^2 2\theta_{13}$. Although this does not exhibit intrinsic octant degeneracy, there can be uncertainties due to the $\sin^2 \theta_{13}$ factor. It was shown in [23,24] that combining the reactor measurement of θ_{13} with the accelerator data will be helpful for extraction of information on octant from this channel. Thus, the precise measurement of θ_{13} from the reactor experiments is expected to enhance the octant sensitivity coming from this channel. The combination of the disappearance and appearance channel measurements in long baseline experiments can also be helpful in resolving octant degeneracy because of the different functional dependence of the two probabilities on θ_{23} . This creates a synergistic effect so that the octant sensitivity of both channels combined is higher [19,21,25]. T2K collaboration has performed a full three flavour analysis using information from both $(\nu_\mu - \nu_\mu)$ and $(\nu_\mu - \nu_e)$ channels. They obtain best-fit $\sin^2 \theta_{23} \sim 0.52$ with a preference for NH [7]. MINOS collaboration has also completed their combined analysis of disappearance and

appearance data and have also included atmospheric neutrino data in their analysis [3]. They get a best-fit at $\sin^2 \theta_{23} = 0.41$ for IH. The first NO ν A disappearance results with 2.74×10^{20} protons on target, give best-fit of $\sin^2 \theta_{23} = 0.43 \oplus 0.60$ [9]. The latest analysis of Super Kamiokande atmospheric neutrino data shows a weak preference for NH-HO [26]. Global analysis of neutrino data including all the different information gives the best-fit in LO for NH and in HO for IH [5,6]. Thus it is clear from the above discussion that at present the situation regarding octant of θ_{23} is quite intriguing.

There have been studies on the possibility of determining the octant from combined study of the experiments T2K and NO ν A using their full projected exposure [19,25]. It was observed that the main problem in octant resolution arises due to the unknown value of δ_{CP} in the subleading terms of $P_{\mu e}$ which gives rise to octant– δ_{CP} degeneracy. Also, the lack of knowledge about hierarchy can create further problem with the occurrence of wrong hierarchy–wrong octant solutions [22]. Recently it was pointed out in [19,21] that equal neutrino and antineutrino runs can help in resolving octant– δ_{CP} degeneracy. The reason being the octant– δ_{CP} combination suffering from degeneracy in neutrino probabilities are not degenerate for the antineutrino probabilities. It was shown for instance in [19] that combining T2K and NO ν A running in equal neutrino and antineutrino mode for 2.5 years each and 3 years each respectively can identify the correct octant at 2σ C.L. irrespective of hierarchy and δ_{CP} if $\theta_{23} \leq 41^\circ$ or $\geq 49.5^\circ$.

The degeneracies can also be alleviated if neutrinos pass through large distances in matter so that resonant matter effects develop. This is the case of the atmospheric neutrinos passing through matter. In this case the leading order term in $P_{\mu e}$ goes as $\sin^2 \theta_{23} \sin^2 2\theta_{13}^m$. However, since at resonance $\sin^2 2\theta_{13}^m \approx 1$, the octant degeneracy is resolved. Further, the $P_{\mu\mu}$ channel also contains an octant sensitive term $\sin^4 \theta_{23} \sin^2 2\theta_{13}^m$ which enhances the sensitivity [27]. Octant sensitivity can also come from the Δm_{21}^2 dependent term which gives rise to an excess of sub-GeV electron like events for the atmospheric neutrinos [28,29]. In addition the antineutrino component in atmospheric neutrino flux can also help in resolving octant ambiguity. It was shown that combined analysis of T2K and NO ν A with atmospheric neutrino data can give enhanced octant sensitivity [25]. The effect was found to be larger in multi-megaton water detectors like PINGU [30] or a LArTPC detector, sensitive to both muon and electron events [25].

The current best-fit value for δ_{CP} is close to $-\pi/2$ although at 3σ C.L. the whole range of $[0, 2\pi]$ remains allowed [5,6]. The δ_{CP} sensitivity of an experiment is often understood in terms of the CP asymmetry between the neutrinos and antineutrinos.

$$A_{cp} = \frac{P_{\mu e} - P_{\bar{\mu} \bar{e}}}{P_{\mu e} + P_{\bar{\mu} \bar{e}}} \sim \frac{\sin \delta_{CP}}{\sin \theta_{13}} \tag{1}$$

However the diagnostics used for probing CP violation is the sum total of the χ^2 contribution of the neutrinos and antineutrinos: $\chi_{total}^2 = \chi_{\nu}^2 + \chi_{\bar{\nu}}^2$ which does not show the above dependence [31]. Hence one needs to understand the actual role played by antineutrinos, if any, for determination of CP violation. Indeed one already has a hint for non-zero δ_{CP} from only neutrino runs of T2K and NO ν A. Whereas the confirmation of CP violation independently from antineutrino runs in these experiments cannot be undermined, it has already been observed in the case of T2K that unless the parameter space contains octant degeneracy the antineutrinos do not play any role for discovery of CP violation [32,33]. However for the NO ν A experiments antineutrinos seem to be playing some role even when there is no octant degeneracy [32]. In this work, it is one of our goals to understand the role of antineutrinos for enhancing CP sensitivity for the DUNE baseline. In particular we explore whether the antineutrino runs can play any non-trivial contribution to

the total χ^2 if octant and hierarchy are assumed to be known and if so then what are the physics issues involved.

The current generation superbeam experiments T2K and NO ν A are off-axis experiments using narrow band beams to reduce the backgrounds at the high energy tail. However the future generation high statistics accelerator experiments plan to use on-axis configurations and high intensity wide band beams enabling them to explore oscillations over a larger energy range. The examples for this are the European initiative LBNO and LBNE which was proposed in US using the FermiLab beamline. In 2014 it was proposed to combine these activities in a coherent international long-baseline neutrino program hosted at Fermilab with the detector at the Sanford Underground Research Facility (SURF) in South Dakota. On Jan. 30, 2015 the LBNE collaboration was officially dissolved, the new collaboration selected the name Deep Underground Neutrino Experiment (DUNE). The baseline is 1300 km and the proposed detector is a 40 kt (or 34 kt) modular Liquid Argon Time Projection Chamber (LArTPC) with the first phase being a 10 kt detector. There are several studies of the physics prospects of a 1300 km baseline LArTPC using a wide band beam [34]. In particular octant and/or CP sensitivity of such a set-up has been considered in [35–40]. In [35] the octant and CP sensitivity reach of a 10 kt LArTPC detector for LBNE combined with T2K and NO ν A was studied. In [36] the minimum exposure for DUNE in conjunction with T2K, NO ν A and ICAL@INO experiment was computed for giving a octant sensitivity with $\Delta\chi^2 = 25$ and a CP sensitivity with $\Delta\chi^2 = 9$ for 40% and $\sim 70\%$ coverage of δ_{CP} . In [37] the octant sensitivity of a 10 kt and 35 kt detector was studied with and without the near detector and also the role of precise knowledge of θ_{13} coming from reactor experiments, in improving the sensitivities were studied. In [38] octant and CP sensitivity results were presented for a 10 kt detector and effect of including a near detector as well as the role of atmospheric neutrinos were considered. In [39] octant and CP sensitivity of a 35 kt detector, with and without magnetization, was studied. All these papers considered equal neutrino and antineutrino run for the octant sensitivity. Variation of proportion of neutrino and antineutrino run was studied in [36] for only IH and $\theta_{23} = 39^\circ$ for octant sensitivity and NH and $\theta_{23} = 51^\circ$ for CP sensitivity. This issue was also discussed in [41] for a setup with a baseline of 1540 km where they concluded that for true hierarchy as NH equal neutrino and antineutrino run is better whereas for true hierarchy as IH 30% antineutrino run is optimal. These conclusions were drawn for true $\theta_{23} = 45^\circ$ and the results were presented in terms of fraction of δ_{CP} for which a 3σ signal of CP violation can be obtained.

In this work, our main goal to understand the role of antineutrinos for enhancing octant and CP sensitivity for the DUNE baseline. In particular, we study the impact of the broadband nature of the beam and the role of enhanced matter effects as compared to the currently running beam-based experiments T2K and NO ν A which have shorter baselines and hence less matter effects. To the best of our knowledge these features have not been emphasized earlier in the literature. In particular, a deeper understanding of the role played by antineutrinos will help in optimizing the amount of antineutrino run. We present the results of the octant sensitivity using different combinations of neutrino–antineutrino run (i) as a function of true δ_{CP} for fixed values of true θ_{23} (ii) as a function of true θ_{23} for fixed values of true δ_{CP} and (iii) also in the true (θ_{23} – δ_{CP}) plane. These three kinds of plots allow us to study the dependence of octant-sensitivity on these two parameters in an exhaustive manner. In addition we present the allowed regions in the true- θ_{23} –test θ_{23} plane for both hierarchies and for true $\delta_{CP} = \pm 90^\circ$. These plots give the precision of θ_{23} at these values of δ_{CP} . It is worthwhile to mention here that one of the main aims of the DUNE collaboration is to measure the parameter δ_{CP} which underscores the importance of combining neutrino and antineutrino runs. However the main role that the antineutrinos play in

Table I
Representative values of neutrino oscillation parameters.

	$\sin^2 2\theta_{13}$	$\sin^2 \theta_{12}$	θ_{23}	Δm_{21}^2 (eV ²)	Δm_{31}^2 (eV ²)	δ_{CP}
True values	0.1	0.31	35°–55°	7.60×10^{-5}	2.40×10^{-3}	–180° to +180°
Test values	0.085–0.115	Fixed	35°–55°	Fixed	$(2.15\text{--}2.65) \times 10^{-3}$	–180° to +180°

the determination of δ_{CP} is the removal of octant degeneracy and thus both issues are intimately connected. To emphasize this point we also present the figures showing the CP discovery potential of DUNE for the cases when octant is assumed to be known and unknown. In particular we explore whether the antineutrino runs can play any non-trivial contribution to the total χ^2 if octant and hierarchy are assumed to be known and if so then what are the physics issues involved. We study how much fraction of antineutrino run is optimum for values of θ_{23} in lower and upper octants and in addition to the CP fractions, also show explicitly which are the CP values for which antineutrino run can be important. Note that most of the earlier works in literature have considered equal neutrino and antineutrino run for determination of octant and δ_{CP} in DUNE. We present the results by varying the antineutrino component in the run. This constitutes another new feature of our study.

The plan of the paper goes as follows: in the next section we give the experimental and simulation details of DUNE that have been taken into consideration. In Section 3 we discuss the physics of the octant and CP sensitivity of the DUNE experiment in detail. In Section 4 we present our results. Section 4.1 contains the results for octant sensitivity and Section 4.2 is devoted for the discussions on CP sensitivity and role of antineutrinos in DUNE. Finally we summarize and conclude in Section 5.

2. Experimental and simulation details

In this paper we have simulated the DUNE experiment using the GLOBES package [42,43]. In our simulation, we have considered a 10 kt configuration of the detector. This experiment is based on the existing Neutrinos at the Main Injector (NuMI) beamline design and the beam flux peaks at 2.5 GeV. Far detector will be located 4,850 feet underground. One of the options for DUNE is to have an initial beam power of 1.2 MW which will be increased to 2.3 MW later [44]. In our simulation we consider neutrino flux [45] corresponding to 1.2 MW beam power which gives 10^{21} protons on target (POT) per year. This corresponds to a proton energy of 120 GeV. In Table I we list the representative values for the neutrino oscillation parameters that we have used in our numerical simulation. These values are consistent with the results obtained from global-fit of world neutrino data [46–48]. Systematic errors are taken into account using the method of pulls [49,50] as outlined in [51]. We have also added 5% prior on $\sin^2 2\theta_{13}$ in our numerical simulation. The systematic errors and efficiencies corresponding to signal and background are taken from [34]. Note that the values of these quantities given in [44] are somewhat different. Using these may change our numerical results to some extent though the main physics issues addressed in this work will not be altered.

3. Physics of octant sensitivity for a 1300 km baseline

The probabilities that are relevant for the DUNE experiment are $P_{\mu e}$ and $P_{\mu\mu}$ and the corresponding probabilities for the antineutrinos. In presence of matter, the relevant oscillation

probabilities can be expanded perturbatively in terms of small parameters $\alpha (\equiv \Delta m_{21}^2 / \Delta m_{31}^2)$ and θ_{13} as follows, [52–54]

$$P_{\mu e} = \underbrace{4s_{13}^2 s_{23}^2 \frac{\sin^2(A-1)\Delta}{(A-1)^2}}_{\mathcal{O}_o} + \underbrace{\alpha^2 \cos^2 \theta_{23} \sin^2 2\theta_{12} \frac{\sin^2 A \Delta}{A^2}}_{\mathcal{O}_2} \tag{2}$$

$$+ \underbrace{\alpha s_{13} \sin 2\theta_{12} \sin 2\theta_{23} \cos(\Delta + \delta_{cp}) \frac{\sin(A-1)\Delta}{(A-1)} \frac{\sin A \Delta}{A}}_{\mathcal{O}_1}$$

$$P_{\mu\mu} = 1 - \sin^2 2\theta_{23} \sin^2 \Delta + \mathcal{O}(\alpha, s_{13}) \tag{3}$$

where,

$$\Delta \equiv \frac{\Delta m_{31}^2 L}{4E}, A \equiv \frac{2EV}{\Delta m_{31}^2} \equiv \frac{VL}{2\Delta}, \text{ and } V = \pm \sqrt{2} G_F n_e \tag{4}$$

These expressions are derived assuming constant matter density approximation. Similar expressions for antineutrino probabilities can be obtained by replacing $\delta_{CP} \rightarrow -\delta_{CP}$ and $V \rightarrow -V$. The ‘+(-)’ sign here represents neutrino (antineutrino). For NH, Δm_{31}^2 is positive and for IH, Δm_{31}^2 is negative. Hence, in the neutrino oscillation probability A is positive for NH and negative for IH. For antineutrinos, the sign of A gets reversed.

It is clear from the above expressions that to leading order $P_{\mu\mu}$ suffers from intrinsic octant degeneracy between θ_{23} and $\pi/2 - \theta_{23}$. $P_{\mu e}$ does not suffer from intrinsic degeneracy and the octant sensitivity comes mainly from this channel. However since $P_{\mu e}$ depends on $\sin^2 \theta_{23}$, the χ^2 is an increasing function of θ_{23} for this case and the wrong octant minima from this channel always occurs for 45° . On the other hand $P_{\mu\mu}$ forces the minima to $\sim \pi/2 - \theta_{23}$, where the appearance channel has a large octant sensitive contribution.

However although $P_{\mu e}$ does not suffer from intrinsic degeneracy it is possible to have

$$P_{\mu e}(\Delta, \theta_{23}^{tr}, \delta_{CP}^{tr}) = P_{\mu e}(\Delta, \theta_{23}^{wr}, \delta_{CP}^{wr}), \tag{5}$$

where the suffix *tr* (*wr*) denotes the true (wrong) values of the parameters. The above equation implies that apart from the true solution one can also get duplicate solutions with right hierarchy–wrong octant–wrong δ_{CP} (RH–WO–W δ_{CP}). Note that unlike in the case of $P_{\mu\mu}$, for $P_{\mu e}$ one needs to consider the variation of θ_{23} over the whole of the opposite octant in order to identify the degenerate solution. Apart from this, if the hierarchy is unknown then one can also have

$$P_{\mu e}(\Delta, \theta_{23}^{tr}, \delta_{CP}^{tr}) = P_{\mu e}(-\Delta, \theta_{23}^{wr}, \delta_{CP}^{wr}). \tag{6}$$

This corresponds to solutions with wrong hierarchy–wrong octant–wrong δ_{CP} (WH–WO–W δ_{CP}). As pointed out in [22] the most generalized case assuming θ_{13} as fixed, gives rise to total eight possibilities corresponding to different combinations of right (wrong) hierarchy and/or octant and/or δ_{CP} . From Fig. 1 one can see that for the DUNE baseline degenerate solutions with right- δ_{CP} do not come unlike the case of the experiments T2K and NO ν A [22]. This is because due to matter effects the bands for NH and IH are much more well separated and hence the intersection at right δ_{CP} do not occur. In this work we show how the octant sensitivity is affected by the wrong solutions defined in Eqs. (5) and (6). We also discuss how the δ_{CP} sensitivity is affected by the occurrence of wrong octant solutions. We put emphasis on the role of antineutrinos and point out some unexpected behaviour due to matter effects.

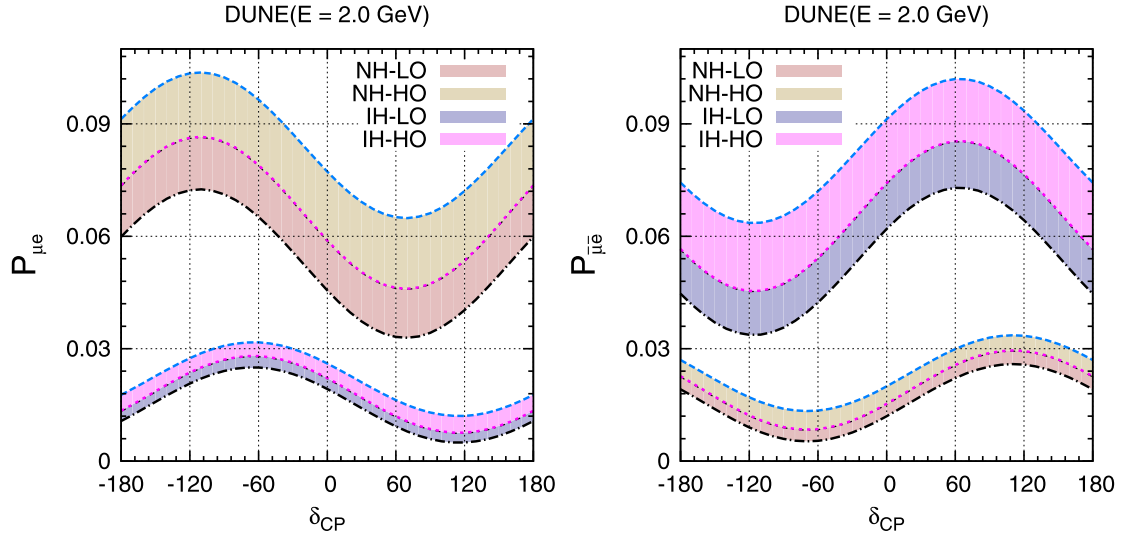


Fig. 1. Left panel (right panel) represents $P_{\mu e}$ ($P_{\bar{\mu} e}$) for DUNE. Here the bands are over current 3σ range of θ_{23} [48]. For LO, NH (LO, IH) we consider the range of θ_{23} over 38.8° – 45° (39.4° – 55°) and for HO, NH (HO, NH) we consider the range of θ_{23} over 45° – 53.3° (45° – 53.1°).

Fig. 1 describes the oscillation probability in presence of earth matter for $L = 1300$ km and $E = 2$ GeV. The bands are due to the variation of θ_{23} (see figure caption for details). The neutrino oscillation probability for NH gets significant enhancement in presence of earth’s matter as compared to IH as shown in the left panel. It is seen that the maximum probability for NH can become more than 3-times than that of IH. But in the case of antineutrinos the scenario gets reversed as A and δ_{CP} changes their sign, as can be observed in the right panel. This can be understood from Eq. (2) that the \mathcal{O}_o term is Δ dependent which enhances the probability value for the given set of oscillation parameters for NH as compared to IH for neutrino and $(\mathcal{O}_1, \mathcal{O}_2)$ terms are α and α^2 suppressed respectively.

Note that for vacuum oscillation maxima, Δ corresponds to 90° . Thus in the appearance channel probability (cf. Eq. (2)), $\delta_{CP} = -90^\circ$ ($+90^\circ$) correspond to maximum (minimum) point in the probability for neutrinos. For antineutrinos it is the opposite. Thus, for these values of δ_{CP} , octant sensitivity is expected to be maximum if there is no degeneracy. Note that with the inclusion of matter effect, the appearance channel probability maxima does not coincide with the vacuum maxima and in that case the maximum and minimum points in the probability do not come exactly at $\pm 90^\circ$ but gets slightly shifted. This can be seen from Fig. 1. However for illustration, we will take $\delta_{CP} = \pm 90^\circ$ as the reference points to describe the physics of octant in DUNE.

It is to be observed that, if we draw a horizontal line at particular probability value then the different intersection points with the given band lead to different degenerate solutions. The occurrence of octant degeneracies that can be inferred from these plots are summarized in Table II. From the above discussions as well as from earlier studies it is clear that the nature of octant– δ_{CP} degeneracy is different for neutrinos and antineutrinos and therefore combined neutrino–antineutrino run is helpful for resolving the octant degeneracy [19,21,35]. Also note that the behaviour of octant– δ_{CP} degeneracy in neutrinos and antineutrinos is same for both NH and IH.

The probability plot as given in Fig. 1 is done for an energy of 2 GeV. However it is possible that because of the broad-band nature of the beam the occurrence of degeneracy at a particular energy may not be true over the whole energy range. Thus for DUNE, one can still get some

Table II

The octant degenerate parameter space for neutrinos and antineutrinos. Here, LO = Lower octant, HO = Higher octant, UHP = Upper half plane ($0^\circ < \delta_{CP} < 180^\circ$) and LHP = Lower half plane ($-180^\circ < \delta_{CP} < 0^\circ$).

Octant degeneracy	ν	$\bar{\nu}$
LHP, LO	degenerate with UHP, HO	no degeneracy
UHP, LO	no degeneracy	degenerate with LHP, HO
LHP, HO	no degeneracy	degenerate with UHP, LO
UHP, HO	degenerate with LHP, LO	no degeneracy

amount of octant sensitivity, even in the degenerate parameter space outlined in Table II, when integrated over all the energy bins.

It is to be noted that Fig. 1 does not demonstrate any hierarchy degeneracy since the two bands corresponding to NH and IH remain non-overlapping. However conclusions drawn at probability level need to be substantiated by a proper χ^2 analysis to determine with what significance the hierarchy degeneracy is actually resolved by DUNE. Therefore we will present the results of octant sensitivity either for both cases – right and wrong hierarchy or by marginalizing over the hierarchy.

4. Results

4.1. Octant discovery χ^2 for a 10 kt detector

In this section we discuss the octant sensitivity of DUNE for a 10 kt detector volume which is the projected detector volume for DUNE in the first phase. The statistical χ^2 for octant sensitivity is calculated by taking the correct octant in the true spectrum and the wrong octant in the test spectrum in the following formula

$$\chi_{\text{stat}}^2 = \sum_i 2 \left[N_i^{\text{test}} - N_i^{\text{true}} - N_i^{\text{true}} \log \left(\frac{N_i^{\text{test}}}{N_i^{\text{true}}} \right) \right], \quad (7)$$

where N_i is the number of events in the i th energy bin. In Fig. 2 we show the χ^2 for octant discovery which is the combined sensitivity coming from appearance channel, disappearance channel and $\sin^2 2\theta_{13}$ prior i.e.,

$$\chi^2 = \chi_{\text{ap}}^2 + \chi_{\text{disap}}^2 + \chi_{\text{prior}}^2 \quad (8)$$

as a function of true δ_{CP} .

We consider the representative true values of $\theta_{23} = 39^\circ$ for LO and $\theta_{23} = 51^\circ$ for HO. χ^2 is marginalized over test values of θ_{23} over opposite octant. We give the plots separately for true and false hierarchy. This shows for what parameters and to what extent the octant sensitivity is affected by the lack of knowledge of hierarchy. Depending on the true parameters, we get four combinations of (hierarchy–octant): NH-LO, NH-HO, IH-LO, IH-HO. For all the plots in the upper row of Fig. 2, dark-blue curves are for True(NH)–Test(NH) and magenta curves are for True(NH)–Test(IH) while for the lower row dark-blue curves correspond to True(IH)–Test(IH) and magenta curves correspond to True(IH)–Test(NH). Below we discuss the results for each true combination.

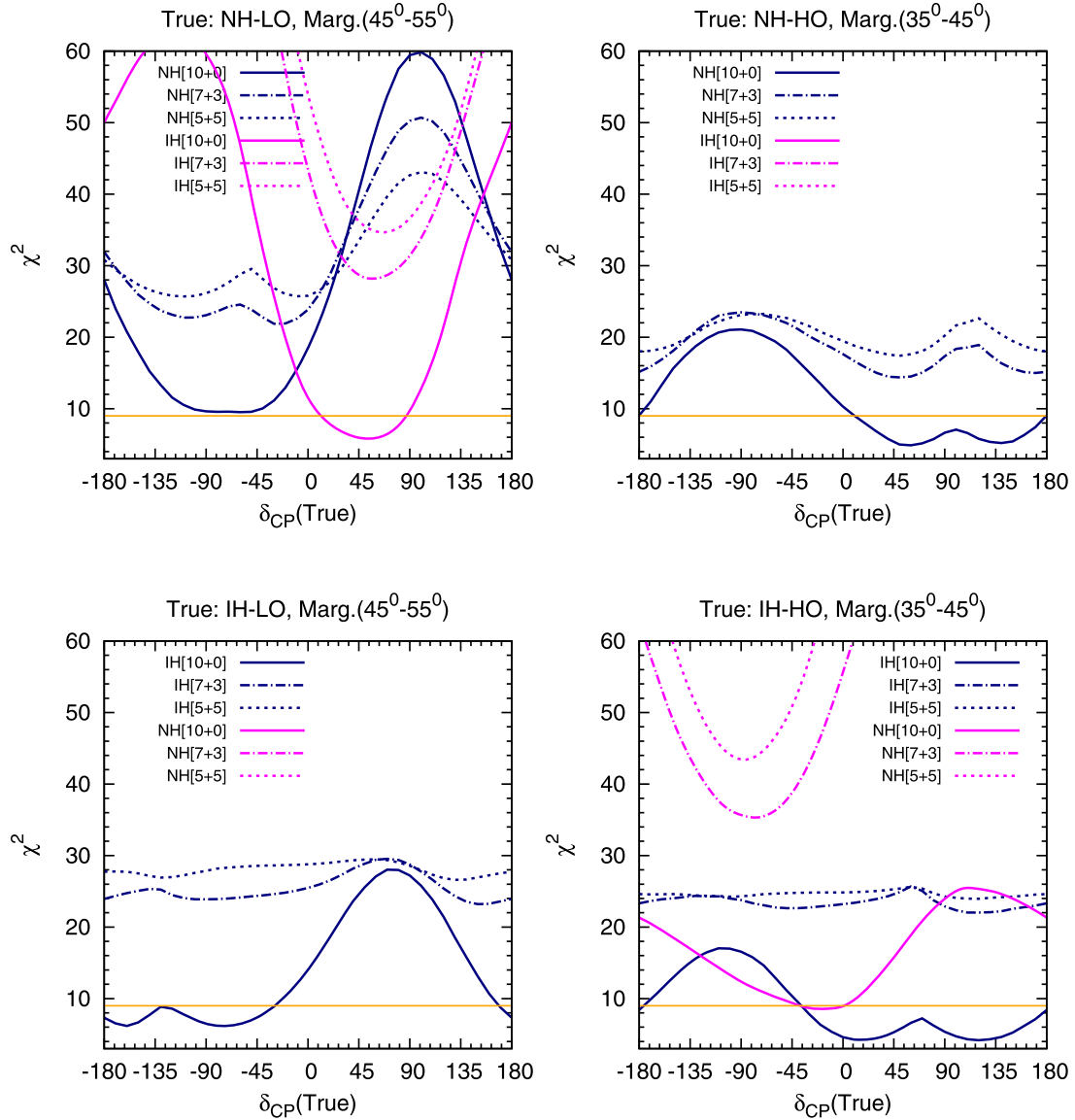


Fig. 2. Octant discovery χ^2 for DUNE. Left (right) panel is for LO (HO), where true (θ_{23}) is considered as 39° (51°) and test (θ_{23}) is marginalized over $(45^\circ$ to $55^\circ)$ for LO and $(35^\circ$ to $45^\circ)$ for HO. The labels NH, IH inside the plots signify test hierarchy.

- NH-LO** ($\theta_{23}^{\text{true}} = 39^\circ$): The figure for true NH-LO shows that for values of δ_{CP} in the lower half plane, a 10 year neutrino run of DUNE can resolve the octant degeneracy at 3σ C.L. The inclusion of antineutrino run helps in enhancing the octant sensitivity for δ_{CP} in LHP ($-180^\circ < \delta_{CP} < 0^\circ$) and θ_{23} in LO since the antineutrino probability is devoid of octant degeneracy. Note that in this case though pure neutrino run suffers from octant degeneracy, still we get χ^2 around 10. This is one of the unique features of the broad-band beam where the degeneracy does not exist over the entire energy range and one can still have some octant sensitivity from the neutrino channel. For the UHP ($0^\circ < \delta_{CP} < 180^\circ$) on the other hand the neutrino data gives a better octant sensitivity since antineutrinos are plagued with degeneracies for LO, as shown by the blue curves. However the scenario changes if we assume the hierarchy is not known. In that case the antineutrino run is seen to help to remove wrong hierarchy–wrong octant solutions in spite of having degeneracies, as is seen from the magenta curves. In order to understand this point we have plotted the appearance channel

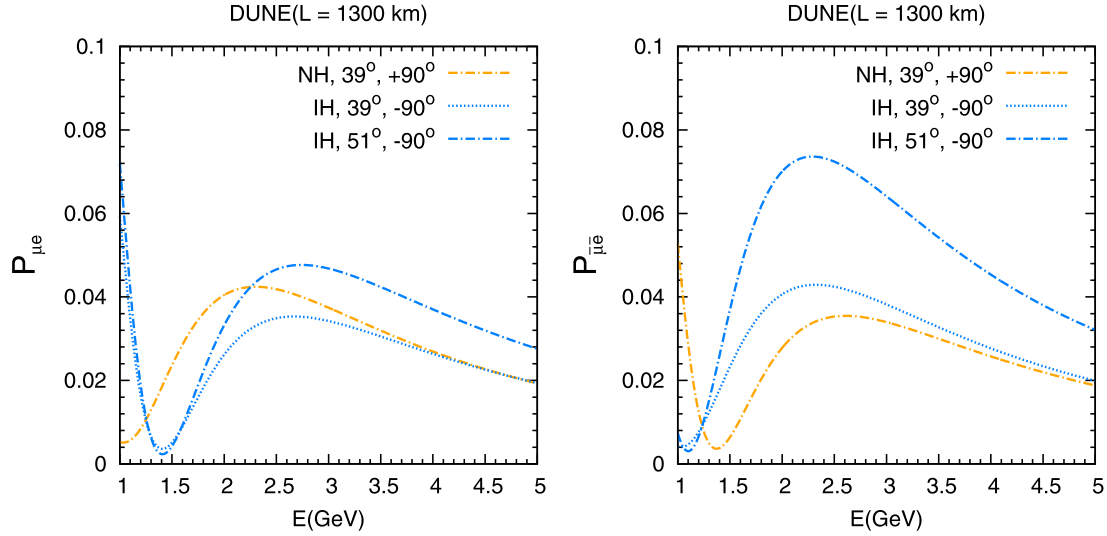


Fig. 3. Here, left panel (right panel) represents $P_{\mu e}$ ($P_{\mu \bar{e}}$) as a function of energy for DUNE and hierarchy corresponds to orange (light blue) curve is NH (IH). (For interpretation of the references to color in this figure, the reader is referred to the web version of this article.)

probability vs energy in Fig. 3. The left panel is for neutrinos and the right panel is for antineutrinos. In the left panel we see that the orange curve ($\delta_{CP} = +90^\circ$) is well separated from the dotted blue curve ($\delta_{CP} = -90^\circ$) near the oscillation maxima for $\theta_{23} = 39^\circ$. But when marginalized over θ_{23} , the dashed blue curve which corresponds to $\delta_{CP} = -90^\circ$ and $\theta_{23} = 51^\circ$, overlaps with the orange curve to give WH–WO–W δ_{CP} solution.¹ On the other hand in the right panel we see that due the marginalization of θ_{23} the dashed blue curve moves far away from the orange curve resolving the degeneracy. Note that if we marginalize over hierarchy then for UHP the minimum will come at the WH solution with only neutrino data and hence octant degeneracy is not resolved at 3σ for $9^\circ < \delta_{CP} < 90^\circ$ belonging to the UHP. However with 7 + 3 years run the octant degeneracy is resolved with a $\chi^2 > 25$ even without the knowledge of the true hierarchy for all values of δ_{CP} . With 5 + 5 year run in most part of UHP the minima occurs with the RH solution. But for $45^\circ < \delta_{CP} < 115^\circ$, the WH minima is below the one with RH.

- **NH–HO** ($\theta_{23} = 51^\circ$) For this case from Fig. 1 it is seen that for ($51^\circ, -90^\circ, \text{NH}$) no octant degeneracy prevails at the probability level for neutrinos whereas antineutrinos have octant degeneracy. Also, antineutrinos have less statistics. Thus we expect that only neutrino run should give a better sensitivity. But, we notice from the top right figure of Fig. 2, that addition of antineutrino gives higher χ^2 value as compared to only neutrino mode [10 + 0]. In order to understand this feature in the first panel of Fig. 4 we plot the χ^2 vs test δ_{CP} .

The curve for only antineutrinos indeed confirm the occurrence of degeneracies close to $\delta_{CP} \sim 90^\circ$. However at that point the neutrino χ^2 is very high. Thus, when the neutrino and antineutrino data are combined the overall minima is governed by the neutrinos and so comes close to the true value of $\delta_{CP} = -90^\circ$. At this point both neutrinos and antineutrinos have octant sensitive contribution. This is shown in Table III where we illustrate the contributions from the neutrinos and antineutrinos separately for the appearance channel. It is evident that as we increase the antineutrino component the contribution from neutrino channel reduces

¹ Due to the presence of $P_{\mu\mu}$ channel, the wrong octant minima comes around $\theta_{23} = 51^\circ$ for true $\theta_{23} = 39^\circ$.

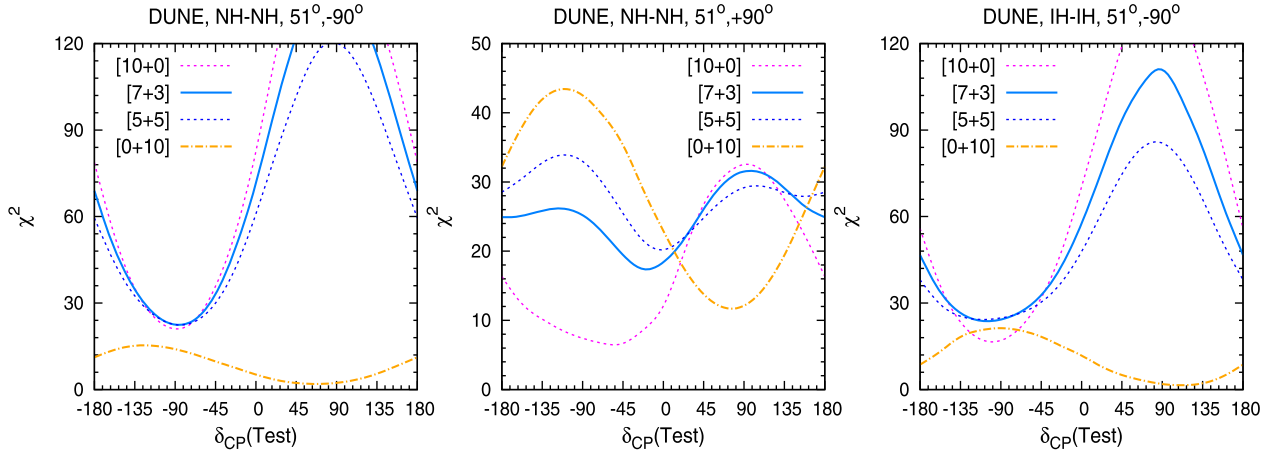


Fig. 4. Octant χ^2 vs test (δ_{CP}) for DUNE.

Table III

Here, [10 + 0], [7 + 3] and [5 + 5] refers to ($\nu + \bar{\nu}$) runs of DUNE, where as (8 + 0), (5 + 3) and (4 + 4) refers to ($\nu + \bar{\nu}$) runs of T2K. The numbers in the parenthesis correspond to T2K. Also ‘‘Test parameters’’ refer to the test values where χ^2 minimum appears and remaining oscillation parameters are same as true parameters.

($\nu + \bar{\nu}$)	Test parameters	$\chi_{ap,\nu}^2$	$\chi_{ap,\bar{\nu}}^2$	$\chi_{disap,(\nu+\bar{\nu})}^2$	Prior	Total
	NH, 51° , -90° (true)					
[10 + 0](8 + 0)	$\theta_{23} = 41.5^\circ$ (41°) $\sin^2 2\theta_{13} = 0.115$ (0.106)	11.5(6.65)	0	0.5(0.35)	9(1.44)	21.05(8.44)
[7 + 3](5 + 3)	same as [10 + 0](8 + 0)	9.14(4.28)	1.99(1.44)	1.97(0.37)	9(1.44)	22.46(7.18)
[5 + 5](4 + 4)	same as [10 + 0](8 + 0)	7.21(3.46)	2.98(1.44)	3.34(0.37)	9(1.44)	22.52(6.72)
	IH, 51° , -90° (true)					
[10 + 0](8 + 0)	$\theta_{23} = 40^\circ$ (41°), $\delta_{CP} = -105^\circ$ (-90°) $\sin^2 2\theta_{13} = 0.112$ (0.106)	10.86(5.23)	0	0.09(1.47)	5.76(1.44)	16.71(8.14)
[7 + 3](5 + 3)	same as [10 + 0](8 + 0)	8.22(3.36)	8.10(1.33)	1.62(0.96)	5.76(1.44)	23.71(7.09)
[5 + 5](4 + 4)	$\theta_{23} = 40.5^\circ$ (41°), $\delta_{CP} = -120^\circ$ (-90°) $\sin^2 2\theta_{13} = 0.112$ (0.103)	6.46(3.37)	9.78(2.08)	2.14(0.84)	5.76(0.36)	24.15(6.66)

whereas that from the antineutrino channel increases. Thus although the antineutrino channel has degeneracy the minima does not come at the point of degeneracy as it is governed by the neutrinos. Even then the total χ^2 ($= \chi_{ap,\nu}^2 + \chi_{ap,\bar{\nu}}^2$) from appearance channel (11.13, 10.19), corresponding to [7 + 3] and [5 + 5] respectively, is less than the pure neutrino run. However, the total χ^2 for the mixed run is higher.

To understand this point we list the contribution from the disappearance χ^2 and it is seen that although for pure neutrino run the disappearance channel does not have any octant sensitive contribution to the total χ^2 for mixed runs this channel also provide some octant sensitivity. This arises because due to matter effects the neutrino and antineutrino probabilities are different and hence the χ^2 minima comes at different places. When one combines neutrino and antineutrino run then this creates a synergy and hence some octant sensitivity arises from the disappearance channel also. Due to this reason when one combines appearance and disappearance channels then addition of antineutrino runs actually gives a slight increase in χ^2 . In the UHP on the other hand the octant sensitivity increases with antineutrino run. This is

clear since for $P_{\mu e}$ the neutrino channel suffers from octant degeneracy whereas the antineutrino channel does not and the addition of antineutrinos help to overcome the degeneracy. To illustrate this point further in the middle panel of Fig. 4 we plot the χ^2 vs test δ_{CP} for true values (51° , 90°). In this case the pure neutrino run gives the minima in the LHP close to $\delta_{CP} \sim -45^\circ$ whereas pure antineutrino gives minima near the true value. However when we combine neutrino and antineutrino runs then the overall minima comes in between and moves towards the antineutrino minima as the $\bar{\nu}$ component is increased. At this point there is octant sensitive contribution from both neutrinos and antineutrinos. Thus the antineutrino data helps in this case by trying to shift the minima away from the degenerate point. We also compare the χ^2 for DUNE with that of T2K, given in parentheses in Table III, to understand the role of broadband beam and enhanced matter effect. It is seen from the last column that for T2K the χ^2 reduces with increasing antineutrinos as is expected. Note that this is in contrast to DUNE due to its broadband nature and enhanced matter effect.

- **IH-LO** ($\theta_{23} = 39^\circ$): In this case for LHP the antineutrino run enhances the sensitivity because they do not suffer from octant degeneracy as can be seen from Table II. But for the UHP the antineutrino probability has octant degeneracy. Thus again we expect that in UHP adding antineutrino data should reduce the sensitivity. But the figure shows a slight enhancement. This can again be explained by similar reasoning as for the NH, 51° and -90° case. There is also the finite contribution from the disappearance channel enhancing the octant sensitivity when the neutrino and antineutrino runs are combined. These combinations of hierarchy–octant can resolve octant degeneracy at 5σ C.L. with $[5 + 5]$ years of $[\nu + \bar{\nu}]$ run for any value of true δ_{CP} as shown in Fig. 2.
- **IH-HO** ($\theta_{23} = 51^\circ$): For this case, for δ_{CP} in LHP the octant sensitivity with pure neutrino run is seen to be above $\chi^2 = 9$ in the interval $-180^\circ < \delta_{CP} < -45^\circ$. Adding antineutrino data helps to raise the χ^2 for octant sensitivity. As before we ask the question how antineutrino data is helpful despite the presence of degeneracies in this channel. This can be explained again similar to the NH-HO case. The third panel of Fig. 4 shows that for pure antineutrinos, there is very small octant sensitivity and the minima comes in the UHP between 90° and 135° . However at the point, in the LHP, where the pure neutrino χ^2 is minimum, antineutrino χ^2 has a large non-zero value and for combined runs the minima is still governed by the neutrinos. Thus the contributions from the antineutrinos are also being added up in spite of having degeneracy. The neutrino and antineutrino contributions from the appearance channel are shown in Table III. It is seen that for IH, because of the enhancement of the antineutrino probability due to matter effect, a large octant sensitive contribution to the χ^2 is obtained. The disappearance channel also gives a small contribution but the contribution from the antineutrino channel is almost comparable or larger than the neutrino channel. It is also to be noted that if hierarchy is not known then for some values of δ_{CP} the minima comes in the wrong hierarchy region for pure neutrino run and the sensitivity is further reduced. Addition of antineutrinos resolves the hierarchy with $\chi^2 \geq 25$ and so the minima does not occur anymore for wrong hierarchy solution. For the UHP the only neutrino run has very poor sensitivity due to degeneracies with δ_{CP} and addition of antineutrino runs help. The UHP is more favourable for resolution of hierarchy– δ_{CP} degeneracy and even with only neutrino run hierarchy is resolved at 3σ for all values of δ_{CP} . Overall, close to $\chi^2 = 25$ sensitivity is achieved for this combination of hierarchy and θ_{23} with $7 + 3$ or $5 + 5$ combination for the whole range of δ_{CP} . For this case also in Table III the T2K χ^2 values are given in parentheses. It is seen from the last column that the overall χ^2 for T2K decreases with enhanced antineutrinos unlike that in DUNE. If one compares the appearance χ^2 values for the

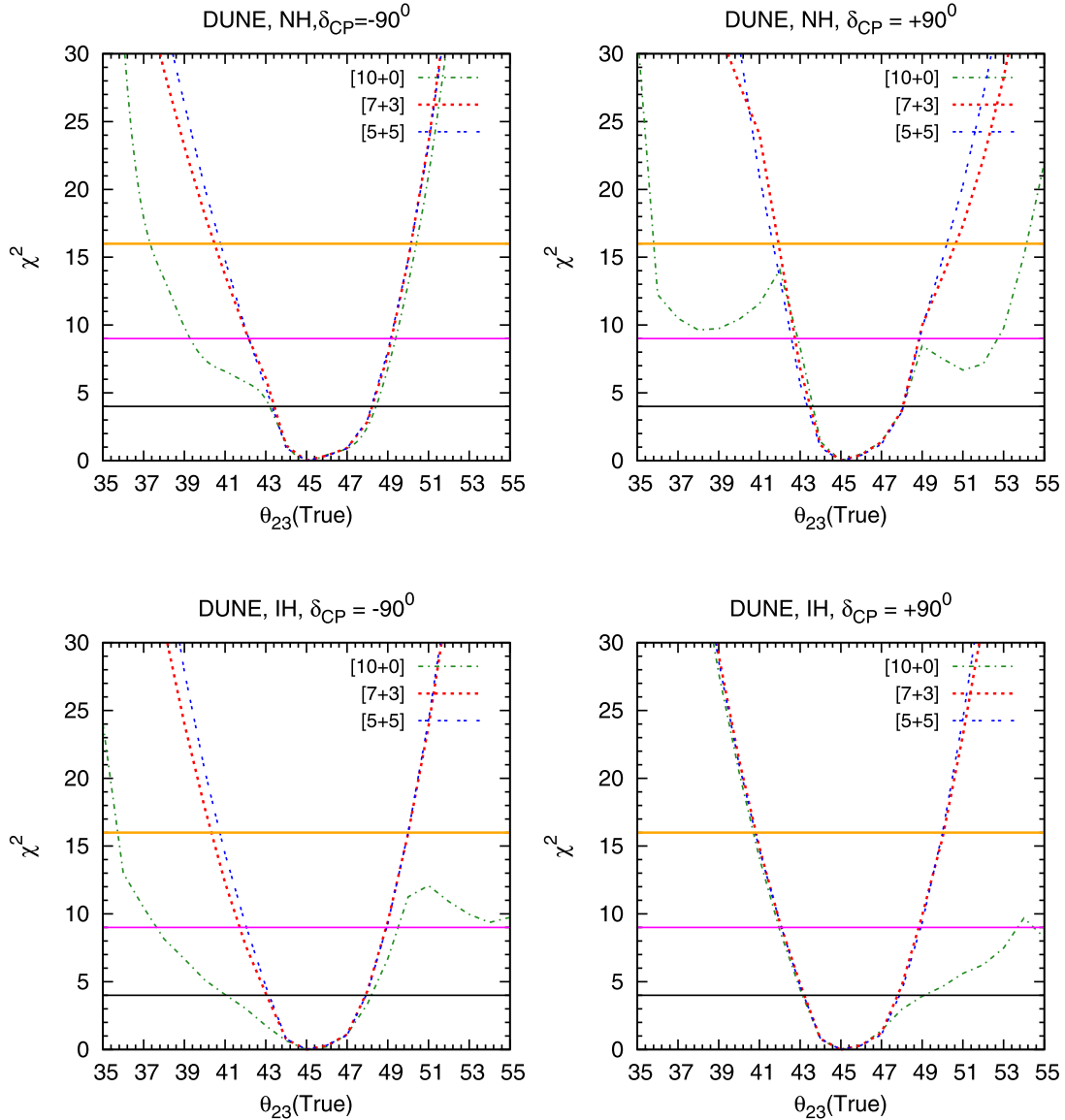


Fig. 5. Octant sensitivity χ^2 for DUNE. Left (right) panel is for $\delta_{CP} = -90^\circ$ ($+90^\circ$), where true hierarchy is considered as NH (IH) for upper (lower) row. Here black, magenta and yellow lines represent χ^2 value at 2σ , 3σ and 4σ respectively.

antineutrino channel for DUNE and T2K then it is seen that the contribution of this channel for DUNE is quite high and comparable or even greater than the neutrino contribution. This is due to the enhanced matter effect associated with IH and HO for the longer baseline of DUNE.

After discussing the role of antineutrinos and disappearance channel in octant sensitivity for DUNE, in Fig. 5 we present the octant χ^2 as a function of true θ_{23} for maximal CP violation. Depending on if the true hierarchy is NH or IH and true δ_{CP} is $\pm 90^\circ$ we get 4 possible combinations. From these figures one can read off the range of θ_{23} for which octant can be determined for $\delta_{CP} = \pm 90^\circ$ at a specified C.L. We see for all the four cases of Fig. 5 that with 7 + 3 years of $(\nu + \bar{\nu})$ run octant can be determined at 3σ (4σ) for $\delta_{CP} = \pm 90^\circ$ excepting for the range $41.5^\circ < \theta_{23} < 49^\circ$ ($40.5^\circ < \theta_{23} < 50.7^\circ$). From the figures we also see that 7 + 3 and 5 + 5 combinations give almost same sensitivity. However for the pure neutrino run the ranges are different

Table IV
Ranges of θ_{23} for which octant can be resolved at 3σ (4σ) for [10 + 0] configuration for 10 kt detector.

True parameter	θ_{23} range for 3σ (4σ)
NH, $\delta_{CP} = -90^\circ$	$< 39^\circ$ (37.4°) and $> 49^\circ$ (50.6°)
NH, $\delta_{CP} = 90^\circ$	$< 43^\circ$ (35.7) and $> 53^\circ$ (54°)
IH, $\delta_{CP} = -90^\circ$	$< 37^\circ$ (35.7) and $> 49^\circ$ (55°)
IH, $\delta_{CP} = 90^\circ$	$< 42^\circ$ (40) and $> 54^\circ$ (55°)

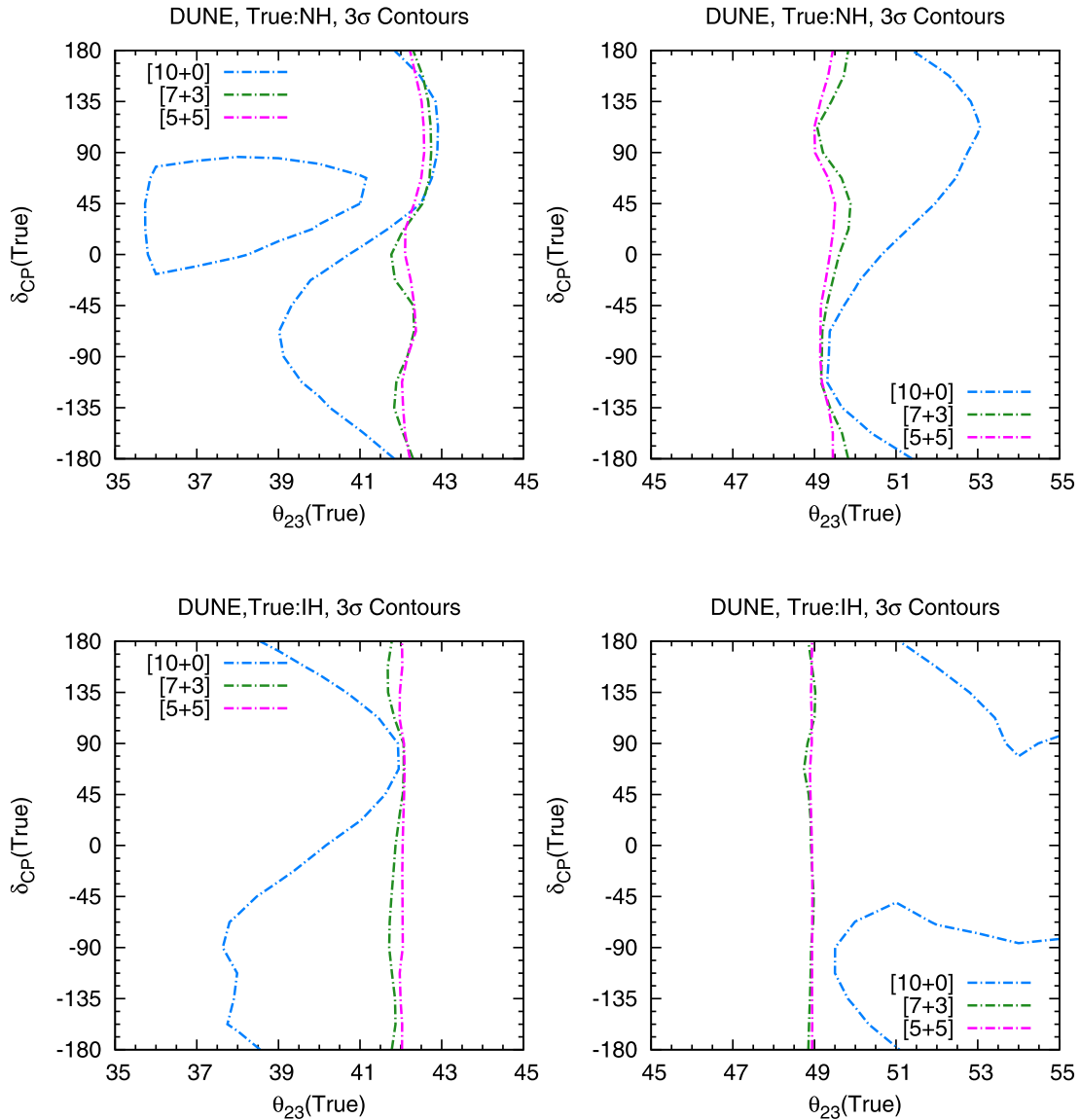


Fig. 6. Contour plots in true(θ_{23} , δ_{CP}) plane, here true hierarchy is NH (IH) for upper (lower) row and left (right) panel is for LO (HO). Marginalization over hierarchy is done. The allowed regions are to the right (left) side of the contours in the left (right) panel. (For interpretation of the references to color in this figure, the reader is referred to the web version of this article.)

and also vary depending on the true values of δ_{CP} and hierarchy. In Table IV we give the ranges of θ_{23} for which octant can be resolved at 3σ and 4σ with pure neutrino run.

So far we have focused on the cases for which either true θ_{23} was fixed or true δ_{CP} was fixed. In Fig. 6 we give the 3σ exclusion plots in true(θ_{23} – δ_{CP}) plane. We consider all possible true

values of δ_{CP} from $(-180^\circ$ to $+180^\circ)$ and θ_{23} in lower octant from 35° – 45° and higher octant from 45° – 55° . This figure shows the role of antineutrino run in the full range of allowed δ_{CP} and θ_{23} parameter space. The allowed region for the left (right) panel is the R.H.S. (L.H.S.) of each curve of the true $(\theta_{23}-\delta_{CP})$ plane.² We observe by comparing the left and the right panels that DUNE can provide better constraints on θ_{23} parameter space in case of LO as compared to HO. For NH-LO the antineutrino run is necessary for the LHP and part of UHP. Only in the range $90^\circ < \delta_{CP} < 135^\circ$ the only neutrino run i.e., the $[10 + 0]$ configuration gives a slightly better sensitivity. On the other hand for NH-HO the antineutrinos play a more prominent role for δ_{CP} in the UHP. For IH-LO the antineutrino run is again important apart from near $\delta_{CP} \sim 90^\circ$, for which the improvement in sensitivity by adding antineutrinos is not very significant. For IH-HO the antineutrinos play important role in the full parameter space. Also the exclusion plots show that if true θ_{23} lies between $(43^\circ$ – $49^\circ)$ then it is not possible to resolve octant degeneracy at 3σ C.L. by DUNE using 10 kt detector. Overall one can say that antineutrino runs are necessary for most of the parameter region and $7 + 3$ and $5 + 5$ give similar sensitivities. Note that in the context of LBNO 75%–25% ($\nu - \bar{\nu}$) was recommended in [55].

Finally in Fig. 7 we plot the 3σ precision contours in the true θ_{23} –test θ_{23} plane for $\delta_{CP} = \pm 90^\circ$. These figures reflect the relation between octant degeneracy and precision of θ_{23} . The upper panels are for normal hierarchy and the lower panels are for inverted hierarchy. From these plots we see that for pure neutrino run there are other allowed values of θ_{23} apart from the true value, if $\theta_{23} \in$ LO (HO) at $\delta_{CP} = -90^\circ$ ($+90^\circ$). This happens because of the octant degeneracy. As we have already seen, for $\delta_{CP} = -90^\circ$ ($+90^\circ$), neutrinos suffer from octant degeneracy in LO (HO) in both the hierarchies and this in turn affects the precision of θ_{23} which is clearly seen from the figures. Adding antineutrinos help to improve the precision and both $7 + 3$ and $5 + 5$ give almost similar precision of θ_{23} . But as one approaches the maximal value of θ_{23} , the precision becomes worse due to the difficulty in determining the octant around those values of θ_{23} .

4.2. Antineutrinos, octant degeneracy and CP discovery potential of DUNE

In this section we present the CP discovery χ^2 of DUNE as a function of true δ_{CP} . CP violation discovery potential of an experiment is defined by its capability of distinguishing a true value of δ_{CP} other than 0° and 180° . We present these figures for the case where hierarchy and octant are assumed to be unknown and known. The main aim of this section is to elucidate the role of antineutrinos in discovering δ_{CP} and the interconnection with the octant degeneracy.

The Fig. 8 plots the CP discovery χ^2 as function of true δ_{CP} for the case when hierarchy and octant are assumed to be unknown. From the different panels it is seen that:

- The antineutrino runs play an important role for (i) LO near true $\delta_{CP} = -90^\circ$ and (ii) HO near true $\delta_{CP} = +90^\circ$. This is true for both NH and IH. Note from Table II that these are the regions where neutrino probabilities exhibit octant degeneracy. Since antineutrino probabilities do not possess this degeneracy, addition of these helps in the removal of the degeneracy and enhancement of CP sensitivity.
- For true hierarchy as NH, $+90^\circ$ -LO and -90° -HO do not have octant degeneracy for neutrinos whereas antineutrinos have degeneracy (see Table II). Even then $7 + 3$ gives almost

² For NH-LO, DUNE[10 + 0] (top left panel of Fig. 6), the area enclosed by the blue curve also corresponds to the allowed region.

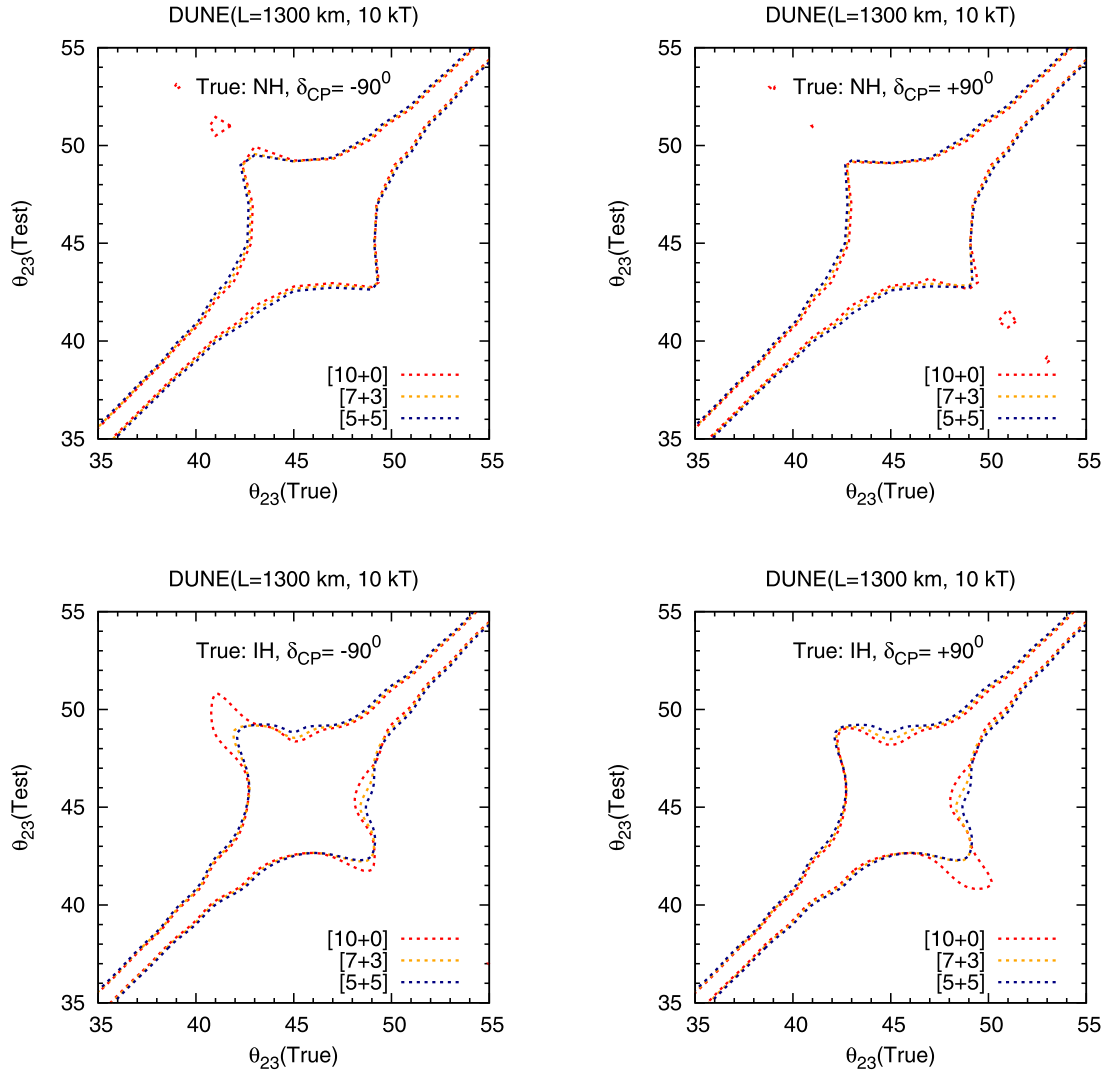


Fig. 7. θ_{23} precision plots of DUNE in True(θ_{23})–Test(θ_{23}) plane at 3σ C.L. Here top (bottom) row is for NH(IH).

same result as $10 + 0$ notwithstanding the loss of statistics. In both cases this happens due to tension between the neutrino and antineutrino χ^2 s.

- For $+90^\circ$ -LO the minima for $10 + 0$ comes at $\delta_{CP} = 180^\circ$ whereas replacing 3 years of neutrino run by antineutrino run shifts the χ^2_{min} at $\delta_{CP} = 0^\circ$ where the neutrino contribution is higher and thus $7 + 3$ becomes comparable to $10 + 0$.
- For the case of -90° -HO and neutrinos the CPV χ^2 is a falling function of θ_{13} , and the minima comes at 0.109 while for $7 + 3$ it comes at 0.106. The neutrino contribution at $\sin^2 \theta_{13} = 0.106$ being higher the overall χ^2 for $7 + 3$ becomes greater.
- Similarly, for true hierarchy IH, $+90^\circ$ -LO and -90° -HO are free from octant degeneracy for neutrinos. But still the CP sensitivity for these cases are slightly better for combined neutrino–antineutrino run (for both $7 + 3$ and $5 + 5$ case) as compared to pure neutrino run. This happens because due to matter effects the $P_{\bar{\mu}e}$ is higher than $P_{\mu e}$ for IH (see Fig. 1). Thus addition of antineutrinos enhances the appearance χ^2 .

In Fig. 9 we present the same plots as that of Fig. 8 but assuming the hierarchy and octant to be known.

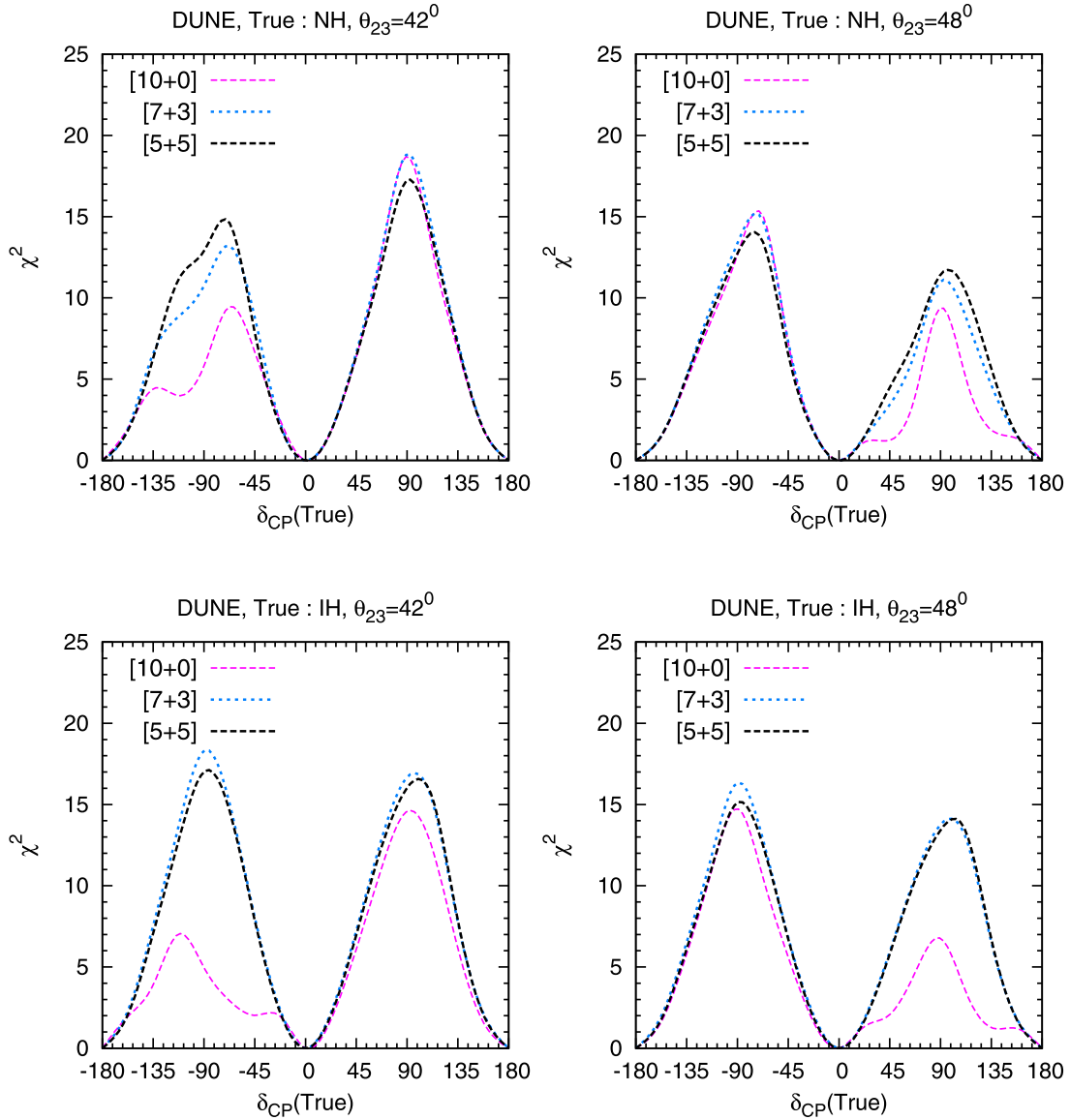


Fig. 8. CPV χ^2 for DUNE when hierarchy and octant are unknown.

- Comparing with the plots in Fig. 8 we see that the CP sensitivity for -90° -LO improves for the $10 + 0$ case, for both the hierarchies. In fact for -90° -LO-NH, $10 + 0$ gives the best sensitivity if the octant is known. This establishes the fact that, the antineutrino run was instrumental for removing the wrong octant solutions.
- For $+90^\circ$ -NH-HO although there is some improvement for the $10 + 0$ case as compared to the case of unknown octant, the CP sensitivity of $7 + 3$ and $5 + 5$ are still better than $10 + 0$. This implies that though octant is known, antineutrinos play some role in enhancing the CP sensitivity.
 - To understand the above point in more detail in Fig. 10 we plot the CPV discovery χ^2 for different channels vs test θ_{23} in the correct octant (since octant is assumed to be known) for a particular value of true δ_{CP} . The top left panel of Fig. 10 shows that, for neutrinos and true value of $+90^\circ$ -NH- 48° , the CP sensitivity of the appearance channel is an increasing function of test θ_{23} . But as the precision of θ_{23} (which comes from the disappearance channel) is poor near the maximal value, the combined χ^2 minimum does not occur at the true θ_{23} value (which is $\theta_{23} = 48^\circ$) but occurs at $\theta_{23} = 45^\circ$. For antineutrinos (top right

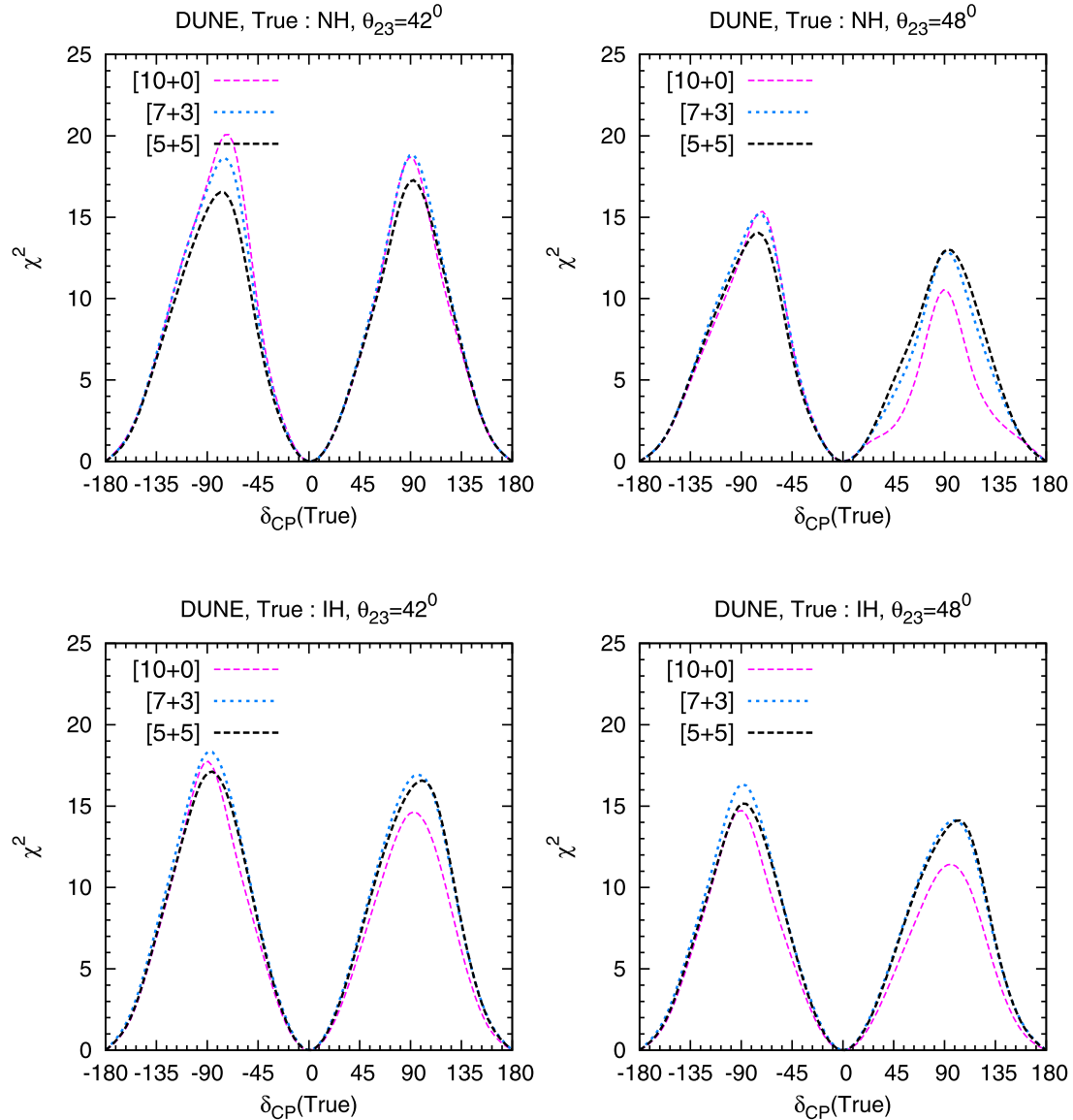


Fig. 9. CPV χ^2 for DUNE when hierarchy and octant are known.

panel), the nature of the disappearance channel χ^2 is same as that of neutrinos but the appearance χ^2 decreases as test θ_{23} increases. Because of this opposite behaviour when antineutrinos are combined with neutrinos, the χ^2 minima shifts to the correct value of θ_{23} and the overall CP sensitivity at the true point is enhanced. The poor θ_{23} precision of $+90^\circ$ -HO-NH in neutrinos arise due to the higher matter effect. Due to which the subleading matter terms start to contribute in the disappearance channel which affect the θ_{23} precision. Note that this does not happen for -90° -NH-HO (despite matter is high) because even though the precision of θ_{23} is poor near the maximal value of θ_{23} for $\delta_{CP} = -90^\circ$ the appearance channel sensitivity is a decreasing function of test θ_{23} and this causes the overall minima to occur at the correct value of θ_{23} . This can be seen from the right panel of the middle row of Fig. 10.

- Also note that for true $+90^\circ$ -NH 42° (left panel of middle row of Fig. 10), the precision of θ_{23} near the maximal value is quite good as compared to $\theta_{23} = 48^\circ$. This is because for lower octant, the denominator in the χ^2 is smaller as compared to that in HO and thus a better θ_{23} precision is obtained.

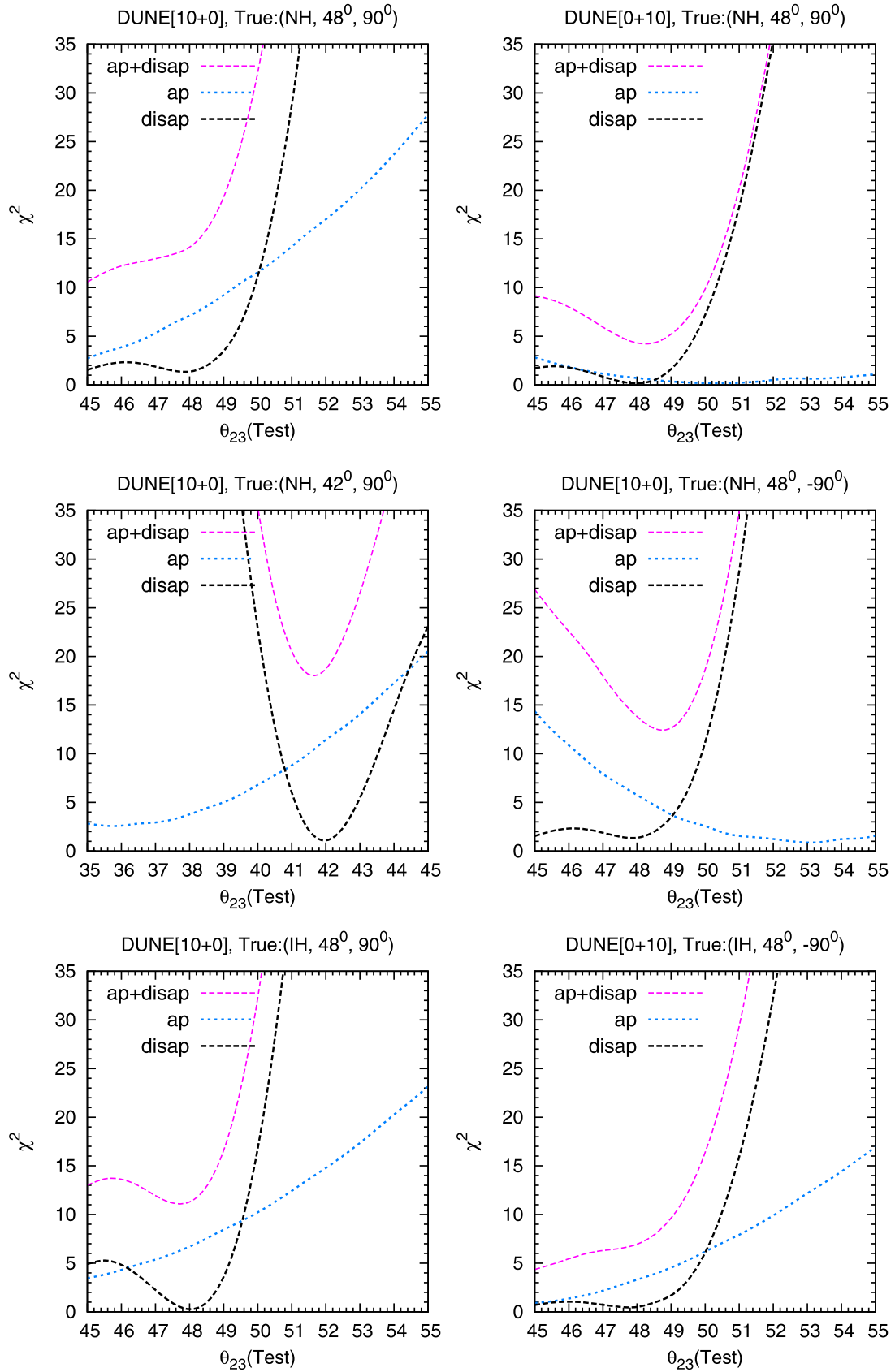


Fig. 10. CPV χ^2 for DUNE when hierarchy and octant are known.

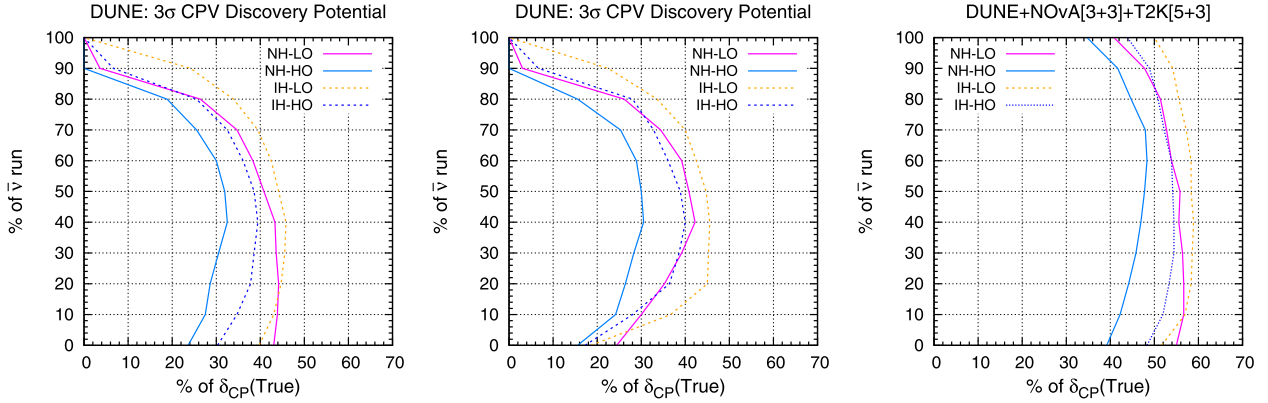


Fig. 11. CP violation discovery χ^2 at 3σ C.L. in (% of $\delta_{CP}(True)$, % of antineutrino run) plane. Here, first and second column are for DUNE and third column is for DUNE + NO ν A[3 + 3] + T2K[5 + 3]. Also y-axis represents the % of antineutrino run out of total 10 years of $[\nu + \bar{\nu}]$ run in DUNE. In first (second and third) column we consider hierarchy and octant are known (unknown).

- For true hierarchy IH, even $\theta_{23} = 48^\circ$ has a good precision near the maximal value for neutrinos (bottom left panel of Fig. 10). This is because for IH the matter effect is less for neutrinos and thus θ_{23} precision measurement capability of the disappearance channel is better as can be seen comparing the top and bottom left panels of Fig. 10. But since the matter effect is more for antineutrinos, the precision of θ_{23} for IH and antineutrinos is poor (bottom right panel).
- Similarly for $+90^\circ$ -HO-IH although the octant is known the antineutrino run gives an enhanced χ^2 . This is due to matter effects in antineutrinos for IH which makes $P_{\bar{\mu}e}$ higher than the corresponding neutrino probabilities (see Fig. 1). This increases the appearance χ^2 in presence of antineutrinos. For similar reasons the χ^2 for 7 + 3 is slightly higher than 10 + 0 for -90° -LO-IH.

In the first and second panels of Fig. 11, we plot the percentage of antineutrino run vs percentage of δ_{CP} values for which CP violated can be discovered at 3σ C.L. in DUNE for four cases encompassing both hierarchies and octants. The first (second) panel represents when octant and hierarchy are known (unknown). From both plots it is seen that with dominant antineutrino or neutrino run a lesser CP fraction is reached. Overall 40% antineutrino run seems to be optimum in all cases. Comparing these two plots it is seen that when octant is known then greater percentage of CP fraction can be probed with less antineutrino component. The maximum CP coverage can be achieved for IH-HO and minimum for NH-HO.

In the third panel of Fig. 11 the same is plotted by combining NO ν A and T2K with DUNE. From the figure we can see that the percentage of δ_{CP} that can be probed is enhanced in all cases. The curves are now much flatter implying that even with pure neutrino or antineutrino runs considerable CP coverage can be obtained. This is due to the contribution from NO ν A and T2K. In Fig. 12 we show the dependence of percentage of δ_{CP} that can be probed as a function θ_{23} . This figure is drawn assuming 60% neutrino and 40% antineutrino run which is the optimal configuration as seen in Fig. 11. The coverage of δ_{CP} for which CP violation can be discovered at 3σ C.L. is better for IH. For NH specially close to 45° the coverage is less due to the poor precision of θ_{23} as discussed earlier.

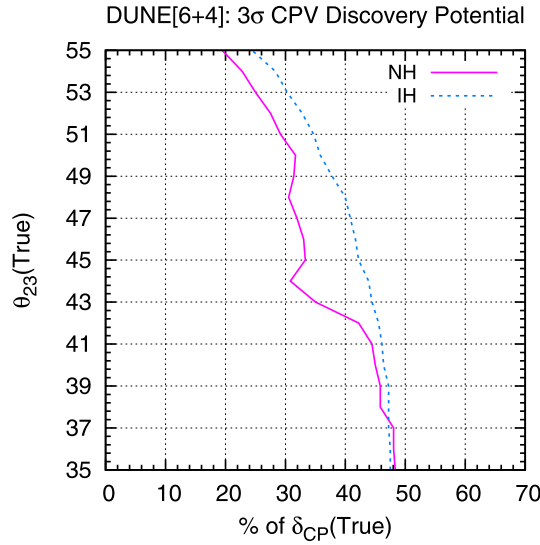


Fig. 12. CP violation discovery χ^2 at 3σ C.L. for DUNE[6 + 4] for all true θ_{23} when hierarchy and octant are unknown.

5. Summary and conclusions

In this paper we perform a detailed investigation of the octant and δ_{CP} sensitivity of the future generation superbeam experiment DUNE which has a baseline of 1300 km. We analyze in detail the physics of the antineutrinos for the DUNE baseline and what kind of synergy can be offered by the addition of antineutrinos to pure neutrino runs. In the context of the long baseline experiments with source–detector distance <1000 km it is well known that the octant sensitivity comes mainly from the combination of $P_{\mu e}$ and $P_{\mu\mu}$ channels. For $P_{\mu e}$ channel the χ^2 is a rising function of θ_{23} and consequently the minima in the wrong octant always comes at 45° . On the other hand $P_{\mu\mu}$ being governed by $\sin^2 2\theta_{23}$, the minima comes close to $\pi/2 - \theta_{23}$ with no octant sensitivity. When both channels are combined then the global minima comes closer to $\pi/2 - \theta_{23}$ where the appearance channel contributes a large octant sensitive χ^2 . However the appearance channel is also affected by the occurrence of octant– δ_{CP} degeneracy which can lead to spurious solutions. The nature of this degeneracy is the same for both the hierarchies but has a complementary nature for neutrinos and antineutrinos i.e., the δ_{CP} and octant combination for which there is degeneracy in neutrinos is devoid of this for antineutrinos. The upshot is that the combination of neutrino and antineutrino runs helps to solve this degeneracy. On the other hand the statistics is more for neutrinos. This leads to the question of what is the optimal combination of neutrino and antineutrino run for giving the maximum benefit for octant determination. This issue has been addressed in this work in the context of the DUNE experiment. We also discuss to what extent the broad-band nature of the beam and enhanced matter effect influences the octant sensitivity and if any new features emerge as compared to the previous narrow-band off-axis experiments with baseline <1000 km. We find that for the DUNE baseline addition of antineutrinos are helpful in general. This statement holds true even when there may be some degeneracy associated with the antineutrino channel and one expects the pure neutrino run to give the best results. This occurs because of opposing tendencies of neutrino and antineutrino χ^2 s. We find that when $\bar{\nu}$ is combined with ν then the overall χ^2 minimum is still governed by the neutrinos because of higher statistics. At this point the antineutrino contribution to χ^2 is higher and hence adding these enhances octant sensitivity inspite of the associated octant degeneracy. One should also note that due to the broadband nature of the beam the degeneracy may be limited for few en-

ergy bins only. Note that, due to the broad-band nature of the beam, the octant sensitivity coming from pure neutrino run is also quite high at the true values where neutrino probabilities are themselves degenerate. The antineutrino contribution can be more for IH since due to enhanced matter effects the corresponding probabilities can be much higher than the neutrino probabilities. Thus even if the main octant sensitivity comes from the neutrinos, the broad-band nature compounded with the higher matter effect leads to some octant sensitivity coming from antineutrino channels in case of IH. In addition we find that a small octant sensitive contribution comes from the disappearance channel when neutrino and antineutrino runs are combined although pure neutrino or pure antineutrino runs do not have this sensitivity. This happens because, due to matter effect the neutrino and antineutrino probabilities are slightly different and hence the minima comes at slightly different position for each case. When combined, there is a tension between these two which gives rise to a small octant sensitive χ^2 contribution. Note that these features arising due to matter effects have not been highlighted in the literature earlier.

Taking two representative values of θ_{23} in the lower octant (39°) and higher octant (51°) we study the behaviour of χ^2 with δ_{CP} for both NH and IH. We find that for a 10 kt mass of the detector although for some δ_{CP} values $(3-4)\sigma$ sensitivity can be achieved with only neutrino run, overall adding antineutrinos is helpful. For a $7 + 3$ year ($\nu + \bar{\nu}$) run, close to 4σ sensitivity can be achieved over all values of δ_{CP} . It is found that $7 + 3$ and $5 + 5$ do not give significantly different results. We compute the χ^2 as a function of true θ_{23} for maximum CP violation. From this study we find that with $7 + 3$ years option octant degeneracy can be resolved at 3σ excepting the range $41.5^\circ < \theta_{23} < 49^\circ$. Increasing the antineutrino component and making runtime $5 + 5$ does not make any discernible difference to the results. Finally we also study the octant sensitivity in the true($\theta_{23}-\delta_{CP}$) plane which checks the validity of the conclusions drawn earlier over the whole parameter range. We find that for 10 kt year mass the antineutrino run enhances the range of θ_{23} over which octant sensitivity can be achieved. Including antineutrino runs, octant sensitivity can be obtained at 3σ excepting the range $43^\circ < \theta_{23} < 49^\circ$ not only for maximal violation of δ_{CP} but over the whole range. In this case with only neutrino run octant remains undetermined over a large parameter space. We also present the 3σ precision contours in the true θ_{23} -test θ_{23} plane. These plots show that adding antineutrino runs also help in obtaining improved precision on θ_{23} .

We also present results on the CP violation discovery potential of DUNE emphasizing the role played by the antineutrinos. The CP sensitivity of any long-baseline experiment is affected by the occurrence of the wrong-hierarchy-wrong octant-wrong δ_{CP} solutions. Since the antineutrinos help in removing these solutions, one of the main role of the antineutrinos in enhancing CP sensitivity is to remove these wrong solutions. We present results for cases where hierarchy and octant are unknown and known and compare the role of the antineutrinos in both situations. We find that when octant is not known then in parameter spaces where octant degeneracy is manifest the antineutrino component increases CP sensitivity by removing wrong octant solutions. This is the case for instance for LO, $\delta_{CP} \sim -90^\circ$ and HO, $\delta_{CP} \sim +90^\circ$ for both hierarchies. However even when the octant is known addition of antineutrinos can improve the result because of the tension between the two χ^2 s which raises the overall χ^2 . The contribution from the antineutrino channel is higher for IH since due to matter effects the antineutrino probability is higher than the corresponding neutrino probability. At $\delta_{CP} = \pm 90^\circ$, a greater than 3σ sensitivity is achieved in all cases. We have also explored how addition of antineutrinos affects the fraction of δ_{CP} values for which CP sensitivity can be probed at 3σ level. We find that when octant is known, same sensitivity can be achieved with a lesser fraction of antineutrinos for both hierarchies. The maximum CP fraction is achieved for IH-LO. Overall the best result comes with 60% neutrino and 40% antineutrino runs for all the four cases.

In conclusion, we have explored the role of antineutrinos in enhancing octant and CP sensitivity for a 1300 km experiment with a broad-band beam as is planned by the DUNE collaboration. We emphasize on the importance of antineutrino run in resolving octant ambiguity and increasing CP sensitivity. Although for some specific parameters only neutrino run can give 3σ octant sensitivity for a 10 kt detector mass of DUNE, overall a balanced neutrino–antineutrino run gives better sensitivity. For the case of δ_{CP} discovery also in most of the parameter space antineutrinos play an important role due to synergistic effects between neutrinos and antineutrinos even under the assumption of octant to be known.

Acknowledgements

The authors would like to thank Sushant K. Raut for his help in GLOBES and also for many useful discussions regarding DUNE.

References

- [1] K. Eguchi, et al., KamLAND, Phys. Rev. Lett. 92 (2004) 071301, arXiv:hep-ex/0310047.
- [2] R. Wendell, et al., Super-Kamiokande Collaboration, Phys. Rev. D 81 (2010) 092004, arXiv:1002.3471.
- [3] P. Adamson, et al., MINOS Collaboration, Phys. Rev. Lett. 112 (2014) 191801, arXiv:1403.0867.
- [4] K. Abe, et al., T2K Collaboration, arXiv:1409.7469, 2014.
- [5] M.C. Gonzalez-Garcia, M. Maltoni, T. Schwetz, Nucl. Phys. B 908 (2016) 199, arXiv:1512.06856.
- [6] F. Capozzi, E. Lisi, A. Marrone, D. Montanino, A. Palazzo, Nucl. Phys. B 908 (2016) 218, arXiv:1601.07777.
- [7] K. Abe, et al., T2K, Phys. Rev. D 91 (2015) 072010, arXiv:1502.01550.
- [8] P. Adamson, et al., NOvA, Phys. Rev. Lett. 116 (2016) 151806, arXiv:1601.05022.
- [9] P. Adamson, et al., NOvA, Phys. Rev. D 93 (2016) 051104, arXiv:1601.05037.
- [10] V. Barger, D. Marfatia, K. Whisnant, Phys. Rev. D 65 (2002) 073023, arXiv:hep-ph/0112119.
- [11] J. Burguet-Castell, M. Gavela, J. Gomez-Cadenas, P. Hernandez, O. Mena, Nucl. Phys. B 646 (2002) 301, arXiv:hep-ph/0207080.
- [12] H. Minakata, H. Nunokawa, J. High Energy Phys. 0110 (2001) 001, arXiv:hep-ph/0108085.
- [13] G.L. Fogli, E. Lisi, Phys. Rev. D 54 (1996) 3667, arXiv:hep-ph/9604415.
- [14] K. Abe, et al., T2K, Phys. Rev. Lett. 107 (2011) 041801, arXiv:1106.2822.
- [15] Y. Abe, et al., Double Chooz Collaboration, J. High Energy Phys. 1410 (2014) 86, arXiv:1406.7763.
- [16] F.P. An, et al., Phys. Rev. Lett. 115 (2015) 111802, arXiv:1505.03456.
- [17] J. Ahn, et al., RENO Collaboration, Phys. Rev. Lett. 108 (2012) 191802, arXiv:1204.0626.
- [18] S. Prakash, S.K. Raut, S.U. Sankar, Phys. Rev. D 86 (2012) 033012, arXiv:1201.6485.
- [19] S.K. Agarwalla, S. Prakash, S.U. Sankar, J. High Energy Phys. 1307 (2013) 131, arXiv:1301.2574.
- [20] P. Machado, H. Minakata, H. Nunokawa, R.Z. Funchal, arXiv:1307.3248, 2013.
- [21] P. Coloma, H. Minakata, S.J. Parke, Phys. Rev. D 90 (2014) 093003, arXiv:1406.2551.
- [22] M. Ghosh, P. Ghoshal, S. Goswami, N. Nath, S.K. Raut, Phys. Rev. D 93 (2016) 013013, arXiv:1504.06283.
- [23] P. Huber, M. Lindner, T. Schwetz, W. Winter, J. High Energy Phys. 11 (2009) 044, arXiv:0907.1896.
- [24] H. Minakata, H. Sugiyama, Phys. Lett. B 580 (2004) 216, arXiv:hep-ph/0309323.
- [25] A. Chatterjee, P. Ghoshal, S. Goswami, S.K. Raut, J. High Energy Phys. 1306 (2013) 010, arXiv:1302.1370.
- [26] J. Kameda, Talk given at NuFact, 2015.
- [27] S. Choubey, P. Roy, Phys. Rev. Lett. 93 (2004) 021803, arXiv:hep-ph/0310316.
- [28] O.L.G. Peres, A.Y. Smirnov, Phys. Lett. B 456 (1999) 204, arXiv:hep-ph/9902312.
- [29] M.C. Gonzalez-Garcia, M. Maltoni, A.Yu. Smirnov, Phys. Rev. D 70 (2004) 093005, arXiv:hep-ph/0408170.
- [30] S. Choubey, A. Ghosh, J. High Energy Phys. 1311 (2013) 166, arXiv:1309.5760.
- [31] M. Ghosh, P. Ghoshal, S. Goswami, S.K. Raut, Nucl. Phys. B 884 (2014) 274, arXiv:1401.7243.
- [32] M. Ghosh, Phys. Rev. D 93 (2016) 073003, arXiv:1512.02226.
- [33] J. Evslin, S.-F. Ge, K. Hagiwara, J. High Energy Phys. 02 (2016) 137, arXiv:1506.05023.
- [34] C. Adams, et al., LBNE Collaboration, arXiv:1307.7335, 2013.
- [35] S.K. Agarwalla, S. Prakash, S. Uma Sankar, J. High Energy Phys. 1403 (2014) 087, arXiv:1304.3251.
- [36] M. Ghosh, S. Goswami, S.K. Raut, ArXiv e-prints, arXiv:1412.1744, 2014.

- [37] K. Bora, D. Dutta, P. Ghoshal, *Mod. Phys. Lett. A* 30 (2015) 1550066, arXiv:1405.7482.
- [38] V. Barger, A. Bhattacharya, A. Chatterjee, R. Gandhi, D. Marfatia, et al., *Phys. Rev. D* 89 (2014) 011302, arXiv:1307.2519.
- [39] V. Barger, A. Bhattacharya, A. Chatterjee, R. Gandhi, D. Marfatia, et al., arXiv:1405.1054, 2014.
- [40] K.N. Deepthi, C. Soumya, R. Mohanta, *New J. Phys.* 17 (2015) 023035, arXiv:1409.2343.
- [41] S.K. Agarwalla, T. Li, A. Rubbia, *J. High Energy Phys.* 1205 (2012) 154, arXiv:1109.6526.
- [42] P. Huber, M. Lindner, W. Winter, *Comput. Phys. Commun.* 167 (2005) 195, arXiv:hep-ph/0407333.
- [43] P. Huber, J. Kopp, M. Lindner, M. Rolinec, W. Winter, *Comput. Phys. Commun.* 177 (2007) 432, arXiv:hep-ph/0701187.
- [44] R. Acciarri, et al., DUNE, arXiv:1512.06148, 2015.
- [45] D. Cherdack, Private communication, 2014.
- [46] M.C. Gonzalez-Garcia, M. Maltoni, T. Schwetz, *J. High Energy Phys.* 11 (2014) 052, arXiv:1409.5439.
- [47] F. Capozzi, G. Fogli, E. Lisi, A. Marrone, D. Montanino, et al., *Phys. Rev. D* 89 (2014) 093018, arXiv:1312.2878.
- [48] D. Forero, M. Tortola, J. Valle, arXiv:1405.7540, 2014.
- [49] M.C. Gonzalez-Garcia, M. Maltoni, *Phys. Rev. D* 70 (2004) 033010, arXiv:hep-ph/0404085.
- [50] G. Fogli, E. Lisi, A. Marrone, D. Montanino, A. Palazzo, *Phys. Rev. D* 66 (2002) 053010, arXiv:hep-ph/0206162.
- [51] R. Gandhi, et al., *Phys. Rev. D* 76 (2007) 073012, arXiv:0707.1723.
- [52] E.K. Akhmedov, R. Johansson, M. Lindner, T. Ohlsson, T. Schwetz, *J. High Energy Phys.* 04 (2004) 078, arXiv:hep-ph/0402175.
- [53] A. Cervera, et al., *Nucl. Phys. B* 579 (2000) 17, arXiv:hep-ph/0002108.
- [54] M. Freund, *Phys. Rev. D* 64 (2001) 053003, arXiv:hep-ph/0103300.
- [55] C.R. Das, J. Maalampi, J. Pulido, S. Vihonen, *J. High Energy Phys.* 02 (2015) 048, arXiv:1411.2829.

Neutrino masses and mixing in A_5 with flavor antisymmetryAnjan S. Joshipura^{1,*} and Newton Nath^{1,2,†}¹*Physical Research Laboratory, Navarangpura, Ahmedabad 380 009, India*²*Indian Institute of Technology, Gandhinagar, Ahmedabad 382424, India*

(Received 22 June 2016; published 24 August 2016)

We discuss the consequences of assuming that the (Majorana) neutrino mass matrix M_ν and the charged lepton mass matrix M_l satisfy $S_\nu^T M_\nu S_\nu = -M_\nu$ and $T_l^\dagger M_l M_l^\dagger T_l = M_l M_l^\dagger$ with respect to some discrete groups S_ν and T_l contained in A_5 . These assumptions lead to a neutrino mass spectrum with two degenerate and one massless neutrino and also constrain mixing among them. We derive possible mixing patterns following from the choices $S_\nu = Z_2, Z_2 \times Z_2$, and $T_l = Z_2, Z_2 \times Z_2, Z_3, Z_5$ as subgroups of A_5 . One predicts the maximal atmospheric neutrino mixing angle θ_{23} and μ - τ reflection symmetry in a large number of cases, but it is also possible to obtain nonmaximal values for θ_{23} . Only the third column of the neutrino mixing matrix can be obtained at the leading order due to degeneracy in masses of two of the neutrinos. We take up a specific example within the A_5 group and identify Higgs vacuum expectation values which realize the above assumptions. Nonleading terms present in this example are shown to lead to splitting among degenerate pairs and a consistent description of both neutrino masses and mixing angles.

DOI: 10.1103/PhysRevD.94.036008

I. INTRODUCTION

Two decades of neutrino oscillation experiments have determined five of the key parameters describing oscillations of three neutrinos. These are three mixing angles θ_{ij} , ($i, j = 1, 2, 3; i < j$) and two (mass)² differences Δ_\odot and Δ_A controlling the oscillations of the solar and the atmospheric neutrinos, respectively. The overall neutrino mass scale and three CP -violating phases still remain to be determined. There already exists a hint that the CP phase δ may be nearly maximal.

Theoretical frameworks describing neutrino masses and mixing angles try to understand the values of the observed parameters and aim to predict the unknown ones. Flavor symmetries provide a concrete framework to do this. A systematic approach based on flavor symmetries has evolved in the past several years; see reviews in Refs. [1–5], and references therein. This is based on the observation that patterns of neutrino masses and mixing are intimately linked to the residual symmetries of the neutrino and the charged lepton mass matrices [6–8]. These residual symmetries of mass matrices can be related to the full symmetry G_f of the underlying theory by assuming that the former symmetries are contained in G_f . This provides a direct link between the group theoretical structure of G_f and the observed mixing angles. This approach has been used to predict various mixing patterns consistent with observations in a large number of cases with many different discrete symmetry groups G_f [1–5,9].

The above approach is also generalized to link both the mass and the mixing patterns of neutrinos to some underlying symmetries. Three possible neutrino mass patterns

provide a good zeroth-order approximation to the observed neutrino mass spectrum, a fully degenerate spectrum, a quasidegenerate spectrum with two degenerate neutrinos, and a spectrum with two massive and one massless neutrinos. A systematic procedure is evolved to relate these patterns to the underlying discrete symmetries. A general analysis is presented for three classes of groups: the discrete von Dyck groups in the case of the degenerate and quasidegenerate spectrums [10], all possible discrete subgroups of $SU(3)$ having a three-dimensional irreducible representation in the case of the quasidegenerate neutrinos [11], and a large class of discrete subgroups of $U(3)$ in the case of one massless neutrino [12–14].

The basic assumption in the above approaches is that the underlying theory is invariant under some discrete group G_f but the Higgs vacuum expectation value (VEV) determining neutrino mass matrix M_ν and the Hermitian combination of the charged lepton mass matrix $M_l M_l^\dagger$ remain invariant under smaller subgroups G_ν and G_l of G_f . The structure of these groups and their embedding in G_f is sufficient for the determination of mixing patterns without the knowledge of the detailed dynamics. A different dynamical possibility was studied in Ref. [15]¹. Here it is assumed that the Higgs vacuum expectation values breaking flavor group G_f lead to a neutrino mass matrix which displays antisymmetry. Specifically, M_ν satisfies

$$S_\nu^T M_\nu S_\nu = -M_\nu \quad (1)$$

for some subgroups S_ν of G_f . This assumption was shown [15] to constrain not just the mixing angles but also the

* anjan@prl.res.in

† newton@prl.res.in

¹An antisymmetry under the $\mu - \tau$ exchange was first introduced in Ref. [16] where this was imposed as an effective (anti) symmetry on the neutrino mass matrix in the flavor basis.

neutrino mass spectrum which could be determined purely from the group theoretical arguments. Detailed mixing and mass patterns allowed within the discrete subgroups $\Delta(3N^2)$ and $\Delta(6N^2)$ and a specific dynamical realization of the basic idea in the case of the group $A_4 \equiv \Delta(3.2^2)$ were discussed in Ref. [15]. Also, it was shown in a specific example that the antisymmetry of the mass matrix can arise from the minimization of some suitable potential. Here we pursue this idea further and apply it to the symmetry group A_5 . We discuss mass patterns and all the mixing patterns possible within A_5 using the idea of flavor antisymmetry of the neutrino mass matrix. A_5 has been used in the past [17–23] to predict the neutrino mixing patterns assuming flavor symmetry. The mixing patterns predicted here are quite different compared to these cases.

A detailed analysis of A_5 also becomes interesting from a related point of view. It was shown [24] that all the discrete subgroups of $O(3)$ can lead to universal prediction $\theta_{23} = \frac{\pi}{4}$ and $|\delta| = \frac{\pi}{2}$ when G_ν is chosen as $Z_2 \times Z_2$ or Z_m and G_l is chosen as Z_n , $m, n \geq 3$. As we will see, the same predictions also follow when the neutrino mass matrix possesses residual antisymmetry instead of symmetry.

We review in the next section some of the properties of the group A_5 relevant for our study. We introduce the idea of flavor antisymmetry in Sec. III and discuss its consequences. Section IV is devoted to a detailed discussion of various mixing patterns possible within the group A_5 under the assumption of flavor antisymmetry. Section V discusses the explicit realization of the ideas discussed in the previous section. The last section summarizes the findings.

II. A_5 AND ITS ABELIAN SUBGROUPS

The group theory of A_5 is discussed in several papers [17–20,25]. We summarize here the features which we require for a subsequent analysis. The A_5 group has 60 elements and five conjugacy classes. The group can be represented in terms of three generators E , f_1 , and H :

$$\begin{aligned} H &= 1/2 \begin{pmatrix} -1 & \mu_- & \mu_+ \\ \mu_- & \mu_+ & -1 \\ \mu_+ & -1 & \mu_- \end{pmatrix}, \\ E &= \begin{pmatrix} 0 & 1 & 0 \\ 0 & 0 & 1 \\ 1 & 0 & 0 \end{pmatrix}, \\ f_1 &= \begin{pmatrix} 1 & 0 & 0 \\ 0 & -1 & 0 \\ 0 & 0 & -1 \end{pmatrix}, \end{aligned} \quad (2)$$

respectively, with $\mu_\pm = 1/2(-1 \pm \sqrt{5})$ which provide a faithful three-dimensional irreducible representation. The above equation defines the basis of the representation labeled as 3_1 , and we will refer to this basis as the

symmetry basis. Multiple products of these generate all 60 elements of A_5 . It is convenient for our purpose to discuss these elements in terms of the Z_n subgroups they form. We list them and their required properties below.

- (i) \mathcal{Z}_2 .—The 15 Z_2 subgroups of A_5 are generated by the elements

$$\begin{aligned} O_2 \equiv & (f_a, H, f_a H f_a, E H E^{-1}, E^{-1} H E, E f_a H f_a E^{-1}, \\ & E^{-1} f_a H f_a E), \end{aligned} \quad (3)$$

where $a = 1, 2, 3$, $f_2 = E^2 f_1 E$, $f_3 = E^2 f_2 E$, and f_1 is given by Eq. (2). One also needs the matrices which diagonalize the elements in O_2 when Z_2 is used as a residual symmetry. These get determined by a matrix V_H which diagonalizes H . Let V_H be such a matrix, and then

$$V_H^\dagger H V_H = \text{diag}(1, -1, -1). \quad (4)$$

Explicitly,

$$V_H = \begin{pmatrix} \frac{1}{2} & -\frac{\sqrt{3}}{2} & 0 \\ \frac{\mu_-}{2} & \frac{\mu_-}{2\sqrt{3}} & \frac{\mu_+}{\sqrt{3}} \\ \frac{\mu_+}{2} & \frac{\mu_+}{2\sqrt{3}} & -\frac{\mu_-}{\sqrt{3}} \end{pmatrix}. \quad (5)$$

The above V_H is arbitrary up to a unitary rotation in the 23 plane. We shall use the above explicit form for the subsequent analysis. We can express all the elements of A_5 in the form QPQ^{-1} . This simplifies their diagonalization, since $U_{QPQ^{-1}} = QU_P$, where U_g diagonalizes the element g . Using this, the matrices diagonalizing all 15 elements in O_2 can be expressed in terms of V_H and are given by the following set:

$$\mathcal{U}_2 \equiv (I, V_H, f_a V_H, E V_H, E^{-1} V_H, E f_a V_H, E^{-1} f_a V_H). \quad (6)$$

The respective entries of this set correspond to matrices which diagonalize the corresponding elements of O_2 .

- (ii) $\mathcal{Z}_2 \times \mathcal{Z}_2$.—Not all 15 elements in O_2 commute among themselves. But one can find five sets of three commuting elements among O_2 . These three along with the identity form a $Z_2 \times Z_2$ subgroup of A_5 . These subgroups are listed in Table I. Since S_1 and S_2 in the table commute, they can be simultaneously diagonalized by a matrix U_c . We shall define U_c as

$$\begin{aligned} U_c^\dagger S_1 U_c &= f_1 = \text{diag}(1, -1, -1), \\ U_c^\dagger S_2 U_c &= f_3 = \text{diag}(-1, -1, 1). \end{aligned} \quad (7)$$

TABLE I. Elements of the five $Z_2 \times Z_2$ subgroups of A_5 along with their combined diagonalizing matrices U_c defined in the text. S_1 , S_2 , and S_3 together with the identity form a $Z_2 \times Z_2$ subgroup of A_5 .

S_1	S_2	S_3	U_c
f_1	f_3	f_2	I
H	$E^{-1}f_2Hf_2E$	$Ef_3Hf_3E^{-1}$	$V_H R_\mu$
f_1Hf_1	$E^{-1}f_1Hf_1E$	$Ef_1Hf_1E^{-1}$	$f_1V_H R_\mu$
f_2Hf_2	$E^{-1}f_3Hf_3E$	EHE^{-1}	$f_2V_H R_\mu$
f_3Hf_3	$E^{-1}HE$	$Ef_2Hf_2E^{-1}$	$f_3V_H R_\mu$

The same matrix U_c also puts $S_3 = S_1S_2$ into a diagonal form f_2 . As before, the matrix U_c can also be expressed in terms of V_H diagonalizing H and a real rotation R_μ in the 23 plane:

$$R_\mu = \begin{pmatrix} 1 & 0 & 0 \\ 0 & -\sin\theta_\mu & \cos\theta_\mu \\ 0 & \cos\theta_\mu & \sin\theta_\mu \end{pmatrix}, \quad (8)$$

where

$$\tan\theta_\mu = \mu_- - 1.$$

U_c for all five subgroups are given in Table I.

- (iii) Z_3 subgroups.—The 20 elements generating Z_3 subgroups of A_5 are given by the set

$$O_3 = (E^m, f_a E^m f_a, A^m, EA^m E^{-1}, E^{-1}A^m E, AE^m A^{-1}, Af_{2,3} E^m f_{2,3} A^{-1}). \quad (9)$$

$m = 1, 2, a = 1, 2, 3$, and the matrix $A \equiv Hf_1$. The matrices diagonalizing these elements can be expressed in terms of the matrices U_ω and U_A which diagonalize E and A , respectively:

$$U_3 = (U_\omega, f_a U_\omega, U_A, EU_A, E^{-1}U_A, AU_\omega, Af_{2,3}U_\omega). \quad (10)$$

U_ω is given by

$$U_\omega = \frac{1}{\sqrt{3}} \begin{pmatrix} 1 & 1 & 1 \\ 1 & \omega & \omega^2 \\ 1 & \omega^2 & \omega \end{pmatrix}, \quad (11)$$

$\omega = e^{\frac{2\pi i}{3}}$ and U_A can be found in the Appendix of Ref. [24].

- (iv) Z_5 subgroups.—There are 24 different Z_5 subgroups within A_5 . Their generating elements can be expressed in terms of $T \equiv f_1EH$, E , and $f_{1,2,3}$ as follows:

$$O_5 = (T^p, f_2 T^p f_2, ET^p E^{-1}, E^{-1}T^p E, Ef_2 T^p f_2 E^{-1}, E^{-1}f_2 T^p f_2 E), \quad (12)$$

where $p = 1, 2, 3, 4$. This set is diagonalized by

$$U_5 = (U_T, f_2 U_T, EU_T, E^{-1}U_T, Ef_2 U_T, E^{-1}f_2 U_T), \quad (13)$$

where U_T is a matrix diagonalizing T . Its explicit form is given in the Appendix of Ref. [24].

The elements in the sets $O_{2,3,5}$ along with the identity constitute all 60 elements of A_5 . We note that all the matrices diagonalizing the set O_3 and O_5 possess the following general form as explicitly shown in Ref. [24]:

$$U = \begin{pmatrix} x_1 & z_1 & z_1^* \\ x_2 & z_2 & z_2^* \\ x_3 & z_3 & z_3^* \end{pmatrix}, \quad (14)$$

where x_1, x_2 , and x_3 are real. We shall use this form to derive the properties of the mixing matrix in the following.

III. FLAVOR ANTISYMMETRY AND NEUTRINO MASS TEXTURES

We first briefly review the implications of the assumption of flavor antisymmetry [15] represented by Eq. (1), where S_ν is assumed to be any 3×3 matrix belonging to a discrete subgroup of $SU(3)$. The very assumption of flavor antisymmetry implies that (at least) one of the neutrinos remains massless. This simply follows by taking the determinant of Eq. (1) and noting that $\text{Det}(S_\nu) = 1$. Other implications of Eq. (1) become clear in a basis with diagonal S_ν . Let S_ν be diagonalized by a unitary matrix V_{S_ν} as

$$V_{S_\nu}^\dagger S_\nu V_{S_\nu} = D_S \equiv \text{diag}(\lambda_1, \lambda_2, \lambda_3), \quad (15)$$

with $\lambda_1 \lambda_2 \lambda_3 = 1$. The unitarity of S_ν implies that $\lambda_{1,2,3}$ are some roots of unity. It was argued [15] that only two possible forms of D_S can lead to a neutrino mass matrix with two massive neutrinos. These are given by

$$\begin{aligned} D_{1S} &= \text{diag}(\lambda, -\lambda^*, -1), \\ D_{2S} &= \text{diag}(\pm i, \mp i, 1), \end{aligned} \quad (16)$$

and their permutations. $\lambda^{2p} = 1$ for some integer p .² The group generated by the residual symmetry S_ν having the diagonal form D_{1S} (D_{2S}) is Z_{2p} (Z_4). Define

²Note that Eq. (1) requires that $S_\nu^{2p} = 1$ if M_ν is not identically zero and S_ν has finite order. This translates to $\lambda^{2p} = 1$.

$$\tilde{M}_\nu = V_{S_\nu}^T M_\nu V_{S_\nu}. \quad (17)$$

Then the allowed textures of \tilde{M}_ν get determined by the allowed forms of D_S . There exist only four allowed textures for \tilde{M}_ν which correspond to one massless and a degenerate or nondegenerate pair of neutrinos. If $\lambda = 1$, then the relevant texture is given by

$$\tilde{M}_\nu = m_0 \begin{pmatrix} 0 & c_\nu & s_\nu e^{i\beta_\nu} \\ c_\nu & 0 & 0 \\ s_\nu e^{i\beta_\nu} & 0 & 0 \end{pmatrix}, \quad (18)$$

where $c_\nu = \cos \theta_\nu$ and $s_\nu = \sin \theta_\nu$. \tilde{M}_ν describes a massless and a degenerate pair of neutrinos. Three other textures are possible for other values of λ , but as we shall see only the case given in Eq. (18) can get realized in A_5 .

A. The allowed residual symmetries in A_5

We now discuss the possible residual symmetries of the leptonic mass matrices within A_5 and the resulting mixing patterns. The choices of residual antisymmetry of M_ν within A_5 are restricted. These can be obtained simply from the characters χ of all 60 elements. χ is real for all the elements. In this case, the eigenvalues of any element are given by

$$\left(1, \frac{1}{2} \left(\chi - 1 + \sqrt{(\chi - 1)^2 - 4} \right), \frac{1}{2} \left(\chi - 1 - \sqrt{(\chi - 1)^2 - 4} \right) \right). \quad (19)$$

These eigenvalues must have the form displayed in one of the two equations given in (16) in order for an element with character χ to be able to be a viable antisymmetry operator. Elements belonging to the Z_3 and Z_5 subgroups have $\chi = 0$ and $(-\mu_+, -\mu_-)$. Their eigenvalues following from above do not have these forms. Thus, the only viable choice for the antisymmetry operator S_ν can be any element in the set O_2 having character -1 and eigenvalues $(1, -1, -1)$. We shall require that at least one of the symmetries of M_ν acts according to Eq. (1). We will thus consider two possible choices of the residual neutrino symmetries: (i) $S_\nu = Z_2$ as the antisymmetry and (ii) $S_\nu = Z_2 \times Z_2$, where one of the Z_2 transforms M_ν into its negative and the other leaves it invariant. In contrast, the eigenvalues of the residual symmetry of $M_l M_l^\dagger$ are not restricted, and we can take any of the Z_n of A_5 as the residual symmetry T_l . We shall consider the following choices for T_l : (a) (Z_3, Z_5) groups generated by (O_3, O_5) , (b) five $Z_2 \times Z_2$ subgroups, or (c) elements of the Z_2 subgroups contained in O_2 . The possible choices of S_ν and T_l determine the leptonic mixing matrix.

Elements in O_2 when used as the antisymmetry operator lead to a unique form for the neutrino mass matrix \tilde{M}_ν given

in Eq. (18). This texture describes a pair of degenerate and one massless neutrino. Residual antisymmetry in this case is Z_2 . The neutrino mass matrix in Eq. (18) can be diagonalized by a matrix V_ν :

$$V_\nu^T \tilde{M}_\nu V_\nu = \text{diag}(m_0, m_0, 0), \quad (20)$$

where

$$V_\nu = \begin{pmatrix} \frac{1}{\sqrt{2}} & -\frac{i}{\sqrt{2}} & 0 \\ \frac{c_\nu}{\sqrt{2}} & \frac{ic_\nu}{\sqrt{2}} & -s_\nu \\ \frac{s_\nu}{\sqrt{2}} e^{-i\beta_\nu} & \frac{is_\nu}{\sqrt{2}} e^{-i\beta_\nu} & c_\nu e^{-i\beta_\nu} \end{pmatrix} \begin{pmatrix} \cos \psi & -\sin \psi & 0 \\ \sin \psi & \cos \psi & 0 \\ 0 & 0 & 1 \end{pmatrix}. \quad (21)$$

The arbitrary rotation by an angle ψ originates due to degeneracy in the masses. It follows from Eqs. (17) and (20) that the matrix M_ν is diagonalized by the product $V_{S_\nu} V_\nu$. Thus, the neutrino mixing matrix with the residual antisymmetry Z_2 in the symmetry basis is given by

$$U_\nu^I = V_{S_\nu} V_\nu. \quad (22)$$

Note that the U_ν^I gets determined by the structure of S_ν and essentially two unknown angles θ_ν and β_ν . The unknowns can be fixed if the residual symmetry is chosen as $Z_2 \times Z_2$. Consider the $Z_2 \times Z_2$ groups generated by $S_{1\nu} = S_1$ and $S_{2\nu} = S_2$, where S_1 and S_2 are as in Table I. They satisfy, respectively,

$$S_1^T M_\nu S_1 = -M_\nu, \quad S_2^T M_\nu S_2 = M_\nu. \quad (23)$$

As discussed in the previous section, both S_1 and S_2 are diagonalized by U_c as given in Table I. The structure of the neutrino mass matrix in this case becomes transparent in the basis with diagonal S_1, S_2 . Let

$$M'_\nu = U_c^T M_\nu U_c. \quad (24)$$

Equation (23) reduces in the prime basis to

$$f_1^T M'_\nu f_1 = -M'_\nu, \quad f_3^T M'_\nu f_3 = M'_\nu. \quad (25)$$

The first of these equations implies the form (18) for M'_ν . The second imposed on this then leads to the restriction $s_\nu = 0$ and $c_\nu = 1$. The final M'_ν is determined by an overall scale m_0 and is diagonalized by $U_{12} \equiv R_{12}(\frac{\pi}{4}) \text{diag}(1, i, 1)$. It follows from this and Eq. (24) that M_ν is diagonalized by

$$U_\nu^{II} = U_c U_{12} = U_c R_{12} \left(\frac{\pi}{4} \right) \text{diag}(1, i, 1). \quad (26)$$

The matrix U_l diagonalizing $M_l M_l^\dagger$ also gets determined by its symmetry. Assume that

$$T_l^\dagger M_l M_l^\dagger T_l = M_l M_l^\dagger. \quad (27)$$

This implies that T_l commutes with $M_l M_l^\dagger$. Hence, the matrix U_{T_l} diagonalizing T_l can be taken to be the matrix which diagonalizes $M_l M_l^\dagger$ also. The three possible choices of T_l referred as (a), (b), and (c) above lead to specific forms of U_l :

$$\begin{aligned} U_l^a &= U_{3,5}, \\ U_l^b &= U_c, \\ U_l^c &= U_2 U_{23}. \end{aligned} \quad (28)$$

Here, $U_{3,5}$ are given by any matrix in the set \mathcal{U}_3 [Eq. (10)] and \mathcal{U}_5 [Eq. (13)] when T_l belongs to O_3 or O_5 , respectively. U_c is given in Table I for T_l belonging to $Z_2 \times Z_2$. There is some arbitrariness in the choice of U_l when T_l is chosen as any of the elements O_2 forming a Z_2 . These elements have eigenvalues $(1, -1, -1)$, and the matrix diagonalizing T_l is arbitrary up to a unitary rotation in the 23 plane. This rotation can be taken without the loss of generality to $U_{23} \equiv \text{diag}(1, 1, e^{i\theta_l}) R_{23}(\theta_l)$. Various combinations of $U_l^{a,b,c}$ and $U_\nu^{I,II}$ give all possible $U \equiv U_l^\dagger U_\nu$ in A_5 .

IV. MIXING PATTERNS IN A_5

As discussed, all possible structures of the Pontecorvo-Maki-Nakagawa-Sakata (PMNS) matrix U in A_5 with flavor antisymmetry are given by

$$U \sim U_l^{\dagger a,b,c} U_\nu^{I,II}. \quad (29)$$

Not all of these give a viable mixing pattern for neutrinos, as we will show. Before discussing individual choices, we first derive a fairly general property of the mixing matrix with flavor antisymmetry. If (a) the neutrino mass matrix shows flavor antisymmetry [Eq. (1)], with $S_\nu^2 = 1$ and a real mixing matrix V_ν , or (b) if it has residual symmetry structure $Z_2 \times Z_2$ as in Eq. (23) and if the charged lepton matrix $M_l M_l^\dagger$ is invariant under a residual symmetry Z_3 or Z_5 within A_5 , then the mixing matrix can be chosen to have the property

$$|U_{\mu i}| = |U_{\tau i}|, \quad (i = 1, 2, 3). \quad (30)$$

This property known as the μ - τ reflection symmetry [26] or generalized μ - τ symmetry was derived [27] using a generalized definition of CP . The same result was derived from more general assumptions in the case of nondegenerate neutrinos [24,28] as well as for a pair of degenerate neutrinos [10,24]. The basic assumption in these cases was the existence of a real residual symmetry. The same result also follows when the symmetry is replaced by antisymmetry as we discuss below.

The equality $|U_{\mu 3}| = |U_{\tau 3}|$ implies the maximal atmospheric mixing angle. The equality $|U_{\mu 2}| = |U_{\tau 2}|$ then leads to the maximal CP phase $|\delta| = \frac{\pi}{2}$ if the neutrinos are nondegenerate and $s_{13} \neq 0$. For the degenerate solar pair, the first two columns of U depend on an unknown mixing angle ψ as given in Eq. (21). But by considering a ψ -invariant combination of the observables, it was argued [10] that one instead gets $|\delta - \kappa| = \frac{\pi}{2}$, where κ is the Majorana phase.

The proof of Eq. (30) is straightforward and follows the proof given in Ref. [24] in the case of flavor symmetry. Assume that neutrino mass matrix \hat{M}_ν has the structure (18) with $\beta_\nu = 0$. Then it is diagonalized by $U_\nu^I = U_2 V_\nu$. Here U_2 belonging to the set \mathcal{U}_2 is real. For $\beta_\nu = 0$, one therefore gets $U_\nu^I = O_\nu P$, with O_ν being a real orthogonal matrix and $P = \text{diag}(1, i, 1)$. A similar structure of U_ν also holds in case II with $Z_2 \times Z_2$ symmetry, since in this case the neutrino mixing matrix U_ν is given by U_ν^{II} [Eq. (26)], which also can be written as an orthogonal matrix times a phase matrix because of the reality of U_c . The charged lepton mixing matrix, on the other hand, has a general structure specified by Eq. (14) when the residual charge lepton symmetry is either Z_3 or Z_5 . It is then easy to see that U_l as in Eq. (14) and U_ν as O_ν times a diagonal phase matrix lead to Eq. (30). This result does not follow when the residual symmetry of the charged leptons is Z_2 or $Z_2 \times Z_2$, since in this case U_l does not have the form given in Eq. (14).

Let us now discuss individual choices of residual symmetries and their viability or otherwise. We will work out various mixing patterns for various choices and confront them with the results of the global fits as given in Refs. [29–31]. For definiteness, we shall use the results given in Ref. [31]. The structures of $U^{I,II}$ appearing in Eq. (29) are determined only up to a rotation in the 12 plane, and the solar angle remains undetermined at the leading order. The third column of U is, however, independent of the unknown angle and can be predicted group theoretically at the zeroth order. We shall thus concentrate on the prediction of θ_{13} and θ_{23} determined by the third column of $|U|$. Also, the ordering of eigenvalues of T_l cannot be determined group theoretically. A change in this ordering permutes the rows of U . Thus, any of the entries of the third column $|U_{i3}|$ may be identified with the physical mixing elements $|U_{\alpha 3}|$ ($\alpha = e, \mu, \tau$). In view of this, we shall consider different orderings which can give viable mixing patterns.

A. $S_\nu = Z_2$ and $T_l = Z_3$ or Z_5

There are 15 different choices of Z_2 and $20 + 24$ choices of the $Z_3 + Z_5$ symmetry within A_5 . Specific forms of U_l and U_ν as discussed before can be used to obtain $|U_{i3}|$ in all these cases. They are determined by the unknown angles θ_ν and β_ν . While the dependence of $|U_{i3}|$ on these is different

for different choices of residual symmetries, all the choices share the following features.

- (i) If $\beta_\nu = 0$, then Eq. (14) holds for the specific ordering of eigenvectors of T_l as given in Eq. (30). The atmospheric mixing angle is predicted to be maximal for all the values of θ_ν . In this case, $|U_{e3}|$ is to be identified with the 13 element of $|U|$, since $|U_{23}| = |U_{33}|$. In all these cases, $|U_{e3}|$ depends on θ_ν , which can be chosen to obtain the correct s_{13}^2 .
- (ii) If $\beta_\nu \neq 0$, then any of $|U_{i3}|$ can be identified with $|U_{e3}|$. It is possible in this case to choose two unknowns θ_ν and β_ν to obtain the correct θ_{13} and θ_{23} . Let us discuss a specific example with $S_\nu = E^2 f_1 H f_1 E$ and $T_l = E$ as an illustration. They, respectively, generate Z_2 antisymmetry in M_ν and Z_3 symmetry in $M_l M_l^\dagger$. The mixing matrix is given by $U = U_\omega^\dagger E^2 f_1 V_H V_\nu$ with V_H as in Eq. (5) and U_ω as in (11). The third column of the mixing matrix is then given by

$$\begin{aligned} |U_{13}|^2 &= \frac{1}{9} |c_\nu(1 + 2\mu_+) - s_\nu e^{i\beta_\nu}|^2, \\ |U_{23}|^2 &= \frac{1}{36} |-2c_\nu(1 - \omega\mu_+) \\ &\quad + s_\nu e^{i\beta_\nu}(\mu_+ + 3\omega + \omega^2\mu_-)|^2, \\ |U_{33}|^2 &= \frac{1}{36} |-2c_\nu(1 - \omega^2\mu_+) \\ &\quad + s_\nu e^{i\beta_\nu}(\mu_+ + 3\omega^2 + \omega\mu_-)|^2. \end{aligned} \quad (31)$$

For $\beta_\nu = 0$, one gets $|U_{23}|^2 = |U_{33}|^2$ in accordance with the general result discussed above. In this case, the identification of $|U_{13}|^2$ with $|U_{e3}|^2$ leads to the result $\theta_{23} = \frac{\pi}{4}$. $\theta_\nu = 0.959$ then leads to $s_{13}^2 \sim 0.024$. Any of $|U_{i3}|^2$ can be identified with $|U_{e3}|^2$ when β_ν is nonzero; e.g., the choice $\beta_\nu = -1.076$ and $\theta_\nu = -0.801$ leads to $|U_{i3}|^2 = (0.444, 0.024, 0.532)$. In this case, $|U_{23}|^2$ plays the role of $|U_{e3}|^2$. This specific ordering in U can be obtained by exchanging the first and the second column of U_ω .

B. $S_\nu = Z_2 \times Z_2$ and $T_l = Z_3$ or Z_5

In this case, S_ν can be chosen in five different ways corresponding to five different $Z_2 \times Z_2$ subgroups. The corresponding neutrino mixing matrix U_ν is given by Eq. (26). As before, T_l can be chosen in 44 different ways with U_l in either \mathcal{U}_3 or \mathcal{U}_5 . Unlike in the previous case, both U_ν and U_l get completely fixed group theoretically. This case also predicts the maximal atmospheric mixing angle as already outlined. Possible values of θ_{13} are also fixed. An explicit evaluation of various cases reveals that in all the cases one gets either $\theta_{13} = 0$ or $s_{13}^2 > 0.1$. The zero value for θ_{13} occurs, for example, when $S_1 = H$, $S_2 = E^2 f_2 H f_2 E$, and $T_l = f_3 E f_3$. One would require

relatively large perturbations in this case to get θ_{13} within its 3σ range.

C. $S_\nu = Z_2 \times Z_2$ and $T_l = Z_2$

This case is characterized by completely determined $U_\nu = U_\nu^{II}$ and $U_l = U_l^c$ containing two unknowns θ_l and β_l . The explicit form of U_l^c is given in Eq. (28), while U_c can be any of the five forms given in Table I. U_l in this case does not have the general form given in Eq. (14). As a result, one does not obtain Eq. (30) corresponding to the μ - τ reflection symmetry, and the atmospheric mixing angle is not predicted to be maximal. But this case has the following interesting feature. An explicit evaluation of $U = U_l^{c\dagger} U_\nu^{II}$ reveals that one of the entries in the third column of U is independent of the unknown angles θ_l and β_l and can be predicted group theoretically. The third column of the mixing matrix U in this case is given by

$$\begin{aligned} |U_{13}|^2 &= |(U_{T_l}^\dagger U_\nu^{II})_{13}|^2, \\ |U_{23}|^2 &= |c_l (U_{T_l}^\dagger U_\nu^{II})_{23} + s_l e^{-i\beta_l} (U_{T_l}^\dagger U_\nu^{II})_{33}|^2, \\ |U_{33}|^2 &= |-s_l (U_{T_l}^\dagger U_\nu^{II})_{23} + c_l e^{-i\beta_l} (U_{T_l}^\dagger U_\nu^{II})_{33}|^2, \end{aligned} \quad (32)$$

where T_l belongs to the set \mathcal{O}_2 and U_{T_l} to \mathcal{U}_2 . We get an interesting pattern when we identify T_l with $S_{1\nu} = S_1$ residing in $Z_2 \times Z_2$. There exist five such choices, and, in all these cases, the mixing matrix U is independent of the explicit form of U_{T_l} . One gets from Eqs. (26) and (28)

$$U = U_{23}^\dagger R_\mu R_{12} \left(\frac{\pi}{4} \right) \text{diag}(1, i, 1).$$

The neutrino mass matrix $M_{\nu f} \equiv U_l^T M_\nu U_l$ in the flavor basis has the following form in this case:

$$M_{\nu f} = m_0 \begin{pmatrix} 0 & e^{i\beta_l} c_\mu s_l - c_l s_\mu & e^{i\beta_l} c_l c_\mu + s_l s_\mu \\ e^{i\beta_l} c_\mu s_l - c_l s_\mu & 0 & 0 \\ e^{i\beta_l} c_l c_\mu + s_l s_\mu & 0 & 0 \end{pmatrix}, \quad (33)$$

where $c_l = \cos \theta_l$, $c_\mu = \cos \theta_\mu$, etc. This form can be obtained by imposing $L_e - L_\mu - L_\tau$ symmetry on $M_{\nu f}$ as has been done in the past. Here, this symmetry arises as an effective symmetry of $M_{\nu f}$ from a very different set of basic symmetries. This symmetry leads to a degenerate pair of neutrinos and vanishing θ_{13} . The atmospheric mixing angle is determined as $\sin^2 \theta_{23} = |e^{i\beta_l} c_l c_\mu + s_l s_\mu|^2$. Perturbations to this symmetry have been studied in the past [32–34]. It is possible to simultaneously generate the correct solar scale, solar angle, and θ_{13} with suitable but relatively large perturbations. Consider perturbing the zero entries in Eq. (33) by

$$\delta M_{\nu f} = m_0 \begin{pmatrix} \epsilon_1 & 0 & 0 \\ 0 & \epsilon_2 & \epsilon_4 \\ 0 & \epsilon_4 & \epsilon_3 \end{pmatrix}. \quad (34)$$

Parameters $|\epsilon|$ are assumed less than the dominant entry of $M_{\nu f}$. We give here one example of perturbations which reproduces the observed spectrum within 3σ :

$$\{\epsilon_1, \epsilon_2, \epsilon_3, \epsilon_4\} = \{-0.284497, 0.284497, -0.0748816, 0.182915\} \quad (35)$$

leading to

$$\left\{ \frac{\Delta m_{\text{sol}}^2}{\Delta m_{\text{atm}}^2}, s_{12}^2, s_{13}^2, s_{23}^2 \right\} = \{0.0339706, 0.358739, 0.0243674, 0.443736\}. \quad (36)$$

We have taken $\beta_l = 0$ and $\cos(\theta_l - \theta_\mu) \approx -0.69$. The values of parameters required to get the above values are quite large, and the solar angle is also near to its 3σ limit. We have verified by randomly varying the parameters over a large range that this is a general feature of this case. A relatively large perturbation to the basic symmetry may come from some soft breaking as discussed, for example, in Ref. [34].

We get a nonzero $|U_{13}|^2$ when T_l is not identified with S_1 . One could determine these values for different choices of T_l . The predicted $|U_{13}|^2$ is found from the explicit evaluation of various cases to take one of the three values (0.095, 0.25, 0.65). Of these, only the last value provides a good leading-order prediction. $|U_{13}|^2 \sim 0.65$ can be identified in this case with either $|U_{\mu 3}|^2$ or $|U_{\tau 3}|^2$, as this gives s_{23}^2 close to its 3σ range 0.38–0.64 [31]. This amounts to a reordering of the eigenvectors of T_l . An example of this choice is provided by $S_1 = f_3 H f_3$, $S_2 = E^{-1} H E$, and $T_l = f_1 H f_1$. $|U_{i3}|^2$ are given in this case by

$$\begin{aligned} |U_{13}|^2 &= \frac{1}{4}(2 + \mu_+) \approx 0.654, \\ |U_{23}|^2 &= \frac{|\mu_+ c_l + 2(1 + \mu_+) s_l e^{-i\beta_l}|^2}{12(2 + \mu_+)}, \\ |U_{33}|^2 &= \frac{|-\mu_+ s_l + 2(1 + \mu_+) c_l e^{-i\beta_l}|^2}{12(2 + \mu_+)}. \end{aligned} \quad (37)$$

One could identify either the second or the third entry with s_{13}^2 and determine θ_l accordingly; e.g., $\theta_l \sim 1.6488$ and $\beta_l = 0$ lead to $s_{13}^2 \equiv |U_{33}|^2 \sim 0.024$ giving $s_{23}^2 c_{13}^2 \equiv |U_{13}|^2 \sim 0.654$. The resulting $\sin^2 \theta_{23}$ is given by 0.67. A small perturbation to this case can lead to θ_{23} within the 3σ range and also split the degeneracy.

D. $S_\nu = Z_2$ and $T_l = Z_2 \times Z_2$

In this case, the Z_2 can be generated by any of the 15 elements in O_2 , while T_l is generated by $T_{1l} \equiv S_1$ and $T_{2l} \equiv S_2$, where S_1 and S_2 form any of the five $Z_2 \times Z_2$ subgroups listed in Table I. The PMNS matrix in this case is given by $U = U_1^{b\dagger} U_{S_\nu} V_\nu$. Just as in the previous case, the atmospheric mixing angle is not predicted to be maximal, but now, unlike it, both the angles s_{13}^2 and s_{23}^2 depend on the unknown parameters θ_ν and β_ν . Not all the choices of the residual symmetries lead to viable values of θ_{13} and θ_{23} in spite of the presence of the two unknowns. We determine the allowed patterns by fitting θ_ν and β_ν to the observed values of θ_{13} and θ_{23} . This allows us to identify cases which provide viable patterns of the mixing angles. One finds essentially three patterns this way. Examples of the residual symmetries, the patterns, and best fit values of θ_ν and β_ν in each of these cases are listed below:

$$\begin{aligned} S_\nu = f_3 H f_3: \theta_\nu &= 1.42417, & \beta_\nu &= 1.84521, \\ & s_{13}^2 = 0.024, & s_{23}^2 &= 0.455, \\ S_\nu = f_2 H f_2: \theta_\nu &= -0.487, & \beta_\nu &= 0, \\ & s_{13}^2 = 0.0244, & s_{23}^2 &= 0.676, \\ S_\nu = H: \theta_\nu &= -0.6716, & \beta_\nu &= -1.1620, \\ & s_{13}^2 = 0, & s_{23}^2 &= 0.455. \end{aligned} \quad (38)$$

All the above cases occur for the choice $T_{1l} = H$ and $T_{2l} = E^{-1} f_2 H f_2 E$. Similar results follow for different choices of $Z_2 \times Z_2$ as T_l but with alternative choices of S_ν . The first case given above reproduces the observed values of the mixing angles θ_{13} and θ_{23} . The second choice gives a θ_{23} on the verge of its 3σ value but correct s_{13}^2 . Thus, a small perturbation to this case can lead to a viable pattern. The third choice corresponding to $s_{13}^2 = 0$ would need significant corrections from the perturbations and is analogous to the case already discussed in Sec. IV C.

E. $S_\nu = Z_2 \times Z_2$ and $T_l = Z_2 \times Z_2$

In this case, the residual symmetries of neutrinos and the charged leptons correspond to (different) $Z_2 \times Z_2$ groups. Because of the presence of two Z_2 groups, there are no undetermined parameters and the mixing angles θ_{13} , θ_{23} get predicted group theoretically. Since we have five different $Z_2 \times Z_2$ subgroups, there are 20 different choices which would lead to a nontrivial mixing matrix U . None of these correspond to even good zeroth-order values. The predicted third column of $|U|^2$ in all these cases is

$$|U_{i3}|^2 = \begin{pmatrix} 0.0954915 \\ 0.25 \\ 0.654508 \end{pmatrix} \quad (39)$$

and its permutations. These predictions are quite far from the observed mixing angles.

V. EXPLICIT REALIZATION WITH $A_5 \times Z_3$ SYMMETRY

We now discuss a realization of the above group theoretical discussion choosing specific examples of S_ν and T_l . We discuss the necessary Higgs fields and vacuum structure needed to implement the above symmetries. The model presented here is very similar to the one presented in Ref. [24], the main difference being that the neutrino symmetry considered in this reference is replaced by neutrino antisymmetry. The implementation of antisymmetry needs the imposition of an additional discrete symmetry, which we choose as Z_3 . We use supersymmetry as a basic ingredient.

Irreducible representations (IR) of A_5 are $1 + 3_1 + 3_2 + 4 + 5$, where 3_1 and 3_2 are nonequivalent IR. We assign l_L , l^c to 3_1 , which is explicitly generated by E, H , and f_1 given in Eq. (2). It follows from the product rule

$$3_1 \times 3_1 = (1 + 5)_{\text{symm}} + 3_{\text{antisym}}$$

that the symmetric neutrino mass matrix can arise from $1 + 5$ and the charged lepton masses can arise from all three IR. The neutrino masses are generated from a 5-plet $\eta_{5\nu}$ of a flavon. The various fields transform under Z_3 as

$$(l_L, \eta_\nu) \rightarrow \omega(l_L, \eta_{5\nu}), \quad l^c \rightarrow \omega^2 l^c.$$

The standard Higgs fields H_u and H_d and Higgs triplet Δ are singlets of $A_5 \times Z_3$.

The neutrino masses are generated from the following superpotential using the type-II seesaw mechanism:

$$W_\nu = \frac{1}{2\Lambda} (l_L \Delta l_L)_5 h_{5\nu} \eta_{5\nu}. \quad (40)$$

Note that the singlet term $(l_L \Delta l_L)_1$ allowed by A_5 is prevented above due to the Z_3 symmetry. The charged lepton masses are generated by three additional flavons, a singlet η_{1l} , a 5-plet η_{5l} , and a 3-plet η_{3l} all transforming trivially under Z_3 . The relevant superpotential is

$$W_l = \frac{1}{\Lambda} [h_{sl}(l_L H_d l^c)_1 \eta_{1l} + h_{5l}(l_L H_d l^c)_5 \eta_{5l} + h_{3l}(l_L H_d l^c)_3 \eta_{3l}]. \quad (41)$$

The Z_3 symmetry separates the neutrino and the charged lepton sectors and does not allow flavons of one sector to couple to the other sector at the leading order.

We specialize to a particular choice of symmetries already discussed in Sec. IV A. This corresponds to $T_l = E$ and $S_\nu = E^2 f_1 H f_1 E$. The above S_ν can serve as an antisymmetry of the neutrino mass matrix if the 5-plet $\eta_{5\nu}$ has an antisymmetric vacuum expectation value:

$$S_\nu(5) \langle \eta \rangle_{5\nu} = -\langle \eta \rangle_{5\nu}. \quad (42)$$

$S_\nu(5)$ in Eq. (42) corresponds to the five-dimensional representation of S_ν . This representation can be obtained from the basic generators defined as a, b , and c in Ref. [20] by noting the correspondence $E = b, f_3 = a$, and $H = bc$. This leads to

$$S_\nu(5) = \begin{pmatrix} \frac{1}{2} & 0 & -\frac{1}{2} & \frac{1}{2\sqrt{2}} & \frac{\sqrt{3}}{2} \\ 0 & \frac{1}{2} & -\frac{1}{2} & -\frac{1}{\sqrt{2}} & 0 \\ -\frac{1}{2} & -\frac{1}{2} & 0 & -\frac{1}{2\sqrt{2}} & \frac{\sqrt{3}}{2} \\ \frac{1}{2\sqrt{2}} & -\frac{1}{\sqrt{2}} & -\frac{1}{2\sqrt{2}} & -\frac{1}{4} & -\frac{\sqrt{3}}{4} \\ \frac{\sqrt{3}}{2} & 0 & \frac{\sqrt{3}}{2} & -\frac{\sqrt{3}}{4} & \frac{1}{4} \end{pmatrix}. \quad (43)$$

The antisymmetry of $\langle \eta_{5\nu} \rangle$ together with A_5 symmetry in W_ν results in the flavor antisymmetric mass matrix. It is worth noting that, unlike in the case of symmetry, Eq. (42) breaks the symmetry S_ν completely and it does not remain as a residual symmetry. But, just as in the case with symmetry, a broken solution given in Eq. (42) may also arise from the minimization of a suitable superpotential but would need enlargement in the model. This is explicitly demonstrated [15] in a simpler case of the group A_4 .

Denoting the VEV $\langle \eta_{5\nu} \rangle$ as $(s_1, s_2, s_3, s_4, s_5)^T$, Eq. (42) is solved for

$$s_2 = s_3 - s_1, \quad s_4 = \sqrt{2}s_3 - \frac{3s_1}{\sqrt{2}}, \quad s_5 = -\sqrt{\frac{3}{2}}s_1. \quad (44)$$

Inserting this solution in Eq. (40), we get the neutrino mass matrix

$$M_\nu^0 = m_0 \begin{pmatrix} \frac{-3+\sqrt{5}+y(1-\sqrt{5})}{2\sqrt{2}} & \frac{1}{\sqrt{2}} & \frac{y}{\sqrt{2}} \\ \frac{1}{\sqrt{2}} & \frac{-2\sqrt{5}+y(1+\sqrt{5})}{2\sqrt{2}} & \frac{y-1}{\sqrt{2}} \\ \frac{y}{\sqrt{2}} & \frac{y-1}{\sqrt{2}} & \frac{3+\sqrt{5}-2y}{2\sqrt{2}} \end{pmatrix}, \quad (45)$$

which satisfies the flavor antisymmetry [Eq. (1)] with respect to $S_\nu = E^2 f_1 H f_1 E$. This matrix has only one complex parameter $y \equiv \frac{s_3}{s_1}$ apart from an overall scale. In particular, $\tilde{M}_\nu \equiv V_{S_\nu}^T M_\nu V_{S_\nu}$ has the form given in Eq. (18) with

$$\tan \theta_\nu e^{i\beta_\nu} = -\frac{1 + \mu_+ \frac{s_3}{s_1}}{(\mu_+ - \mu_-) + \mu_- \frac{s_3}{s_1}}, \quad (46)$$

where $V_{S_\nu} = E^2 f_1 V_H$ diagonalizes $S_\nu = E^2 f_1 H f_1 E$. The neutrino mixing matrix is then given by $U_\nu = E^2 f_1 V_H V_\nu$ with V_ν as given in Eq. (21) and θ_ν and β_ν given by Eq. (46) in terms of $\frac{s_3}{s_1}$. The charged lepton mixing matrix is analogously determined by the form of M_l obtained from W_l . W_l and the residual symmetry $T_l = E$ coincide with the one already discussed in Ref. [24]. The T_l -invariant vacuum configuration discussed in Ref. [24] leads to the following charged lepton mass matrix:

$$M_l = \begin{pmatrix} m_0 & m_1 - m_2 & m_1 + m_2 \\ m_1 + m_2 & m_0 & m_1 - m_2 \\ m_1 - m_2 & m_1 + m_2 & m_0 \end{pmatrix}, \quad (47)$$

where $m_{0,1,2}$, respectively, label the singlet, triplet, and 5-plet contributions to M_l . $M_l M_l^\dagger$ is diagonalized by the matrix (11) which also diagonalizes T_l :

$$U_\omega^\dagger M_l M_l^\dagger U_\omega = \text{diag}(m_1^2, m_2^2, m_3^2)$$

with eigenvalues

$$\begin{aligned} \lambda_1^2 &= m_0^2 + 4|m_1|^2 + 4m_{1R}m_0, \\ \lambda_2^2 &= m_0^2 + |m_1|^2 + 3|m_2|^2 + 2\sqrt{3}\text{Im}(m_1 m_2^*) \\ &\quad - 2m_0(m_{1R} + \sqrt{3}m_{2I}), \\ \lambda_3^2 &= m_0^2 + |m_1|^2 + 3|m_2|^2 - 2\sqrt{3}\text{Im}(m_1 m_2^*) \\ &\quad - 2m_0(m_{1R} - \sqrt{3}m_{2I}). \end{aligned} \quad (48)$$

Here, $m_{1R,2R}$ and $m_{1I,2I}$, respectively, denote the real and imaginary parts of $m_{1,2}$. m_0 is assumed real without loss of generality.

The identification of eigenvalues $\lambda_{1,2,3}^2$ with the physical charged lepton masses $m_{e,\mu,\tau}^2$ depends on the choice of parameters $m_{0,1,2}$. In particular, one can choose these parameters in a way that gives $\lambda_2^2 = m_e^2$, $\lambda_1^2 = m_\mu^2$, and $\lambda_3^2 = m_\tau^2$. With this identification,

$$U_l = \frac{1}{\sqrt{3}} \begin{pmatrix} 1 & 1 & 1 \\ \omega & 1 & \omega^2 \\ \omega^2 & 1 & \omega \end{pmatrix}. \quad (49)$$

This U_l together with $U_\nu = E^2 f_1 V_H V_\nu$ gives the mixing matrix U which is already worked out in Eq. (31). The above form of U_l leads to the identification $|U_{23}|^2 = s_{13}^2$ and $|U_{13}|^2 = c_{13}^2 s_{23}^2$. The values of θ_ν and β_ν giving the correct s_{13}^2 and s_{23}^2 were already determined in Sec. III. This translates to the following values of the model parameter $\frac{s_3}{s_1}$ when Eq. (46) is used:

$$\frac{s_3}{s_1} \approx 0.9979 e^{-0.7181i}. \quad (50)$$

Nonzero neutrino masses remain degenerate at the leading order. They can be split, and the solar angle can be determined by perturbations which break antisymmetry at the nonleading order. A simple perturbation can be generated by introducing a singlet flavon $\eta_{1\nu}$ transforming as $\eta_{1\nu} \rightarrow \omega^2 \eta_{1\nu}$ under Z_3 . This flavon leads to a nonleading term

$$\frac{h_{1\nu}}{2\Lambda^2} (I_l \Delta I_L)_1 \eta_{1\nu}^2$$

in W_ν . This generates a diagonal perturbation which can be parameterized as

$$M_\nu = m_0 (\hat{M}_\nu^0 + \epsilon I)$$

with $\hat{M}_\nu^0 \equiv \frac{M_\nu^0}{m_0}$ and $|\epsilon| \ll 1$. This simple perturbation is enough to generate the solar splitting without disturbing the zeroth-order values of s_{13}^2 and s_{23}^2 significantly. One could vary $\frac{s_3}{s_1}$ around the zeroth-order value determined in Eq. (50) and find the region of parameters which fits the data with $|\epsilon| < 0.1$. This procedure leads to a solution close to the best fit values of all parameters. For example, $\frac{s_3}{s_1} = 1.00019 e^{-0.711498i}$ and $\epsilon = 0.0168241$ lead to

$$\begin{aligned} \sin^2 \theta_{12} &= 0.295455, & \sin^2 \theta_{13} &= 0.0235172, \\ \sin^2 \theta_{23} &= 0.449634, & \frac{\Delta m_{\text{sol}}^2}{\Delta m_{\text{atm}}^2} &= 0.0285398. \end{aligned} \quad (51)$$

VI. SUMMARY

We have studied the consequences of an ansatz of flavor antisymmetry in the context of the flavor group A_5 assuming that S_ν in Eq. (1) and T_l in Eq. (27) are contained in the group A_5 . These assumptions constrain the mixing pattern which we have determined in various cases. The use of flavor antisymmetry in the context of the A_5 group necessarily leads to a degenerate pair of neutrinos in addition to a massless one. This is a good zeroth-order prediction. Small perturbations splitting the degeneracy can lead to viable neutrino masses. The predicted neutrino mass hierarchy is inverted.

We have considered discrete subgroups Z_2 and $Z_2 \times Z_2$ of A_5 as residual symmetries of M_ν and discrete groups Z_3 , Z_5 , Z_2 , and $Z_2 \times Z_2$ contained in A_5 as symmetries of $M_l M_l^\dagger$ and worked out the resulting mixing patterns at the leading order in all the cases. The third column of the mixing matrix and hence the angles θ_{13} and θ_{23} get determined at this order. Various predictions discussed in Sec. III can be summarized as follows:

- (i) It is possible to get a universal prediction of the maximal atmospheric mixing angle with the choice S_ν as Z_2 or $Z_2 \times Z_2$ and T_l as any element in Z_3 and Z_5 . For $S_\nu = Z_2$, one can also get the correct θ_{13} at the leading order, while the case of $S_\nu = Z_2 \times Z_2$ predicts either $\theta_{13} = 0$ or large $s_{13}^2 \geq 0.1$.
- (ii) The case $T_l = Z_2$ and $S_\nu = Z_2 \times Z_2$ does not predict maximal θ_{23} but can be used to predict one of the entries of the third column. The other entry gets determined by an unknown angle inherent to the use of the Z_2 groups. The viable predictions within this case are either $\theta_{13} = 0$ or $s_{23}^2 c_{13}^2 = 0.65$. The former requires a large perturbation, and we have presented a typical set of such perturbations which lead to the correct description of the masses and mixing angle.
- (iii) The case $S_\nu = Z_2$ and $T_l = Z_2 \times Z_2$ involves an unknown angle and a phase. Not all possible choices of S_ν and T_l in this category can lead to correct mixing in spite of the presence of two unknowns. We have identified cases which lead to the correct description of the mixing angles θ_{13} and θ_{23} .

- (iv) The case of both S_ν and T_l belonging to different $Z_2 \times Z_2$ subgroups of A_5 is fully predictive without any unknowns. But none of the possible cases within this category lead even to a good zeroth-order prediction.

We have supplemented the group theoretical derivation of the mixing patterns in A_5 with a concrete example. We have determined the Higgs content and the required vacuum pattern which realizes one of the viable cases discussed group theoretically. The use of a concrete model also allows a systematic discussion of possible perturbations, and we have given an example of a perturbation within the model which can be used to split the degeneracy of neutrinos and which can give the correct descriptions of all mixing angles and masses.

ACKNOWLEDGMENTS

The work of A. S. J. was supported by BRNS (DAE) through the Raja Ramanna Fellowship.

-
- [1] G. Altarelli and F. Feruglio, *Rev. Mod. Phys.* **82**, 2701 (2010).
 - [2] G. Altarelli, F. Feruglio, and L. Merlo, *Fortschr. Phys.* **61**, 507 (2013).
 - [3] A. Y. Smirnov, *J. Phys. Conf. Ser.* **335**, 012006 (2011).
 - [4] H. Ishimori, T. Kobayashi, H. Ohki, Y. Shimizu, H. Okada, and M. Tanimoto, *Prog. Theor. Phys. Suppl.* **183**, 1 (2010).
 - [5] S. F. King and C. Luhn, *Rep. Prog. Phys.* **76**, 056201 (2013).
 - [6] C. Lam, *Phys. Lett. B* **656**, 193 (2007).
 - [7] C. Lam, *Phys. Rev. Lett.* **101**, 121602 (2008).
 - [8] C. Lam, *Phys. Rev. D* **78**, 073015 (2008).
 - [9] R. M. Fonseca and W. Grimus, arXiv:1410.4133.
 - [10] D. Hernandez and A. Y. Smirnov, *Phys. Rev. D* **88**, 093007 (2013).
 - [11] A. S. Joshipura and K. M. Patel, *Phys. Rev. D* **90**, 036005 (2014).
 - [12] A. S. Joshipura and K. M. Patel, *Phys. Lett. B* **727**, 480 (2013).
 - [13] A. S. Joshipura and K. M. Patel, *J. High Energy Phys.* **04** (2014) 009.
 - [14] S. F. King and P. O. Ludl, *J. High Energy Phys.* **06** (2016) 147.
 - [15] A. S. Joshipura, *J. High Energy Phys.* **11** (2015) 186.
 - [16] W. Grimus, S. Kaneko, L. Lavoura, H. Sawanaka, and M. Tanimoto, *J. High Energy Phys.* **01** (2006) 110.
 - [17] L. L. Everett and A. J. Stuart, *Phys. Rev. D* **79**, 085005 (2009).
 - [18] F. Feruglio and A. Paris, *J. High Energy Phys.* **03** (2011) 101.
 - [19] G.-J. Ding, L. L. Everett, and A. J. Stuart, *Nucl. Phys.* **B857**, 219 (2012).
 - [20] I. de Medeiros Varzielas and L. Lavoura, *J. Phys. G* **41**, 055005 (2014).
 - [21] J. Gehrlein, S. T. Petcov, M. Spinrath, and X. Zhang, *Nucl. Phys.* **B899**, 617 (2015).
 - [22] J. Gehrlein, S. T. Petcov, M. Spinrath, and X. Zhang, *Nucl. Phys.* **B896**, 311 (2015).
 - [23] J. Gehrlein, J. P. Oppermann, D. Schfer, and M. Spinrath, *Nucl. Phys.* **B890**, 539 (2014).
 - [24] A. S. Joshipura and K. M. Patel, *Phys. Lett. B* **749**, 159 (2015).
 - [25] W. Grimus and P. O. Ludl, *J. Phys. A* **45**, 233001 (2012).
 - [26] P. Harrison and W. Scott, *Phys. Lett. B* **547**, 219 (2002).
 - [27] W. Grimus and L. Lavoura, *Phys. Lett. B* **579**, 113 (2004).
 - [28] H.-J. He, W. Rodejohann, and X.-J. Xu, *Phys. Lett. B* **751**, 586 (2015).
 - [29] D. Forero, M. Tortola, and J. Valle, *Phys. Rev. D* **90**, 093006 (2014).
 - [30] M. Gonzalez-Garcia, M. Maltoni, and T. Schwetz, *J. High Energy Phys.* **11** (2014) 052.
 - [31] F. Capozzi, G. L. Fogli, E. Lisi, A. Marrone, D. Montanino, and A. Palazzo, *Phys. Rev. D* **89**, 093018 (2014).
 - [32] H. S. Goh, R. N. Mohapatra, and S.-P. Ng, *Phys. Lett. B* **542**, 116 (2002).
 - [33] G. Altarelli and R. Franceschini, *J. High Energy Phys.* **03** (2006) 047.
 - [34] W. Grimus and L. Lavoura, *J. Phys. G* **31**, 683 (2005).

Phenomenological study of extended seesaw model for light sterile neutrino

Newton Nath,^{a,b} Monojit Ghosh,^c Srubabati Goswami^a and Shivani Gupta^d

^aPhysical Research Laboratory,
Navarangpura, Ahmedabad 380 009, India

^bIndian Institute of Technology,
Gandhinagar, Ahmedabad-382424, India

^cDepartment of Physics, Tokyo Metropolitan University,
Hachioji, Tokyo 192-0397, Japan

^dCenter of Excellence for Particle Physics (CoEPP), University of Adelaide,
Adelaide SA 5005, Australia

E-mail: newton@prl.res.in, monojit@tmu.ac.jp, sruba@prl.res.in,
shivani.gupta@adelaide.edu.au

ABSTRACT: We study the zero textures of the Yukawa matrices in the minimal extended type-I seesaw (MES) model which can give rise to $\sim eV$ scale sterile neutrinos. In this model, three right handed neutrinos and one extra singlet S are added to generate a light sterile neutrino. The light neutrino mass matrix for the active neutrinos, m_ν , depends on the Dirac neutrino mass matrix (M_D), Majorana neutrino mass matrix (M_R) and the mass matrix (M_S) coupling the right handed neutrinos and the singlet. The model predicts one of the light neutrino masses to vanish. We systematically investigate the zero textures in M_D and observe that maximum five zeros in M_D can lead to viable zero textures in m_ν . For this study we consider four different forms for M_R (one diagonal and three off diagonal) and two different forms of (M_S) containing one zero. Remarkably we obtain only two allowed forms of m_ν ($m_{e\tau} = 0$ and $m_{\tau\tau} = 0$) having inverted hierarchical mass spectrum. We re-analyze the phenomenological implications of these two allowed textures of m_ν in the light of recent neutrino oscillation data. In the context of the MES model, we also express the low energy mass matrix, the mass of the sterile neutrino and the active-sterile mixing in terms of the parameters of the allowed Yukawa matrices. The MES model leads to some extra correlations which disallow some of the Yukawa textures obtained earlier, even though they give allowed one-zero forms of m_ν . We show that the allowed textures in our study can be realized in a simple way in a model based on MES mechanism with a discrete Abelian flavor symmetry group $Z_8 \times Z_2$.

KEYWORDS: Beyond Standard Model, Neutrino Physics

ARXIV EPRINT: [1610.09090](https://arxiv.org/abs/1610.09090)

Contents

1	Introduction	1
2	Minimal extended type I seesaw mechanism	3
3	Formalism	5
3.1	5 zeros in M_D and diagonal M_R	7
3.2	5 zeros in M_D and non-diagonal M_R corresponding to $L_e - L_\mu$ flavor symmetry	7
3.2.1	Textures leading to $m_{e\tau} = 0$	7
3.2.2	Textures leading to $m_{\tau\tau} = 0$	8
3.3	5 zeros in M_D and non-diagonal M_R corresponding to $L_e - L_\tau$ flavor symmetry	8
3.3.1	Textures leading to $m_{e\tau} = 0$	8
3.3.2	Textures leading to $m_{\tau\tau} = 0$	8
3.4	5 zeros in M_D and non-diagonal M_R corresponding to $L_\mu - L_\tau$ flavor symmetry	9
3.4.1	Structures leading to $m_{e\tau} = 0$	9
3.4.2	Structures leading to $m_{\tau\tau} = 0$	9
4	Active neutrino mass matrix with one zero texture	9
4.1	Case I: $m_{e\tau} = 0$	11
4.2	Case II: $m_{\tau\tau} = 0$	12
5	Comparison of low and high energy neutrino mass matrix elements	13
5.1	NLO correction for MES model	18
6	Symmetry realization	19
7	Conclusions	21

1 Introduction

Neutrino oscillation experiments have established the fact that neutrinos have tiny mass and they change from one flavor to another during their propagation. This requires the Standard Model (SM) of particle physics to be extended in order to generate their masses. The standard 3-flavor neutrino oscillation scenario has six key parameters. These are the two mass squared differences ($\Delta m_{i1}^2, = m_i^2 - m_1^2, i = 2, 3$) which control the oscillations of the solar and atmospheric neutrinos respectively, three mixing angles θ_{ij} ($i, j = 1, 2, 3; i < j$) and a Dirac CP phase, δ_{13} . Global analysis of three flavor neutrino oscillation data from [1–3] give us the best fit values and the allowed 3σ ranges of these parameters. In 3-flavor paradigm, there are two more CP violating phases if neutrinos are Majorana particles. But as Majorana phases do not appear in the neutrino oscillation probability,

they are not measurable in the oscillation experiments. Apart from these phases another major unknown is the absolute value of the neutrino mass since oscillation experiments are only sensitive to the mass squared differences. Planck data provide an upper bound on sum of neutrino masses to be ≤ 0.23 eV [4] at 95% C.L. The sensitivity for the neutrino masses in the upcoming Karlsruhe Tritium Neutrino experiment (KATRIN) is expected to be around 200 meV (90% C.L.) [5].

Another interesting aspect of neutrino oscillation experiments is the search for the existence of a light sterile neutrino. As sterile neutrinos are SM singlets they do not take part in the weak interactions. But they can mix with the active neutrinos. Therefore, sterile neutrinos can be probed in neutrino oscillation experiments. The oscillation results from LSND experiment showed the evidence of at least one sterile neutrino having mass in the \sim eV scale [6–8]. The latest data of MiniBooNE experiment [9] also have some overlap with the allowed regions of the LSND experiment and hence support the existence of the sterile neutrino hypothesis. The recently observed Gallium anomaly can also be explained by the sterile neutrino hypothesis [10]. Another evidence of eV sterile neutrino comes from the reactor antineutrino flux studies. This shows the deficit in the observed and predicted event rate of electron antineutrino flux and the ratio is 0.943 ± 0.023 at 98.6% C.L. [11]. Recent analysis of the Planck data shows the possibility of light sterile neutrino in the eV scale if one deviates slightly from the base Λ CDM model [4]. In short, the scenario with a light sterile neutrino is quite riveting at present and many future experiments are proposed to confirm/falsify this [12]. Although it is possible to have a better fit of neutrino oscillation data with more than one light sterile neutrino [13–15], the 3+1 scheme i.e., three active neutrinos and one sterile neutrino in the sub-eV and eV scale respectively, is considered to be minimal. There are three different ways to add sterile neutrino in SM mass patterns and these are, (i) 3+1 scheme in which three active neutrinos are of sub-eV scale and sterile neutrino is of eV scale [16, 17], (ii) 2+2 scheme in which two different pairs of neutrino mass states differ by eV^2 but this scheme was disfavored by solar and atmospheric data [18], and (iii) 1+3 scheme in which three active neutrinos are in eV scale and sterile neutrino is lighter than active neutrinos. This scenario is however disfavored from cosmology [19, 20]. Hence, we focus on the 3+1 scenario in our study.

Flavor symmetry models giving rise to eV sterile neutrinos have been studied in the literature [21–23]. These models might require modifications to usual seesaw framework [24, 25]. In the explicit seesaw models the eV scale sterile neutrinos with their mass suppressed by Froggatt - Nielsen mechanism can be naturally accommodated in non Abelian A_4 flavor symmetry [22, 26, 27]. S_3 bimodel or schizophrenic models for light sterile neutrinos are also widely studied [28, 29]. In order to have a theoretical understanding of the origin of eV sterile neutrino as well as admixtures between sterile and active neutrinos, the authors of refs. [22, 26, 27] have studied an extension to the canonical type-I seesaw model. This model is known as “minimal extended type - I seesaw” (MES) model. In the MES model a fermion singlet, S , is added along with three right handed neutrinos. This extension results into an eV scale sterile neutrino naturally, without imposing tiny mass scale or Yukawa term for this neutrino.

In this paper, for the first time we study the various possible textures of the Dirac neutrino mass matrix, M_D , Majorana neutrino mass matrix, M_R and the mass matrix M_S

that originate from the Yukawa interaction between right handed neutrinos with the gauge singlet within the framework of MES model and classify the allowed possibilities. Several papers have studied the consequences of imposing zeros in the neutrino mass matrix in standard three neutrino [30–40] and the 3+1 framework [41–45]. The more natural study would be to explore the zeros in the Yukawa matrices that appear in the Lagrangian rather than light neutrino mass matrix, m_ν . It has been noted by many authors [46–50] that the zeros of the Dirac neutrino mass matrix M_D and the right handed Majorana mass matrix M_R are the progenitors of zeros in the effective Majorana mass matrix m_ν through type - I seesaw mechanism. We also seek extra correlations connecting the parameters of the active and sterile sector which can put further constraints on the allowed possibilities. This motivates us to look for zeros in various neutrino mass matrices in the MES model which can lead to viable texture zeros in neutrino mass matrix.

We classify different structures of M_D , M_R and M_S that can give allowed textures for the light neutrino mass matrix m_ν . Interestingly the only allowed form of m_ν that we obtain are the two one zero textures — namely $m_{e\tau} = 0$ and $m_{\tau\tau} = 0$ which are phenomenologically allowed and have the inverted hierarchical mass spectrum. For a m_ν originating from ordinary seesaw mechanism both these textures are viable. However, in the MES model, because of extra correlations connecting active and sterile sector, not all Yukawa matrices that give $m_{e\tau} = 0$ or $m_{\tau\tau} = 0$ for m_ν are allowed. We study these additional correlations and tabulate the allowed textures. We also include a discussion on the impact of NLO corrections in this model. In this context it is also important to study the origin of zero textures. Here, we show that it is possible to obtain various zero entries in lepton mass matrices with an Abelian discrete symmetry group $Z_8 \times Z_2$. An alternative approach to obtain lepton mixing is discussed in [51] by considering non-Abelian symmetry group. We follow the method discussed in [52] to obtain Abelian discrete symmetry group which can generate viable zero textures in m_ν . Their method is based on type - I seesaw and we extend it to apply on MES model.

The paper is organized in the following manner. In the next section a brief review of the MES model is given. In section 3 and its subsections we list the various forms of M_D , M_R and M_S that lead to viable textures in m_ν . In section 4 we discuss the implication of the allowed forms of one zero textures in m_ν obtained in section 3. The following section 5 discusses the results obtained from the comparison of low energy and high energy neutrino mass matrices and the extra correlations connecting active and sterile sector. Symmetry realizations for the allowed zero textures are discussed in section 6. The summary of our findings and conclusions are presented in section 7.

2 Minimal extended type I seesaw mechanism

In this section we describe the basic structure of MES model. Here, the fermion content of the SM is extended by three right handed neutrinos together with a gauge singlet field S . One can get a natural eV-scale sterile neutrino without inserting any small Yukawa

coupling in this model [22, 26]. The Lagrangian containing the neutrino masses is given by,

$$-\mathcal{L}_{\mathcal{M}} = \bar{\nu}_L M_D \nu_R + \bar{S}^c M_S \nu_R + \frac{1}{2} \bar{\nu}_R^c M_R \nu_R + h.c. \quad (2.1)$$

Here, M_D, M_R are the (3×3) Dirac and Majorana mass matrices respectively and M_S is a (1×3) coupling matrix between right handed neutrinos with the gauge singlet. In the basis (ν_L, ν_R^c, S^c) , the (7×7) neutrino mass matrix can be expressed as,

$$M_\nu^{7 \times 7} = \begin{pmatrix} 0 & M_D & 0 \\ M_D^T & M_R & M_S^T \\ 0 & M_S & 0 \end{pmatrix}. \quad (2.2)$$

Considering the hierarchical mass spectrum of these mass matrices i.e. $M_R \gg M_S > M_D$, in analogy of type - I seesaw, the right handed neutrinos are much heavier compared to the electroweak scale and thus they will decouple at the low scale. Therefore, eq. (2.2) can be block diagonalized using seesaw mechanism and the effective neutrino mass matrix in the basis (ν_L, S^c) can be written as,

$$M_\nu^{4 \times 4} = - \begin{pmatrix} M_D M_R^{-1} M_D^T & M_D M_R^{-1} M_S^T \\ M_S (M_R^{-1})^T M_D^T & M_S M_R^{-1} M_S^T \end{pmatrix}. \quad (2.3)$$

Note that the rank of $M_\nu^{4 \times 4}$ is three (see [26]) and hence one of the light neutrino remains massless.

Considering the case that $M_S > M_D$, one can apply seesaw approximation once again on eq. (2.3) to obtain the active neutrino mass matrix as,¹

$$m_\nu^{3 \times 3} \simeq M_D M_R^{-1} M_S^T (M_S M_R^{-1} M_S^T)^{-1} M_S (M_R^{-1})^T M_D^T - M_D M_R^{-1} M_D^T, \quad (2.4)$$

whereas the mass of the sterile neutrino is given by,

$$m_s \simeq -M_S M_R^{-1} M_S^T. \quad (2.5)$$

Note that the zero textures of fermion mass matrices in the context of type - I seesaw mechanism studied in [46–48, 50], leading to viable texture zeros in $m_\nu^{3 \times 3}$ can be different from that of MES model because of the presence of the first term of eq. (2.4). The active-sterile neutrino mixing matrix is given by,

$$V \simeq \begin{pmatrix} (1 - \frac{1}{2} R R^\dagger) U' & R \\ -R^\dagger U' & 1 - \frac{1}{2} R^\dagger R \end{pmatrix}, \quad (2.6)$$

where $R_{3 \times 1}$ governs the strength of active-sterile mixing and can be expressed as,

$$R_{3 \times 1} = M_D M_R^{-1} M_S^T (M_S M_R^{-1} M_S^T)^{-1}. \quad (2.7)$$

Essentially, $R_{3 \times 1} = (V_{e4}, V_{\mu 4}, 0)^T$ is suppressed by the ratio $\mathcal{O}(M_D)/\mathcal{O}(M_S)$. Additionally in our formalism we assume $|V_{\tau 4}| = 0$, which is allowed by the current active sterile neutrino mixing data.

¹Note that r.h.s. of eq. (2.4) does not vanish since $(M_S)_{1 \times 3}$ is a vector rather than a square matrix.

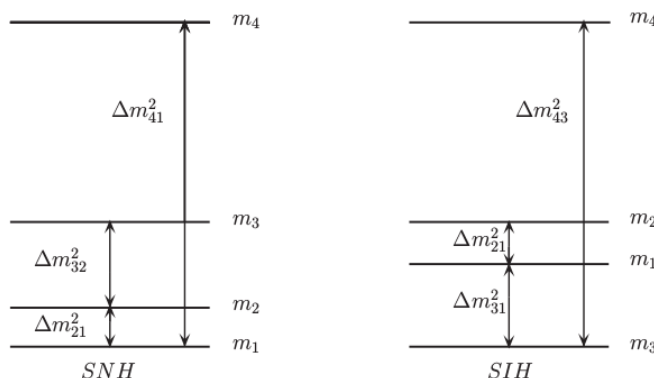


Figure 1. Allowed mass spectrum in 3+1 scheme for normal (SNH) and inverted (SIH) mass hierarchy.

	SNH	SIH
m_1	0	$\sqrt{\Delta m_{31}^2}$
m_2	$\sqrt{\Delta m_{21}^2}$	$\sqrt{\Delta m_{21}^2 + \Delta m_{31}^2}$
m_3	$\sqrt{\Delta m_{21}^2 + \Delta m_{32}^2}$	0
m_4	$\sqrt{\Delta m_{41}^2}$	$\sqrt{\Delta m_{43}^2}$

Table 1. Neutrino mass spectrum for normal and inverted hierarchies. Δm_{12}^2 , Δm_{31}^2 (Δm_{32}^2) are the solar and atmospheric mass squared differences and Δm_{41}^2 (Δm_{43}^2) is the active sterile mass squared difference. The allowed ranges of these three mass squared differences are given in table 2.

As the sterile neutrino mass ($\sim \text{eV}$) is heavier than active neutrinos, therefore, the mass pattern in the active sector can be arranged in two different ways. We denote 3+1 scenario as (SNH) when the three active neutrinos follow normal hierarchy ($m_1 < m_2 \ll m_3$) and the second choice is (SIH) when the three active neutrinos follow inverted hierarchy $m_3 \ll m_1 \approx m_2$) as shown in figure 1. These masses can be expressed in terms of the mass squared differences obtained from oscillation experiments as given in table 1. The best fit values along with 3σ ranges of neutrino oscillation parameters used in our numerical analysis are given in table 2. In the next section we systematically explore the various zero texture structures of M_D , M_R and M_S which can give rise to viable zero textures of $m_\nu^{3 \times 3}$.

3 Formalism

In our formalism, the charge lepton mass matrix, M_l , is considered to be diagonal. For the right handed Majorana neutrino mass matrix, we consider four different structures:

- (i) Diagonal M_R having three zeros i.e.,

$$M_R = \begin{pmatrix} r_1 & 0 & 0 \\ 0 & r_2 & 0 \\ 0 & 0 & r_3 \end{pmatrix} \tag{3.1}$$

Parameter	Best Fit	3 σ Range
$\Delta m_{21}^2 [10^{-5} \text{ eV}^2]$	7.37	6.93–7.97
$\Delta m_{31}^2 [10^{-3} \text{ eV}^2]$ (NH)	2.50	2.37–2.63
$\Delta m_{31}^2 [10^{-3} \text{ eV}^2]$ (IH)	2.46	2.33–2.60
$\sin^2 \theta_{12} / 10^{-1}$	2.97	2.50–3.54
$\sin^2 \theta_{13} / 10^{-2}$ (NH)	2.14	1.85–2.46
$\sin^2 \theta_{13} / 10^{-2}$ (IH)	2.18	1.86–2.48
$\sin^2 \theta_{23} / 10^{-1}$ (NH)	4.37	3.79–6.16
$\sin^2 \theta_{23} / 10^{-1}$ (IH)	5.69	3.83–6.37
δ_{13} / π (NH)	1.35	0–2
δ_{13} / π (IH)	1.32	0–2
R_ν (NH)	0.0295	0.0263–0.0336
R_ν (IH)	0.0299	0.0266–0.0342
$\Delta m_{\text{LSND}}^2 (\Delta m_{41}^2 \text{ or } \Delta m_{43}^2) \text{ eV}^2$	1.63	0.87–2.04
$ V_{e4} ^2$	0.027	0.012–0.047
$ V_{\mu 4} ^2$	0.013	0.005–0.03
$ V_{\tau 4} ^2$	–	< 0.16

Table 2. The latest best-fit and 3 σ ranges of active ν oscillation parameters from [3]. The current constraints on sterile neutrino parameters are from the global analysis [53–55]. Here R_ν is the solar to atmospheric mass squared difference ratio.

(ii) non-diagonal minimal form of M_R having four zeros with $\text{Det } M_R \neq 0$ i.e.,

$$M_R = \begin{pmatrix} 0 & r_2 & 0 \\ r_2 & 0 & 0 \\ 0 & 0 & r_1 \end{pmatrix}; \quad \begin{pmatrix} 0 & 0 & r_2 \\ 0 & r_1 & 0 \\ r_2 & 0 & 0 \end{pmatrix}; \quad \begin{pmatrix} r_1 & 0 & 0 \\ 0 & 0 & r_2 \\ 0 & r_2 & 0 \end{pmatrix}. \quad (3.2)$$

These three non-diagonal forms of M_R correspond to $L_e - L_\mu$, $L_e - L_\tau$ and $L_\mu - L_\tau$ flavor symmetry respectively. Such forms of M_R in the context of zero textures in type-I seesaw model have been considered for instance in [56]. $M_S = (s_1, s_2, s_3)$ being a 1×3 matrix can have one zero or two zeros. In [26], an A_4 based model was considered with 2 zeros in M_S and 3 zeros in M_D to obtain the $m_\nu^{3 \times 3}$ as given by eq. (2.4). But, in our analysis we find that mass matrices with 5 zeros in M_D and two zeros in M_S do not lead to any viable textures in m_ν . The only allowed possibility therefore is one zero in M_S result in three possible structures. We find that the maximum number of zeros of M_D that can give phenomenologically allowed zero textures in m_ν is five. The possible combinations of M_D , M_R and M_S that lead to phenomenologically viable textures of m_ν are discussed in the following subsections.

3.1 5 zeros in M_D and diagonal M_R

First let us assume M_R to be diagonal. As M_D is a non-symmetric 3×3 matrix, 5 zeros can be arranged in ${}^9C_5 = 126$ ways. Thus considering 126 cases of M_D together with 3 cases of M_S and 1 case of M_R , we obtain total 378 possible structures of m_ν . Out of all possible combinations of these matrices the only allowed texture that we obtain is the one zero texture in m_ν with $m_{e\tau} = 0$. Here, we have three possible forms of M_S and these are,

$$M_S^{(1)} = (0, s_2, s_3), M_S^{(2)} = (s_1, 0, s_3), \text{ and } M_S^{(3)} = (s_1, s_2, 0). \quad (3.3)$$

The various forms of M_D which lead to viable texture $m_{e\tau} = 0$ are presented below:

$$M_S^{(1)}, M_D^{(1)} = \begin{pmatrix} 0 & 0 & a_3 \\ b_1 & 0 & b_3 \\ c_1 & 0 & 0 \end{pmatrix}, M_D^{(2)} = \begin{pmatrix} 0 & a_2 & 0 \\ b_1 & 0 & b_3 \\ c_1 & 0 & 0 \end{pmatrix}, M_D^{(3)} = M_D^{(1)} Z_{23}, M_D^{(4)} = M_D^{(2)} Z_{23}. \quad (3.4)$$

$$M_S^{(2)}, M_D^{(5)} = \begin{pmatrix} 0 & 0 & a_3 \\ 0 & b_2 & b_3 \\ 0 & c_2 & 0 \end{pmatrix}, M_D^{(6)} = \begin{pmatrix} a_1 & 0 & 0 \\ 0 & b_2 & b_3 \\ 0 & c_2 & 0 \end{pmatrix}, M_D^{(7)} = M_D^{(5)} Z_{13}, M_D^{(8)} = M_D^{(6)} Z_{13}. \quad (3.5)$$

$$M_S^{(3)}, M_D^{(9)} = \begin{pmatrix} a_1 & 0 & 0 \\ 0 & b_2 & b_3 \\ 0 & 0 & c_3 \end{pmatrix}, M_D^{(10)} = \begin{pmatrix} 0 & a_2 & 0 \\ 0 & b_2 & b_3 \\ 0 & 0 & c_3 \end{pmatrix}, M_D^{(11)} = M_D^{(9)} Z_{12}, M_D^{(12)} = M_D^{(10)} Z_{12}. \quad (3.6)$$

Here, Z_{12} , Z_{13} and Z_{23} are the permutation matrices that exchange first and second columns, first and third columns and second and third columns respectively. Therefore, we observe that out of 126 cases only 12 above forms of $M_D^{(i)}$, $i = 1 - 12$ give the allowed texture $m_{e\tau} = 0$ of m_ν when M_R is diagonal

3.2 5 zeros in M_D and non-diagonal M_R corresponding to $L_e - L_\mu$ flavor symmetry

The form of M_R that we consider here corresponds to flavor symmetry $L_e - L_\mu$ as given in eq. (3.2). Among the 378 possibilities we obtain two allowed one zero textures of m_ν , namely $m_{e\tau} = 0$ and $m_{\tau\tau} = 0$. We observe that out of total 126 forms of M_D , only four structures give rise to $m_{e\tau} = 0$ while eight structures give rise to $m_{\tau\tau} = 0$. We list them below:

3.2.1 Textures leading to $m_{e\tau} = 0$

$$M_S^{(3)}, M_D^{(13)} = \begin{pmatrix} a_1 & 0 & 0 \\ 0 & b_2 & b_3 \\ 0 & 0 & c_3 \end{pmatrix}, M_D^{(14)} = \begin{pmatrix} 0 & a_2 & 0 \\ 0 & b_2 & b_3 \\ 0 & 0 & c_3 \end{pmatrix}, M_D^{(15)} = M_D^{(13)} Z_{12}, M_D^{(16)} = M_D^{(14)} Z_{12}. \quad (3.7)$$

3.2.2 Textures leading to $m_{\tau\tau} = 0$

$$M_S^{(1)}, M_D^{(17)} = \begin{pmatrix} a_1 & a_2 & 0 \\ b_1 & 0 & 0 \\ 0 & c_2 & 0 \end{pmatrix}, M_D^{(18)} = \begin{pmatrix} a_1 & 0 & a_3 \\ b_1 & 0 & 0 \\ 0 & c_2 & 0 \end{pmatrix}, \quad (3.8)$$

$$M_D^{(19)} = \begin{pmatrix} a_1 & 0 & 0 \\ b_1 & b_2 & 0 \\ 0 & c_2 & 0 \end{pmatrix}, M_D^{(20)} = \begin{pmatrix} a_1 & 0 & 0 \\ b_1 & 0 & b_3 \\ 0 & c_2 & 0 \end{pmatrix}.$$

$$M_S^{(2)}, M_D^{(21)} = \begin{pmatrix} 0 & a_2 & a_3 \\ 0 & b_2 & 0 \\ c_1 & 0 & 0 \end{pmatrix}, M_D^{(22)} = \begin{pmatrix} a_1 & a_2 & 0 \\ 0 & b_2 & 0 \\ c_1 & 0 & 0 \end{pmatrix}, \quad (3.9)$$

$$M_D^{(23)} = \begin{pmatrix} 0 & a_2 & 0 \\ b_1 & b_2 & 0 \\ c_1 & 0 & 0 \end{pmatrix}, M_D^{(24)} = \begin{pmatrix} 0 & a_2 & 0 \\ 0 & b_2 & b_3 \\ c_1 & 0 & 0 \end{pmatrix}.$$

3.3 5 zeros in M_D and non-diagonal M_R corresponding to $L_e - L_\tau$ flavor symmetry

The form of M_R that we consider in this subsection corresponds to flavor symmetry $L_e - L_\tau$ as given in eq. (3.2). In this case also we observe that out of total 126 cases of M_D , only four structures of M_D give rise to $m_{e\tau} = 0$ and eight forms of M_D give rise to texture $m_{\tau\tau} = 0$. We list them below. Note that these forms of M_D are different from those obtained in the earlier subsection.

3.3.1 Textures leading to $m_{e\tau} = 0$

$$M_S^{(2)}, M_D^{(25)} = \begin{pmatrix} 0 & 0 & a_3 \\ 0 & b_2 & b_3 \\ 0 & c_2 & 0 \end{pmatrix}, M_D^{(26)} = \begin{pmatrix} 0 & 0 & a_3 \\ b_1 & b_2 & 0 \\ 0 & c_2 & 0 \end{pmatrix}, M_D^{(27)} = M_D^{(25)} Z_{13}, M_D^{(28)} = M_D^{(26)} Z_{13}. \quad (3.10)$$

3.3.2 Textures leading to $m_{\tau\tau} = 0$

$$M_S^{(1)}, M_D^{(29)} = \begin{pmatrix} a_1 & a_2 & 0 \\ b_1 & 0 & 0 \\ 0 & 0 & c_3 \end{pmatrix}, M_D^{(30)} = \begin{pmatrix} a_1 & 0 & a_3 \\ b_1 & 0 & 0 \\ 0 & 0 & c_3 \end{pmatrix}, \quad (3.11)$$

$$M_D^{(31)} = \begin{pmatrix} a_1 & 0 & 0 \\ b_1 & b_2 & 0 \\ 0 & 0 & c_3 \end{pmatrix}, M_D^{(32)} = \begin{pmatrix} a_1 & 0 & 0 \\ b_1 & 0 & b_3 \\ 0 & 0 & c_3 \end{pmatrix}.$$

$$M_S^{(3)}, M_D^{(33)} = \begin{pmatrix} 0 & a_2 & a_3 \\ 0 & 0 & b_3 \\ c_1 & 0 & 0 \end{pmatrix}, M_D^{(34)} = \begin{pmatrix} a_1 & 0 & a_3 \\ 0 & 0 & b_3 \\ c_1 & 0 & 0 \end{pmatrix}, \quad (3.12)$$

$$M_D^{(35)} = \begin{pmatrix} 0 & 0 & a_3 \\ 0 & b_2 & b_3 \\ c_1 & 0 & 0 \end{pmatrix}, M_D^{(36)} = \begin{pmatrix} 0 & 0 & a_3 \\ b_1 & 0 & b_3 \\ c_1 & 0 & 0 \end{pmatrix}.$$

3.4 5 zeros in M_D and non-diagonal M_R corresponding to $L_\mu - L_\tau$ flavor symmetry

The form of M_R that we consider here corresponds to flavor symmetry $L_\mu - L_\tau$ as given in eq. (3.2). Here also we observe that out of 126 cases of M_D only four structures of M_D give rise to texture $M_{e\tau} = 0$ and 8 forms of M_D give rise to texture $M_{\tau\tau} = 0$. But these forms of M_D are different from those obtained in the earlier two subsections:

3.4.1 Structures leading to $m_{e\tau} = 0$

$$M_S^{(1)}, M_D^{(37)} = \begin{pmatrix} 0 & a_2 & 0 \\ b_1 & 0 & b_3 \\ c_1 & 0 & 0 \end{pmatrix}, M_D^{(38)} = \begin{pmatrix} 0 & 0 & a_3 \\ b_1 & 0 & b_3 \\ c_1 & 0 & 0 \end{pmatrix}, M_D^{(39)} = M_D^{(37)} Z_{23}, M_D^{(40)} = M_D^{(38)} Z_{23}. \tag{3.13}$$

3.4.2 Structures leading to $m_{\tau\tau} = 0$

$$M_S^{(2)}, M_D^{(41)} = \begin{pmatrix} a_1 & a_2 & 0 \\ 0 & b_2 & 0 \\ 0 & 0 & c_3 \end{pmatrix}, M_D^{(42)} = \begin{pmatrix} 0 & a_2 & a_3 \\ 0 & b_2 & 0 \\ 0 & 0 & c_3 \end{pmatrix}, \tag{3.14}$$

$$M_D^{(43)} = \begin{pmatrix} 0 & a_2 & 0 \\ 0 & b_2 & b_3 \\ 0 & 0 & c_3 \end{pmatrix}, M_D^{(44)} = \begin{pmatrix} 0 & a_2 & 0 \\ b_1 & b_2 & 0 \\ 0 & 0 & c_3 \end{pmatrix}.$$

$$M_S^{(3)}, M_D^{(45)} = \begin{pmatrix} 0 & a_2 & a_3 \\ 0 & 0 & b_3 \\ 0 & c_2 & 0 \end{pmatrix}, M_D^{(46)} = \begin{pmatrix} a_1 & 0 & a_3 \\ 0 & 0 & b_3 \\ 0 & c_2 & 0 \end{pmatrix},$$

$$M_D^{(47)} = \begin{pmatrix} 0 & 0 & a_3 \\ b_1 & 0 & b_3 \\ 0 & c_2 & 0 \end{pmatrix}, M_D^{(48)} = \begin{pmatrix} 0 & 0 & a_3 \\ 0 & b_2 & b_3 \\ 0 & c_2 & 0 \end{pmatrix}. \tag{3.15}$$

Note that in general the entries of the Yukawa matrices M_D , M_R and M_S are complex (of the form $pe^{i\theta}$). However some of the phases can be absorbed by redefinition of the leptonic fields. For the case when M_R is diagonal, the number of un-absorbed phases is two — one each in M_D and M_S whereas for the off-diagonal M_R only one phase remains in M_S . In this section we do not explicitly write the phases. However in section 5 where we discuss specific cases, the phases are explicitly included.

4 Active neutrino mass matrix with one zero texture

The (3×3) light neutrino mass matrix being symmetric, there are 6 possible cases of one zero textures with a vanishing lowest mass and these are studied in details in refs. [57–60]. In the above section we observed that in context of MES model only viable textures of m_ν that we obtain are $m_{e\tau} = 0$ and $m_{\tau\tau} = 0$. According to the recent studies [59–61], both these textures are ruled out for normal hierarchy when the lowest mass m_1 is zero

but they can be allowed for the inverted hierarchy even when then lowest mass m_3 is zero.² This kind of mass pattern can be obtained completely from group theoretical point of view if one assumes that Majorana neutrino mass matrix displays flavor antisymmetry under some discrete subgroup of $SU(3)$ as discussed in [62, 63]. In this section we re-analyse the textures $m_{e\tau} = 0$ and $m_{\tau\tau} = 0$ for the inverted hierarchical mass spectrum assuming $m_3 = 0$ in the light of recent neutrino oscillation data as given in table 2. In our analysis we find that correlations among various oscillation parameters become highly constrained as compared to the earlier studies. This is due to the recent constraints on the 3σ ranges of the mass squared differences and θ_{13} as compared to earlier results in [58–60].³

In three neutrino paradigm, low energy Majorana neutrino mass matrix can be diagonalized as,

$$m_\nu^{3\times 3} = U' \text{diag}(m_1, m_2, m_3) U'^T. \quad (4.1)$$

Here, $U' = U.P$ ($P = \text{diag}(1, e^{i\alpha}, e^{i(\beta+\delta_{13})})$) is a lepton mixing matrix in the basis where M_l is diagonal. The Pontecorvo-Maki-Nakagawa-Sakata (PMNS) matrix U has 3 mixing angles and a CP violation phase δ_{13} .

The elements of neutrino mass matrix can be calculated from eq. (4.1) are,

$$(m_\nu^{3\times 3})_{ab} = m_1 U_{a1} U_{b1} + m_2 U_{a2} U_{b2} e^{2i\alpha} + m_3 U_{a3} U_{b3} e^{2i(\beta+\delta_{13})}, \quad (4.2)$$

where, $a, b = e, \mu$ and τ and $m_i (i = 1, 2, 3)$ are given in table 1. We express elements of m_ν as m_{ab} in the text.

Imposing the condition of zero texture for IH with $m_3 = 0$ in the above equation we get,

$$m_1 U_{a1} U_{b1} + m_2 U_{a2} U_{b2} e^{2i\alpha} = 0, \quad (4.3)$$

which can be simplified to obtain the mass ratio

$$\frac{m_1}{m_2} e^{-2i\alpha} = -\frac{U_{a2} U_{b2}}{U_{a1} U_{b1}}. \quad (4.4)$$

Let, $q = \frac{m_1}{m_2} e^{-2i\alpha}$ we get

$$\alpha = -\frac{1}{2} \text{Arg}(q), \quad (4.5)$$

$$|q| = \frac{m_1}{m_2} = \left| -\frac{U_{a2} U_{b2}}{U_{a1} U_{b1}} \right|. \quad (4.6)$$

Let us define the ratio of the two mass squared differences as,

$$R_\nu = \frac{\Delta m_{21}^2}{|\Delta m_{31}^2|} = \frac{1 - |q|^2}{|q|^2}. \quad (4.7)$$

The R_ν defined above can be calculated either using the current neutrino mass squared differences as given in table 2 or by calculating $|q|$. If the value of R_ν calculated using $|q|$

²We also observed that both these textures are disallowed for NH with the most recent data.

³The latest constraint on $|\Delta m_{31}^2|$ comes from T2K and NO ν A including both appearance and disappearance modes [64–67]. Whereas reanalysis of KamLAND data shows decrease in the value of Δm_{21}^2 and $\sin^2 \theta_{12}$ as discussed in [3].

falls in the allowed 3σ range of R_ν from the current data, then we say the texture under consideration is allowed by the current data. As given in table 2 we vary the Dirac CP phase δ_{13} from $0^\circ < \delta_{13} < 360^\circ$ while the relevant Majorana phase α in the range $0^\circ < \alpha < 180^\circ$ and find the correlations among different parameters, specially the predictions for α and δ_{13} .

We also study the effective Majorana neutrino mass, m_{ee} , governing neutrinoless double beta decay ($0\nu\beta\beta$) for these allowed textures. In three flavor paradigm this can be written as,

$$m_{ee} = |\sum U_{ei}^2 m_i| = |m_1 c_{12}^2 c_{13}^2 + m_2 e^{2i\alpha} c_{13}^2 s_{12}^2 + m_3 e^{2i\beta} s_{13}^2|. \quad (4.8)$$

where $c_{ij}(s_{ij}) = \cos\theta_{ij}(\sin\theta_{ij})$, ($i < j$, $i, j = 1, 2, 3$). From the above equation we understand that m_{ee} depends on the Majorana phases but not on the Dirac phase. Various experiments such as CUORE [68], GERDA [69], SuperNEMO [70], KamLAND-ZEN [71] and EXO [72] are looking for signatures for neutrinoless double beta decay ($0\nu\beta\beta$). The current experiments provide bounds on the effective Majorana mass m_{ee} from the non-observation of $0\nu\beta\beta$. For instance, the combined results from KamLAND-ZEN and EXO-200 [71] give the upper bound on the effective Majorana neutrino mass as $m_{ee} < (0.12 - 0.25)$ eV where the range signifies the uncertainty in the nuclear matrix elements. The future experiments can improve this limit by one order of magnitude. Below we discuss the various correlations that we obtain for the allowed textures.

4.1 Case I: $m_{e\tau} = 0$

The Majorana mass matrix element $m_{e\tau}$ in 3-flavor case can be written as,

$$m_{e\tau} = m_1 U_{e1} U_{\tau 1} + m_2 U_{e2} U_{\tau 2} e^{2i\alpha} + m_3 U_{e3} U_{\tau 3} e^{2i(\beta+\delta_{13})}. \quad (4.9)$$

Imposing the condition of zero texture with vanishing lowest mass ($m_3 = 0$) for IH, we get,

$$|m_1 U_{e1} U_{\tau 1} + m_2 U_{e2} U_{\tau 2} e^{2i\alpha}| = 0, \quad (4.10)$$

$$|m_1 c_{12} c_{13} (s_{12} s_{23} - c_{12} c_{23} s_{13} e^{i\delta}) + m_2 s_{12} c_{13} (-c_{12} s_{23} - s_{12} c_{23} s_{13} e^{i\delta})^2 e^{2i\alpha}| = 0. \quad (4.11)$$

From the above equation we obtain the mass ratio as below

$$\frac{m_2}{m_1} \approx 1 - \frac{s_{13} \cos \delta_{13}}{\tan \theta_{23} s_{12} c_{12}} + \mathcal{O}(s_{13}^2). \quad (4.12)$$

The mass ratio $\frac{m_2}{m_1}$ should be greater than 1. For this to happen $\cos \delta_{13}$ should be negative. We find that due to the interplay of the terms $\mathcal{O}(s_{13})$ and $\mathcal{O}(s_{13}^2)$ the phase δ_{13} is restricted to the range $[85^\circ - 95^\circ]$ and $[265^\circ - 275^\circ]$. The effective mass, m_{ee} as function of Majorana phase α is constrained due to very small allowed range of α ($5^\circ < \alpha < 10^\circ$, $170^\circ < \alpha < 175^\circ$) as shown in Eq. (4.8). The allowed range of m_{ee} for this texture is $0.046 \text{ eV} < m_{ee} < 0.05 \text{ eV}$ and which can be probed in future experiments. Also, this texture predicts Dirac CP phase $\sim 270^\circ$ which is in agreement with the indications from the current ongoing oscillation experiments like T2K and NO ν A. There is however no constrain on the values of the neutrino mixing angles θ_{13} and θ_{23} seen in right panel of figure 2 for this texture.

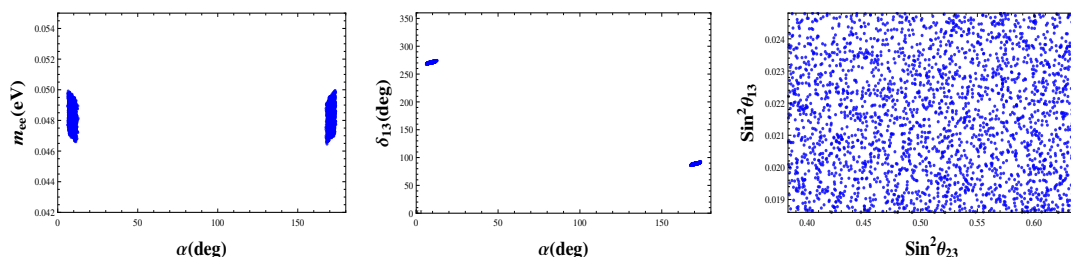


Figure 2. Correlation plots of $m_{e\tau} = 0$ for IH with vanishing m_3 in 3 neutrino paradigm.

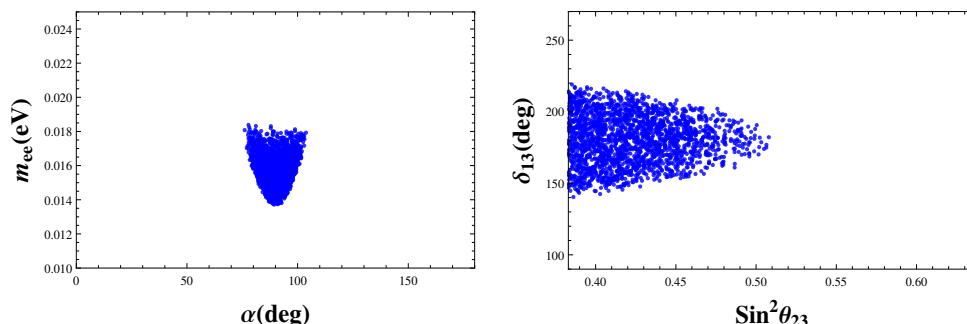


Figure 3. Correlation plots of $m_{\tau\tau} = 0$ for IH with vanishing m_3 in 3 neutrino paradigm.

4.2 Case II: $m_{\tau\tau} = 0$

The Majorana mass matrix element $m_{\tau\tau}$ in 3-flavor case can be written as,

$$m_{\tau\tau} = m_1 U_{\tau 1}^2 + m_2 U_{\tau 2}^2 e^{2i\alpha} + m_3 U_{\tau 3}^2 e^{2i(\beta+\delta_{13})}. \quad (4.13)$$

Imposing the condition of texture zero with vanishing lowest mass ($m_3 = 0$) for IH, we get,

$$|m_1 U_{\tau 1}^2 + m_2 U_{\tau 2}^2 e^{2i\alpha}| = 0, \quad (4.14)$$

$$|m_1 (s_{12}s_{23} - c_{12}c_{23}s_{13}e^{i\delta})^2 + m_2 (-c_{12}s_{23} - s_{12}c_{23}s_{13}e^{i\delta})^2 e^{2i\alpha}| = 0. \quad (4.15)$$

The mass ratio from the above equation can be written as

$$\frac{m_2}{m_1} \approx \frac{s_{12}^2}{c_{12}^2} \left[1 - \frac{2 \cot \theta_{23} s_{13} \cos \delta_{13}}{c_{12} s_{12}} \right] + \mathcal{O}(s_{13}^2). \quad (4.16)$$

Since this mass ratio $\frac{m_2}{m_1}$ is always greater than 1 from oscillation data, we find that $\cos \delta_{13}$ should be negative for this texture as well. As can be seen from figure 3 that δ_{13} is constrained in the range $140^\circ < \delta_{13} < 220^\circ$. We observe that, due to the more constrained values of mass squared differences and θ_{13} from present data, as considered in our analysis, the atmospheric mixing angle θ_{23} is restricted to be below maximal. In the earlier analysis [58–60] there was no preferred octant of θ_{23} . The values of $\theta_{23} > 45^\circ$ are disallowed for this texture as can be seen in figure 3. The effective mass, m_{ee} , being function of unknown Majorana phase α as seen in Eq. (4.8) is constrained due to very small allowed range of α ($80^\circ < \alpha < 110^\circ$). The allowed range of m_{ee} for this texture is 0.014 eV

$< m_{ee} < 0.018 \text{ eV}$ which is smaller compared to the case $m_{e\tau}=0$ where a vanishing element is off-diagonal. The allowed values of the effective mass m_{ee} for diagonal texture $m_{\tau\tau}$ are on the lower side having no overlap with non diagonal texture zero $m_{e\tau}$. Thus, m_{ee} can be used to distinguish between diagonal and off-diagonal one texture zero classes with a vanishing neutrino mass. Note that allowed ranges of δ_{13} and m_{ee} are more constrained in our analysis as compared to references [58, 59] again due to the recent improved constraints on the mass squared differences and θ_{13} at 3σ .

5 Comparison of low and high energy neutrino mass matrix elements

In this section we obtain the light neutrino neutrino mass matrix (m_ν) (eq. (2.4)), sterile mixing matrix (m_s) (eq. (2.5)) and the active sterile mixing matrix (R) (eq. (2.7)) using the different forms of M_D , M_S and M_R given in section (III) of the MES model. Since in the MES model both the active neutrino mass matrix m_ν and the active sterile mixing matrix R depends on the parameters of M_S , M_D and M_R , this can induce additional correlations between active and sterile sector. Similarly, the mass of the sterile neutrino m_s depends on M_S and M_R . Hence expressing the various variables in terms of the parameters of these matrices one can get some interrelations.

For an illustration we will discuss three specific cases. In case I and II we discuss $m_{e\tau} = 0$ assuming diagonal structure of M_R and in the case III we talk about $m_{\tau\tau} = 0$ by considering the off diagonal form of M_R . Note that here we consider the complex phases in our calculation. We compare high energy mass matrix with low energy mass matrix after the decoupling of the eV sterile neutrino as discussed in section II.

- Case I: considering the forms of $M_S^{(1)}$, $M_D^{(1)}$ and diagonal M_R from eq. (3.4),

$$M_S^{(1)} = (0, s_2, s_3 e^{i\rho_2}), M_D^{(1)} = \begin{pmatrix} 0 & 0 & a_3 \\ b_1 & 0 & b_3 e^{i\rho_1} \\ c_1 & 0 & 0 \end{pmatrix}, M_R = \text{diag}(r_1, r_2, r_3) \quad (5.1)$$

and using them in eqs. (2.4), (2.5 and 2.7) we get the low energy neutrino mass matrix, the sterile mass and the active sterile mixing matrix as,

$$m_\nu^{3 \times 3} = \begin{pmatrix} -\frac{a_3^2 s_2^2}{(r_3 s_2^2 + r_2 s_3^2 e^{2i\rho_2})} & -\frac{a_3 b_3 e^{i\rho_1} s_2^2}{(r_3 s_2^2 + r_2 s_3^2 e^{2i\rho_2})} & 0 \\ \cdot & -\frac{b_1^2}{r_1} - \frac{b_3^2 s_2^2 e^{2i\rho_1}}{(r_3 s_2^2 + r_2 s_3^2 e^{2i\rho_2})} & -\frac{b_1 c_1}{r_1} \\ \cdot & \cdot & -\frac{c_1^2}{r_1} \end{pmatrix}, \quad (5.2)$$

$$m_s = -\left(\frac{s_2^2}{r_2} + \frac{s_3^2 e^{2i\rho_2}}{r_3} \right), \quad R = \begin{pmatrix} \frac{a_3 r_2 s_3 e^{i\rho_2}}{(r_3 s_2^2 + r_2 s_3^2 e^{2i\rho_2})} \\ \frac{b_3 r_2 s_3 e^{i(\rho_1 + \rho_2)}}{(r_3 s_2^2 + r_2 s_3^2 e^{2i\rho_2})} \\ 0 \end{pmatrix} = \begin{pmatrix} V_{e4} \\ V_{\mu 4} \\ 0 \end{pmatrix}. \quad (5.3)$$

From eq. (5.2) and (5.3) it can be seen that

$$\frac{m_{\mu\tau}}{m_{\tau\tau}} = \frac{b_1}{c_1}, \quad \frac{V_{e4}}{V_{\mu 4}} = \frac{a_3}{b_3} e^{-i\rho_1} = \frac{m_{ee}}{m_{e\mu}} \quad (5.4)$$

Here m_{ab} , $a, b = e, \mu, \tau$ are the low energy neutrino mass matrix elements. The eigen values of $m_\nu^{3 \times 3}$ will give the masses of the three active neutrinos. Note that, only allowed hierarchy in our case is IH and hence $m_3 = 0$ and $m_s = m_4 = \sqrt{\Delta m_{43}^2}$. From eq. (5.4) we get,

$$\left| \frac{V_{e4}}{V_{\mu 4}} \right| = \left| \frac{m_{ee}}{m_{e\mu}} \right|. \quad (5.5)$$

We find that the l.h.s. of eq. (5.5) lies in the range (0.63 – 3.06) whereas r.h.s. lies in (3.9 - 5.9) in their 3σ range. This shows that there is no overlapping between l.h.s. and r.h.s. of eq. (5.5) and hence disallowed from current neutrino oscillation data. We observe that out of 12 forms of $M_D^{(i)}$, ($i = 1, 2, \dots, 12$) as given in eq. (3.4)–(3.6), 6 of them ($M_D^{(2)}, M_D^{(4)}, M_D^{(6)}, M_D^{(8)}, M_D^{(9)}$ and $M_D^{(11)}$) do not lead to the correlation given in eq. (5.5) and these $M_D^{(i)}$'s are not ruled out. Hence a detail analysis of one of these $M_D^{(i)}$'s is discussed below in Case II.

- Case II: considering the form of $M_S^{(1)}, M_D^{(2)}$ and diagonal M_R given in eq. (3.4),

$$M_S^{(1)} = (0, s_2, s_3 e^{i\rho_2}), M_D^{(2)} = \begin{pmatrix} 0 & a_2 & 0 \\ b_1 & 0 & b_3 e^{i\rho_1} \\ c_1 & 0 & 0 \end{pmatrix}, M_R = \text{diag}(r_1, r_2, r_3) \quad (5.6)$$

and using them in eqs. (2.4), (2.5 and 2.7) we get the texture $m_{e\tau} = 0$,

$$m_\nu^{3 \times 3} = \begin{pmatrix} -\frac{a_2^2 s_3^2 e^{2i\rho_2}}{(r_3 s_2^2 + r_2 s_3^2 e^{2i\rho_2})} & \frac{a_2 b_3 s_2 s_3 e^{i(\rho_1 + \rho_2)}}{(r_3 s_2^2 + r_2 s_3^2 e^{2i\rho_2})} & 0 \\ \cdot & -\frac{b_1^2}{r_1} - \frac{b_3^2 s_2^2 e^{2i\rho_1}}{(r_3 s_2^2 + r_2 s_3^2 e^{2i\rho_2})} & -\frac{b_1 c_1}{r_1} \\ \cdot & \cdot & -\frac{c_1^2}{r_1} \end{pmatrix}. \quad (5.7)$$

The sterile mass and active sterile mixing becomes

$$m_s = -\left(\frac{s_2^2}{r_2} + \frac{s_3^2 e^{2i\rho_2}}{r_3} \right), \quad R = \begin{pmatrix} \frac{a_2 r_3 s_2}{(r_3 s_2^2 + r_2 s_3^2 e^{2i\rho_2})} \\ \frac{b_3 r_2 s_3 e^{i(\rho_1 + \rho_2)}}{(r_3 s_2^2 + r_2 s_3^2 e^{2i\rho_2})} \\ 0 \end{pmatrix} = \begin{pmatrix} V_{e4} \\ V_{\mu 4} \\ 0 \end{pmatrix}. \quad (5.8)$$

It can be seen from the above equations that

$$\frac{m_{\mu\tau}}{m_{\tau\tau}} = \frac{b_1}{c_1}, \quad \frac{m_{ee}}{m_{e\mu}} = -\frac{a_2 s_3}{b_3 s_2} e^{i(\rho_2 - \rho_1)} \quad (5.9)$$

From eq. (5.7) we get the following relation between the light neutrino mass matrix elements,

$$m_{\mu\mu} = \frac{b_1}{c_1} m_{\mu\tau} - \frac{b_3 s_2}{a_2 s_3} e^{i(\rho_1 - \rho_2)} m_{e\mu} = \frac{m_{e\mu}^2}{m_{ee}} + \frac{m_{\mu\tau}^2}{m_{\tau\tau}}$$

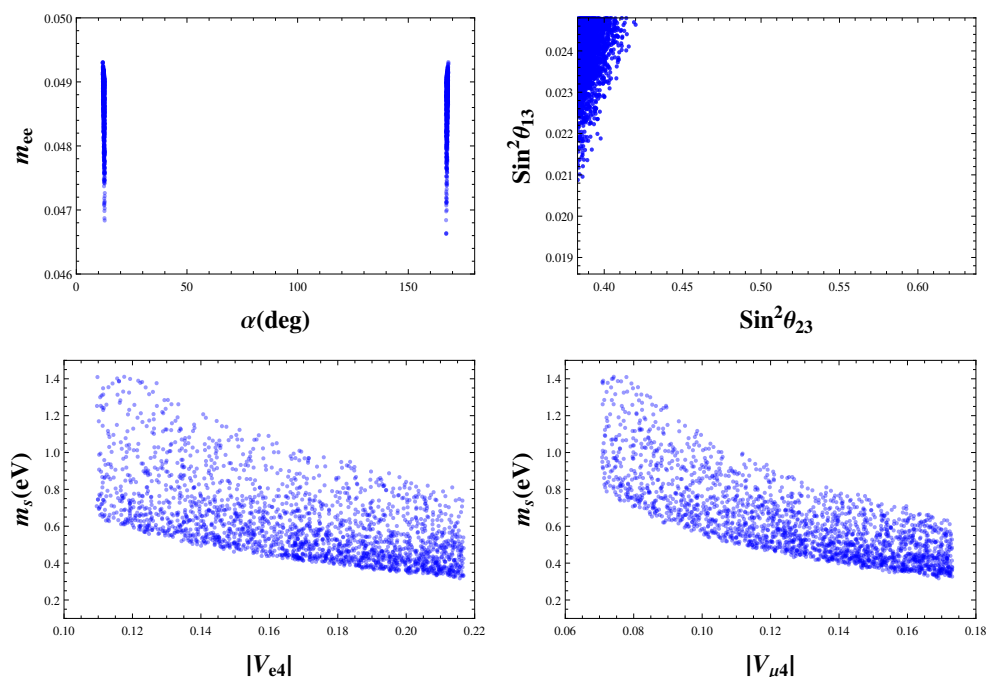


Figure 4. Correlation plots for case II.

which implies,

$$m_{ee} = \frac{m_{e\mu}^2 m_{\tau\tau}}{m_{\mu\mu} m_{\tau\tau} - m_{\mu\tau}^2}. \quad (5.10)$$

To obtain eq. (5.10) we have used the correlations of eq. (5.9). Now to test the viability of these structures of M_D , M_R and M_S , we look for the parameter space in which both the conditions $m_{e\tau} = 0$ and eq. (5.10) are satisfied simultaneously. In the upper panels of figure 4, we have plotted the correlations obtained between different low energy parameters in this scenario. Comparing these correlations with figure 2 (which corresponds to only $m_{e\tau} = 0$), we find that the MES model disfavours a large area in the $\sin^2 \theta_{23} - \sin^2 \theta_{13}$ plane and allows θ_{23} values in the lower octant: $0.383 < \sin^2 \theta_{23} < 0.42$ whereas the admissible values of θ_{13} ($0.021 < \sin^2 \theta_{13} < 0.0248$) are near the higher side of it's allowed range. However the values of α and m_{ee} which are predicted by the two cases are similar. The prediction of the texture with $m_{e\tau} = 0$ is $6^\circ < \alpha < 13^\circ$ and $167^\circ < \alpha < 174^\circ$ while the MES model predicts a slightly constrained range $11.7^\circ < \alpha < 13^\circ$ and $167^\circ < \alpha < 168.1^\circ$. In this case we also obtain another correlation for sterile neutrino mass from this model of the form,

$$m_s = \left| -\frac{m_{e\mu}}{V_{e4} V_{\mu 4}} \right|. \quad (5.11)$$

In the lower panels of figure 4, we have plotted the prediction of m_s as given by eq. (5.11) by varying V_{e4} and $V_{\mu 4}$ within their allowed range as given in table 2. This is obtained when both the conditions i.e., $m_{e\tau} = 0$ and eq. (5.10) is satisfied

simultaneously. From the figures we see that the prediction of m_s by this model is consistent with data coming from the SBL experiments.

- Case III: considering the cases for the off-diagonal forms of M_R given in eqs. (3.7)–(3.15), we find that out of the 36 $M_D^{(i)}$, ($i = 13, 14, \dots, 48$), 19 cases lead to exactly the same correlation depicted by eq. (5.5). This is not allowed from current oscillation data as discussed earlier. Among the remaining 17 cases 11 $M_D^{(i)}$ (for $i = 17, 19, 22, 23, 30, 32, 34, 42, 43, 44$ and 45) lead to a correlation of the form,

$$\left| \frac{V_{e4}}{V_{\mu4}} \right| = \left| \frac{m_{e\tau}}{m_{\mu\tau}} \right|. \quad (5.12)$$

This is also not satisfied by current neutrino oscillation data as the r.h.s. of eq. (5.12) lies in the range (3.8 – 4.7) showing no overlapping with l.h.s. The remaining six forms of $M_D^{(i)}$ are $M_D^{(18)}$, $M_D^{(21)}$, $M_D^{(29)}$, $M_D^{(33)}$, $M_D^{(41)}$ and $M_D^{(46)}$. All these forms of M_D and the corresponding forms of M_R and M_S lead to neutrino mass matrix with $m_{\tau\tau} = 0$. We found that, all these M_D 's lead a correlation of the form,

$$\left| \frac{V_{e4}}{V_{\mu4}} \right| = \left| \frac{m_{e\mu}}{m_{\mu\mu}} \right| \quad (5.13)$$

which is satisfied by current oscillation data. The r.h.s. of eq. (5.12) lies in the range (1.8–2.3) which shows complete overlap with l.h.s. (0.63–3.06). For illustration, we consider $M_D^{(18)}$ with corresponding M_R and $M_S^{(1)}$ and using them in eqs. (2.4), (2.5 and 2.7) we get ,

$$m_\nu^{3 \times 3} = \begin{pmatrix} \frac{a_1 s_2 (a_1 s_2 r_1 + 2a_3 s_3 r_2 e^{i\rho_2})}{r_2^2 s_3^2 e^{2i\rho_2}} & \frac{b_1 s_2 (a_1 s_2 r_1 + a_3 s_3 r_2 e^{i\rho_2})}{r_2^2 s_3^2 e^{2i\rho_2}} & -\frac{a_1 c_2}{r_2} \\ \cdot & \frac{b_1^2 s_3^2 r_1}{r_2^2 s_3^2} e^{-2i\rho_2} & -\frac{b_1 c_2}{r_2} \\ \cdot & \cdot & 0 \end{pmatrix}, \quad (5.14)$$

$$m_s = -\frac{s_3^2}{r_1} e^{2i\rho_2}, \quad R = \begin{pmatrix} \frac{a_1 s_2 r_1 + a_3 s_3 r_2 e^{i\rho_2}}{r_2 s_3^2 e^{2i\rho_2}} \\ \frac{b_1 s_2 r_1}{r_2 s_3^2 e^{2i\rho_2}} \\ 0 \end{pmatrix} = \begin{pmatrix} V_{e4} \\ V_{\mu4} \\ 0 \end{pmatrix}. \quad (5.15)$$

From the above matrices we find the following correlation,

$$m_s = \left| -\frac{m_{e\mu}}{V_{e4} V_{\mu4}} \right|. \quad (5.16)$$

also the correlation mentioned by eq. (5.13). We find that both the equations (5.13 and 5.16) are consistent with the current oscillation data. The simultaneous validity of equations (5.13 and 5.16) lead to light sterile neutrino mass in the range $1.4 \text{ eV} < m_s < 3.5 \text{ eV}$ which is marginally allowed by global analysis as seen from figure 5. However, individual experiments (MINOS, IceCube, Daya Bay) still allow higher value of sterile neutrino mass [73–76].

In table 3 and table 4 we summarize the allowed cases that we obtained in our study for texture $m_{e\tau} = 0$ and $m_{\tau\tau} = 0$ respectively.

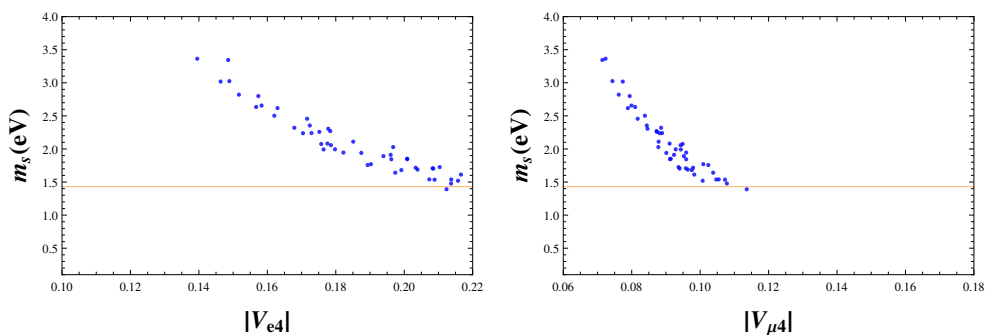


Figure 5. Sterile neutrino mass from eqs. (5.16) for $m_{\tau\tau} = 0$. The yellow line is the current upper bound on m_s as given by global analysis of 3+1 neutrino oscillation data.

Case	M_S	M_D	M_R	Correlations
I	$(0, s_2, s_3)$	$\begin{pmatrix} 0 & a_2 & 0 \\ b_1 & 0 & b_3 \\ c_1 & 0 & 0 \end{pmatrix}$	$\text{diag}(r_1, r_2, r_3)$	$m_{ee} = \frac{m_{e\mu}^2 m_{\tau\tau}}{m_{\mu\mu} m_{\tau\tau} - m_{\mu\tau}^2}$ $m_s = \left -\frac{m_{e\mu}}{V_{e4} V_{\mu 4}} \right $
II	$(0, s_2, s_3)$	$\begin{pmatrix} 0 & 0 & a_3 \\ b_1 & b_2 & 0 \\ c_1 & 0 & 0 \end{pmatrix}$	$\text{diag}(r_1, r_2, r_3)$	Same as Case I
III	$(s_1, 0, s_3)$	$\begin{pmatrix} 0 & 0 & a_3 \\ 0 & b_2 & b_3 \\ 0 & c_2 & 0 \end{pmatrix}$	$\text{diag}(r_1, r_2, r_3)$	Same as Case I
IV	$(s_1, 0, s_3)$	$\begin{pmatrix} a_1 & 0 & 0 \\ b_2 & b_2 & 0 \\ 0 & c_2 & 0 \end{pmatrix}$	$\text{diag}(r_1, r_2, r_3)$	Same as Case I
V	$(s_1, s_2, 0)$	$\begin{pmatrix} 0 & a_2 & 0 \\ 0 & b_2 & b_3 \\ 0 & 0 & c_3 \end{pmatrix}$	$\text{diag}(r_1, r_2, r_3)$	Same as Case I
VI	$(s_1, s_2, 0)$	$\begin{pmatrix} a_1 & 0 & 0 \\ b_1 & 0 & b_3 \\ 0 & 0 & c_3 \end{pmatrix}$	$\text{diag}(r_1, r_2, r_3)$	Same as Case I

Table 3. The various forms of M_D , M_R and M_S which leads to a phenomenologically allowed $m_{e\tau} = 0$.

Case	M_S	M_D	M_R	Correlations
I	$(0, s_2, s_3)$	$\begin{pmatrix} a_1 & 0 & a_3 \\ b_1 & 0 & 0 \\ 0 & c_2 & 0 \end{pmatrix}$	$\begin{pmatrix} 0 & r_2 & 0 \\ r_2 & 0 & 0 \\ 0 & 0 & r_1 \end{pmatrix}$	$m_s = \left -\frac{m_{e\mu}}{V_{e4}V_{\mu4}} \right $
II	$(s_1, 0, s_3)$	$\begin{pmatrix} a_1 & a_2 & 0 \\ 0 & b_2 & 0 \\ c_1 & 0 & 0 \end{pmatrix}$	$\begin{pmatrix} 0 & r_2 & 0 \\ r_2 & 0 & 0 \\ 0 & 0 & r_1 \end{pmatrix}$	Same as Case I
III	$(0, s_2, s_3)$	$\begin{pmatrix} a_1 & a_2 & 0 \\ b_1 & 0 & 0 \\ 0 & 0 & c_3 \end{pmatrix}$	$\begin{pmatrix} 0 & 0 & r_2 \\ 0 & r_1 & 0 \\ r_2 & 0 & 0 \end{pmatrix}$	Same as Case I
IV	$(s_1, s_2, 0)$	$\begin{pmatrix} 0 & a_2 & a_3 \\ 0 & 0 & b_3 \\ c_1 & 0 & 0 \end{pmatrix}$	$\begin{pmatrix} 0 & 0 & r_2 \\ 0 & r_1 & 0 \\ r_2 & 0 & 0 \end{pmatrix}$	Same as Case I
V	$(s_1, 0, s_3)$	$\begin{pmatrix} a_1 & a_2 & 0 \\ 0 & b_2 & b_3 \\ 0 & 0 & c_3 \end{pmatrix}$	$\begin{pmatrix} r_1 & 0 & 0 \\ 0 & 0 & r_2 \\ 0 & r_2 & 0 \end{pmatrix}$	Same as Case I
VI	$(s_1, s_2, 0)$	$\begin{pmatrix} a_1 & a_2 & 0 \\ 0 & b_2 & b_3 \\ 0 & 0 & c_3 \end{pmatrix}$	$\begin{pmatrix} r_1 & 0 & 0 \\ 0 & 0 & r_2 \\ 0 & r_2 & 0 \end{pmatrix}$	Same as Case I

Table 4. The various forms of M_D , M_R and M_S which leads to a phenomenologically allowed $m_{\tau\tau} = 0$.

5.1 NLO correction for MES model

In section 3, the structures of various mass matrices are obtained using the leading order expression of $m_\nu^{3 \times 3}$ as given by equation (2.4) which give rise to texture zeros with exact cancellation. However, if $M_D/M_S \sim 0.1$ NLO corrections can be important. In this section, we discuss the effect of NLO correction terms for MES model corresponding to the allowed texture zeros. The NLO correction term can be calculated following the standard algorithm given in [77]. To calculate the NLO term, let us rewrite equation (2.3) in the form,

$$M_\nu^{4 \times 4} = \begin{pmatrix} \mathcal{M}_L & \mathcal{M}_D^T \\ \mathcal{M}_D & \mathcal{M}_R \end{pmatrix} \quad (5.17)$$

where,

$$\begin{aligned} \mathcal{M}_L &= M_D M_R^{-1} M_D^T, \quad \mathcal{M}_D = M_S (M_R^{-1})^T M_D^T, \quad \mathcal{M}_R = M_S M_R^{-1} M_S^T \\ (m_\nu^{3 \times 3})_{NLO} &= \frac{1}{2} [\mathcal{M}_D^T \mathcal{M}_R^{-1} \mathcal{M}_R^{-1*} \mathcal{M}_D^* \mathcal{M}_L + (\text{last term})^T] \\ &\quad - \frac{1}{2} \mathcal{M}_D^T \mathcal{M}_R^{-1} [\mathcal{M}_D \mathcal{M}_D^\dagger \mathcal{M}_R^{-1*} + (\text{last term})^T] \mathcal{M}_R^{-1} \mathcal{M}_D \\ &= \frac{1}{2} [M_D M_R^{-1} M_S^T (M_S M_R^{-1} M_S^T)^{-1} (M_S^* M_R^{-1*} M_S^\dagger)^{-1} M_S^* (M_R^{-1})^\dagger M_D^\dagger M_D M_R^{-1} M_D^T \\ &\quad + (\text{last term})^T] \end{aligned} \quad (5.18)$$

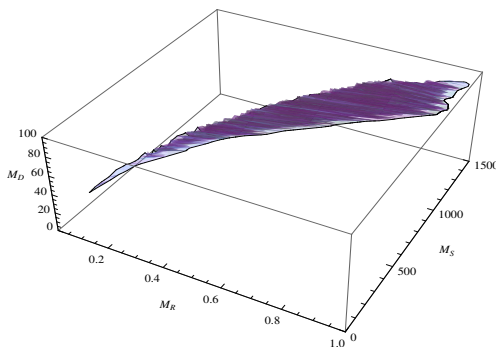


Figure 6. This plot shows the allowed parameter spaces of M_D (GeV), M_R (in units of 10^{15} GeV) and M_S (GeV) which lead to NLO correction term $\sim 10^{-5}$ eV or less.

$$\begin{aligned}
 & -\frac{1}{2} M_D M_R^{-1} M_S^T (M_S M_R^{-1} M_S^T)^{-1} [M_S (M_R^{-1})^T M_D^T M_D^* (M_R^{-1})^* M_S^\dagger \\
 & (M_S M_R^{-1} M_S^T)^{-1*} + (\text{last term})^T] (M_S M_R^{-1} M_S^T)^{-1} M_D M_R^{-1} M_S^T
 \end{aligned} \tag{5.19}$$

In the second line we use the form of \mathcal{M}_L , \mathcal{M}_D and \mathcal{M}_R as given by equation (5.18) to obtain the final form given by equation (5.19). We see that the contribution of the NLO terms of equation (5.19) are proportional to $M_D^4/M_R M_S^2$. This implies that a term of the order $M_D^4/M_R M_S^2$ will add to every term of $m_\nu^{3 \times 3}$ as given by the equation (5.7). To get the specific form of NLO correction term, in equation (5.19), we use the specific forms of M_D , M_R and M_S used for obtaining equation (5.7). The NLO correction term we obtain for (1,3) element of equation (5.7) is $\sim \frac{a_3 b_3 b_1 c_1 r_2^2 s_3^2}{2r_1 (r_3 s_2^2 + r_2 s_3^2)^2}$, which is of the order of $M_D^4/M_R M_S^2$, where a_3 , b_3 , b_1 , c_1 are elements of M_D , r_1 , r_2 are elements of M_R and s_2 , s_3 are elements of M_S . We see here that because of NLO corrections, we no longer have exact cancellation leading to $m_{e\tau} = 0$, unlike the leading order case. But, if we consider representative values of parameters say, $M_D \sim 80$ GeV, $M_R \sim 6 \times 10^{14}$ GeV and $M_S \sim 1000$ GeV then we find that $m_\nu \sim 0.011$ eV, $m_s \sim 1.6$ eV, $R \sim 0.1$ and $\text{NLO} \sim 10^{-5}$ eV. In figure 6 we show the allowed parameter spaces of M_D , M_R and M_S which can lead to NLO correction term $\sim 10^{-5}$ eV or less.⁴ Hence, there exist a parameter space where we can safely neglect NLO correction terms in our analysis compared to leading order terms and consider the texture zero even with the inclusion of the NLO term.⁵ Thus, all the model predictions corresponding to leading order terms remain unchanged. Note that similar conclusions can also be obtained for the texture $m_{\tau\tau} = 0$.

6 Symmetry realization

Singular one zero neutrino mass matrices can be realized using a discrete Abelian flavor symmetry within the context of MES mechanism. Earlier in [52] authors studied the possibilities to enforce zero textures in arbitrary entries of the fermion mass matrices by

⁴In our numerical analysis texture zero (say, $m_{e\tau} = 0$) corresponds to $m_{e\tau} = 10^{-5}$ eV.

⁵We notice that the set of M_D , M_R and M_S which do not give $\text{NLO} \sim 10^{-5}$ eV do not give the one zero textures.

Lepton doublet	$(Z_8 \times Z_2)$	RH Singlet	$(Z_8 \times Z_2)$	ν fields	$(Z_8 \times Z_2)$	Higgs doublet	$(Z_8 \times Z_2)$
\bar{D}_{L_e}	$(\omega^6, -1)$	e_R	$(\omega^2, -1)$	ν_{eR}	$(\omega^5, 1)$	ϕ	$(1, 1)$
\bar{D}_{L_μ}	$(\omega^3, 1)$	μ_R	$(\omega^5, 1)$	$\nu_{\mu R}$	$(\omega^2, -1)$	ϕ'	$(\omega^3, 1)$
\bar{D}_{L_τ}	$(\omega^5, 1)$	τ_R	$(1, 1)$	$\nu_{\tau R}$	$(1, 1)$	ϕ''	$(\omega^2, 1)$

Table 5. Here, \bar{D}_{L_l} denote $SU(2)_L$ doublets and l_R, ν_{lR} ($l = e, \mu, \tau$) are the right-handed (RH) $SU(2)_L$ singlet for charged lepton and neutrino fields respectively. Also, ϕ, ϕ' and ϕ'' are the Higgs doublets.

means of Abelian symmetries in the context of type - I seesaw mechanism. We adopt the same approach to probe the zero textures of m_ν in the context of MES mechanism. We observe that one zero textures of m_ν with a vanishing mass can be realized by $Z_8 \times Z_2$ symmetry. To realize the texture structures we extend the SM particle composition by three right handed neutrinos ($\nu_{eR}, \nu_{\mu R}, \nu_{\tau R}$) as required in MES model and two more Higgs doublets (ϕ', ϕ'') in addition to the SM one (ϕ). Few $SU(2)_L$ scalar singlets ($\chi_i, i = 1, 2$) are required to realize diagonal M_R whereas two singlets $\lambda_i, i = 1, 2$ helps in realizing one zero texture structure of M_S . Note that the model that we discuss here to get the zero texture structure is general, flexible and in no way unique. The additional discrete group Z_2 is introduced to restrict some of the unwanted terms in the Lagrangian. For illustration, we present the detailed symmetry realization of our two viable textures of m_ν ($m_{e\tau}, m_{\tau\tau} = 0$). The particle assignments for ($m_{e\tau} = 0$ which is allowed by current data (case II) under the action of $Z_8 \times Z_2$ symmetry are given in table 5.

According to the charge assignments of the leptonic field given in table 5 the bilinears $\bar{D}_{L_l} l_R, \bar{D}_{L_l} \nu_{lR}$ and $\nu_{lR}^T C^{-1} \nu_{lR}$ relevant for M_l, M_D and M_R transform as,

$$\bar{D}_{L_l} l_R \sim \begin{pmatrix} 1 & \omega^3 & \omega^6 \\ \omega^5 & 1 & \omega^3 \\ \omega^7 & \omega^2 & \omega^5 \end{pmatrix}, \quad \bar{D}_{L_l} \nu_{lR} \sim \begin{pmatrix} \omega^3 & 1 & \omega^6 \\ 1 & \omega^5 & \omega^3 \\ \omega^2 & \omega^7 & \omega^5 \end{pmatrix}, \quad \nu_{lR} \nu_{lR}^T \sim \begin{pmatrix} \omega^2 & \omega^7 & \omega^5 \\ \omega^7 & \omega^4 & \omega^2 \\ \omega^5 & \omega^2 & 1 \end{pmatrix},$$

where $\omega = e^{\pi i/4}, \omega^8 = 1$. We introduce three $SU(2)_L$ doublet Higgs (ϕ, ϕ', ϕ''). One of these Higgs doublet ϕ , is invariant under Z_8 while the other two fields transforms as: $\phi' \rightarrow \omega^3 \phi'$ ($\tilde{\phi}' \rightarrow \omega^5 \tilde{\phi}'$) and $\phi'' \rightarrow \omega^2 \phi''$ ($\tilde{\phi}'' \rightarrow \omega^6 \tilde{\phi}''$). The $(Z_8 \times Z_2)$ invariant Yukawa Lagrangian than becomes

$$-\mathcal{L}_Y = Y_{ee} \bar{D}_{L_e} e_R \phi + Y_{\mu\mu} \bar{D}_{L_\mu} \mu_R \phi + Y_{\tau\tau} \bar{D}_{L_\tau} \tau_R \phi + Y_{e\mu} \bar{D}_{L_e} \nu_{\mu R} \tilde{\phi} + Y_{\mu e} \bar{D}_{L_\mu} \nu_{eR} \tilde{\phi} + Y_{\mu\tau} \bar{D}_{L_\mu} \nu_{\tau R} \tilde{\phi}' + Y_{\tau e} \bar{D}_{L_\tau} \nu_{eR} \tilde{\phi}'' + h.c.. \quad (6.1)$$

here all $\tilde{\phi} = i\tau_2 \phi^*$. The Higgs fields acquires the vacuum expectation values $\langle \phi \rangle_o \neq 0$ and results in the M_l and M_D of the following form,

$$M_l = \begin{pmatrix} m_e & 0 & 0 \\ 0 & m_\mu & 0 \\ 0 & 0 & m_\tau \end{pmatrix}, \quad M_D = \begin{pmatrix} 0 & a_2 & 0 \\ b_1 & 0 & b_3 \\ c_1 & 0 & 0 \end{pmatrix}. \quad (6.2)$$

Here $m_e = Y_{ee} \langle \phi \rangle_o, m_\mu = Y_{\mu\mu} \langle \phi \rangle_o, m_\tau = Y_{\tau\tau} \langle \phi \rangle_o$. The elements of M_D are $a_2 = Y_{e\mu} \langle \phi^* \rangle_o, b_1 = Y_{\mu e} \langle \phi^* \rangle_o, b_3 = Y_{\mu\tau} \langle \phi'^* \rangle_o$ and $c_1 = Y_{\tau e} \langle \phi''^* \rangle_o$. For the right-handed Majorana mass

Scalar singlet	$(Z_8 \times Z_2)$	Scalar singlet	$(Z_8 \times Z_2)$
χ_1	$(\omega^6, 1)$	λ_1	$(1, 1)$
χ_2	$(\omega^4, 1)$	λ_2	$(\omega^2, -1)$

Table 6. Here, scalar singlet χ_1 and χ_2 give M_R whereas λ_1 and λ_2 give M_S .

Lepton doublet	$(Z_8 \times Z_2)$	RH Singlet	$(Z_8 \times Z_2)$	ν fields	$(Z_8 \times Z_2)$	Higgs doublet	$(Z_8 \times Z_2)$
\bar{D}_{Le}	$(1, 1)$	e_R	$(1, 1)$	ν_{eR}	$(\omega^3, 1)$	ϕ	$(1, 1)$
$\bar{D}_{L\mu}$	$(\omega^5, -1)$	μ_R	$(\omega^3, -1)$	$\nu_{\mu R}$	$(\omega^5, 1)$	ϕ'	$(\omega^3, 1)$
$\bar{D}_{L\tau}$	$(\omega^3, 1)$	τ_R	$(\omega^2, 1)$	$\nu_{\tau R}$	$(1, -1)$		

Table 7. The fields descriptions are same as given in table 5.

matrix (M_R) and for the mass matrix M_S , we introduce few $SU(2)_L$ scalar singlets and their transformation under $Z_8 \times Z_2$ is given in the table 6. Thus the mass matrices M_R and M_S becomes,

$$M_R = \begin{pmatrix} r_1 & 0 & 0 \\ 0 & r_2 & 0 \\ 0 & 0 & r_3 \end{pmatrix}, \quad M_S = \begin{pmatrix} 0 & s_2 & s_3 \end{pmatrix}. \quad (6.3)$$

We also give the transformation to the singlet field S as $(\omega^6, -1)$ under $(Z_8 \times Z_2)$ which will prevent the term of the form $\bar{S}^c S$ as demand by the MES model will still give the correct form of M_S .

Using the minimal extended type I seesaw given in Eqn (2.4) with the mass matrices M_D , M_R and M_S as discussed above leads to effective neutrino mass matrix m_ν with a texture zero at (1,3) position.

Similarly, one can assign the various fields transformation under the action of $(Z_8 \times Z_2)$ to obtain the texture with $m_{\tau\tau} = 0$. The form of $M_D^{(18)}$, M_R and M_S used to get $m_{\tau\tau} = 0$ are given in eq. (3.8). We summarize the fields transformations in the table 7. Here, no extra scalar singlet is needed to obtain the mass structure of M_R which has $L_e - L_\mu$ symmetry and for M_S we need two scalar singlets (λ_1, λ_2) which transform under $Z_8 \times Z_2$ as $(\omega^2, 1)$ and $(\omega^7, -1)$ respectively. We also give transformation to singlet field S as $(\omega, 1)$ under $(Z_8 \times Z_2)$ which will prevent the term $\bar{S}^c S$. Note that symmetry realization of this texture is more economical than the $m_{e\tau} = 0$ texture.

7 Conclusions

In this paper we have studied the low energy phenomenology of the minimal extended type I seesaw model which can accommodate an eV scale light sterile neutrino [22, 26]. This model is motivated by the recent experimental evidences which support the existence of light sterile neutrinos in addition to three active neutrinos. In this model, apart from three right handed neutrinos, an extra gauge singlet S is added to the SM. Under the minimal

extended seesaw mechanism, this model give rise to three active neutrinos in the sub-eV scale with one of the active neutrinos having vanishing mass and one sterile neutrino in the eV scale. In this model the Dirac mass matrix, M_D , is an arbitrary 3×3 complex matrix, the Majorana mass matrix M_R is a 3×3 complex symmetric matrix and M_S which couples the right handed neutrinos and the singlet S is a 1×3 matrix.

We obtain different textures of M_D , M_R and M_S that give rise to phenomenologically allowed zero textures in the low energy neutrino mass matrix, m_ν . The maximum number of zeros in M_D that results in viable m_ν are found to be five. Thus, there are 126 different possible structures of M_D to be probed. We consider four possible structures of M_R with one diagonal and three non diagonal forms. The maximum number of zeros in M_S is one as two zeros do not result in phenomenologically viable textures of m_ν . This leads to three possible structures of M_S . After analyzing all the different combinations we obtain only two viable one zero textures of m_ν ($m_{e\tau} = 0$ and $m_{\tau\tau} = 0$) with different possible structures of M_D , M_R and M_S . We study these textures of m_ν in the light of the current oscillation data. Both these textures have inverted hierarchical mass spectrum and we get constraints on observables like effective Majorana neutrino mass m_{ee} and Dirac CP phase δ_{13} . For the texture $m_{e\tau} = 0$, we obtain the allowed values of Dirac CP phase δ_{13} is around $\pm 90^\circ$. Note that $\delta_{13} \sim -90^\circ$ is favored by current neutrino oscillation experiments. For $m_{\tau\tau} = 0$, δ_{13} lies between $(150^\circ - 240^\circ)$. The allowed range for the effective Majorana mass is different for both these textures. It can thus be used to distinguish between the two textures. Also, in our study we observed that due to improved constraints on the mass squared differences and θ_{13} the texture $m_{\tau\tau} = 0$ disfavours higher octant of θ_{23} .

Next we studied the predictions of the MES model for the Yukawa matrices that gave viable forms of m_ν and check whether any extra correlations can come from the model. This is expected since in the framework of this model both the active and sterile neutrino masses as well as the active sterile mixing depend on the parameters of the Yukawa matrices M_D , M_R and M_S . Thus, there may be additional relations between different observables, which are the predictions of the model. We find that some of the Yukawa matrices which can generate allowed one zero textures $m_{e\tau} = 0$ and $m_{\tau\tau} = 0$ in the active neutrino mass matrix, m_ν , cannot satisfy the extra correlations coming from the predictions of the MES model. Our analysis reveals that due to these additional correlations among the $126 \times 4 \times 3 = 1512$ possible combinations of M_D , M_R and M_S , only 6 combinations giving $m_{e\tau} = 0$ and other 6 combinations giving $m_{\tau\tau} = 0$ are allowed from the current oscillation data. The 6 allowed combinations which give $m_{e\tau} = 0$, reveal severe restrictions on the values of θ_{23} and θ_{13} due to the extra correlations in the MES model and only the lower octant of θ_{23} and relatively higher values of θ_{13} remains allowed. In addition an interesting correlation is obtained connecting the mass of the sterile neutrino to the active sterile mixing parameters which also involves the light neutrino masses and mixing. Thus this correlation connects the active and the sterile sector. For $m_{e\tau} = 0$ the prediction for the sterile neutrino mass obtained from the MES model is in complete agreement with what is obtained from global analysis. The texture, $m_{\tau\tau} = 0$ also predicts a correlation for sterile neutrino mass. This however is in marginal agreement with the global analysis. We also explored the consequences of NLO correction terms in our analysis and depicted

the parameter space in M_D , M_R and M_S for which the NLO corrections can be neglected as compared to the leading order term. Finally, working within the framework of MES mechanism, we present simple discrete Abelian symmetry models $Z_8 \times Z_2$ leading to the two phenomenologically allowed zero textures of m_ν .

In conclusion, we analyzed the low energy prediction of the minimal extended seesaw model that can give an eV scale sterile neutrino. We emphasize that this task is performed for the first time in this paper. The results described in our analysis shows the compatibility of this model to the neutrino oscillation data. We also find correlations that can be tested in future experiments. This kind of study is indispensable to test the viability of a given model in the context of present and forthcoming neutrino oscillation experiments.

Acknowledgments

Authors are grateful to Anjan Joshipura for discussions and useful comments in the initial stages of the work. The work of SG is supported by the Australian Research Council through the ARC Center of Excellence for Particle Physics (CoEPP Adelaide) at the Terascale (CE110001004). The work of MG is supported by the ‘‘Grant-in-Aid for Scientific Research of the Ministry of Education, Science and Culture, Japan’’, under Grant No. 25105009.

Open Access. This article is distributed under the terms of the Creative Commons Attribution License ([CC-BY 4.0](https://creativecommons.org/licenses/by/4.0/)), which permits any use, distribution and reproduction in any medium, provided the original author(s) and source are credited.

References

- [1] M.C. Gonzalez-Garcia, M. Maltoni and T. Schwetz, *Global Analyses of Neutrino Oscillation Experiments*, *Nucl. Phys. B* **908** (2016) 199 [[arXiv:1512.06856](https://arxiv.org/abs/1512.06856)] [[INSPIRE](#)].
- [2] D.V. Forero, M. Tortola and J.W.F. Valle, *Neutrino oscillations refitted*, *Phys. Rev. D* **90** (2014) 093006 [[arXiv:1405.7540](https://arxiv.org/abs/1405.7540)] [[INSPIRE](#)].
- [3] F. Capozzi, E. Lisi, A. Marrone, D. Montanino and A. Palazzo, *Neutrino masses and mixings: Status of known and unknown 3ν parameters*, *Nucl. Phys. B* **908** (2016) 218 [[arXiv:1601.07777](https://arxiv.org/abs/1601.07777)] [[INSPIRE](#)].
- [4] PLANCK collaboration, P.A.R. Ade et al., *Planck 2015 results. XIII. Cosmological parameters*, *Astron. Astrophys.* **594** (2016) A13 [[arXiv:1502.01589](https://arxiv.org/abs/1502.01589)] [[INSPIRE](#)].
- [5] S. Mertens, *Status of the katrin experiment and prospects to search for kev-mass sterile neutrinos in tritium β -decay*, *Physics Proc.* **61** (2015) 267.
- [6] LSND collaboration, C. Athanassopoulos et al., *Evidence for $\bar{\nu}_\mu \rightarrow \bar{\nu}_e$ oscillations from the LSND experiment at LAMPF*, *Phys. Rev. Lett.* **77** (1996) 3082 [[nuc1-ex/9605003](https://arxiv.org/abs/nuc1-ex/9605003)] [[INSPIRE](#)].
- [7] LSND collaboration, C. Athanassopoulos et al., *Evidence for $\nu_\mu \rightarrow \nu_e$ neutrino oscillations from LSND*, *Phys. Rev. Lett.* **81** (1998) 1774 [[nuc1-ex/9709006](https://arxiv.org/abs/nuc1-ex/9709006)] [[INSPIRE](#)].
- [8] LSND collaboration, A. Aguilar-Arevalo et al., *Evidence for neutrino oscillations from the observation of anti-neutrino(electron) appearance in a anti-neutrino(muon) beam*, *Phys. Rev. D* **64** (2001) 112007 [[hep-ex/0104049](https://arxiv.org/abs/hep-ex/0104049)] [[INSPIRE](#)].

- [9] MINIBoONE collaboration, A.A. Aguilar-Arevalo et al., *A Combined $\nu_\mu \rightarrow \nu_e$ and $\bar{\nu}_\mu \rightarrow \bar{\nu}_e$ Oscillation Analysis of the MiniBooNE Excesses*, [arXiv:1207.4809](#) [INSPIRE].
- [10] C. Giunti and M. Laveder, *Statistical Significance of the Gallium Anomaly*, *Phys. Rev. C* **83** (2011) 065504 [[arXiv:1006.3244](#)] [INSPIRE].
- [11] G. Mention, M. Fechner, T. Lasserre, T.A. Mueller, D. Lhuillier, M. Cribier et al., *The Reactor Antineutrino Anomaly*, *Phys. Rev. D* **83** (2011) 073006 [[arXiv:1101.2755](#)] [INSPIRE].
- [12] K.N. Abazajian et al., *Light Sterile Neutrinos: A White Paper*, [arXiv:1204.5379](#) [INSPIRE].
- [13] J. Kopp, M. Maltoni and T. Schwetz, *Are there sterile neutrinos at the eV scale?*, *Phys. Rev. Lett.* **107** (2011) 091801 [[arXiv:1103.4570](#)] [INSPIRE].
- [14] J.M. Conrad, C.M. Ignarra, G. Karagiorgi, M.H. Shaevitz and J. Spitz, *Sterile Neutrino Fits to Short Baseline Neutrino Oscillation Measurements*, *Adv. High Energy Phys.* **2013** (2013) 163897 [[arXiv:1207.4765](#)] [INSPIRE].
- [15] C. Giunti and M. Laveder, *3+1 and 3+2 Sterile Neutrino Fits*, *Phys. Rev. D* **84** (2011) 073008 [[arXiv:1107.1452](#)] [INSPIRE].
- [16] J.J. Gomez-Cadenas and M.C. Gonzalez-Garcia, *Future tau-neutrino oscillation experiments and present data*, *Z. Phys. C* **71** (1996) 443 [[hep-ph/9504246](#)] [INSPIRE].
- [17] S. Goswami, *Accelerator, reactor, solar and atmospheric neutrino oscillation: Beyond three generations*, *Phys. Rev. D* **55** (1997) 2931 [[hep-ph/9507212](#)] [INSPIRE].
- [18] M. Maltoni, T. Schwetz, M.A. Tortola and J.W.F. Valle, *Constraining neutrino oscillation parameters with current solar and atmospheric data*, *Phys. Rev. D* **67** (2003) 013011 [[hep-ph/0207227](#)] [INSPIRE].
- [19] J. Hamann, S. Hannestad, G.G. Raffelt, I. Tamborra and Y.Y.Y. Wong, *Cosmology seeking friendship with sterile neutrinos*, *Phys. Rev. Lett.* **105** (2010) 181301 [[arXiv:1006.5276](#)] [INSPIRE].
- [20] E. Giusarma et al., *Constraints on massive sterile neutrino species from current and future cosmological data*, *Phys. Rev. D* **83** (2011) 115023 [[arXiv:1102.4774](#)] [INSPIRE].
- [21] E.J. Chun, A.S. Joshipura and A. Yu. Smirnov, *QuasiGoldstone fermion as a sterile neutrino*, *Phys. Rev. D* **54** (1996) 4654 [[hep-ph/9507371](#)] [INSPIRE].
- [22] J. Barry, W. Rodejohann and H. Zhang, *Light Sterile Neutrinos: Models and Phenomenology*, *JHEP* **07** (2011) 091 [[arXiv:1105.3911](#)] [INSPIRE].
- [23] C.-S. Chen and R. Takahashi, *Hierarchically Acting Sterile Neutrinos*, *Eur. Phys. J. C* **72** (2012) 2089 [[arXiv:1112.2102](#)] [INSPIRE].
- [24] A. de Gouvêa, J. Jenkins and N. Vasudevan, *Neutrino Phenomenology of Very Low-Energy Seesaws*, *Phys. Rev. D* **75** (2007) 013003 [[hep-ph/0608147](#)] [INSPIRE].
- [25] P.S. Bhupal Dev and A. Pilaftsis, *Light and Superlight Sterile Neutrinos in the Minimal Radiative Inverse Seesaw Model*, *Phys. Rev. D* **87** (2013) 053007 [[arXiv:1212.3808](#)] [INSPIRE].
- [26] H. Zhang, *Light Sterile Neutrino in the Minimal Extended Seesaw*, *Phys. Lett. B* **714** (2012) 262 [[arXiv:1110.6838](#)] [INSPIRE].
- [27] J. Heeck and H. Zhang, *Exotic Charges, Multicomponent Dark Matter and Light Sterile Neutrinos*, *JHEP* **05** (2013) 164 [[arXiv:1211.0538](#)] [INSPIRE].

- [28] R. Allahverdi, B. Dutta and R.N. Mohapatra, *Schizophrenic Neutrinos and ν -less Double Beta Decay*, *Phys. Lett. B* **695** (2011) 181 [[arXiv:1008.1232](#)] [[INSPIRE](#)].
- [29] A.C.B. Machado and V. Pleitez, *Schizophrenic active neutrinos and exotic sterile neutrinos*, *Phys. Lett. B* **698** (2011) 128 [[arXiv:1008.4572](#)] [[INSPIRE](#)].
- [30] S. Dev, S. Kumar, S. Verma and S. Gupta, *Phenomenology of two-texture zero neutrino mass matrices*, *Phys. Rev. D* **76** (2007) 013002 [[hep-ph/0612102](#)] [[INSPIRE](#)].
- [31] Z.-z. Xing, *Texture zeros and Majorana phases of the neutrino mass matrix*, *Phys. Lett. B* **530** (2002) 159 [[hep-ph/0201151](#)] [[INSPIRE](#)].
- [32] Z.-z. Xing, *A Full determination of the neutrino mass spectrum from two zero textures of the neutrino mass matrix*, *Phys. Lett. B* **539** (2002) 85 [[hep-ph/0205032](#)] [[INSPIRE](#)].
- [33] B.R. Desai, D.P. Roy and A.R. Vaucher, *Three neutrino mass matrices with two texture zeros*, *Mod. Phys. Lett. A* **18** (2003) 1355 [[hep-ph/0209035](#)] [[INSPIRE](#)].
- [34] S. Dev, S. Kumar, S. Verma and S. Gupta, *CP violation in two texture zero neutrino mass matrices*, *Phys. Lett. B* **656** (2007) 79 [[arXiv:0708.3321](#)] [[INSPIRE](#)].
- [35] S. Dev, S. Kumar, S. Verma and S. Gupta, *Phenomenological implications of a class of neutrino mass matrices*, *Nucl. Phys. B* **784** (2007) 103 [[hep-ph/0611313](#)] [[INSPIRE](#)].
- [36] S. Kumar, *Implications of a class of neutrino mass matrices with texture zeros for non-zero θ_{13}* , *Phys. Rev. D* **84** (2011) 077301 [[arXiv:1108.2137](#)] [[INSPIRE](#)].
- [37] H. Fritzsch, Z.-z. Xing and S. Zhou, *Two-zero Textures of the Majorana Neutrino Mass Matrix and Current Experimental Tests*, *JHEP* **09** (2011) 083 [[arXiv:1108.4534](#)] [[INSPIRE](#)].
- [38] D. Meloni and G. Blankenburg, *Fine-tuning and naturalness issues in the two-zero neutrino mass textures*, *Nucl. Phys. B* **867** (2013) 749 [[arXiv:1204.2706](#)] [[INSPIRE](#)].
- [39] P.O. Ludl, S. Morisi and E. Peinado, *The Reactor mixing angle and CP-violation with two texture zeros in the light of T2K*, *Nucl. Phys. B* **857** (2012) 411 [[arXiv:1109.3393](#)] [[INSPIRE](#)].
- [40] W. Grimus and P.O. Ludl, *Two-parameter neutrino mass matrices with two texture zeros*, *J. Phys. G* **40** (2013) 055003 [[arXiv:1208.4515](#)] [[INSPIRE](#)].
- [41] M. Ghosh, S. Goswami and S. Gupta, *Two Zero Mass Matrices and Sterile Neutrinos*, *JHEP* **04** (2013) 103 [[arXiv:1211.0118](#)] [[INSPIRE](#)].
- [42] M. Ghosh, S. Goswami, S. Gupta and C.S. Kim, *Implication of a vanishing element in the $3+1$ scenario*, *Phys. Rev. D* **88** (2013) 033009 [[arXiv:1305.0180](#)] [[INSPIRE](#)].
- [43] Y. Zhang, *Majorana neutrino mass matrices with three texture zeros and the sterile neutrino*, *Phys. Rev. D* **87** (2013) 053020 [[arXiv:1301.7302](#)] [[INSPIRE](#)].
- [44] N. Nath, M. Ghosh and S. Gupta, *Understanding the masses and mixings of one-zero textures in $3+1$ scenario*, *Int. J. Mod. Phys. A* **31** (2016) 1650132 [[arXiv:1512.00635](#)] [[INSPIRE](#)].
- [45] D. Borah, M. Ghosh, S. Gupta, S. Prakash and S.K. Raut, *Analysis of four-zero textures in the $3+1$ neutrino framework*, *Phys. Rev. D* **94** (2016) 113001 [[arXiv:1606.02076](#)] [[INSPIRE](#)].
- [46] G.C. Branco, D. Emmanuel-Costa, M.N. Rebelo and P. Roy, *Four Zero Neutrino Yukawa Textures in the Minimal Seesaw Framework*, *Phys. Rev. D* **77** (2008) 053011 [[arXiv:0712.0774](#)] [[INSPIRE](#)].

- [47] S. Goswami and A. Watanabe, *Minimal Seesaw Textures with Two Heavy Neutrinos*, *Phys. Rev. D* **79** (2009) 033004 [[arXiv:0807.3438](#)] [[INSPIRE](#)].
- [48] S. Goswami, S. Khan and A. Watanabe, *Hybrid textures in minimal seesaw mass matrices*, *Phys. Lett. B* **693** (2010) 249 [[arXiv:0811.4744](#)] [[INSPIRE](#)].
- [49] S. Choubey, W. Rodejohann and P. Roy, *Phenomenological consequences of four zero neutrino Yukawa textures*, *Nucl. Phys. B* **808** (2009) 272 [Erratum *ibid.* **B 818** (2009) 136] [[arXiv:0807.4289](#)] [[INSPIRE](#)].
- [50] L. Lavoura, *New texture-zero patterns for lepton mixing*, *J. Phys. G* **42** (2015) 105004 [[arXiv:1502.03008](#)] [[INSPIRE](#)].
- [51] R.M. Fonseca and W. Grimus, *Classification of lepton mixing matrices from finite residual symmetries*, *JHEP* **09** (2014) 033 [[arXiv:1405.3678](#)] [[INSPIRE](#)].
- [52] W. Grimus, A.S. Joshipura, L. Lavoura and M. Tanimoto, *Symmetry realization of texture zeros*, *Eur. Phys. J. C* **36** (2004) 227 [[hep-ph/0405016](#)] [[INSPIRE](#)].
- [53] S. Gariazzo, C. Giunti, M. Laveder, Y.F. Li and E.M. Zanvanin, *Light sterile neutrinos*, *J. Phys. G* **43** (2016) 033001 [[arXiv:1507.08204](#)] [[INSPIRE](#)].
- [54] C. Giunti, *Oscillations beyond three-neutrino mixing*, talk given at *Neutrino 2016*, London, U.K., July 4–9, 2016.
- [55] T. Schwetz, *Global oscillation fits with sterile neutrinos*, talk given at *Sterile Neutrino at the Crossroads*, Virginia Tech, VA, U.S.A., September 25–28, 2011.
- [56] S. Goswami, S. Khan and W. Rodejohann, *Minimal Textures in Seesaw Mass Matrices and their low and high Energy Phenomenology*, *Phys. Lett. B* **680** (2009) 255 [[arXiv:0905.2739](#)] [[INSPIRE](#)].
- [57] A. Merle and W. Rodejohann, *The Elements of the neutrino mass matrix: Allowed ranges and implications of texture zeros*, *Phys. Rev. D* **73** (2006) 073012 [[hep-ph/0603111](#)] [[INSPIRE](#)].
- [58] E.I. Lashin and N. Chamoun, *The One-zero Textures of Majorana Neutrino Mass Matrix and Current Experimental Tests*, *Phys. Rev. D* **85** (2012) 113011 [[arXiv:1108.4010](#)] [[INSPIRE](#)].
- [59] R.R. Gautam, M. Singh and M. Gupta, *Neutrino mass matrices with one texture zero and a vanishing neutrino mass*, *Phys. Rev. D* **92** (2015) 013006 [[arXiv:1506.04868](#)] [[INSPIRE](#)].
- [60] L. Lavoura, W. Rodejohann and A. Watanabe, *Reproducing lepton mixing in a texture zero model*, *Phys. Lett. B* **726** (2013) 352 [[arXiv:1307.6421](#)] [[INSPIRE](#)].
- [61] K. Harigaya, M. Ibe and T.T. Yanagida, *Seesaw Mechanism with Occam’s Razor*, *Phys. Rev. D* **86** (2012) 013002 [[arXiv:1205.2198](#)] [[INSPIRE](#)].
- [62] A.S. Joshipura, *Neutrino masses and mixing from flavour antisymmetry*, *JHEP* **11** (2015) 186 [[arXiv:1506.00455](#)] [[INSPIRE](#)].
- [63] A.S. Joshipura and N. Nath, *Neutrino masses and mixing in A_5 with flavor antisymmetry*, *Phys. Rev. D* **94** (2016) 036008 [[arXiv:1606.01697](#)] [[INSPIRE](#)].
- [64] T2K collaboration, K. Abe et al., *Measurements of neutrino oscillation in appearance and disappearance channels by the T2K experiment with 6.6×10^{20} protons on target*, *Phys. Rev. D* **91** (2015) 072010 [[arXiv:1502.01550](#)] [[INSPIRE](#)].
- [65] T2K collaboration, M. Ravonel Salzgeber, *Anti-neutrino oscillations with T2K*, [[arXiv:1508.06153](#)] [[INSPIRE](#)].

- [66] NOVA collaboration, P. Adamson et al., *First measurement of electron neutrino appearance in NOvA*, *Phys. Rev. Lett.* **116** (2016) 151806 [[arXiv:1601.05022](#)] [[INSPIRE](#)].
- [67] NOVA collaboration, P. Adamson et al., *First measurement of muon-neutrino disappearance in NOvA*, *Phys. Rev. D* **93** (2016) 051104 [[arXiv:1601.05037](#)] [[INSPIRE](#)].
- [68] CUORE collaboration, P. Gorla, *The CUORE experiment: Status and prospects*, *J. Phys. Conf. Ser.* **375** (2012) 042013 [[INSPIRE](#)].
- [69] J.F. Wilkerson et al., *The Majorana demonstrator: A search for neutrinoless double-beta decay of germanium-76*, *J. Phys. Conf. Ser.* **375** (2012) 042010 [[INSPIRE](#)].
- [70] A.S. Barabash, *SeperNEMO double beta decay experiment*, *J. Phys. Conf. Ser.* **375** (2012) 042012 [[arXiv:1112.1784](#)] [[INSPIRE](#)].
- [71] KAMLAND-ZEN collaboration, A. Gando et al., *Limit on Neutrinoless $\beta\beta$ Decay of ^{136}Xe from the First Phase of KamLAND-Zen and Comparison with the Positive Claim in ^{76}Ge* , *Phys. Rev. Lett.* **110** (2013) 062502 [[arXiv:1211.3863](#)] [[INSPIRE](#)].
- [72] EXO-200 collaboration, M. Auger et al., *Search for Neutrinoless Double-Beta Decay in ^{136}Xe with EXO-200*, *Phys. Rev. Lett.* **109** (2012) 032505 [[arXiv:1205.5608](#)] [[INSPIRE](#)].
- [73] DAYA BAY collaboration, F.P. An et al., *Improved Search for a Light Sterile Neutrino with the Full Configuration of the Daya Bay Experiment*, *Phys. Rev. Lett.* **117** (2016) 151802 [[arXiv:1607.01174](#)] [[INSPIRE](#)].
- [74] ICECUBE collaboration, M.G. Aartsen et al., *Searches for Sterile Neutrinos with the IceCube Detector*, *Phys. Rev. Lett.* **117** (2016) 071801 [[arXiv:1605.01990](#)] [[INSPIRE](#)].
- [75] MINOS collaboration, P. Adamson et al., *Search for Sterile Neutrinos Mixing with Muon Neutrinos in MINOS*, *Phys. Rev. Lett.* **117** (2016) 151803 [[arXiv:1607.01176](#)] [[INSPIRE](#)].
- [76] MINOS, DAYA BAY collaboration, P. Adamson et al., *Limits on Active to Sterile Neutrino Oscillations from Disappearance Searches in the MINOS, Daya Bay and Bugey-3 Experiments*, *Phys. Rev. Lett.* **117** (2016) 151801 [[arXiv:1607.01177](#)] [[INSPIRE](#)].
- [77] W. Grimus and L. Lavoura, *The Seesaw mechanism at arbitrary order: Disentangling the small scale from the large scale*, *JHEP* **11** (2000) 042 [[hep-ph/0008179](#)] [[INSPIRE](#)].